STAR FORMATION ACROSS THE GALAXY : OBSERVATIONS AND MODELLING OF THE SPECTRAL ENERGY DISTRIBUTIONS OF YOUNG STARS

Thomas Pierre Robitaille

A Thesis Submitted for the Degree of PhD
at the
University of St. Andrews

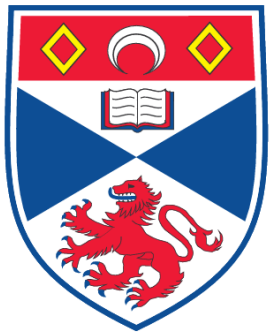

2009

Star Formation across the Galaxy

Observations and Modelling of the Spectral Energy Distributions of Young Stars

by

Thomas Pierre Robitaille

Submitted for the degree of Doctor of Philosophy in Astrophysics

5th September 2008

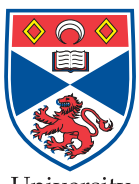

University
of
St Andrews

Declaration

I, Thomas Robitaille, hereby certify that this thesis, which is approximately 50,000 words in length, has been written by me, that it is the record of work carried out by me and that it has not been submitted in any previous application for a higher degree.

Date Signature of candidate

I was admitted as a research student in September 2005 and as a candidate for the degree of PhD in September 2005; the higher study for which this is a record was carried out in the University of St Andrews between 2005 and 2008.

Date Signature of candidate

I hereby certify that the candidate has fulfilled the conditions of the Resolution and Regulations appropriate for the degree of PhD in the University of St Andrews and that the candidate is qualified to submit this thesis in application for that degree.

Date Signature of supervisor

Copyright Agreement

In submitting this thesis to the University of St Andrews we understand that we are giving permission for it to be made available for use in accordance with the regulations of the University Library for the time being in force, subject to any copyright vested in the work not being affected thereby. We also understand that the title and the abstract will be published, and that a copy of the work may be made and supplied to any bona fide library or research worker, that my thesis will be electronically accessible for personal or research use unless exempt by award of an embargo as requested below, and that the library has the right to migrate my thesis into new electronic forms as required to ensure continued access to the thesis. We have obtained any third-party copyright permissions that may be required in order to allow such access and migration, or have requested the appropriate embargo below.

The following is an agreed request by candidate and supervisor regarding the electronic publication of this thesis: Access to Printed copy and electronic publication of thesis through the University of St Andrews.

Date Signature of candidate

Date Signature of supervisor

Abstract

In the last few decades, the emergence of large-scale infrared surveys has led to a revolution in the study of star formation. In particular, NASA's *Spitzer Space Telescope* has recently carried out mid- and far-infrared observations of numerous star formation regions with unprecedented resolution and sensitivity, and has uncovered thousands of forming stars. In combination with present and future large-scale near-infrared and sub-mm surveys, spectral energy distributions from near-infrared to mm wavelengths will be available for these thousands of young stars. Never before has there been such a wealth of multi-wavelength data for so many young stars.

Traditional techniques for studying the physical properties of young stars through their spectral energy distributions have usually focused either on the analysis of many sources using simple observational diagnostics such as colours or spectral indices, or on the analysis of a few sources through the detailed modelling of their full spectral energy distributions.

The work presented in the first part of this thesis aims to bridge these two techniques through the efficient modelling of the spectral energy distributions of many young stars. In particular, the technique developed for this work makes it straightforward to find out how well different physical parameters are constrained, whether any parameters are degenerate, and whether additional data would resolve the degeneracies.

In the second part of this thesis, a census of intrinsically red sources observed by *Spitzer* in the Galactic plane is presented, including a catalogue of over 11,000 likely young stellar objects. This sample of sources is the largest uniformly selected sample of young stars to date, and effectively provides a map of the sites of star formation in the mid-plane of the Milky-Way. In parallel, this census has uncovered over 7,000 candidate asymptotic giant branch stars, of which over 1,000 are variable at 4.5 or 8.0 μm.

Acknowledgements

I would first like to thank my supervisor Kenny Wood for his continued support and enthusiasm for the work I have carried out during my PhD. He has always encouraged me to choose my own areas of investigation, and that freedom has prepared me well for the future. I would also like to thank Ian Bonnell, my second supervisor, for many interesting discussions. I am of course deeply indebted to Barb Whitney, with whom I have collaborated on many projects, and who has helped make my work known to the community – I have always considered her as one of my PhD supervisors.

I would also like to thank Ed Churchwell and the GLIMPSE team, including Rémy Indebetouw, Marilyn Meade, Brian Babler, Bob Benjamin, and Barb for having done such a fantastic job at processing the huge amount of *Spitzer* data, and producing such beautiful mid-infrared images of the Galactic Plane. These data have been the inspiration for much of the work presented in this thesis.

I would like to thank all the PhD students in the St Andrews Astronomy group for making life as a PhD student a lot of fun, including the regular lunches at the Whey Pat, everyone in the Astronomy group for interesting coffee-time conversations, and Ian Taylor for making sure that the computers and the network were always running smoothly!

Finally, I would like to thank Katharine for her much needed moral support during my PhD, and my parents and sister for having always been encouraging and enthusiastic about my pursuit of academic studies in Astronomy.

Contents

List of Figures

List of Tables

1

The Formation of Stars

The origin of the Earth, the Planets, the Sun, and the Stars has been one of humanity's oldest questions, yet it is only in the last half-century that we have started to truly understand the processes that ultimately led to their formation. The work presented in this thesis covers a large range of evolutionary stages in the lives of young stars, from the initial collapse of molecular cores to the onset of hydrogen fusion. This chapter gives a brief historical view of the discovery of young stars (§1.1), an overview of our current understanding of the formation of low-, intermediate-, and high-mass stars (§1.2), and a description of the techniques used to study unresolved young stars (§1.3)

1.1 The Nebular Hypothesis

In a letter to Richard Bentley in 1692, Isaac Newton was remarkably insightful in identifying gravity as the main driving force for the formation of stars:

> [...] it seems to me, that if the matter of our Sun and Planets and all the matter in the Universe was eavenly scattered throughout all the heavens, and every particle had an innate gravity towards all the rest and the whole space throughout which this matter was scattered was but finite: the matter on the outside of this space would by its gravity tend towards all the matter on the inside and by consequence fall down to the middle of the whole space and there compose one great spherical mass. But if the matter was eavenly diffused through an infinite space, it would never convene into one mass but some of it convene into one mass and some into another so as to make an infinite number of great masses scattered at great distances from one to another throughout all that infinite space. And thus might the Sun and Fixt stars be formed supposing the matter were of a lucid nature.

However, in the same letter, Newton suggested that the fact that the orbits of the Planets around the Sun all lie close to the same plane, and that all planets move around the Sun in the same direction, was unlikely to be due to natural causes, and instead likely to be due to Divine intervention. The realisation that this apparent coincidence was a consequence of the formation process rather than chance alignment or Divine choice led to the original formulation of the *Nebular Hypothesis*, which was the suggestion that the Sun and Planets had formed out of a rotating cloud or disk of material. This hypothesis was first suggested by Emanuel Swedenborg in 1734, and was further developed by Immanuel Kant, who wrote in *Allgemeine Naturgeschichte und Theorie Des Himmels* in 1755:

> I assume that all the matter making up the spheres belonging to our solar system, all the planets and comets, at the origin of all things was broken down into elementary basic material filling the entire space of the cosmic structure around which these bodies now move. [...] and the chaos began to develop itself at points where the particles had a stronger power of attraction.

Independently of this work, Pierre-Simon Laplace also suggested a similar formation process in 1796, in *Exposition du système du monde*:

> [...] it can only have been a fluid extending out to huge distances. In order to have given [the planets] a circular motion in the same direction around the sun; it follows that this fluid must have surrounded the Sun like an atmosphere. Taking into consideration the planetary motions, we are led to think that because of excessive temperatures, the atmosphere of the sun originally extended well beyond the orbits of all the planets, and that it subsequently contracted to its present day size.

Despite successfully explaining the motions of the planets, the main problem with the Nebular Hypothesis was that had the Sun and Planets formed from the collapse of a rotating cloud or disk, one would expect the Sun to contain much more angular momentum than is currently observed. For this reason, the *Nebular Hypothesis* was dropped in favour of theories involving Sun-grazing collisions ejecting material from the Sun, with this ejected material subsequently condensing into planets.

Nearly two hundred years later, in 1945, Alfred Joy noted 11 irregular variable stars that possessed similar photometric and spectral characteristics (Joy, 1945), including irregular changes in the optical light curves by up to 3 magnitudes, spectral types between F5 and G5, bright variable emission lines including from Hydrogen (such as Hα) and Ca II, and association with dark or bright nebulae. In particular, he found that a number of these sources were located in the constellations of Taurus and Auriga. He named this group of stars after the brightest in the sample, T Tau, and sources with similar properties are still to this day referred to as *T Tauri* stars.

Ambartsumian (1947) was the first to suggest that T Tauri stars were young, because they seemed to be spatially associated with O and B stars, which being massive stars are intrinsically young. T Tauri stars were found to be systematically brighter than main-sequence stars of the same spectral type (Herbig, 1952), suggesting that the former were still in the process of contracting towards the main-sequence, consistent with Ambartsumian's interpretation. As well as emission lines with line profiles suggesting outflow of material (Herbig, 1957a), T Tauri stars were found to exhibit wide absorption lines, which suggested a more rapid rate of stellar rotation than main sequence stars, once again consistent with their presumed youth (Herbig, 1957b).

A few years later, Mendoza (1966) reported the first detection of excess emission at near-infrared wavelengths in a large fraction of T Tauri stars, which he later suggested could be due to thermal emission from circumstellar dust (Mendoza, 1968). Cohen (1973), having observed a sample of T Tauri stars from 2 to 22 μm, found excess emission at mid-infrared wavelengths, and also suggested that the infrared emission could be due to circumstellar dust. It was later found that this dust was in the form of circumstellar disks, and these were believed to be the formation sites of planets, thus re-instating the Nebular Hypothesis as the preferred theory for the origin of the Solar System.

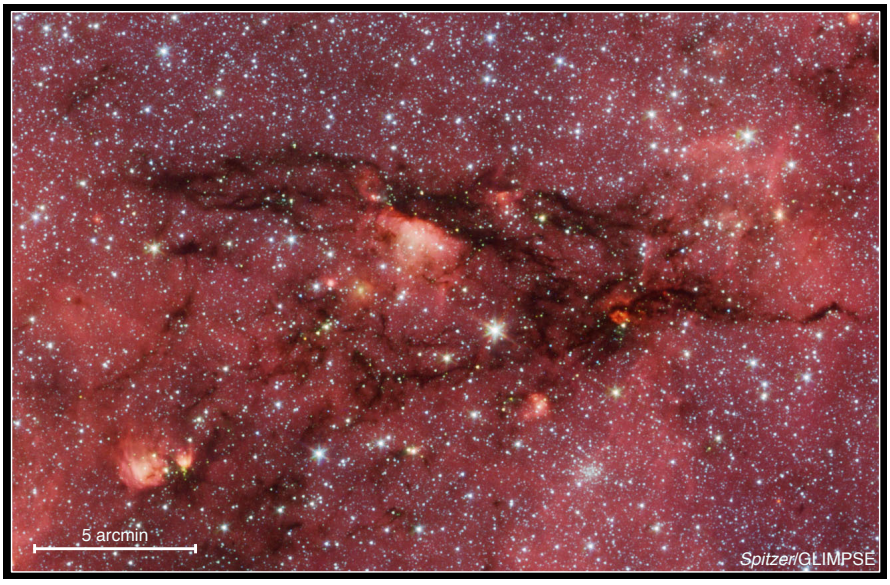

Figure 1.1: *Spitzer*/GLIMPSE image of a dark cloud situated at Galactic longitude $\ell = 14.20°$ and latitude $b = -0.55°$, from 3.6 μm (blue) to 8.0 μm (red). This dark cloud is 20′ long, i.e. over 10 pc assuming the dark cloud is at a distance of ~ 2 kpc.

1.2 The current star-formation paradigm

Since Joy's initial discovery of T Tauri stars, much has been learned about the formation of stars, from brown dwarfs to massive O and B stars. From molecular clouds to the onset of core hydrogen burning, the physical conditions of matter undergo dramatic changes. In particular, the densities and temperatures increase by a factor of 10^{22} and 10^{6} respectively. The chemistry also changes radically: the H_2 in the cores of giant molecular clouds (GMCs) eventually ends up as an ionised plasma in zero-age main-sequence (ZAMS) stars, and complex chemistry takes place on the surface of dust grains, including the formation of organic compounds that may eventually provide the building blocks for Life. Hence, a large number of physical and chemical processes come into play throughout the formation of a star.

The work presented in this thesis is concerned primarily with the stages of evolution ranging from the youngest protostars, which have just begun to collapse from over-densities in the molecular clouds, and in which a hydrostatic core has formed, up to the onset of the ZAMS. Such objects will subsequently be referred to as young stellar objects (YSOs).

1.2.1 The initial conditions for star formation

Star formation in the Milky-Way and other galaxies occurs primarily in GMCs, which are predominantly found in the spiral arms (e.g. Cohen et al., 1980; Dame et al., 1987). These clouds, mostly composed of H_2, have typical masses of 10^4 to $10^6\,M_\odot$, sizes of 10 to 100 pc, densities of 10^{-22} to $10^{-18}\,\mathrm{g\,cm^{-3}}$, and temperatures of approximately 10 K (Stark & Blitz, 1978; Sanders et al., 1985). The shielding to interstellar UV radiation provided by the higher densities relative to the interstellar medium (ISM) allows molecules – such as carbon monoxide (CO), water (H_2O), ammonia (NH_3), hydroxide (OH), and hydrogen cyanide (HCN) – to form. In addition, cosmic dust – microscopic grains composed mostly of carbon and silicon (c.f. §2.1) – accounts for approximately 1% of the mass of GMCs. At the low temperatures of GMCs, H_2 is essentially invisible, so that the masses and properties of molecular clouds are usually probed using emission from CO collisionally excited by H_2, or using thermal emission from dust. In addition, provided that they lie in front of bright diffuse emission or background stars, GMCs can be observed as *dark clouds*. An example of such a dark cloud is shown in Figure 1.1.

What causes GMCs to come into being is still a matter of debate, but current evidence – in particular the low star formation efficiency of GMCs ($\sim 1-2\%$) – suggests that these are unbound and transient structures that are unlikely to exist for more than a few million years. GMCs are observed to be turbulent structures (Larson, 1981), although it is not clear to date which process dominates the feeding of turbulence (gravitational instabilities, outflows or winds from young stars, supernovae, etc.). The density in GMCs is not uniform – instead, there is a whole hierarchy of structure that is sometimes described as fractal (e.g. Stutzki et al., 1998). Sub-structures with masses $\sim 100\,M_\odot$ and sizes of the order of a few parsecs are usually referred to as *clumps*, and sub-structures with masses of 1 to $10\,M_\odot$ and sizes of up to 0.5 pc are usually referred to as *cores*, but these are only arbitrary definitions which mask the continuous fractal nature of the structure from over 100 pc to under 1 pc. Because of the striking similarity between the core mass function and the stellar initial mass function (IMF) (e.g. Nutter & Ward-Thompson, 2007), it has been suggested that at least at the low-mass end, individual cores may form a single star, although this is currently a topic of debate (Goodwin et al., 2008). The fragmentation of massive cores is also a controversial topic, as fragmentation is likely to occur (Bonnell et al., 2004) unless high temperatures or turbulence

are sufficient to prevent this (McKee & Tan, 2003).

1.2.2 The formation of low-mass stars

The first and second collapse

Theoretical studies of the collapse of cores into protostars date back to the initial work by Darwin (1889) and Jeans (1902). An important quantity in the study of star formation is the *Jeans mass*, the minimum mass that a cloud of gas is required to have in order to overcome hydrostatic equilibrium and collapse. It is often written, for a spherical cloud of constant density, as

$$M_J = \left(\frac{3}{4\pi\rho}\right)^{\frac{1}{2}} \left(\frac{5kT}{G\mu m_h}\right)^{\frac{3}{2}} \tag{1.1}$$

Thus, it is easiest to form stars from cold and high density gas than warmer or lower density gas, as this reduces the amount of gas required to undergo gravitational collapse.

The problem of how the collapse proceeds once it has been initiated is not a simple one, and the biggest difficulty in studying this from a theoretical point of view is not only implementing many physical processes (rotation, magnetic fields, radiation pressure and heating, viscosity, etc.) into simulations, but also choosing the initial conditions to use for these simulations. Therefore, the advent of fast computer technology and observations of the possible initial conditions for star formation allowed tremendous progress in this field in the second half of the 20$^{\text{th}}$ century.

A dense collapsing molecular core is cold, with typical temperatures of $T \sim 10\,\text{K}$. Therefore most of the emergent radiation is emitted at mm and sub-mm wavelengths. As shown in Figure 1.2, the emergent SED for such cores is a modified blackbody, usually referred to as a *greybody* (c.f. §2.1) or a 'Class 0' SED (c.f. §1.3). Since the molecular core is cold and optically thin at sub-mm and mm wavelengths, the radiation escapes unhindered, and the collapse of the molecular core is approximately isothermal. As the density reaches $\rho \sim 10^{-12}\,\text{g}\,\text{cm}^{-3}$, the central regions become optically thick to radiation up to far-infrared wavelengths. The core loses its ability to remain cold, the collapse becomes adiabatic, and the temperature therefore begins to increase (Masunaga & Inutsuka, 2000; Stamatellos et al., 2007). As the temperature increases, the peak of the SED shifts to shorter wavelengths, at which the core is even more optically thick, further increasing the temperature. The central region eventually reaches a density of $\rho \sim 10^{-9} - 10^{-8}\,\text{g}\,\text{cm}^{-3}$, and becomes thermally supported: the *first*

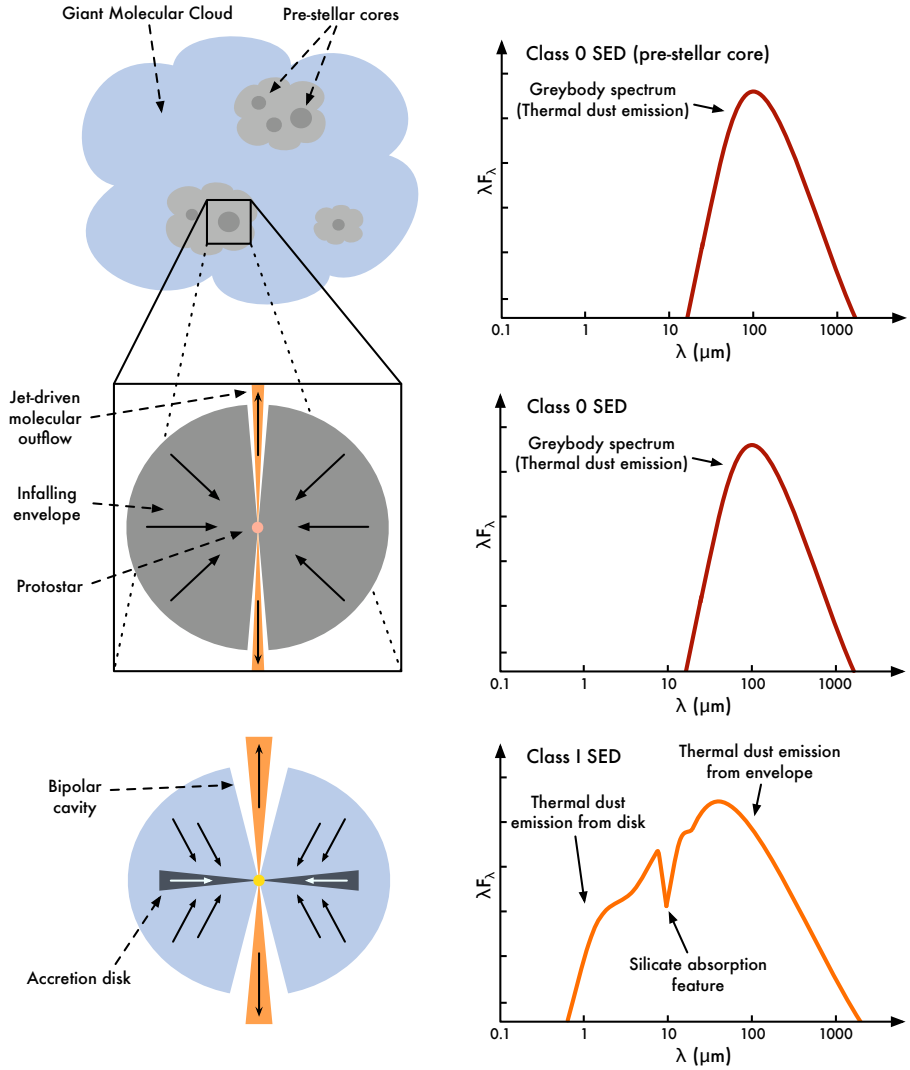

Figure 1.2: *Top left* – schematic of a GMC, with sub-structure visible, including individual cores. *Centre left* – initial spherical collapse of a single core. *Bottom left* – as the core collapses further, angular momentum becomes important and an accretion disk is formed. Infalling material accretes onto the disk, which in turn transports the material inwards to the central protostar. Powerful bipolar outflows also help remove angular momentum. *Right* – emergent SED at each evolutionary stage.

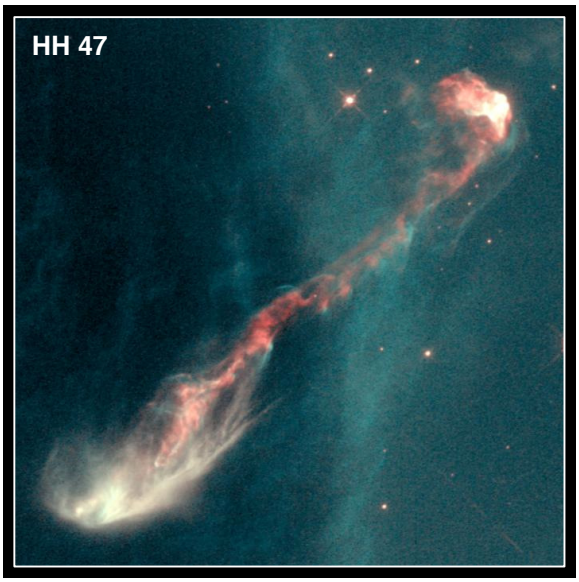

Figure 1.3: HST WFPC2 narrow-band observations of the HH47 parsec-scale protostellar bipolar outflow in Hα and [S II] (Heathcote et al., 1996). Image obtained from the HST press release STScI-1995-24.

hydrostatic core is formed. This hydrostatic core subsequently contracts, with material from the larger scale molecular core accreting onto it, until the temperature of the hydrostatic core reaches T_c ~2,000 K. At this temperature, the H_2 dissociates, absorbing thermal energy, and the hydrostatic balance is broken. A *second collapse* occurs, until the supply of H_2 is exhausted, and a *second hydrostatic core* is formed, onto which material continues to accrete. At this point, the second hydrostatic core is only a few percent of the final mass of the ZAMS star it will become, and is still heavily embedded. Most of the radiation escapes from the cold outer regions of the molecular core, so that the SED still resembles a cold greybody function.

Bipolar outflows

As matter accretes onto the newly formed hydrostatic core, or *protostar*, highly collimated bipolar jets are launched at typical velocities of a few hundred km/s, which transfer momentum to the surrounding molecular gas, forming large-scale outflows with typical velocities of tens of km/s (c.f. reviews by Bachiller, 1996; Reipurth & Bally, 2001; Bally et al., 2007). These large-scale outflows can have masses between 10^{-2} and 200 $M_\odot$, and sizes extending to several parsecs. Jets and outflows emit radiation all across the electromagnetic spectrum. For example, the gas distribution and kinematics of the material in outflows can be traced through CO line observations at mm wavelength. Additionally, the interaction between the outflows and the ISM leads to the formation of shocks, or *Herbig-Haro* objects (Herbig, 1951;

Haro, 1952), with strong Balmer, [O I], [S II], [N I], and [Fe II] emission lines visible at UV and optical wavelengths, and shocked H_2 emission that can also be observed at near- and mid-infrared wavelengths. Outflows can also be observed at radio or X-ray wavelengths. Figure 1.3 shows *Hubble Space Telescope* (HST) observations of optical narrow-band emission from a parsec-scale bipolar outflow originating from a deeply embedded protostar.

While it is generally accepted that rotating accretion disks and open magnetic field lines are responsible for the launching of jets, it is not clear exactly how this is done. One of the main competing theories is the X-wind model, in which material that will form the jet is launched at the inner edge of the accretion disk along open magnetic field lines anchored at the X-point, i.e. the co-rotation radius (see e.g. Shang et al., 2007, and references therein). The other main competing theory is the disk-wind model, in which material is launched from a larger range of radii in the inner regions of the disk along open magnetic field lines threading the disk (see e.g. Konigl & Pudritz, 2000; Pudritz et al., 2007, and references therein). In any case, both theories suggest that small amounts of material from the disk are centrifugally ejected along open magnetic field lines, carrying away angular momentum.

The formation of a disk

As the material falls towards the central core, the conservation of the angular momentum of the infalling gas eventually provides a brake to the collapse. Eventually, gravity is balanced by the centrifugal force of the gas: this is called the *centrifugal barrier*. However, the angular momentum only halts collapse perpendicular to the axis of rotation, so that the collapse can continue parallel to this axis. This leads to the formation of a disk (Terebey et al., 1984). Most of the gas now accretes onto the disk, which then channels material inwards onto the central star (see Figure 1.2). The transport of the material in the disk is due to viscous forces, which allow angular momentum to be transported outwards while matter is transported inwards (Lynden-Bell & Pringle, 1974). The *viscosity* of accretion disks can be parameterised as $\nu = \alpha c_s H$ (Shakura & Syunyaev, 1973), where c_s is the sound speed, H is the disk scaleheight, which determines the maximum eddy size, and the α parameter essentially summarises all the processes that produce viscous forces. The intrinsic molecular viscosity of the gas in disks around pre-main-sequence stars is not enough to account for the observed accretion rates (Pringle, 1981). Instead, it has been suggested that the viscosity in disks around young stars may be primarily due to the magneto-rotational instability (e.g. Tout & Pringle, 1992).

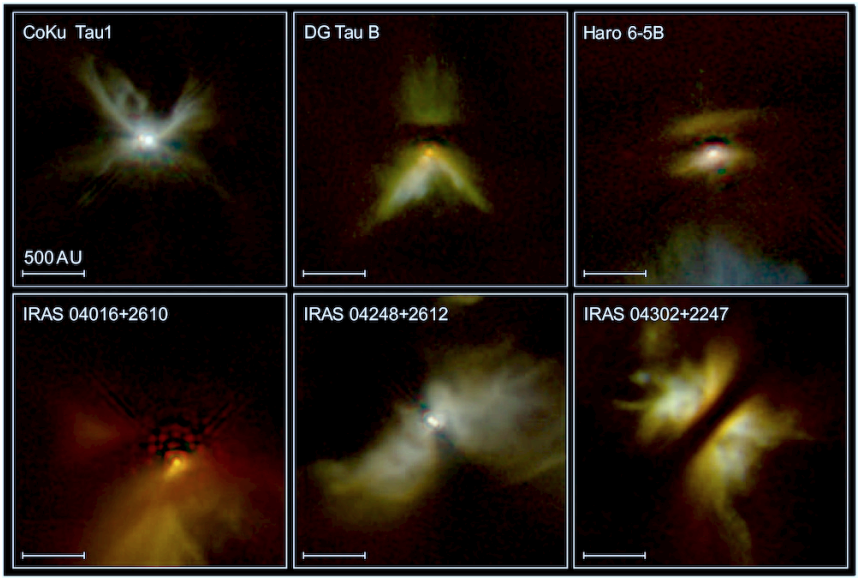

Figure 1.4: HST NICMOS observations of six 'Class I' YSOs in J, H, and K bands (Padgett et al., 1999). Image obtained from the HST press release STScI-1999-05a.

The Classical T Tauri phase

As the main accretion phase subsides, and the central pre-main-sequence (PMS) star approaches its final mass, the envelope starts to become optically thin at infrared wavelengths. The disk and the central source start to contribute significantly to mid-infrared wavelengths, and the YSO displays a 'Class I' SED (see Figure 1.2). Examples of HST observations of such sources are shown in Figure 1.4. After the envelope has dissipated, the protostar is left with a circumstellar disk, also called *protoplanetary disk* (see Figure 1.5). While the presence of disks was originally suggested on theoretical grounds and based on the SEDs of T Tauri and Herbig Ae/Be stars, HST observations laid all doubts to rest by imaging the scattered light from several disks, most famously that of HH30 (see Figure 1.6). The SED of a star with a surrounding disk is typically a 'Class II' SED (see Figure 1.5), essentially a stellar spectrum with thermal dust emission at mid- and far-infrared as well as sub-mm wavelengths. Gas in protoplanetary disks is likely to be in vertical hydrostatic equilibrium at all radii, and therefore the scaleheight of the disk is given by (Shakura & Syunyaev, 1973):

$$\frac{h}{r} = c_s \left(\frac{r}{GM_\star} \right)^{1/2} \tag{1.2}$$

Therefore, disks are likely to be flared, that is, the scaleheight of the disk increases with radius as a power law $h \propto r^\beta$. Dust is initially likely to follow the same distribution as it is

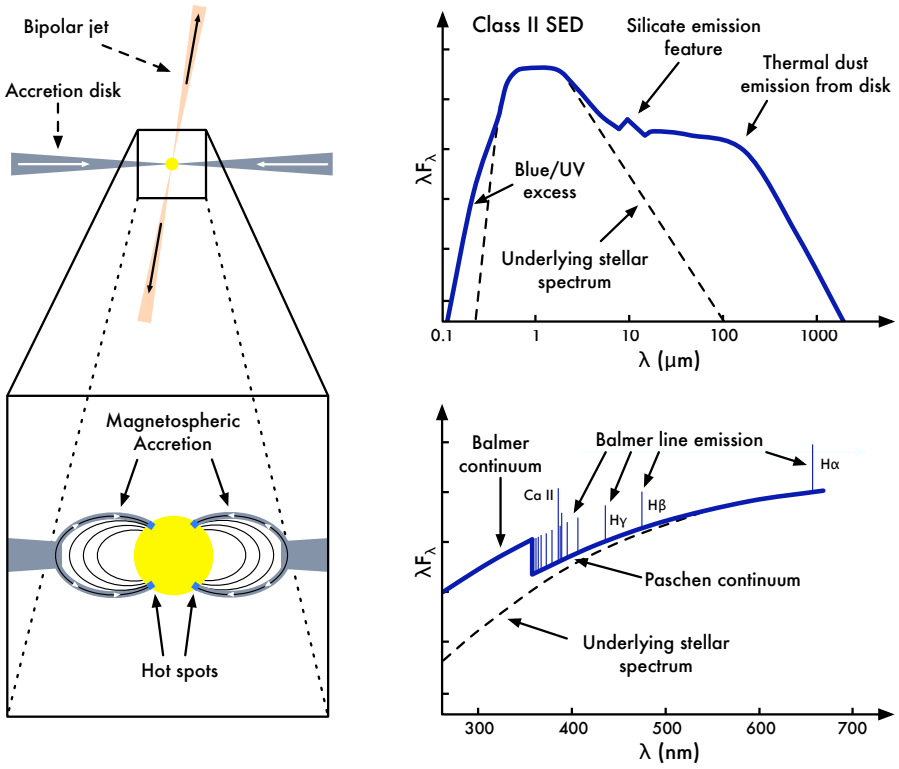

Figure 1.5: *Top left* – once the accretion through the envelope has stopped, the pre-main-sequence star is surrounded only by an optically thick and geometrically thin accretion disk. *Bottom left* – the inner disk is truncated by the magnetic field, and matter is channelled along the magnetic field lines and impacts on the surface of the star at free-fall velocities. *Top right* – emergent Class II SED for a PMS star with an accretion disk. The dashed black line shows the spectrum of the central PMS star. The accretion produces both near-infrared emission, and an excess of emission at optical and UV wavelengths. *Bottom right* – the UV and optical portion of the spectrum, showing the strong Balmer emission lines and strong Balmer and Paschen continuum that results from the accretion (CTTS signatures).

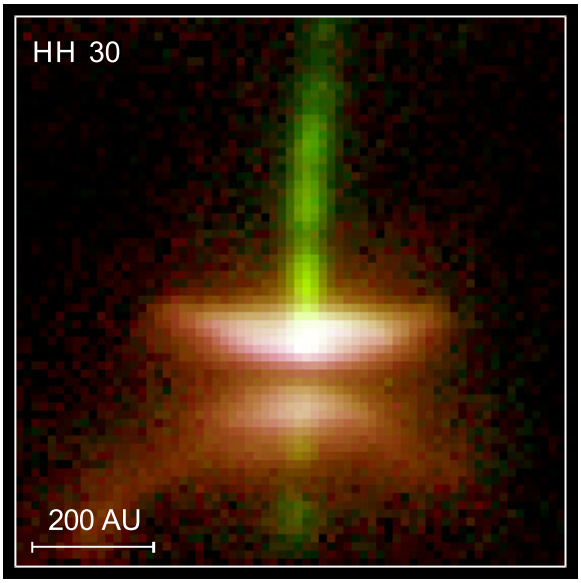

Figure 1.6: HST WFPC2 observations of the HH 30 edge-on disk and bipolar jet (Burrows et al., 1996). Image obtained from the HST press release STScI-1999-05b.

well-coupled to the gas, although at later stages of evolution the dust may settle to the mid-plane of the disk. The flaring of protoplanetary disks was derived observationally by Kenyon & Hartmann (1987) based on the infrared SED of T Tauri stars (c.f. §1.3). By assuming $T \propto r^{-1/2}$, the temperature profile of a flared disk (Kenyon & Hartmann, 1987), and $c_s^2 \propto T$, one finds $\beta = 5/4 = 1.25$.

CTTS disks are said to be *active*, in that their temperature structure is determined not only by the illumination from the central PMS star, but also by the energy liberated via accretion. The accretion of material towards the central star continues. However, the material does not accrete directly onto the PMS star: in the inner parts of the disk, the rotating magnetosphere of the central PMS star is strong enough to carve out a hole typically a few $R_\star$ in size, i.e. the extent of the magnetosphere (Shu et al., 1994; Kenyon et al., 1996). Matter is channelled along the field lines and crashes on to the surface of the star at free-fall velocities (Shu et al., 1994), producing hot spots with temperatures of $T \sim 10^4$ K. This magnetospheric accretion process produces strong Balmer continuum and line emission (including Hα) in the UV ($\lambda < 3800$ Å), and blue Paschen continuum emission in the visible ($\lambda < 5000$ Å), producing both the *UV excess* and *blue veiling* observed in CTTSs (Figure 1.5; Kuhi, 1974; Kuan, 1975; Rydgren et al., 1976).

Because a typical T Tauri star rotates over periods of 1 to 8 days, the rotational modulation

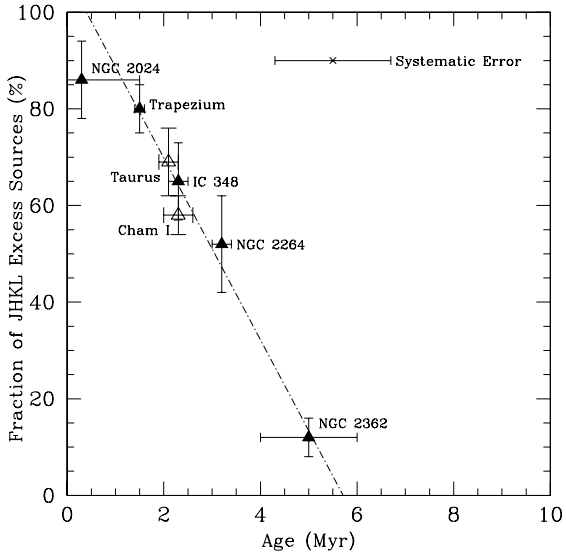

Figure 1.7: Fraction of stars with disks (i.e. JHKL excesses) as a function of mean cluster age for seven young clusters. This suggests that most disks have lifetimes below 6 Myr. Figure taken from Haisch et al. (2001a).

of the hot spots on the stellar surface leads to optical and near-infrared variability (Bouvier et al., 1993; Kenyon et al., 1994; Wood et al., 2000) as well as periodic variations in the scattered light morphology (Wood & Whitney, 1998). The fast rotation also leads to enhanced magnetic dynamo activity, and therefore enhanced radio and X-ray variability. Another cause of strong variability at most wavelengths are so-called FU Orionis outbursts, during which CTTS will brighten dramatically for a short time. This phenomenon is thought to be caused by a temporary increase in the accretion rate, possibly triggered by thermal instabilities (Hartmann & Kenyon, 1985).

Subsequent disk evolution

Over time, the dust grains in the disk are able to coagulate and grow in size, which causes the grains to decouple from the gas, and to settle preferentially at the mid-plane of the disk (Beckwith et al., 1990; Beckwith & Sargent, 1991; Miyake & Nakagawa, 1993; D'Alessio et al., 1999, 2001). The settling increases the dust density at the disk mid-plane, which in turns promotes further dust grain growth. Eventually, the dust grains coagulate into pebbles, the pebbles coagulate into planetesimals, and the planetesimals merge to form rocky planets, or the cores of giant planets. The formation of gas giants occurs while the PMS star is still surrounded by a gaseous disk, either through accretion onto a rocky core, or through gravitational instabilities, although the latter is only likely to occur in massive disks. The surface of the disk is subjected

to X-ray and UV photons from the star, causing hydrogen atoms to be ionised. Their velocity becomes greater than the escape velocity, and they escape from the disk. Thus, the gas in disks around low-mass stars can be removed through photoionisation over timescales of $\sim 10^5$ yr, after a disk lifetime of several million years (Alexander et al., 2006a,b).

Once the dust has also dispersed or has grown to mm or cm-sized pebbles, such that the infrared excess is no longer important, the PMS star heads towards the main sequence. From observations of the disk fraction in seven young clusters, Haisch et al. (2001a) found that most protoplanetary disks are likely to be cleared after 6 Myr (see Figure 1.7). Once the disk has been cleared, the PMS star still displays stronger activity than main-sequence stars and thus such objects can be identified in X-ray surveys. These are referred to as weak-lined T Tauri stars (WTTSs), due to the lack of strong Hα emission. However, WTTSs are not always older than CTTSs, suggesting that the absence of a significant accretion disk may be due to the initial conditions or the environment just as much as time evolution. For example, in close binary systems or high density clusters, accretion disks may not exist for long as they will be disrupted by the orbital motions of the stars.

Clustered star formation

The star formation paradigm described in the current section applies mainly to low- and possibly intermediate-mass stars forming in isolation, as is the case for many young stars in nearby star formation regions such as the Taurus Molecular Cloud (TMC). However, it is not clear that isolated star formation is the dominant mode of star formation. For example, Lada & Lada (2003) suggest that 70 to 90% of all stars formed in GMCs may form in embedded clusters, and that 90% of these may form in dense clusters with 100 or more members. The high stellar densities may affect the evolution of the forming low-mass stars, for example by disrupting or enhancing accretion or ejecting young stars from the clusters through close encounters, and the presence of O or B stars can lead to the photo-evaporation of accretion disks around lower mass stars, as seen in the Trapezium cluster in the Orion Molecular Cloud (OMC).

1.2.3 The formation of intermediate and high-mass stars

Herbig (1960) was the first to search for young intermediate and high-mass stars with similar signatures to T Tauri stars – these are now usually referred to as *Herbig Ae/Be* stars. More generally there is good evidence for disk-like structures (see e.g. Cesaroni et al., 2007, and references therein) and collimated outflows (see e.g. Beuther & Shepherd, 2005, and references therein) around young stars as massive as early B-type. However, the lack of disks and collimated outflows around young O stars suggests that there are a number of physical processes that become important during the formation of O and B stars which lead to important differences in the formation mechanism compared to low- and intermediate-mass stars.

The first problem with the formation of high-mass stars is linked to the initial collapse, namely that a core large enough to produce a massive star may fragment before it is able to form the massive star, resulting instead in several lower-mass objects (e.g. Bonnell et al., 2004). However, it has been suggested that sufficiently high levels of turbulence (McKee & Tan, 2003) may prevent fragmentation.

A second issue is that, assuming spherical accretion, there is a limit to the accretion rate above which the radiation pressure on the dust grains will halt the collapse (e.g. Larson & Starrfield, 1971). This is known as the Eddington accretion limit. Solutions for this have been suggested, including for example non-spherically symmetric accretion, allowing radiation to escape along the poles while accretion proceeds through a geometrically thin and optically thick disk (Krumholz et al., 2005).

Finally, massive stars differ significantly from lower-mass stars in that their rapid evolution means that they are able to reach the main-sequence while accretion is still ongoing. As the accretion proceeds, the mass – and therefore the UV flux – of the central source increases. Eventually, the central star is capable of ionising the accreting gas faster than the gas is accreting. Ionised gas has a higher thermal pressure than neutral gas, and once enough gas has been ionised, this thermal pressure can be sufficient to halt the collapse (e.g. Larson & Starrfield, 1971). In the same way as for the radiation pressure problem, a possible solution is to allow the accretion to proceed through a geometrically thin and optically thick disk while allowing an HII region to expand along the poles (see e.g. models by Keto, 2007).

1.3 The study of spatially unresolved sources

1.3.1 The importance of unresolved sources

Until the advent of sub-mm interferometers, space-based optical and near-infrared telescopes, and ground-based 8 m class telescopes with adaptive optics, most YSOs were unresolved, with the exception of large-scale bipolar outflows and Herbig-Haro objects. Much of what has been described in §1.2 was derived from the wealth of information contained in broadband SEDs and high-resolution optical and near-infrared spectra rather than direct resolved observations.

However, the last two decades have seen the emergence of a number of observations in which circumstellar envelopes and disks can be directly seen (such as those shown in Figures 1.4 and 1.6). Observations of scattered light from dust around young stars on Solar System scales were first made by Beckwith et al. (1984) using speckle interferometry. Since then, numerous observations of scattered light have been carried out, including near-infrared imaging (e.g. Tamura et al., 1991; Kenyon et al., 1993b; Lucas & Roche, 1997), near-infrared polarisation maps (e.g. Whitney et al., 1997), and more recently near-infrared adaptive optics observations (e.g. Close et al., 1997; Stapelfeldt et al., 2003; Fukagawa et al., 2004) and HST observations (e.g. Burrows et al., 1996; Padgett et al., 1999; Grady et al., 1999; Cotera et al., 2001; Stapelfeldt et al., 1998, 2003). Resolved observations of thermal dust emission from disks have also been made at sub-mm wavelengths (e.g. Andrews & Williams, 2007). In parallel, spatially resolved observations of the gas component of disks have also been carried out, mostly through CO line observations (e.g. Beckwith et al., 1986), which allow Keplerian rotation to be observed (e.g Weintraub et al., 1989; Koerner et al., 1993; Dutrey et al., 1994).

While these observations have undoubtedly advanced our understanding of star formation, only a limited number of YSOs are available for such studies, namely those in nearby star formation regions[1]. Detailed studies of nearby objects are invaluable to our understanding of the processes occurring during the formation of stars, but it is also important to study a much larger number of sources in order to understand whether these processes are generally common. In particular, it is not clear that nearby star formation regions such as the TMC, with isolated low-mass star formation, are typical. Instead, it is thought that most young stars may be formed in much larger and more massive star formation regions, such as the OMC. In order

[1]For example, the `circumstellardisks.org` database [1] lists only 84 resolved protoplanetary disks at the time of writing

to reach general conclusions about the formation of stars of all masses, the tens of thousands of YSOs seen in the Milky Way to date and the hundreds of thousands or even millions of young stars that will one day be observed need to be studied, whether they are in nearby star-forming regions (such as the TMC, Perseus, Serpens, Chameleon, Ophiuchius, Lupus, and the OMC), in more distant star-forming regions (such as the Eagle, Omega, and Rosette nebulae), or in yet undiscovered regions. It is likely that most YSOs in the Galaxy will remain unresolved in the next few decades, and most of the information available for these sources will be in the form of broadband SEDs, polarisation measurements, and high-resolution spectra. Therefore, it is important to understand exactly to what extent information can be extracted from these broadband SEDs, especially if the wavelength range over which data are available for a given source is limited.

1.3.2 SED radiation transfer modelling

The main approach to analysing broadband SEDs is to compute radiation transfer models, assuming a given circumstellar dust and gas geometry, as well as dust and gas properties, predicting the emergent SED, and adjusting the parameters until the observations can be reproduced: it is a typical *inverse problem*.

One of the most important examples of the use of broadband SEDs to determine the geometry of dust around young stars was the realisation that in order to reproduce the large infrared and sub-mm emission seen in T Tauri stars, while simultaneously predicting very low visual extinctions, the dust could not be spherically distributed around the stars, but instead had to be in the form of a geometrically thin disk (e.g. Beckwith et al., 1990). Thus, for the same dust mass, and thus the same amount of optically thin sub-mm emission, the visual extinction could be very low, except in the rare case when the disks were viewed edge-on, in which case the optical extinction would be higher than if the dust was spherically distributed around the stars.

Another important result from the analysis of SEDs was the determination of the vertical structure of disks around T Tauri stars. One of the main physical properties that determines the emergent SED for a T Tauri star with a disk is the radial temperature profile of the disk. For a flat passive irradiated disk in local thermodynamic equilibrium (LTE), the temperature profile is given by $T \propto r^{-3/4}$: this is because assuming LTE, the energy emitted by a small patch in the disk, σT^4 is proportional to the incident radiation on that patch, which is propor-

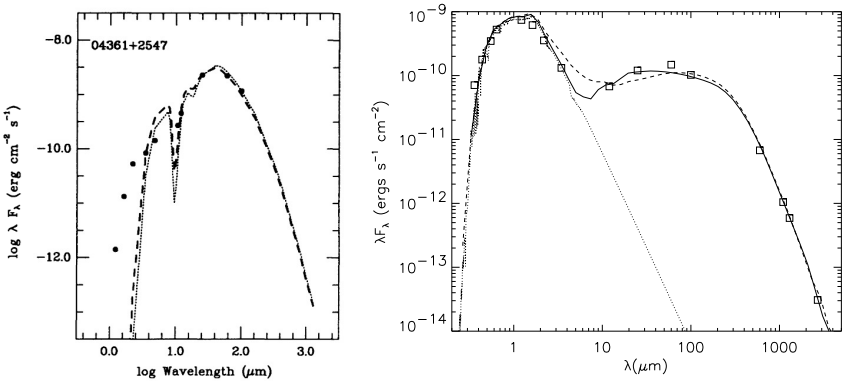

Figure 1.8: *Left* – Observed SED of IRAS 04361+2547 (circles) with fitted models of sources embedded in rotationally flattened envelopes. The short wavelength flux is not well reproduced by the model, because it does not include scattered light from cavities carved out by a bipolar outflow. Figure adapted from Kenyon et al. (1993a). *Right* – Observed SED of GM Auriga (squares), with the best fit that can be achieved if the dust in the disk extends down to $7R_\star$ (dashed line), and a model produced if a planet orbiting at 2.5 AU removes dust in the inner regions of the disk (solid line). Figure taken from Rice et al. (2003).

tional to $1/r^3$, where a factor of $1/r^2$ accounts for the usual dilution of flux with radius from the star, and a factor of $1/r$ accounts for the fact that the amount of light a patch in a flat disk will intercept falls off linearly with radius (e.g. Adams et al., 1987). For an active disk, where the luminosity is due to accretion, the temperature profile is also predicted to be $T \propto r^{-3/4}$ (Lynden-Bell & Pringle, 1974). However, Kenyon & Hartmann (1987) found that the SED of many T Tauri stars could be better explained by a disk in which the temperature profile was shallower, with $T \propto r^{-1/2}$. This temperature dependence can be produced by disks that are flared: the flaring causes more stellar radiation to be intercepted at larger radii, resulting in a shallower temperature profile.

While these examples refer to the general properties of T Tauri stars, SED modelling can be used to determine specific parameters for a given young star, such as the properties of the central source, the inner or outer radius of the disk, the amount of flaring or dust settling, and more generally any parameter which may affect the SED, although whether a given parameter can be determined or not depends on the data available. For example, the deficit of near- and mid-infrared emission relative to longer wavelengths in a number of objects (such as GM Aur, TW Hya, HK Tau, RY Tau, etc.) has often been modelled by a deficit of dust in the inner regions of the disks, possibly due to the effect of unseen planetary companions (Marsh & Mahoney, 1992, 1993; Calvet et al., 2002; Rice et al., 2003; Calvet et al., 2005, c.f. Figure 1.8 for the modelled SED of GM Aur). Similarly, the properties of younger embedded sources can also be

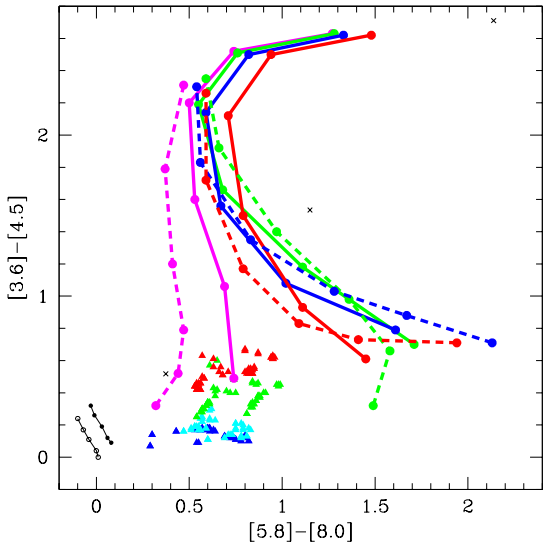

Figure 1.9: Synthetic *Spitzer*/IRAC colours of YSOs derived from model SEDs of protoplanetary disks (triangles) and embedded protostars (circles). Figure taken from Allen et al. (2004).

derived, such as the density structure or accretion rate of the infalling envelope. For example, Kenyon et al. (1993a) showed that the SED of embedded sources in the TMC could be better explained by rotationally flattened envelopes (e.g. Terebey et al., 1984) than by spherically symmetric envelopes, and found infall rate values consistent with those predicted by infall theories (c.f. Figure 1.8 for the modelled SED of IRAS 04361+2547).

The analysis of SEDs using radiation transfer models allows one to gain insight into the physical properties of YSOs, but is typically restricted to small numbers of sources, because computing a single synthetic SEDs can take tens of minutes to hours. In addition, the long computational time also makes it difficult to estimate how unique a given fit is, especially if the wavelength coverage of the observed SED is not complete.

1.3.3 Spectral index and colour analysis

With the recent advent of large-scale infrared surveys of star formation regions, a common method to analyse large numbers of sources with data in a limited wavelength range is instead to use synthetic SEDs to gain an understanding of the relation between physical properties and simple observables such as spectral indices or colours of young stars. For example, the well-known 'Classes' for low-mass YSOs uses the spectral index α, which is the slope of $\log_{10} \lambda F_\lambda$ vs. $\log_{10} \lambda$ longward of 2 μm, to classify a source as embedded ($\alpha > 0$; Class I), a disk source ($-2 < \alpha < 0$; Class II) or a source with an optically thin or no disk ($\alpha < -2$; Class III) (Lada,

1987; Adams et al., 1987). Rather than use a single slope, one can use two or more colours. For example, Lada & Adams (1992) used model SEDs of circumstellar disks to study J−H vs. H−K colour-colour diagrams, and Allen et al. (2004) used model SEDs of circumstellar disks and embedded protostars to study a colour-colour diagram making use of *Spitzer*/IRAC colours (see Figure 1.9).

The main caveat with this type of analysis is that although the general trend between physical parameters and simple observables may be approximately valid, individual objects can deviate from such a classification. For example in the case of spectral indices, an edge-on embedded protostar can have a decreasing slope in the narrow wavelength range of $2-10\,\mu$m if the flux is dominated by scattered light, but edge-on disks can exhibit similar behaviour (Wood et al., 2002b; Grosso et al., 2003). The temperature of the central source also affects the colours in this wavelength range, as does the location of the inner radius of the dust disk: hot stellar sources and large inner dust disk holes can produce red colours in a CTTS (c.f. §3.3.4). Nevertheless, using spectral indices or colours has the advantage that once the analysis of the relation between physical parameters and spectral indices or colours has been carried out, thousands of sources can be simultaneously analysed, which would be unfeasible with manual SED modelling.

1.4 Thesis outline

While SED modelling is typically used for small numbers of sources with extensive wavelength coverage, and spectral index and colour analysis are suitable for large numbers of sources with photometry at only a few wavelengths, there is an increasing number of YSOs for which data are becoming available at more wavelengths than can be realistically used in multi-dimensional colour-colour diagrams. For example, at the present time, there are already thousands of YSOs for which data are available from near- to mid- or far-infrared, and will soon be available up to sub-mm wavelength (c.f. §2.3). Manually modelling each of these SEDs is unrealistic, but no suitable technique has previously been developed to carry out large-scale SED modelling in an automated fashion.

The work described in Chapters 3 and 4 of this thesis is concerned with the development of a large-scale SED modelling technique which has the advantage over previous techniques that it allows the automated modelling of individual SEDs, while being extremely efficient

computationally. It can make use of any amount of data and can explore the degeneracies of parameters rather than being limited to a best fit.

At the same time as developing this SED analysis technique, I have carried out a census of unresolved YSOs in the Galactic plane, which is described in Chapter 5. The census has produced a catalogue of over 11,000 candidate YSOs and over 7,000 asymptotic giant branch (AGB) stars. The catalogue includes fluxes from near-infrared wavelengths to 24 μm for most sources, and is a step towards compiling a large database of YSO SEDs that will benefit from the analysis techniques presented in Chapters 3 and 4.

Chapter 2 provides relevant background information, in particular relating to the properties of cosmic dust (§2.1), Monte-Carlo radiation transfer (§2.2), and previous, current, and future large-scale surveys of star formation regions and of the Galactic mid-plane (§2.3). Finally, Chapter 6 summarises the main findings of this thesis and presents an overview of future work that can be carried out building on the work presented here.

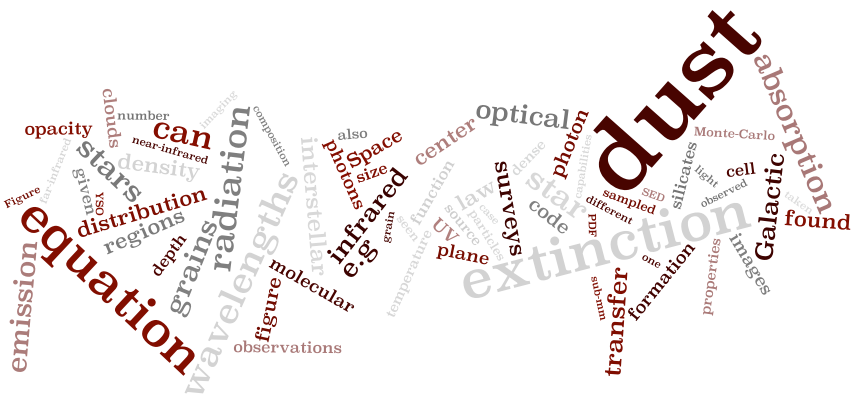

2

Darkness and Light

The work presented in this thesis is primarily concerned with the analysis of the infrared signatures of circumstellar dust around young stars, making use of Monte-Carlo radiation transfer models. Therefore, this chapter contains a description of the properties of dust (§2.1), as well as an introduction to the principles of Monte-Carlo radiation transfer, and to the code used to compute the model SEDs presented in Chapter 3 (§2.2). One of the aims of the analysis technique presented in Chapter 4 is the modelling of large number of sources in recent surveys of star formation regions. Furthermore, the *Spitzer Space Telescope* survey of the Galactic plane is used to search for red sources in Chapter 5. Therefore, a review of recent infrared surveys of the Galactic plane and of star formation regions is given in §2.3.

2.1 Cosmic dust

2.1.1 The importance of dust

Cosmic dust, thought to be microscopic grains composed mostly of carbon (C) and silicon (Si), is now seen as of fundamental importance to the life cycle of stars. It is formed in the atmospheres of AGB stars (Jura, 1986) and supernovae (Wooden et al., 1993), although it is not clear to date what fraction of the dust formed in the latter survive the passage though reverse shocks. It is on the surface of dust grains that H_2 is thought to form in molecular clouds (e.g. Gould & Salpeter, 1963), that more complex molecules including organic compounds are able to form in dense cores, and it is dust that ultimately provides the building blocks of terrestrial planets and in some cases the cores of gas giant planets. While H_2 dominates the mass and dynamics of clouds and protostellar cores, it is essentially invisible at optical, infrared, and sub-mm wavelengths. Instead, it is dust that dominates the scattering, absorption, and reprocessing of radiation at these wavelengths. Dust can even be of great importance from a dynamical point of view; in massive stars in particular, it is its opacity which determines the upper limit to the accretion rate due to radiation pressure (c.f. §1.2.3).

The most important properties of any mixture of dust are the following: (a) the chemical composition of the dust grains, (b) the size distribution of the dust particles in the mixture, (c) the shape of the dust grains. These properties together define the extinction and absorption properties of the dust mixture. The latter can be expressed as a frequency-dependent absorption coefficient per unit mass – or *opacity* – κ_ν. Assuming that the dust is in LTE, the emission coefficient per unit mass j_ν is directly related to the opacity by Kirchoff's law:

$$j_\nu = \kappa_\nu B_\nu(T) \tag{2.1}$$

where $B_\nu(T)$ is the Plank function. Thus, the properties of dust in LTE can be probed through the study of the wavelength-dependent extinction law of starlight through the interstellar medium or dust clouds at UV, optical, and infrared wavelengths, through the study of the dust continuum emission at sub-mm and mm wavelengths, and through the study of emission and absorption features at infrared wavelengths.

2.1.2 Interstellar extinction

The interstellar extinction along a given line of sight is determined by multi-wavelength observations of background stars. This requires assuming intrinsic spectral types for these stars, and comparing theoretical fluxes to the observed fluxes. Historically, this was first done at UV, optical, and near-infrared wavelengths. The interstellar extinction was found to increase from near-infrared to UV wavelengths, with a characteristic bump at 2160 Å (see Figure 2.1). Bless & Savage (1972) determined the extinction law from 0.11 to 2.15 μm, and found that, with the exception of a few regions (such as ρ Ophiuchius and the OMC, both regions of higher density), the interstellar extinction curve in that wavelength range was essentially independent of the line-of-sight in the Galaxy. Cardelli, Clayton, & Mathis (1989) generalised this further, by suggesting that independently of the line-of-sight to background stars, the UV to near-infrared extinction (and therefore opacity) was solely a function of the parameter

$$R_V = \frac{A_V}{E(B-V)}, \tag{2.2}$$

usually referred to as the *total-to-selective extinction* (see Figure 2.1). It was found that the extinction to most stars through the ISM was characterised by $R_V \approx 3.1$ (corresponding to the extinction law derived by Bless & Savage), while the extinction through dense molecular clouds (such as ρ Ophiuchius and the OMC) was better characterised by higher values of R_V, such as $R_V \approx 5$.

Rieke & Lebofsky (1985) extended the determination of the interstellar extinction law to longer wavelengths, by measuring the extinction towards stars in the Galactic centre. One important feature of the extinction law that was found at these wavelengths was the strong absorption feature at 10 μm, attributed to silicates (c.f. §2.1.4 and Figure 2.1). Amongst the longest wavelength measurements of the extinction law available to date are that of Lutz (1999) for the ISM at 20 μm, and that of Flaherty et al. (2007) for dense molecular clouds at 24 μm.

Mathis, Rumpl, & Nordsieck (1977) used the extinction curve between 0.11 and 1 μm to determine the composition and the size distribution of the dust grains assuming spherical grains, and found that combinations of two dust species could adequately reproduce the observed interstellar extinction law, provided that one of these dust species was graphite (i.e.

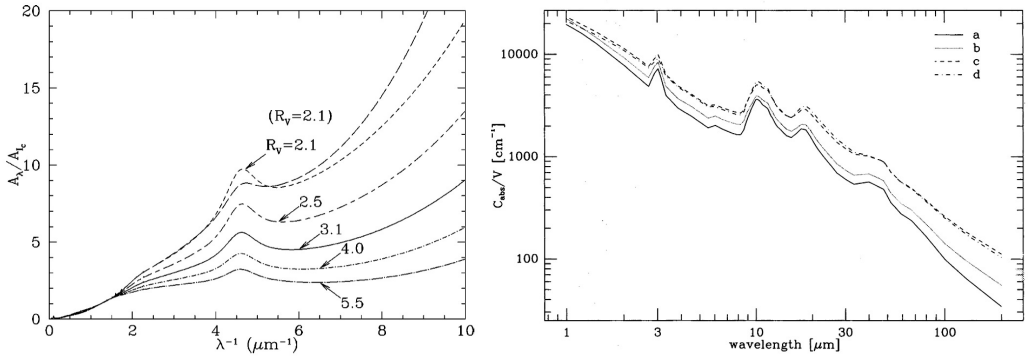

Figure 2.1: *Left* – UV, optical, and near-infrared extinction for different values of R_V. The 2160 Å ($\lambda^{-1} = 4.62\,\mu\text{m}^{-1}$) absorption bump is most clearly seen for low values of R_V. Figure adapted from Draine (2003). *Right* – Evolution of the near- to far-infrared absorption for dust with with ice mantles, assuming a dust grain size distribution from Mathis et al. (1977), as the dust coagulates. The extinction is shown after (a) 0, (b) 2.6×10^3, (c) 2.1×10^4, and (d) 10^5 yr. The absorption feature at 3 μm is due to ices, and the absorption features at 10 and 18 μm are due to silicates. As the dust coagulates, the opacity increases, especially at the longest wavelengths. Figure taken from Ossenkopf (1993).

crystalline carbon). The size distribution of particles was found to be best described by:

$$n(a)da \propto a^{-3.5}\,da \tag{2.3}$$

where a is the dust grain size, 0.005 μm $\leq a \leq$1 μm for graphite, and 0.025 μm $\leq a \leq$0.25 μm for the second species. The presence of the 10 μm absorption feature suggested that most of the non-graphite particles should be in the form of silicates, thus favouring a mix of graphite and silicates for the composition of interstellar dust. The uniformity of the interstellar extinction between different lines of sight was thought to be indicative of a 'universal' size distribution of particles, and that this could be explained if the processes producing the final mixture of dust grains were stochastic in nature.

Kim, Martin, & Hendry (1994) used a maximum entropy method to derive the size distribution of dust grains that could reproduce the parameterised extinction law found by Cardelli et al. (1989), both for R_V=3.1, representative of the standard ISM extinction, and for R_V=5.3, representative of the extinction in a dense molecular cloud. The main finding was that for R_V=3.1, the distribution of grain sizes was roughly consistent with the power-law found by Mathis et al. (1977), while for R_V=5.3 a deficit of small particles ($a < 0.1\,\mu$m) and a modest increase in the number of large particles was necessary to reproduce the extinction law. This was taken as evidence for dust grain growth in dense molecular clouds.

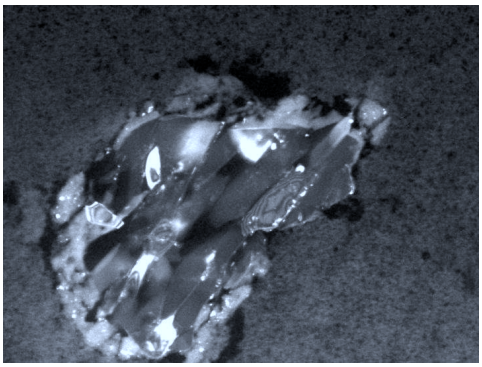

Figure 2.2: Particle of forsterite (a crystalline silicate) captured by the Stardust probe from comet Wild 2. Forsterite is seen in emission at 11.3 μm in some protoplanetary disks. Some pristine interstellar dust grains may be present in the samples collected by Stardust, although none have been found to date. This image was taken from the NASA Stardust home page [2].

2.1.3 Dust continuum emission

At longer wavelengths, where dust extinction is unimportant and thus cannot be accurately measured, it is easiest to use the thermal emission from dust in order to derive dust properties. For dust in LTE, Eq. (2.1) holds, and assuming that the dust is optically thin, the thermal dust emission is given by (Hildebrand, 1983)

$$F_\nu \propto \kappa_\nu B_\nu(T). \tag{2.4}$$

This is usually referred to as a greybody spectrum. Assuming that the temperature of the dust is hot enough that the emergent flux is in the Rayleigh-Jeans tail of the Plank function at sub-mm wavelengths, and that the opacity can be written as a power law $\kappa_\nu \propto \nu^\beta$, one finds that $F_\nu \propto \nu^{2+\beta}$, which can also be written as $F_\nu \propto \nu^\alpha$. Therefore, if a source is observed to have an SED well fit by $F_\nu \propto \nu^\alpha$, then the opacity index β can be found from $\beta = \alpha - 2$. While one would expect values of $\beta = 2$ for interstellar extinction (e.g. Draine & Lee, 1984), various studies found that in protostellar cores and protoplanetary disks, β was generally no larger than 1. For example, Beckwith & Sargent (1991) used sub-mm observations of 29 pre-main-sequence stars in the Taurus and Orion star formation regions to determine that for most of these sources, $-1 < \beta < 1$, which once again was taken as evidence of grain growth.

2.1.4 Dust spectroscopy

While both the R_V-dependent UV to infrared extinction law and the sub-mm emissivity of cosmic dust show that its composition is likely to be dominated by astronomical silicates

and carbonaceous materials, and that grain growth occurs in dense molecular clouds and protostars, these techniques do not probe the chemical composition of the dust directly. This can instead be done by spectroscopic observations of emission and absorption features at infrared wavelengths.

Amongst the most studied spectral signatures of dust in YSOs are the 9.7 μm and 18 μm silicate features, often seen in absorption towards protostars. These features are usually best explained by the presence of amorphous silicates such as pyroxenes (Demyk et al., 1999) or amorphous olivine (Kemper et al., 2004). Amorphous silicates are also seen in emission in protoplanetary disks, and in some cases there is evidence for emission from a small mass fraction of crystalline silicates such as forsterite at 11.3 μm (see Figure 2.2). It is also possible to probe the presence and composition of ice coatings on dust grains through spectroscopy. Ices have been detected in absorption towards protostars, including the H_2O feature at 3 μm (Gillett & Forrest, 1973). Over 40 different ice absorption features are known to date (van Dishoeck, 2004).

Emission lines originally seen in the interstellar medium at mid-infrared wavelengths, and previously known as the unidentified infrared emission (UIR) bands, are now known to originate from polycyclic aromatic hydrocarbon (PAH) molecules (Leger & Puget, 1984; Allamandola et al., 1985). These are large carbon-based molecules, rather than dust grains, and are excited by the absorption of single UV photons (Sellgren, 1984), and are therefore not typically in LTE. PAHs have recently been detected towards protoplanetary disks around stars with sufficient UV flux, such as Herbig Ae/Be stars (Acke & van den Ancker, 2004). It seems therefore plausible that in the ISM and in YSOs, the size distribution of carbonaceous grains extends down to PAH molecules (Draine, 2003), and that these reveal their presence through mid-infrared emission when subjected to a significant UV flux.

2.1.5 Dust evolution

One of the most important physical processes that dust is subject to in dense molecular clouds, protostellar envelopes, and disks, is grain growth though coagulation (e.g. Ossenkopf, 1993, see also Figure 2.1), possibly into fractal structures, which would increase the opacity at sub-mm and mm wavelengths (e.g. Ossenkopf & Henning, 1994), in agreement with observations. In parallel, one of the most important chemical processes that occurs is the 'freezing' of molecules onto the surface of dust grains, producing ice 'mantles' around solid 'cores', and

their subsequent evaporation if temperatures exceed $\sim 110 - 120\,\mathrm{K}$ (Fraser et al., 2001). At temperatures above $\sim 1,000 - 2,000\,\mathrm{K}$, silicate and carbonaceous dust grains themselves are sublimated (Duschl et al., 1996).

It is interesting to note that there are therefore at least three characteristic radii in the circumstellar environment of young stars. The largest is the *snow line*, the radius inside which dust grains lose their ice mantles, which is typically a few AU for a solar-mass star (e.g. Lecar et al., 2006). The second is the dust sublimation radius, inside which dust grains are destroyed, typically of the order of $15\,R_\star$ for a solar-mass star (Whitney et al., 2004b). Finally, the third is the magnetospheric disk truncation radius, inside which gas is removed by the rotating magnetosphere of the pre-main-sequence star. This is typically a few stellar radii (e.g. Kenyon et al., 1996, who estimate a truncation radius of 2 to $7\,R_\star$)

2.2 Monte-Carlo Radiation transfer

2.2.1 The equation of radiation transfer

Calculating synthetic SEDs and multi-wavelength images for young stars is a radiation transfer problem: given a luminous protostar surrounded by a distribution of dust, how much of the radiation will escape unhindered, how much will be scattered, and how much will be absorbed and re-emitted? Solving this amounts to solving the *equation of radiation transfer* (ERT), which relates the change in the intensity of light along a light ray to the absorption, scattering, and emission properties of the medium through which it is propagating.

Given a light ray with frequency ν and intensity I_ν travelling an infinitesimal distance ds along a straight line through a medium with emission coefficient per unit mass j_ν and opacity κ_ν, the intensity will change by dI_ν, where dI_ν/ds is given by differential form of the ERT:

$$\frac{dI_\nu}{ds} = -\rho\,\kappa_\nu\,I_\nu + \rho\,j_\nu \tag{2.5}$$

where $-\rho\,\kappa_\nu\,I_\nu$ accounts for absorption of light along ds, and $\rho\,j_\nu$ accounts for radiation emitted along ds as well as radiation scattered into the light path. By defining the source function $S_\nu \equiv j_\nu/\kappa_\nu$, the ERT can be rewritten as:

$$\frac{dI_\nu}{\rho\kappa_\nu\,ds} = -I_\nu + S_\nu \tag{2.6}$$

It is also useful to define the *optical depth* between two points s_1 and s_2 as:

$$\tau(s_1, s_2) \equiv \int_{s_1}^{s_2} \alpha_\nu(s)\, ds, \tag{2.7}$$

In which case the ERT simplifies further to

$$\frac{dI_\nu}{d\tau_\nu} = -I_\nu + S_\nu \tag{2.8}$$

The formal solution to the equation of radiation transfer is then:

$$I_\nu(\tau_\nu) = I_\nu(\tau_{\nu,0})\, e^{-(\tau_\nu - \tau_{\nu,0})} + \int_{\tau_{\nu,0}}^{\tau_\nu} S_\nu(\tau'_\nu)\, e^{-(\tau_\nu - \tau'_\nu)} d\tau'_\nu. \tag{2.9}$$

where the distance along the ray is expressed in terms of the optical depth τ_ν.

2.2.2 Monte-Carlo techniques

While it is possible to solve the ERT analytically or semi-analytically for simple systems such as plane-parallel or simple spherical geometries (Chandrasekhar, 1960) in order to predict the emergent spectra, the main difficulty in computing $I_\nu(\tau_\nu)$ in more complex cases is that the relation between the optical depth τ_ν and physical displacement s is a function of the density $\rho(s)$, which may not be a simple function of s. Monte-Carlo radiation transfer allows solutions to more complex 3-dimensional geometries to be found very easily by removing the need for analytical integration. The philosophy of a Monte-Carlo radiation transfer code is that it simulates the transfer of radiation in a very similar way to the way light propagates in Nature. The elementary entity is a *photon*, which is a packet of energy (rather than a single physical photon). The principle of Monte-Carlo radiation transfer is to emit and follow the propagation of a large number of these photons in order to compute the emergent spectrum.

Many of the physical processes are described through probability distribution functions (PDFs), such as the spectrum of sources of radiation, scattering angles, and optical depths to travel. A random value x can be selected from a PDF $P(x)$ defined in the range $[a, b]$ by normalising the PDF, finding the corresponding cumulative distribution function (CDF), generating a random number $\xi \in [0, 1]$, and finding the value of x such that the CDF is equal to ξ. This amounts to solving the following equation for x, given a random number $\xi \in [0, 1]$

$$\xi = \frac{\int_a^x P(x')\,dx'}{\int_a^b P(x')\,dx'} \tag{2.10}$$

Photons are given an initial position on an source (e.g. a point source or a sphere). The initial direction of propagation of the photons is sampled randomly from pre-determined PDFs. These PDFs can be set up to produce for example a point source with isotropic emission, or a sphere with limb darkening. Photons can also be emitted preferentially from certain areas of the sources (e.g. hot accretion spots) or from a diffuse volume, such as in the case of photons emitted from accreting gas in a disk. The frequency of the photons can be sampled from observed or synthetic spectra.

Photons are then allowed to propagate a certain distance until they either escape from the system or interact with dust grains. The optical depth a photon will travel before interacting is randomly sampled from the following PDF:

$$P(\tau)\,d\tau = e^{-\tau}\,d\tau \tag{2.11}$$

Random values of τ can be sampled using Eq. (2.10), which gives:

$$\tau = -\ln \xi \tag{2.12}$$

In order to determine how far the photon will *physically* travel, it is necessary to solve Eq. (2.7). In the case of non-trivial density distributions, this requires numerical integration. This would be computationally expensive in the case of a complex analytical function, or simply impossible in the case of a numerically determined density distribution (e.g. from hydrodynamical simulations). Therefore, a common solution is to discretise the density function, by binning the density onto a spherical polar (r,θ,ϕ) or Cartesian (x,y,z) grid that is made up of 'cells' of constant density. As well as being computationally efficient, this technique therefore allows completely arbitrary density distributions to be specified, including ones that cannot even be expressed analytically. Thus, a photon starts off from the source, at a given location in a cell. Because the density is constant inside the cell, it is easy to relate the physical distance to the optical depth. If the photon only needs to travel within the cell to reach the sampled optical depth, the integration is finished. Otherwise, the photon is moved to the edge of the cell, is transferred to the next cell, and the propagation is repeated until it

has travelled the required optical depth.

Once the photon has reached the required optical depth, it is either scattered or absorbed. Whether it is scattered or absorbed is determined by the albedo of the dust ω. In the case of scattering, the new direction of the photon is determined from the scattering properties of the dust. For example, the dust might be preferentially forward-scattering. Once a new direction has been sampled, the Stokes parameters are updated appropriately (see e.g. Chandrasekhar, 1960). If instead the photon is absorbed, it is immediately re-emitted isotropically by sampling the frequency from the emissivity $j_\nu = \kappa_\nu B_\nu(T)$. A new optical depth is sampled, and the process is repeated until the photon escapes from the system or is re-absorbed by a source. The process is typically repeated for millions of photons, which are binned into SEDs and images as they escape from the system.

In order to determine the emission coefficient j_ν for photons re-emitted from dust in LTE, the temperature of each cell is required. This can be done by assuming a simple initial temperature distribution (such as a power-law), then carrying out the radiation transfer a first time, and updating the temperature of each cell based on the total amount of energy that each cell has absorbed. After updating the temperatures, the radiation transfer can be run again, and the process repeated, until the temperature distribution converges (e.g. Lucy, 1999). Another technique is to update the temperature in each cell after each absorption, and to correct for previous over- or under-estimation of the temperature by sampling photons from 'difference' emission coefficient functions (Bjorkman & Wood, 2001).

2.2.3 Implementation

The implementation of this algorithm used for the work presented in this thesis is the radiation transfer code written by Barbara Whitney and collaborators. The code and its applications are extensively described in Whitney et al. (2003a,b, 2004b). The propagation of 'photons' and the density structure is fully 3-D, but the density structures chosen have no ϕ dependence, so the emergent 'photons' can be binned into SEDs as a function of θ only. This type of code is referred to as 2-D, to emphasise the assumption that the dust distribution is axisymmetric. Disk accretion luminosity is taken into account. The temperature correction follows the method proposed by Bjorkman & Wood. The code is written in FORTRAN 77, and at the time of writing is publicly available [3].

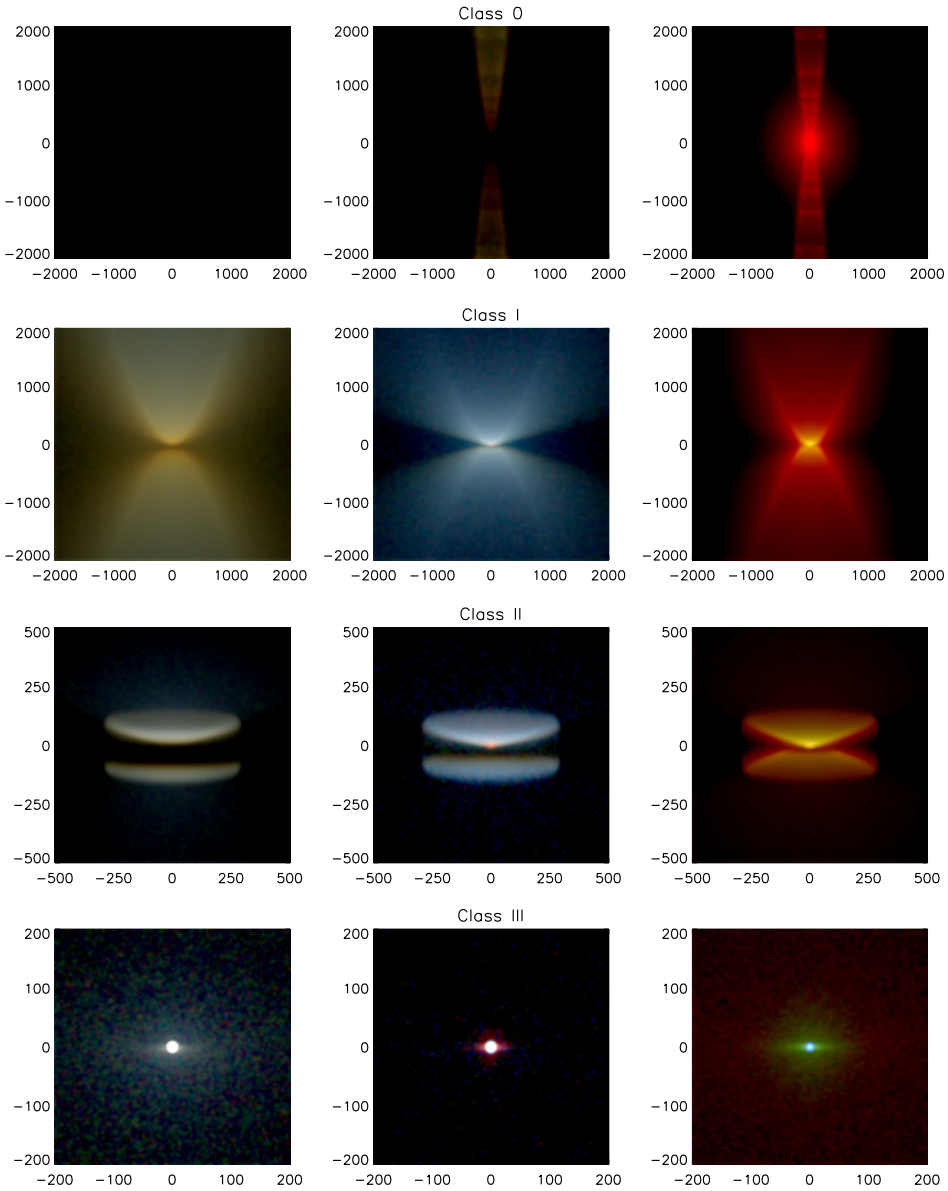

Figure 2.3: Synthetic images produced by the radiation transfer code discussed in §2.2.3. From top to bottom: Deeply embedded protostar, embedded protostar, pre-main sequence star with an optically thick circumstellar disk, and pre-main sequence star with an optically thin disk. From left to right: near infrared images (1.25 to 2.15 μm), mid-infrared images (3.6 to 8.0 μm), and mid- to far-infrared images (8.0 to 70 μm). The intensity scale is logarithmic, and the viewing angle is 80°, i.e. nearly edge-on. The image scale is in AU. This figure was adapted from Whitney et al. (2003a).

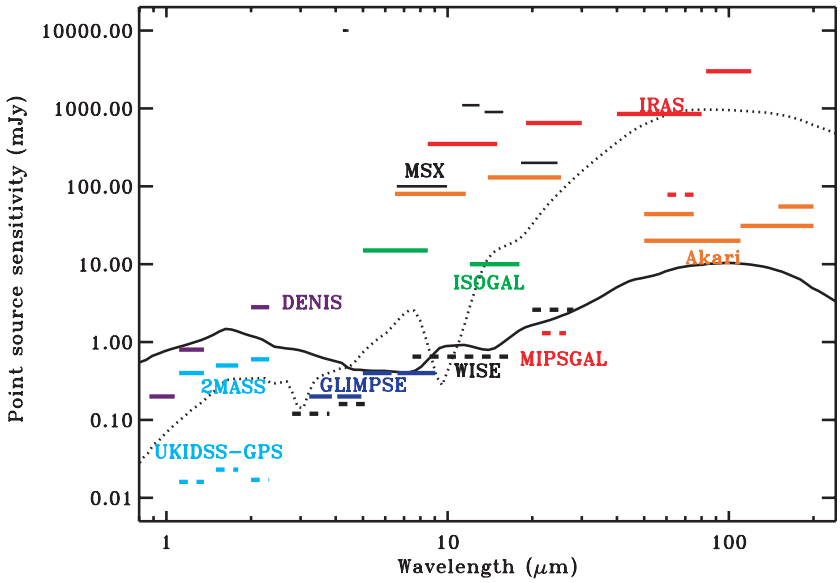

Figure 2.4: Sensitivity of previous and current surveys of the Galactic plane. Figure taken from Benjamin et al. (2003)

The code can compute SEDs for many viewing angles, and images for a given viewing angle and at different wavelengths. Polarisation spectra and images can be also computed for the Stokes parameters Q, U, and V. Figure 2.3 shows examples of near-, mid-, and far-infrared synthetic images for four different density distributions, representing four stages of evolution of a forming low-mass star, to demonstrate the capabilities of the code.

2.3 Large-scale surveys of star formation regions

While infrared observations of samples of young stars date back to Mendoza (1968) and Cohen (1973), the last few decades have seen the emergence of large-scale surveys of entire star formation regions, of the Galactic plane, and of the whole sky at infrared wavelengths. This section reviews the major large-scale surveys that have been invaluable to studies of star formation. Figure 2.4 graphically summarises the sensitivity limits of the different surveys.

The Infrared Astronomical Satellite: The Infrared Astronomical Satellite (IRAS), launched in January 1983, remained operational until November 1983 (Neugebauer et al., 1984). In that time, IRAS surveyed much of the sky at 12, 25, 60, and 100 μm with a $\sim 1'$ resolution. The average 10σ point-source sensitivity was 0.7, 0.65. 0.85, and 3.0 Jy at the four wavelengths respectively (Neugebauer et al., 1984). While providing far-infrared fluxes for many previously known T Tauri stars (Rucinski, 1985), IRAS also allowed the detection of many pre-

viously unknown protostars (e.g. Young et al., 1986; Beichman et al., 1986; Jennings et al., 1987), and over 1,700 embedded massive star candidates (Wood & Churchwell, 1989).

The Infrared Space Observatory: The Infrared Space Observatory (ISO), launched in November 1995, was a telescope with a 60 cm diameter mirror (Kessler et al., 1996). ISO remained operational until May 1998, and carried several instruments, including mid- and far-infrared spectrographs (SWS and LWS) covering wavelengths from 2 to 200 μm, and two imaging cameras (ISOCAM and ISOPHOT), providing imaging capabilities from 2.5 to 240 μm. ISO carried out a survey at 7 μm and 15 μm of a number of regions distributed throughout the Galactic plane (Omont et al., 2003), with a point-source sensitivity (at best) of 9 mJy and 7 mJy at 7 μm and 15 μm. This survey revealed over 700 YSO candidates (Felli et al., 2002b). ISO also provided unprecedented infrared spectroscopic capabilities, allowing a wealth of spectral lines – such as those due to silicates, ices, PAHs, H_2, CO, OH, and CO_2 – to be observed in YSOs (see e.g. review by van Dishoeck, 2004).

The Midcourse Space Experiment: The *Midcourse Space Experiment* (MSX) satellite, launched in April 1996, and operational until February 1997, was a Ballistic Missile Defence Organisation experiment which provided a demonstration of the technology that could allow space-based tracking of ballistic missiles during their midcourse flight phase. The MSX satellite carried out a number of scientific observations, including a survey of the Galactic plane (Price et al., 2001) between 1996 and 1997 at 8.28 μm (band A), 12.13 μm (band C), 14.65 μm (band D), and 21.3 μm (band E) with a pixel size of 18.3 μm. The point source sensitivity was approximately 0.16, 1.2, 1.0, and 3.0 Jy in the four bands respectively[1]. These observations have since been used to systematically search for hundreds of massive YSOs (Hoare et al., 2004).

The Two Micron All-Sky Survey: The Two Micron All-Sky Survey (2MASS) is a ground-based near-infrared all-sky survey carried out between 1997 and 2001 (Skrutskie et al., 2006). The observations consist of imaging in three bands: J (1.25 μm), H (1.65 μm), and K_s (2.15 μm). The 10σ sensitivities are 15.8, 15.1, and 14.3 mag respectively (Skrutskie et al., 2006). While it is not as sensitive as targeted near-infrared observations of star formation regions, it is nevertheless complementary to large-scale longer wavelength infrared surveys. One interesting use of 2MASS data in the context of star formation is the determination of interstellar ex-

[1]These values are from the Midcourse Space Experiment Point Source Catalog Version 2.3 Explanatory Guide (Figures 23-29)

Figure 2.5: *Spitzer*/GLIMPSE mosaic of the section of the Galactic plane from $\ell = 12.5$ to $15.5°$ and from $b = -1$ to $1°$, from $3.6\,\mu$m (blue) to $8.0\,\mu$m (red).

tinction in molecular clouds, which provides the ability to trace dense molecular cores (e.g. Lombardi et al., 2006).

The Spitzer Space Telescope: The *Spitzer Space Telescope*, one of NASA's *Great Observatories*, is an infrared telescope with a 85 cm diameter mirror, and with imaging and spectroscopic capabilities from $3.6\,\mu$m to $160\,\mu$m (Werner et al., 2004). Launched on the 25th of August 2003, and placed on an Earth-trailing orbit, it is expected to reach the end of its cryogenic mission in April 2009.

Spitzer carries three main instruments. The InfraRed Array Camera (IRAC; Fazio et al., 2004) is a set of 256×256 pixel arrays which provide imaging capabilities at 3.6, 4.5, 5.8, and $8.0\,\mu$m. The pixel size is $1.22''$, giving a field of view of $5.2' \times 5.2'$. The point spread function (PSF) full-width at half maximum (FWHM) is $1.66''$, $1.72''$, $1.88''$, and $1.98''$ from 3.6 to $8.0\,\mu$m respectively. Therefore the PSF is mostly under-sampled at the shortest wavelengths. The InfraRed Spectrograph (IRS; Houck et al., 2004) comprises four spectrograph modules, which once combined give a wavelength coverage of 5.3 to $38\,\mu$m with low ($R \approx 90$) and high ($R \approx 600$) spectral resolutions. Finally, the Multiband Imaging Photometer for Spitzer (MIPS; Rieke et al., 2004) offers imaging capabilities at 24, 70 and $160\,\mu$m, with diffraction limited PSF FWHMs of $6''$, $18''$, and $40''$ respectively.

While *Spitzer* did not carry out an all-sky survey, it has nevertheless produced a wealth of

data, including large surveys of star formation regions. For example, the Galactic Legacy Infrared Mid-Plane Survey Extraordinaire (GLIMPSE; Benjamin et al., 2003) and MIPS Galactic Plane Survey (MIPSGAL; PI Carey) Legacy surveys have mapped over 270 $\deg^2$ of the inner Galactic plane; the Cores-to-Disks (c2d) Legacy project has surveyed five nearby large molecular clouds (Chameleon, Serpens, Lupus, Perseus, and Ophiuchius; Evans et al., 2003); and several projects have surveyed the OMC (Megeath et al., 2005a), the TMC (Hartmann et al., 2005), the Large Magellanic Cloud (LMC) (Chu et al., 2005; Meixner et al., 2006) and Small Magellanic Cloud (SMC), and many other star formation regions (e.g Gutermuth et al., 2004; Megeath et al., 2005b; Allen et al., 2007; Sicilia-Aguilar et al., 2006).

Future telescopes and surveys: In the last few years, the AKARI satellite (previously known as ASTRO-F; Murakami et al., 2007), considered by some as the successor of the IRAS satellite, has completed a survey of the whole sky at mid- and far-infrared wavelengths. At mid-infrared wavelengths, the sensitivity and resolution are similar to that of the MSX satellite, while at far-infrared wavelengths, the sensitivity is almost 100 times higher than IRAS. AKARI data will be of great importance to better constrain the far-infrared SED of YSOs.

In 2009, ESA will launch the *Herschel Space Observatory*, which will provide unprecedented resolution at far-infrared and sub-mm wavelengths. Herschel will survey both a number of individual star-forming regions and the Galactic plane. This will also allow far-infrared and sub-mm constraints on the SEDs of YSOs. In particular, the high resolution ($6''$ at 100 μm) will facilitate the merging of such far-infrared and sub-mm data with arcsecond resolution near- and mid-infrared observations such as those made by *Spitzer*.

Looking further into the future, the *Atacama Large Millimetre/sub-millimetre Array* (ALMA) and the *James Webb Space Telescope* (JWST) are highly anticipated. They should achieve a new level of performance at mm/sub-mm wavelengths and near- and mid-infrared wavelengths respectively, including both dramatic improvements in spatial resolution and sensitivity over current facilities. In particular, both should provide angular resolutions better than $0.1''$. In the context of star formation, they will therefore allow high-resolution observations of nearby YSOs at infrared and mm wavelengths at a similar (or better) resolution to that of HST.

3

Model SEDs for Young Stellar Objects

Adapted from *Robitaille et al., 2006, ApJS, **167**, 256*

A large set of radiation transfer models of axisymmetric YSOs is presented. The models cover a wide range of stellar masses (from 0.1 $M_\odot$ to 50 $M_\odot$) and evolutionary stages (from the early envelope infall stage to the late disk-only stage). SEDs and polarisation spectra have been computed at ten viewing angles for 20,000 physical models, resulting in a total of 200,000 SEDs. The theoretical and observational constraints on the physical conditions of disks and envelopes in YSOs were carefully assessed in order to fully span the corresponding regions in parameter space. In this chapter, the main features of the models and the range of parameters explored are summarised. The models are used to shed light on trends in near- and mid-infrared observations of YSOs (such as changes in the spectral indices and colours of their SEDs), and how these changes can be linked with physical parameters (such as stellar, disk, and infalling envelope parameters).

3.1 Introduction

In order to interpret the SEDs of the many unresolved YSOs seen in recent infrared surveys of star formation regions, it is useful to compute model SEDs for a range of stellar masses and evolutionary stages. Previous examples of model SED grids include those of Adams & Shu (1985), who presented an atlas of 26 synthetic SEDs for embedded protostars for different values of the stellar mass and envelope infall rate; Kenyon et al. (1993a), who similarly computed a small grid of synthetic SEDs for embedded protostars; and D'Alessio et al. (2005), who recently computed 3,000 model SEDs for protoplanetary disks. However, these previous efforts have concentrated mostly on specific mass ranges (e.g. low-mass stars) or evolutionary stages (e.g. protoplanetary disk phase). What has been missing is a large and consistently computed set of models, covering a wide range of evolutionary stages for low- to high-mass stars, from the initial protostellar collapse to dispersing optically thin disks. The work presented in this chapter aims to address this by presenting a new set of 200,000 model SEDs that includes low- to high-mass YSOs from the early embedded phases of evolution to the disk dispersal stage.

The set of models is described in §3.2. Sample model SEDs, polarisation spectra, and colour-colour diagrams, as well as an analysis of spectral index and colour-colour classifications are presented in §3.3. Finally, the findings from this work are summarised in §3.4. A technique that makes use of these models to rapidly fit observed SEDs is subsequently presented in Chapter 4.

3.2 The set of models

3.2.1 The radiation transfer code

Brief description of the code

The Monte-Carlo radiation transfer code used to compute the set of models presented in this chapter was briefly described in §2.2. It includes non-isotropic scattering, polarisation, and thermal emission from dust in a spherical-polar grid, solving for the temperature using the method of Bjorkman & Wood (2001). The circumstellar geometry consists of a rotationally-flattened infalling envelope (Ulrich, 1976; Terebey et al., 1984), bipolar cavities (Whitney & Hartmann, 1993; Whitney et al., 2003a) and a flared accretion disk (Shakura & Syunyaev,

1973; Pringle, 1981; Kenyon & Hartmann, 1987; Chiang & Goldreich, 1997; D'Alessio et al., 1998; Dullemond et al., 2001). The luminosity sources include the central star and disk accretion. The code and the model geometries are described in detail in Whitney et al. (2003a,b).

As will be discussed in §3.2.2, the various model parameters are sampled in order to reproduce a range of evolutionary stages. For example, the envelope accretion rate decreases over time, the bipolar cavities become wider, the dust in the cavities less dense, and the disk radius increases during the early accretion from the envelope.

Dust grain models

The grain models used for this work contain a mixture of astronomical silicates and graphite in solar abundance, using the optical constants of Laor & Draine (1993). The optical properties are averaged over the size distribution and composition, and the heating and emission properties of different grain sizes or composition are not treated separately. This could affect the thermal and chemical properties in the inner regions of the disk (Wolf, 2003) but the effect on the SED is expected to be relatively minor (Wolf, 2003; Carciofi et al., 2004).

The grain properties vary with location in the disk and envelope as follows: the densest regions of the disk ($n_{\rm H_2} > 3.3 \times 10^{-14}\,{\rm g\,cm^{-3}}$) use a grain model with a size distribution that decays exponentially for sizes larger than 50 μm and extends up to 1 mm; this grain model fits the SED of the HH30 disk (Wood et al., 2002b). This is the same as the "Disk mid-plane" grain model described in Table 3 of Whitney et al. (2003a). The rest of the circumstellar geometry uses a grain size distribution with an average particle size slightly larger than the diffuse ISM, and a ratio of total-to-selective extinction $R_V = 3.6$. This is the "KMH" model (Kim, Martin, & Hendry, 1994), referred to as the "Outflow" model in Table 3 of Whitney et al. (2003a). As discussed in §2.1, grains in molecular clouds and protostars show evidence for ice coatings, but these are not included in the models presented in this chapter.

Stellar photospheres

The spectrum of the central source for each model depends on its photospheric temperature and to a lesser extent its surface gravity. For stellar temperatures below 10,000 K, the model stellar photospheres from Brott & Hauschildt (2005) were used, while for stellar temperatures above 10,000 K, the model stellar photospheres from Castelli & Kurucz (2004) were used. In both cases, solar metallicity was assumed. For each YSO model, the stellar photospheres were

Table 3.1: The 14 parameters varied for the 20,000 YSO models

Symbol	Description
$M_\star$	Stellar Mass
$R_\star$	Stellar Radius
$T_\star$	Stellar Temperature
$\dot{M}_{\rm env}$	Envelope accretion rate
$R_{\rm env}^{\rm max}$	Envelope outer radius
$\rho_{\rm cavity}$	Cavity density
$\theta_{\rm cavity}$	Cavity opening angle
$M_{\rm disk}$	Disk mass (gas+dust)
$R_{\rm disk}^{\rm max}$	Disk outer radius
$R_{\rm disk}^{\rm min}$	Disk inner radius
$\dot{M}_{\rm disk}$	Disk accretion rate
$z_{\rm factor}$	Disk scale height factor
β	Disk flaring power
$\rho_{\rm ambient}$	Ambient density

interpolated to the relevant temperature and surface gravity.

Model parameters

The 14 model parameters are shown in Table 3.1. Fortunately, only a few parameters are important at a given evolutionary stage. For example in the youngest stages, the disk is hidden beneath the envelope: the disk inner radius, accretion rate, and to a lesser extent disk mass are the main disk parameters that affect the 1-8 μm fluxes. The presence of an inner disk is required to produce mid-infrared flux and to obscure the central source at edge-on viewing angles, but the dust properties in the disk and the amount of flaring do not have an important effect on the mid-infrared SED. At these young stages, the most important parameters are the envelope accretion rate, the opening angle of the bipolar cavities, the inclination to the line of sight, the disk/envelope inner radius, the stellar temperature and luminosity, and to a lesser extent the disk mass. At later stages, when the envelope has mostly dispersed, the most relevant parameters for the SED are the disk inner radius, accretion rate, mass, and flaring (or dust settling), and the stellar temperature and luminosity (Kenyon & Hartmann, 1987; Lada & Adams, 1992; Chiang & Goldreich, 1997; D'Alessio et al., 1998; Furlan et al., 2005).

The details of the parameter sampling are given in §3.2.2. It is important to note that the aim of this work is to provide model SEDs for stages of evolution that have been suggested by

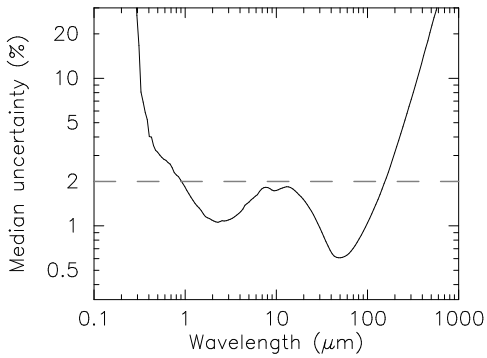

Figure 3.1: The median fractional (one-sigma) error of the flux values for all 200,000 SEDs. For zero fluxes, a fractional error of 100% was used. The dashed line indicates the level of 2% uncertainty, and shows that the median error of the models is less than this in the range $1 - 100\,\mu$m.

theory or observations, rather than to put forward or favour a specific model of evolution for YSOs. In particular, the different models do not follow a set number of YSOs throughout their evolution, but instead sample possible evolutionary stages and stellar masses randomly.

Output of the radiation transfer code

The output from the code presented here consists of flux and polarisation spectra for 250 wavelengths (from 0.01 to $5,000\,\mu$m), computed at 10 viewing angles (from pole-on to edge-on in equal intervals of cosine of the inclination) and in 50 different circular apertures (with radii from 100 to 100,000 AU). Since each one of the 20,000 models produces an SED for each viewing angle, the set of models contains 200,000 SEDs. The code can produce images at specific viewing angles, but these were not computed as doing so would increase the CPU time required tenfold. However, the 50 apertures from $100 - 100,000$ AU amount to a spherically averaged intensity profile for each viewing angle of each model.

All models were convolved with a large number of common filter band-passes ranging from optical to sub-mm wavelengths, including for example optical (e.g. UBVRI), near-infrared (e.g. 2MASS JHK_s), mid- and far-infrared (e.g. IRAC, MSX, IRAS, MIPS), and sub-mm (e.g. Scuba 450 and $850\,\mu$m) filters (see Appendix A for details on the convolution). The polarisation spectra have a lower signal-to-noise than the SEDs, and were therefore smoothed before being convolved with broadband filter band-passes.

The models presented here were computed using 20,000,000 'photons' (energy packets, Bjorkman & Wood, 2001). This produces SEDs with good signal-to-noise ratios for wavelengths spanning $1 - 100\,\mu$m (however, the signal-to noise may also be good outside this

range). The wavelength range at which a model SED has a good signal-to-noise depends on the evolutionary stage of the YSO: SEDs may be noisy at wavelengths shorter than 1 μm, but with a good signal-to noise at sub-mm wavelengths for young embedded sources, or be noisy at wavelengths longer than about 100 μm and with a good signal-to-noise at optical and near-UV wavelengths for low mass stars with protoplanetary disks. Figure 3.1 shows the median noise levels as a function of wavelength (using the SEDs measured in the largest aperture). Uncertainties are available for all SED data points, so they can in effect be used even at wavelengths with lower signal-to-noise. The SEDs can be rebinned to a lower wavelength resolution to reduce these uncertainties.

The time taken for each model to run varies with optical depth and covering factor of circumstellar material as seen from the radiation source. A disk model typically takes an hour to run on a 3 GHz Intel processor, and an embedded protostar can take 10 hours. The total CPU time for the models presented here, which were run on three different computer clusters, was approximately 65,000 hours (or three weeks using approximately 60 CPUs).

The models are available on a dedicated web server [4], which is described in more detail in Appendix B. This includes SEDs for all inclinations and apertures for each model. Various components of the SED can be viewed separately, such as the flux emitted by the disk, star, or envelope, the scattered flux, the thermal flux, and the direct stellar flux, as described further in §3.3.2. Fluxes and magnitudes for common filter functions are also available.

3.2.2 Sampling of the model parameters

In this section, a detailed description of the parameter sampling is presented. Parameter space cannot be explored in its entirety in a completely unbiased manner. Therefore arbitrary decisions were made concerning the ranges of parameter values covered by the models. However, these parameter ranges should be reasonable, as they span those determined from observations and theories. The parameters can be divided into three categories: the central source parameters (stellar mass, radius and temperature), the infalling envelope parameters (the envelope accretion rate, outer radius, inner radius, cavity opening angle and cavity density), and the disk parameters (disk mass, accretion rate, outer radius, inner radius, flaring power, and scale height). Also included is a parameter describing the ambient density surrounding the YSOs.

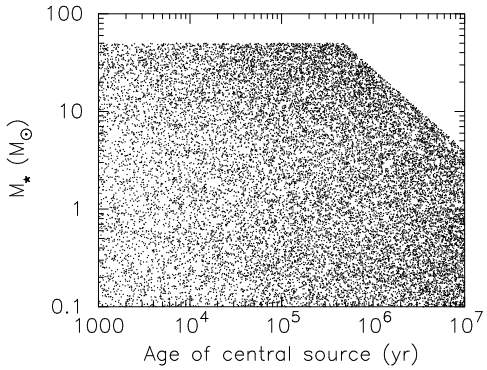

Figure 3.2: The values of the central source mass $M_\star$ and evolutionary age $t_\star$ for the 20,000 models. Each point represents one model.

All the masses, mass accretion rates and densities for the disk and envelope parameters assume a gas-to-dust ratio of 100. The results can be scaled to different gas-to-dust ratios since only the dust is taken into account in the radiation transfer. For example, a disk with a total mass of $0.01\,M_\odot$ in a region where the gas-to-dust ratio is 100 will produce the same SED as a disk with a total mass of $0.1\,M_\odot$ in a region where the gas-to-dust ratio is 1000 (such as a low metallicity galaxy or perhaps the outer Milky Way). In addition to disk masses, the following parameter values should be re-scaled accordingly in regions where the gas-to-dust ratio is not 100: the envelope accretion rates, disk accretion rates, cavity densities and ambient densities. It is only necessary to re-scale the parameter values, and it is not necessary to re-run the radiation transfer models

The stellar parameters

The parameters for the 20,000 YSO models were chosen using the following procedure. First a stellar mass $M_\star$ was randomly sampled from the following PDF:

$$f(M_\star)dM_\star = \frac{1}{\log_e 10}\frac{1}{\log_{10} M_2 - \log_{10} M_1}\frac{dM_\star}{M_\star} \tag{3.1}$$

The masses were sampled between $M_1 = 0.1M_\odot$ and $M_2 = 50M_\odot$. This produced a constant density of models in $\log_{10} M_\star$ space. Following this, a random stellar age $t_\star$ was sampled from a similar PDF:

$$f(t_\star)dt_\star = \frac{1}{6}\,\frac{1}{t_{\rm max}^{1/6} - t_{\rm min}^{1/6}}\,\frac{dt_\star}{t_\star^{5/6}} \tag{3.2}$$

The ages were sampled between $t_{\rm min} = 10^3$ yr and $t_{\rm max} = 10^7$ yr. This distribution produced a density of models close to constant in $\log_{10} t_\star$ space, but with a slight bias towards larger

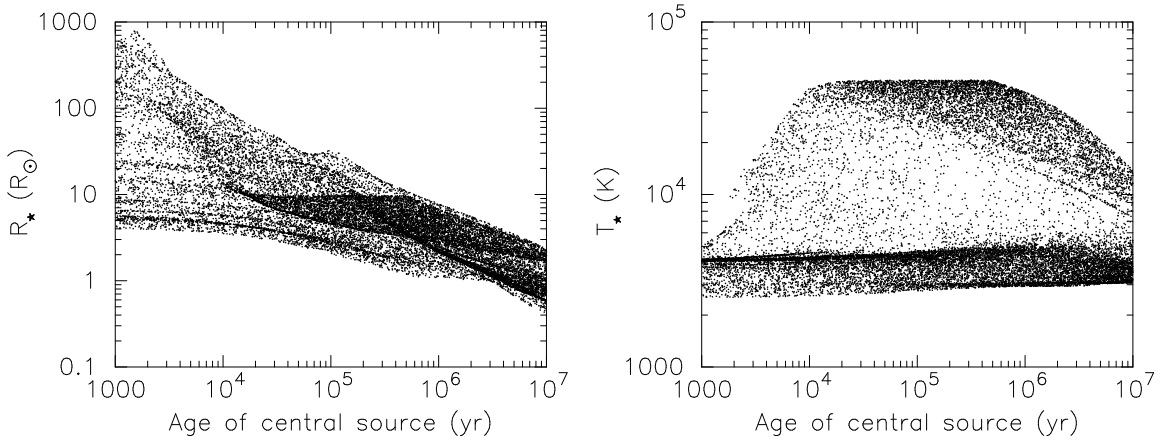

Figure 3.3: The values of the central source radius $R_\star$ (*left*) and temperature $T_\star$ (*right*) as a function of evolutionary age for the 20,000 models. These values were derived from the central source mass and evolutionary age using evolutionary tracks.

values of $t_\star$. This was done to avoid a deficit of disk-only models. In cases where the resulting values of the stellar age were greater than the combined pre-main sequence and main-sequence lifetime of the star (estimated from the sampled masses $M_\star$), the age was resampled until it was within the adequate lifetime. The values of $M_\star$ and $t_\star$ for the 20,000 models are shown in Figure 3.2.

For each set of $M_\star$ and $t_\star$ the values of the stellar radius $R_\star$ and temperature $T_\star$ were found by interpolating pre-main sequence evolutionary tracks (Bernasconi & Maeder 1996 for $M_\star \geq 9\,M_\odot$; Siess et al. 2000 for $M_\star \leq 7\,M_\odot$; a combination of both for $7\,M_\odot < M_\star < 9\,M_\odot$). The values of $T_\star$ and $R_\star$ are shown in Figure 3.3. It is important to note that the evolutionary age of the central sources is not a parameter in the radiation transfer code, and was only used to compute consistent radii and temperatures as well as approximate ranges of disk and envelope parameters. Any errors in the evolutionary tracks can easily be accommodated by the large range of parameter values allowed at a given age. Furthermore it is always possible to reassign a stellar source age to a model if it is found that a different set of evolutionary tracks is more appropriate for pre-main-sequence stars

Once the stellar parameters were determined, these were used to find the disk and envelope parameters. Since there exists no exact relation between the parameters of the central star and those of the circumstellar environment, the values of the various parameters were sampled from ranges that are functions of the evolutionary age of the central source, as well as functions of the stellar masses in certain cases. These ranges were based on theoretical predictions and observations.

The infalling envelope parameters

The azimuthally symmetric density structure $\rho(r,\theta)$ for the rotationally flattened infalling envelope is given in spherical polar co-ordinates by (Ulrich, 1976; Terebey et al., 1984)

$$\rho(r,\theta) = \frac{\dot{M}_{\rm env}}{4\pi\left(GM_\star R_{\rm c}^3\right)^{1/2}}\left(\frac{r}{R_{\rm c}}\right)^{-3/2}\left(1+\frac{\mu}{\mu_0}\right)^{-1/2}\left(\frac{\mu}{\mu_0}+\frac{2\mu_0^2 R_{\rm c}}{r}\right)^{-1}, \qquad (3.3)$$

where $\dot{M}_{\rm env}$ is the envelope accretion rate, $R_{\rm c}$ is the centrifugal radius, $\mu = \cos\theta$ (θ is the polar angle), and μ_0 is cosine of the angle of a streamline of infalling particles as $r \to \infty$. The centrifugal radius $R_{\rm c}$ determines the approximate disk radius and flattening in the envelope structure. The equation for the streamline can be used to determine μ_0:

$$\mu_0^3 + \mu_0(r/R_{\rm c} - 1) - \mu(r/R_{\rm c}) = 0. \qquad (3.4)$$

The range of values sampled for each of the envelope parameters, as well as the final parameter values, are shown in Figure 3.4.

Envelope accretion rate: The values of $\dot{M}_{\rm env}/M_\star$ were sampled from an envelope function that is constant for $t_\star < 10^4$ yr (Shu, 1977; Terebey, Shu, & Cassen, 1984), decreases between 10^5 yr and 10^6 yr (Foster & Chevalier, 1993; Foster, 1994; Hartmann, 2001) and goes to zero around 10^6 yr (Young & Evans, 2005). The range of accretion rate values $\dot{M}_{\rm env}/M_\star$ at a given time is two orders of magnitude wide, and the values were sampled uniformly in $\log[\dot{M}_{\rm env}/M_\star]$. The average values were chosen to match estimates of low-mass (Adams et al., 1987; Kenyon et al., 1993a,b; Whitney et al., 1997) and high-mass YSOs (Wolfire & Cassinelli, 1987; Osorio et al., 1999; Omukai & Palla, 2001; Churchwell, 2002; Yorke & Sonnhalter, 2002; McKee & Tan, 2003; Bonnell et al., 2004). In cases where this value fell below $10^{-9}\left[M_\star/M_\odot\right]^{1/2}\,{\rm yr}^{-1}$, the envelope was discarded, and the YSO model was considered as a disk-only model. Finally, for stellar masses above $20\,M_\odot$ the envelope accretion rate was sampled from the same range of $\dot{M}_{\rm env}$ as a $20\,M_\odot$ model, so that the largest value of $\dot{M}_{\rm env}/M_\star$ is $5\times10^{-4}\,{\rm yr}^{-1}$.

Envelope outer radius: The appropriate envelope outer radius were found by calculating the approximate radius at which the optically thin radiative equilibrium temperature falls to 30 K

(Lamers & Cassinelli, 1999):

$$\frac{R_0}{R_\star} = \frac{1}{2}\left(\frac{T_\star}{30\,\mathrm{K}}\right)^{2.5}. \tag{3.5}$$

The values of $R_{\mathrm{env}}^{\mathrm{max}}$ were sampled uniformly in $\log R$ space between $R_0 \times 4$ and $R_0/4$ (the latter to account for truncation by tidal forces in clusters). The initial range of values for a 1 $M_\odot$ star is shown as an example in Figure 3.4. In cases where $R_{\mathrm{env}}^{\mathrm{max}} > 10^5$ AU, $R_{\mathrm{env}}^{\mathrm{max}}$ was set to 10^5 AU. In cases where $R_{\mathrm{env}}^{\mathrm{max}} < 10^3$ AU and $R_0 \times 4 > 10^3$ AU, $R_{\mathrm{env}}^{\mathrm{max}}$ was re-sampled between 10^3 AU and $R_0 \times 4$. Finally, in cases where $R_0 \times 4 < 10^3$ AU, $R_{\mathrm{env}}^{\mathrm{max}}$ was set to 10^3 AU.

Envelope cavity opening angle: The shape of the outflow cavity is described in cylindrical polar co-ordinates by $z = c\varpi^d$ where ϖ is the radial co-ordinate. For all the models, d was set to 1.5. Taking the cavity opening angle θ_{cavity} to be that for which z=$R_{\mathrm{env}}^{\mathrm{max}}$, c is given by $R_{\mathrm{env}}^{\mathrm{max}}/(R_{\mathrm{env}}^{\mathrm{max}} \tan\theta_{\mathrm{cavity}})$. The cavity opening angle was sampled from a range of values increasing with evolutionary age, as indicated by observations of cavities and outflows in Class 0 and Class I protostars (Zealey et al., 1993; Chandler et al., 1996; Tamura et al., 1996; Lucas & Roche, 1997; Hogerheijde et al., 1998; Velusamy & Langer, 1998; Bachiller & Tafalla, 1999; Padgett et al., 1999; Beuther & Shepherd, 2005; Shepherd, 2005; Arce & Goodman, 2001; Arce & Sargent, 2004, 2006; Arce et al., 2007). In cases where the cavity angle was larger than 60°, it was reset to 90°, assuming that the envelope is mostly dispersed at this stage of evolution.

Envelope cavity density: The density of gas and dust in the envelope cavity was sampled from a range of values following a decreasing function of time, one order of magnitude wide, with values ranging between 10^{-22} and $8 \times 10^{-20}\,\mathrm{g\,cm^{-3}}$. These values correspond to molecular number densities of $n_{\mathrm{H_2}} = 3 \times 10^1 \rightarrow 2 \times 10^4\,\mathrm{cm^{-3}}$ that are typical of observations of molecular outflows (e.g. Moriarty-Schieven et al., 1995a,b). In cases where the cavity density was lower than the ambient density of the surrounding medium (described in the next paragraph) the cavity density was reset to the ambient density. The cavity density was assumed to be constant with radius from the central source for simplicity (as one would expect from a cylindrical outflow with a constant outflow rate).

The ambient density: The infalling envelope is assumed to be embedded in a constant density ISM. This surrounding ambient density can contribute to the extinction, scattering and thermal emission of the circumstellar dust, especially in high-luminosity sources, which can heat up large volumes of the surrounding molecular cloud. In disk-only sources and low-

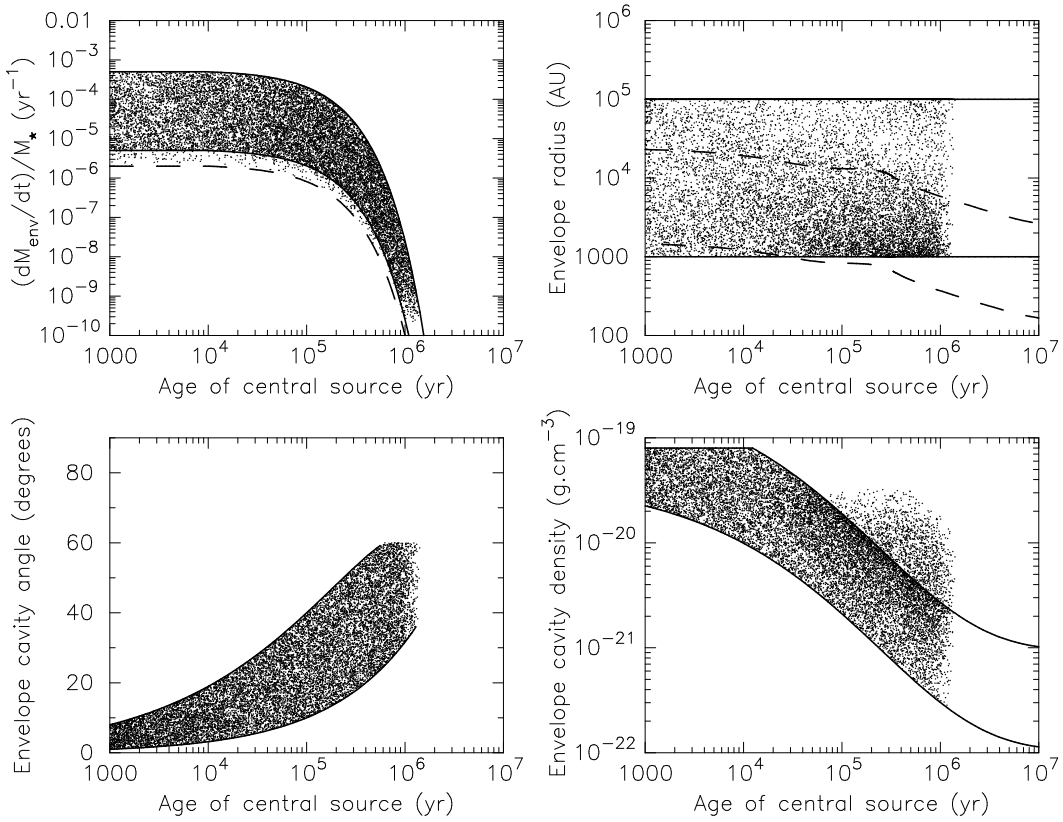

Figure 3.4: The envelope parameters as a function of the evolutionary age for the 20,000 models. *Top left* – The envelope accretion rates were sampled from the range shown by the solid lines, for models with $M_\star < 20\,M_\odot$. For models with $M_\star > 20\,M_\odot$, the envelope accretion rates were sampled from the same range as a $20\,M_\odot$ model, leading to lower values of $\dot{M}_{\rm env}/M_\star$. The dashed line shows the lower limit of $\dot{M}_{\rm env}/M_\star$ values for models with $M_\star > 20\,M_\odot$. *Top right* – The envelope radius. The dashed lines represent the original range that was sampled from, for a $1\,M_\odot$ central source. *Bottom left* – The opening angle of the bipolar cavities. Values above 60° were reset to 90°. *Bottom right* – The cavity density. The values were sampled between the two solid lines; subsequently, any value of the cavity density that was smaller than the ambient density was reset to the ambient density.

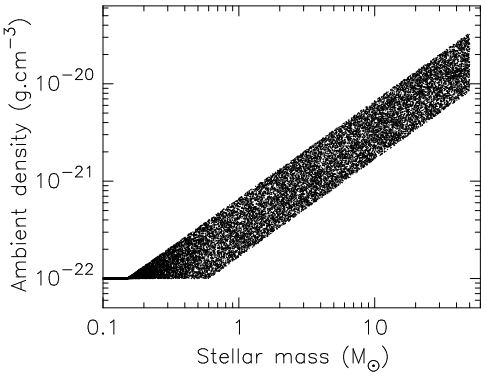

Figure 3.5: The ambient density as a function of the central source mass $M_\star$. A lower limit of $10^{-22}\,\mathrm{g\,cm^{-3}}$ was used.

mass YSOs, the contribution from the ambient density is small, though often non-zero. This density was sampled between $1.67 \times 10^{-22}\,[M_\star/M_\odot]\,\mathrm{g\,cm^{-3}}$ (or $10^{-22}\,\mathrm{g\,cm^{-3}}$, whichever was largest) and $6.68 \times 10^{-22}\,[M_\star/M_\odot]\,\mathrm{g\,cm^{-3}}$, corresponding to values in the range $n_{\mathrm{H_2}} \sim 50 - 200\,[M_\star/M_\odot]\,\mathrm{cm^{-3}}$. This is consistent with typical densities of $n_{\mathrm{H_2}} \sim 100\,\mathrm{cm^{-3}}$ observed in molecular clouds (e.g. Blitz, 1993).

The disk parameters

For the disk structure, a standard flared (azimuthally symmetric) accretion disk density was assumed (Shakura & Syunyaev, 1973; Lynden-Bell & Pringle, 1974; Pringle, 1981; Bjorkman, 1997; Hartmann et al., 1998):

$$\rho(\varpi, z) = \rho_0 \left[1 - \sqrt{\frac{R_\star}{\varpi}}\right] \left(\frac{R_\star}{\varpi}\right)^{\alpha} \exp\left\{-\frac{1}{2}\left[\frac{z}{h}\right]^2\right\}, \tag{3.6}$$

where h is the disk scale height, which increases with radius as $h \propto \varpi^{\beta}$, β is the flaring power, and $\alpha = \beta + 1$ is the radial density exponent. The disk scale height at the dust sublimation radius is set to be that for hydrostatic equilibrium, multiplied by a factor z_{factor}. This factor can be smaller than 1 if there is gas or other opacity inside the dust destruction radius, decreasing the amount of stellar flux incident on the inner wall; or it can be used to mimic dust settling, as described in the disk structure paragraph in this section. The normalisation constant ρ_0 is defined such that the integral of the density $\rho(\varpi, z)$ over the whole disk is equal to M_{disk}. The values for all the disk parameters are shown in Figure 3.6.

Disk mass: The disk mass was sampled from $M_{\mathrm{disk}}/M_\star \sim 0.001 - 0.1$ at early evolutionary stages, and a wider range of masses between 1 and 10 Myr. This allows for disk masses of

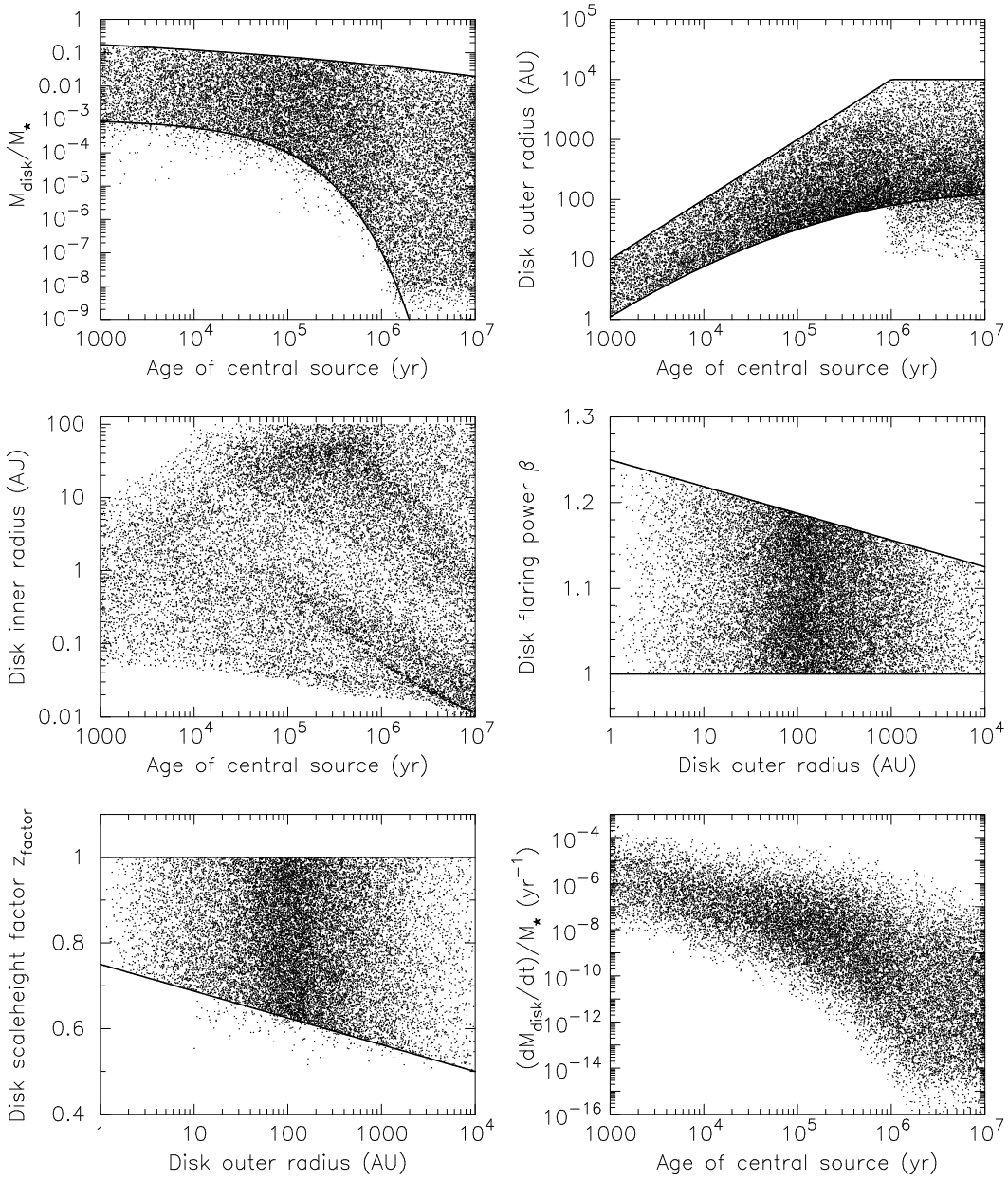

Figure 3.6: The disk parameters as a function of evolutionary age or disk outer radius for the 20,000 models. *Top left* – The disk masses were initially sampled between the two solid lines, and the points that lie below the lower limit are models for which an inner hole has been cleared in the disk. *Top right* – The disk outer radii were initially sampled between the two solid lines, and the points that lie below the lower limit for $t_\star > 10^6$ yr are models for which the outer radius was truncated (this was done only for disk-only models). *Centre left* – The disk inner radius was sampled between $R_{\rm disk}^{\rm min} = 1R_{\rm sub}$ and $R_{\rm disk}^{\rm min} = 100$ AU for two thirds of models, and set to $R_{\rm disk}^{\rm min} = 1R_{\rm sub}$ for the remaining models. *Centre right* – The flaring power β was sampled as a function of $R_{\rm disk}^{\rm max}$ between the two solid lines. *Bottom left* – The disk scale height factor $z_{\rm factor}$ was sampled as a function of $R_{\rm disk}^{\rm max}$ before outer disk truncation from the range defined the two solid lines, and the points below the line are models for which the outer disk radius was truncated, shifting these models to lower values of $R_{\rm disk}^{\rm max}$. *Bottom right* – The disk accretion rate was not sampled directly: instead the values of $\alpha_{\rm disk}$ were randomly sampled between 10^{-3} and 10^{-1}. This plot shows the values of $\dot{M}_{\rm disk}/M_\star$ calculated by the code (using Eq. 3.8).

$\sim 0.001 - 0.1\,M_{\odot}$ typically observed in low-mass YSOs, whether during the early infall phase or during the T-Tauri phase (e.g. Beckwith et al., 1990; Terebey et al., 1993; Dutrey et al., 1996; Kitamura et al., 2002; Looney et al., 2003; Andrews & Williams, 2005), higher disk masses around high-mass YSOs, and disk masses down to $M_{\rm disk}/M_{\star} = 10^{-8}$ after 1 Myr to allow for the disk dispersal stage.

Disk outer radius and envelope centrifugal radius: In a rotating and infalling envelope, material near the poles has little angular momentum, and will fall near to or onto the central source. In contrast, infalling material close to or along the equatorial plane will have the most angular momentum, and will fall to a radius $R_{\rm c}$ in the equatorial plane, where $R_{\rm c}$ is the centrifugal radius (e.g. Cassen & Moosman, 1981; Terebey et al., 1984). Therefore, the centrifugal radius is usually associated with the outer radius of the circumstellar disk. The values of $R_{\rm c}$ were sampled between 1 AU and 10,000 AU, following a time-dependent range of values that allowed for smaller radii in younger models. Theories indicate that the centrifugal radius will grow with time, if the infalling envelope was initially rotating as a solid body (e.g. Adams & Shu, 1986). In Taurus, disk sizes can be imaged directly (Burrows et al., 1996; Padgett et al., 1999) and are typically a few hundred AU for both Class I and II sources. Large disks have been indicated around high-mass stars (see recent review article by Cesaroni et al. 2007 for an exhaustive list); however, some of these observations may have been detecting envelope toroids, which are typically larger than the centrifugal radii in the models presented here. Most observations of massive YSOs suggest typical disk sizes of roughly 500 to 2,000 AU.

For disk-only models, the disk outer radii were sampled from the same time-dependent range of values as that used for the centrifugal radius for models with infalling envelopes. Subsequently, two thirds of disk-only models saw their outer radius truncated. This was done by resetting the disk outer radius to be randomly sampled between 10 AU and the centrifugal radius. This was done to account for the possible truncation of the outer regions of disks in dense clusters due to stellar encounters or photo-evaporation (see e.g. observations by Vicente & Alves 2005 who find that only $\sim 50\,\%$ of disks in the Trapezium cluster are larger than 50 AU; see also simulations of cluster formation by Bate et al. 2003). The disk masses for these models were then recalculated by assuming the original density structure, and removing the truncated mass (not recalculating the disk mass could lead to unrealistically dense disks with small outer radii).

Disk (and envelope) inner radius: For all models, the envelope inner radius was set to the disk inner radius. For one third of all models, the disk inner radius was set to the dust destruction radius $R_{\rm sub}$ empirically determined to be (Whitney et al., 2004b):

$$\frac{R_{\rm sub}}{R_\star} = \left(\frac{T_{\rm sub}}{T_\star}\right)^{-2.1} \tag{3.7}$$

where a value of $T_{\rm sub} = 1,600\,{\rm K}$ was assumed for the dust sublimation temperature. In the remaining two thirds of models, the inner disk/envelope radii were increased. This was done in order to account for binary stars clearing cavities in envelopes in young sources (e.g. Jørgensen et al., 2005), and binary stars or planets clearing out the inner disk in disk models (Lin & Papaloizou, 1979a,b; Artymowicz & Lubow, 1994; Calvet et al., 2002; Rice et al., 2003). For these models, the disk and envelope inner radius were sampled between the dust destruction radius and 100 AU (or the disk outer radius in cases where this was less than 100 AU). The disk masses for these models were then recalculated (as for the disk outer radius).

Disk structure: The disk flaring power β and the scale height factor $z_{\rm factor}$ were sampled from a range that depends on the disk outer radius. For large disks, the average β decreases to prevent geometries that resemble envelopes with curved cavities (which would confuse the interpretation of the SEDs). Both parameters β and $z_{\rm factor}$ together can be used to mimic the effects of dust settling (i.e. low values of β and $z_{\rm factor}$ can be an indication that dust has settled towards the disk mid-plane), and β can also be used to describe various degrees of disk flaring (Kenyon & Hartmann, 1987; Miyake & Nakagawa, 1995; Chiang & Goldreich, 1997; D'Alessio et al., 1998; Furlan et al., 2005; D'Alessio et al., 2006).

Disk accretion rate: In order to sample different disk accretion rates, values of the disk α parameter (c.f. §1.2), which will be written here as $\alpha_{\rm disk}$, were sampled logarithmically between 10^{-3} and 10^{-1}. The disk accretion rate is calculated in the radiation transfer code using (Pringle, 1981; Bjorkman, 1997):

$$\dot{M}_{\rm disk} = \sqrt{18\pi^3}\,\alpha_{\rm disk}\,V_c\,\rho_0\,h_0^3/R_\star\,, \tag{3.8}$$

where $V_c = \sqrt{GM_\star/R_\star}$ is the critical velocity. Accretion shock luminosity on the stellar surface is included following the method of Calvet & Gullbring (1998). Average disk accretion values

are based on the literature (e.g. Valenti et al., 1993; Hartigan et al., 1995; Hartmann et al., 1998; Calvet et al., 2004).

3.2.3 Caveats for the current set of models

This section describes the limitations of the models presented here that will be addressed in future.

- Accretion from the envelope is not accounted for as a luminosity source (as distinct from disk accretion luminosity, which is included). This is likely only important in the very youngest sources, which may not be detected at near or mid-infrared wavelengths. In the inside-out collapse model (Shu et al., 1987), infall occurs from further out in the envelope as time proceeds. In a rotating envelope, this material has more angular momentum and thus impacts further out in the disk, liberating smaller amounts of accretion energy. Once enough mass builds up in the disk to cause it to be gravitationally unstable, large accretion events may occur through the disk (Kenyon et al., 1990; Hartmann et al., 1993; Hartmann & Kenyon, 1996; Vorobyov & Basu, 2005; Green et al., 2006). Therefore, if this scenario applies in most sources, the stellar and disk accretion luminosity included in the current models should be adequate.

- The models presented here do not include multiple source emission (although the radiation transfer code has this capability). This is partially accounted for by allowing for large inner envelope and disk holes at all evolutionary stages, which is likely to be the main effect of a binary system. Whether one or two sources illuminates an envelope from the inside likely has little effect on the emergent SED, but the size of the inner hole created by a binary star system has a large effect on the SED (Jørgensen et al., 2005). Currently, the inner holes are completely evacuated. Future sets of models will have partially evacuated inner holes that could affect the mid-infrared SED.

- The envelope geometry is assumed to be dominated by free-fall rotational collapse. This is a good approximation in the inner regions because rotation and free-fall likely dominate over magnetic effects (Galli & Shu, 1993; Desch & Mouschovias, 2001; Nakamura et al., 1999) (though see Allen et al. (2003) for a discussion of magnetic braking), and observations of radial intensity profiles are consistent with free-fall collapse (Chandler & Richer, 2000; van der Tak et al., 2000; Beuther et al., 2002; Mueller et al., 2002;

Young et al., 2003; Hatchell & van der Tak, 2003). In the outer regions, magnetic fields, turbulence, and other non-ideal initial conditions could affect the density distributions (Foster & Chevalier, 1993; Bacmann et al., 2000; Whitworth & Ward-Thompson, 2001; Allen et al., 2003; Goodwin et al., 2004; Galli, 2005). However, the mid-infrared fluxes are most sensitive to the inner envelope, bipolar cavities, and disk geometries.

- The shape of outflow cavities, and density distributions inside the cavities are uncertain.
- The current set of models does not include heating by an external interstellar radiation field. This is an important heating source for very low-luminosity sources (Young et al., 2004), and was recently shown to be important for the temperature structure and chemistry of high-mass protostellar envelopes (Jørgensen et al., 2006b).
- The current set of models does not include brown dwarfs or brown dwarf precursors.
- The dust models used do not include ice coatings. In addition, the dust in the low-mass disks are not likely to be appropriate for debris disks. The dust models will be improved in future sets of models (e.g. Ossenkopf & Henning, 1994; Wolf, 2003; Wolf & Voshchinnikov, 2004; Carpenter et al., 2005).
- The code does not account for PAH or small-grain continuum emission, which can contribute to mid-infrared emission in YSOs with hot central stellar sources (Habart, Natta, & Krügel, 2004; Ressler & Barsony, 2003).
- The flared disk geometries used may not be appropriate for the very high-mass sources where photoionisation can drive a wind and essentially puff up the disk (Hollenbach et al., 1994; Lugo et al., 2004).
- The stellar evolutionary tracks used are for canonical non-accreting pre-main-sequence stars (Bernasconi & Maeder, 1996; Siess et al., 2000). As mentioned in §3.2.2, the evolutionary tracks are not crucial in the sense that they are only used to get consistent stellar radii and temperatures for star of given masses and approximate evolutionary 'ages'.
- Massive, luminous stars with large inner dust holes (due to the large dust destruction radius) may have optically thick *gas* inside the dust hole, which is not accounted for in the current models. This would add more near-infrared flux from the hotter gas.

- A different geometry may be necessary for very massive dense stellar clusters; that is, a cluster of stars should be embedded in an envelope rather than a single star (Zinnecker et al., 1993; Hillenbrand, 1997; Clarke et al., 2000; Sollins et al., 2005; Allen et al., 2007).

- The models show a jump in far-infrared and sub-mm emission in high-mass sources between those without envelopes and those with even low-density envelopes. This is an artefact due to the fact that for models with envelopes, the spherical polar grid for the radiation transfer extends to the outer radius of the envelope, which can reach 100,000 AU for high-mass YSOs. Since the density in this grid is never set to values lower than the ambient density, the net effect is that there is a lower limit to the envelope mass and therefore to the far-infrared and sub-mm emission, set by the ambient density. On the other hand, for models with no infalling envelope, the outer radius of the grid only extends to the outer radius of the disk which is only thousands of AU at most. Therefore, the lower limit to the far-infrared and sub-mm emission is much lower for these objects.

- Since the emergent flux from the Monte-Carlo code is binned into direction (in equal intervals of $\cos\theta$), it is effectively averaged over a finite range in angle. If the SED changes rapidly with angle, for example, in a geometrically thin edge-on disk source viewed near edge-on, these effects will be washed out. Even though the edge-on angle bin has a fairly narrow range (from 84-96°), more flux emerges from 84° and 96° than from 90°, and the "edge-on" SED, centred on $\theta = 90°$, will reflect that of a slightly less edge-on source. In future sets of models, SEDs will be computed at exact outgoing angles, removing this averaging effect.

All of these issues will be addressed in future sets of models. However, the current models should be adequate for a large range of stellar masses and evolutionary stages, with the exception of very low-luminosity sources ($L < 0.2 L_{\odot}$), sources in very dense clusters ($n > 1,000$ stars pc $^{-3}$), and very massive sources.

3.3 Results and Analysis

3.3.1 Evolutionary stages

As mentioned in Chapter 1, YSOs are traditionally grouped into three 'Classes' according to the spectral index α of their SED, typically measured in the range $\sim 2.0 - 25\,\mu$m (Lada, 1987). Additionally, Class 0 objects are taken to refer to sources that display an SED similar to a 30 K greybody spectrum at sub-mm wavelengths, with little or no near- and mid-infrared flux (Andre, Ward-Thompson, & Barsony, 1993).

The spectral index classification ('Class') can sometimes lead to confusion in terminology, as it has in many cases become synonymous with evolutionary stage; yet, the same object can be classified in different ways depending on viewing angle. For example, an edge-on disk can have a positive spectral index that would make it a Class I object; and a pole-on "embedded" source might have a flat spectrum, rather than a rising one (Calvet et al., 1994). Other effects, such as increased stellar temperature (above the canonical Taurus value of 4,000 K) can lead to positive spectral indices in disk sources (Whitney et al., 2004b).

In discussing the evolutionary stages of the models presented here, a 'Stage' classification analogous to the 'Class' scheme is defined, but referring to the actual evolutionary stage of the objects, based on their physical properties (e.g. disk mass or envelope accretion rate) rather than properties of their SEDs. Stage 0 and I objects have significant infalling envelopes and possibly disks, Stage II objects have optically thick disks (and possible remains of a tenuous infalling envelope), and Stage III objects have optically thin disks. Using this classification alongside the spectral index classification can help avoid any confusion between observable and physical properties: for example, an edge-on disk would be referred to as a Stage II object that may display a Class I SED (rather than an 'edge-on Class II' object).

The exact boundaries between the different Stages are arbitrary in the same way as the Class scheme. In the following sections, Stage 0/I objects are defined as those that have $\dot{M}_{\rm env}/M_\star > 10^{-6}\,{\rm yr}^{-1}$, Stage II objects as those that have $\dot{M}_{\rm env}/M_\star < 10^{-6}\,{\rm yr}^{-1}$ and $M_{\rm disk}/M_\star > 10^{-6}$, and Stage III objects as those that have $\dot{M}_{\rm env}/M_\star < 10^{-6}\,{\rm yr}^{-1}$ and $M_{\rm disk}/M_\star < 10^{-6}$. Note that Stage 0 and I objects have been grouped together, and are referred to throughout this chapter as Stage I objects.

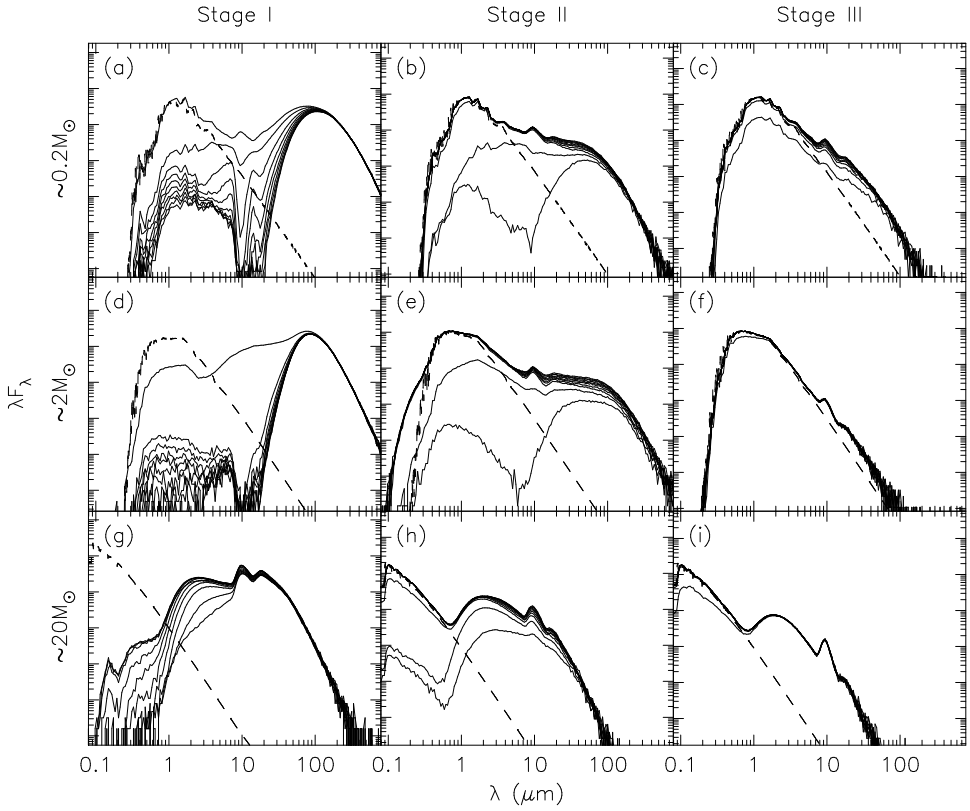

Figure 3.7: Example SEDs from the set of models. Panels (a), (b) and (c) show SEDs for three different $\sim 0.2\,M_{\odot}$ models at Stages I, II and III of evolution respectively. Panels (d), (e) and (f) show SEDs for three different $\sim 2\,M_{\odot}$ models at Stages I, II and III of evolution respectively. Finally, panels (g), (h) and (i) show SEDs for three different $\sim 20\,M_{\odot}$ models at Stages I, II and III of evolution respectively. Each panel shows 10 SEDs, one for each inclination computed. As the stellar masses and evolutionary ages of the models are randomly sampled, the top, centre, and bottom panels only show examples of *possible* evolutionary sequences.

3.3.2 SEDs and polarisation spectra of selected models

Figure 3.7 shows example SEDs, taken from the set of models for low, intermediate, and high mass stars at three stages of evolution. Each panel shows SEDs for the ten viewing angles, with the top spectrum corresponding to the pole-on viewing angle, and the bottom spectrum corresponding to the edge-on viewing angle. Also shown for each SED is the input stellar photosphere. Longward of $10\,\mu$m, the flux is due mainly to reprocessing of absorbed stellar flux by the circumstellar dust. Shortward of $10\,\mu$m the flux is dominated by stellar light (e.g. in Stage III or pole-on Stage I & II models), scattered stellar light (e.g. edge-on Stage I & II models), and warm dust from the inner disk and the bipolar cavities (Whitney et al., 2004b).

Since a Monte-Carlo radiation transfer code was used, it is possible to track various properties as photons propagate through the grid, and for instance to flag each one by its last point

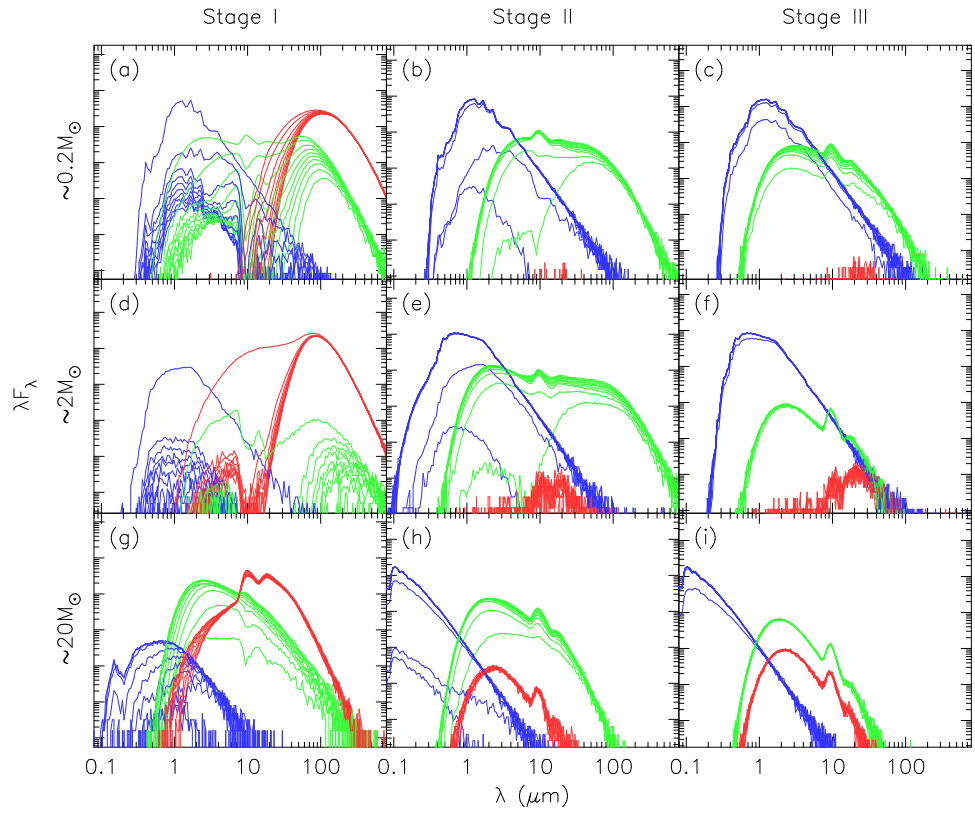

Figure 3.8: The same SEDs as in Figure 3.7, showing the contribution to the SEDs from the energy packets whose last point of origin is the star (blue), the disk (green), and the envelope (red).

of origin. For example, an energy packet absorbed and re-emitted by the disk is considered to have a point of origin in the disk. Scattering is not considered a point of origin; thus, a photon re-emitted by the disk that scatters in the envelope is considered a disk photon. Figure 3.8 shows SEDs for the same models as before, making use of this information. Three separate SEDs are shown for each model and inclination: the blue SED shows the energy packets whose last point of origin was in the stellar photosphere, the green SED shows the energy packets whose last point of origin was in the disk, and the red SED shows the energy packets whose last point of origin was in the envelope. Energy packets originating directly from the star contribute a significant amount of emission in pole-on Stage I objects as well as in Stage II and III objects. Energy packets last emitted by the envelope clearly dominate the SEDs of Stage I models longwards of 10 μm. Finally, energy packets last emitted by the disk dominate the SEDs of Stage II objects longward of near-infrared wavelengths. The envelope emission in disk-only Stage II and III sources is partly due to the ambient density. Other photon properties tracked in the radiation transfer include whether a given photon was last scattered before escaping, or whether a photon escaped directly from the stellar surface without interacting

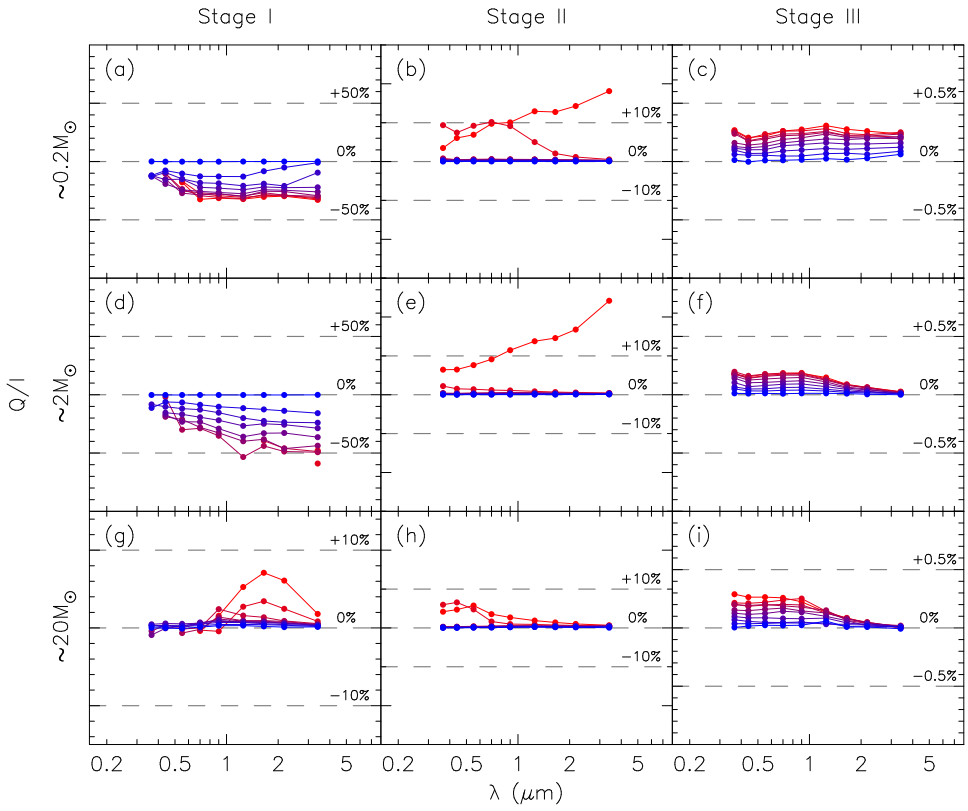

Figure 3.9: The degree of polarisation Q/I for the same models as in Figure 3.7. Fluxes convolved with the UBVRI and JHK_sL passband filters are shown. Blue to red colours indicate pole-on to edge-on viewing angles. Values were not always available for all inclinations due to low signal-to-noise. Note that the y-axis scale changes from left to right.

with the circumstellar dust.

Figure 3.9 shows polarisation results for the same models as Figures 3.7 and 3.8. The models do not have sufficient signal-to-noise to be shown as high-resolution polarisation spectra. However, the polarisation can be smoothed and convolved with broadband filter profiles. Because the models are axisymmetric and only include scattering from spherical grains, the polarisation can be fully described by the Q stokes parameter, $Q/I = P\cos(2\chi)$, where P is the degree of linear polarisation, and χ is the orientation of the polarisation with respect to the axis of symmetry (in these models, this is perpendicular to the disk plane, or parallel to the presumed outflow axis). Negative Q polarisation indicates that the polarisation is aligned parallel to the disk plane, and positive Q polarisation is aligned perpendicular to the disk plane. The first thing to note about the results in Figure 3.9 is that the polarisation sign varies with wavelength and evolutionary Stage. This is shown more clearly in Figure 3.10, which shows K-band polarisation from the entire set of models as a function of evolutionary stage for four selected inclinations. The highly embedded Stage I sources have negative polarisation (that

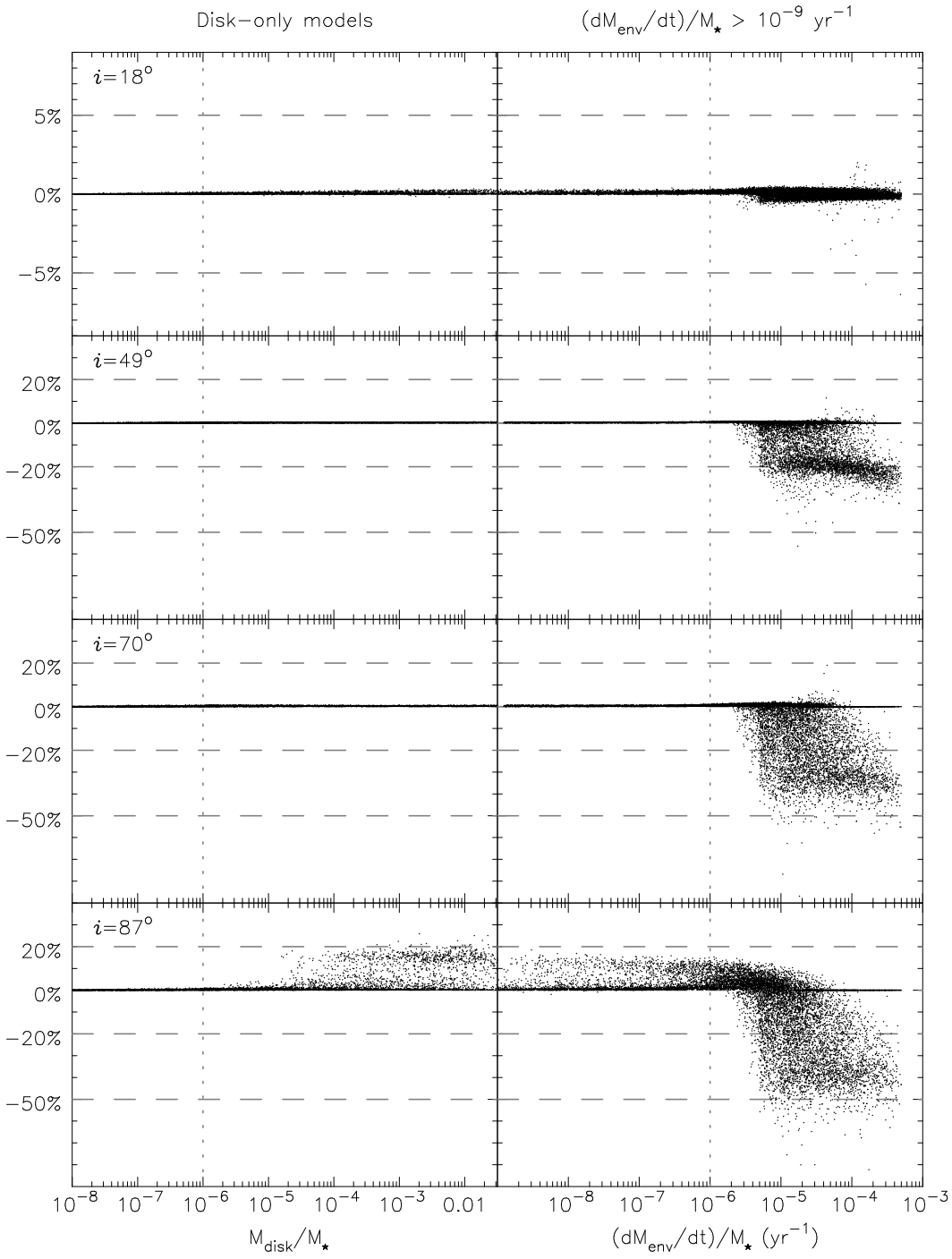

Figure 3.10: The K-band degree of polarisation Q/I for all models presented in this chapter, shown for four different inclinations, versus the disk mass $M_{\rm disk}/M_\star$ for disk-only models (*left*) and the envelope accretion rate $\dot{M}_{\rm env}/M_\star$ for the remaining models (*right*). The vertical dotted lines show the separation between Stage I (*right*), II (*center*) and III (*left*) models (as defined in §3.3.1) on the basis of the physical parameters. Note that the y-axis scale is expanded in the top panel.

is, aligned parallel to the disk plane); and the less embedded Stage I and Stage II sources have positive polarisation. This is an optical depth effect, as discussed in Bastien (1987), Kenyon et al. (1993b) and Whitney et al. (1997). As an optical depth effect, it is also a wavelength effect, since the dust opacity decreases with increasing wavelength. As shown in Figure 3.9, the high-mass Stage I source exhibits a sign change with wavelength. This is a clear signature of a Stage I source, since a Stage II source always has polarisation oriented perpendicular to the disk plane. A Stage I source has polarisation aligned parallel to the disk at short wavelengths, where scattering in the outflow cavities is the main source of polarisation, and the disk is too deeply embedded to be visible. At longer wavelengths the envelope becomes more optically thin, and scattering in the disk plane dominates the polarisation, causing it to become aligned perpendicular to the disk. If a sign change in the polarisation is observed, this information can be used to distinguish a Stage I source from an edge-on Stage II source, which could have a similar SED. However, the reverse is not necessarily true: the absence of a sign change in the polarisation does not necessarily rule out that the source is a Stage I object, since a sign change can occur outside the observed wavelength range.

3.3.3 Spectral index classification

The dependence of spectral index on evolutionary stage

In this section, the spectral indices of the model SEDs are discussed. The traditional definition of the spectral index of an SED (Lada, 1987) is its slope in $\log_{10} \lambda F_\lambda$ vs $\log_{10} \lambda$ space, longward of 2 μm.

This can be taken as the slope in $\log_{10} \lambda F_\lambda$ versus $\log_{10} \lambda$ space of the line joining two flux measurements at wavelengths λ_1 and λ_2, or as the slope of the least-squares fit line to *all* the flux measurements between and including the two wavelengths λ_1 and λ_2. In this section, the notation $\alpha_{[\lambda_1 \& \lambda_2]}$ is used to refer to the former, and $\alpha_{[\lambda_1 \rightarrow \lambda_2]}$ to refer to the latter of these two definitions. Both definitions have been used in the literature (e.g. Myers et al. 1987 and Kenyon & Hartmann 1995 use $\alpha_{[\lambda_1 \& \lambda_2]}$, while Haisch et al. 2001b, Lada et al. 2006, and Jørgensen et al. 2006a use $\alpha_{[\lambda_1 \rightarrow \lambda_2]}$), and in some cases it is not explicitly stated which choice has been made. In this section, the $\alpha_{[\lambda_1 \& \lambda_2]}$ definition is used, as it is unique for each SED for a given λ_1 and λ_2, whereas $\alpha_{[\lambda_1 \rightarrow \lambda_2]}$ depends on which points are included inside the range.

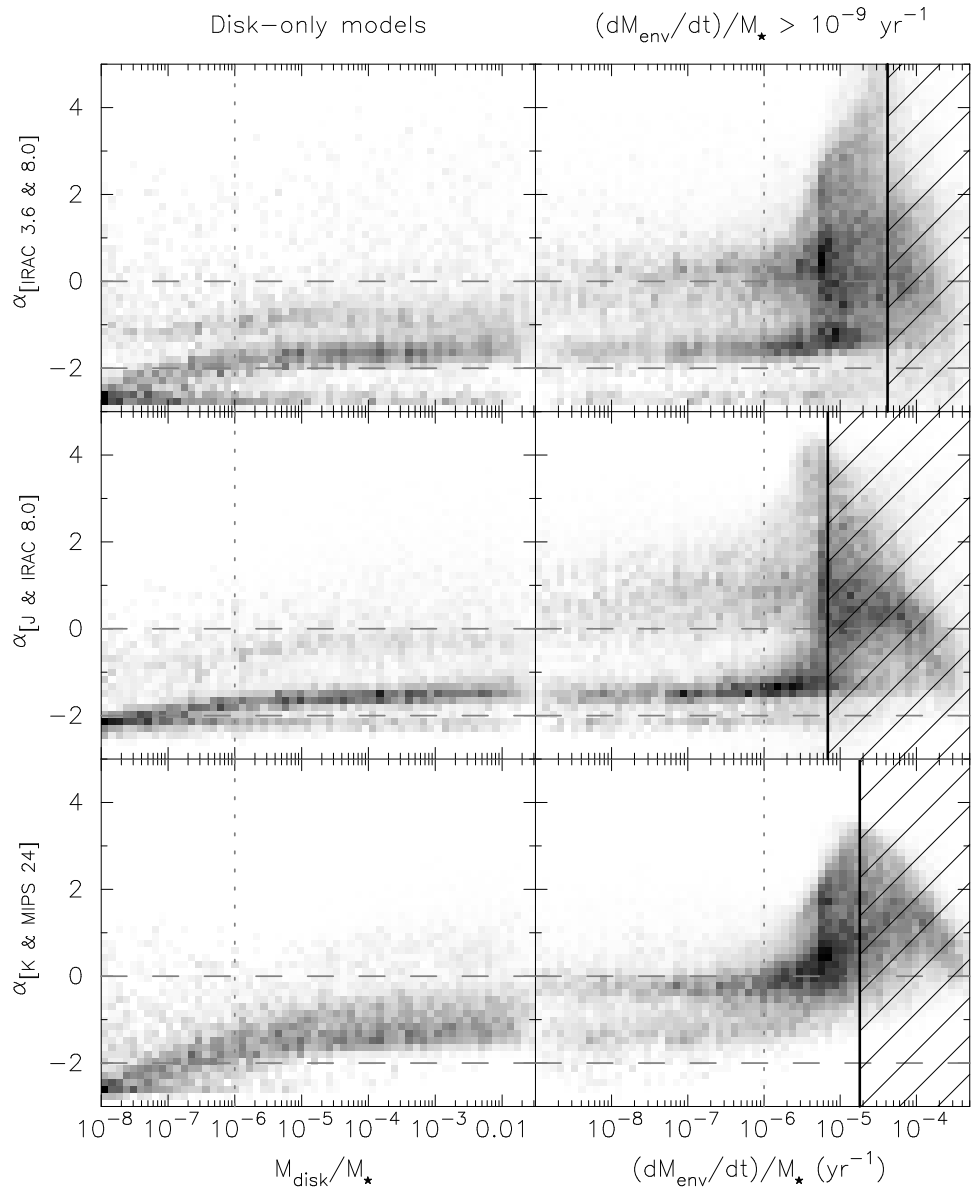

Figure 3.11: *Left* – spectral indices versus the disk mass $M_{\rm disk}/M_\star$ for all disk-only models. *Right* – spectral indices versus the envelope accretion rate $\dot{M}_{\rm env}/M_\star$ for all models with $\dot{M}_{\rm env}/M_\star > 10^{-9}\,{\rm yr}^{-1}$. The spectral indices were calculated using IRAC 3.6 & 8.0 μm fluxes (*top*), J & IRAC 8.0 μm fluxes (*center*), and K & MIPS 24 μm fluxes (*bottom*). The greyscale shows the number of models on a linear scale. The dashed horizontal lines show the separation between Class I, II, and III models on the basis of the spectral indices. The vertical dotted lines are as in Figure 3.10: the left and right panel together show the evolution of the spectral index from Stage III to Stage I models. The hatched region shows the values of $M_{\rm disk}/M_\star$ for which at least 10 % of SEDs have insufficient signal-to-noise in order to compute a spectral index; the trend of decreasing spectral index inside these regions is due to signal-to-noise limitations.

As noted previously (§3.2.1), each SED is computed in 50 different apertures. To match typical point-source photometry observations, the 2760 AU aperture, which corresponds to $\sim 3''$ at a distance of 1 kpc, is used here.

Figure 3.11 shows the dependence of three different spectral indices on the envelope accretion rate and the disk mass. The following spectral indices were computed for all the model SEDs: $\alpha_{[\mathrm{IRAC}\,3.6\,\&\,8.0]}$, $\alpha_{[J\,\&\,\mathrm{IRAC}\,8.0]}$, and $\alpha_{[K\,\&\,\mathrm{MIPS}\,24]}$. In this and following sections $\alpha_{[K\,\&\,\mathrm{MIPS}\,24]}$ is referred to as the 'reference' spectral index since it is close to the commonly used $2.0 - 25\,\mu$m range. In order to calculate a spectral index using either method from a given set of model fluxes, these fluxes were required to have a signal-to-noise of at least 2. The hatched box in Figure 3.11 shows the values of $\dot{M}_{\mathrm{env}}/M_\star$ for which at least 10 % of SEDs had insufficient signal-to-noise for the spectral index calculation.

The bottom panel of Figure 3.11 shows how the reference spectral index depends on the disk mass and the envelope accretion rate:

- The tendency is for the spectral index to increase as the disk mass and the envelope accretion rate increase. Therefore, on average, younger sources tend to have a larger spectral index. However, for a given disk mass or envelope accretion rate, the spread in the values of the spectral index is important. This suggests that although in large samples of sources larger spectral indices are likely to indicate youth, the spectral index of an individual source is not a reliable indicator of its evolutionary stage. For example, a source with a reference spectral index of -0.5 could have virtually any disk mass or envelope accretion rate.

- For disk masses $M_{\mathrm{disk}}/M_\star < 10^{-5}$, the spectral index increases proportionally to $\log_{10} M_{\mathrm{disk}}/M_\star$, whereas above this limit the spectral index is independent of disk mass. This is because for low disk masses the disk is optically thin, and near- and mid-infrared radiation is seen from the whole disk, whereas for larger disk masses the disk is optically thick, and the near- and mid-infrared radiation is only seen from the surface layers of the disk. This is in agreement with the results from Wood et al. (2002a).

- For envelope accretion rates $\dot{M}_{\mathrm{env}}/M_\star < 10^{-6}\,\mathrm{yr}^{-1}$, the spectral index does not vary with $\dot{M}_{\mathrm{env}}/M_\star$. This indicates that the envelope is optically thin and does not contribute significantly to the SED, i.e. the SED is dominated by disk or stellar emission.

- For envelope accretion rates $\dot{M}_{\rm env}/M_\star > 10^{-6}\,{\rm yr}^{-1}$ the range of possible spectral indices widens and the upper limit of this range increases roughly linearly with $\log_{10}\dot{M}_{\rm env}/M_\star$. The widening of the range is likely due to the strong dependence of Stage I colours on viewing angle (Whitney et al., 2003b) and stellar temperature (Whitney et al., 2004b). The increase of the upper limit is expected: as the accretion rate increases the envelope becomes more optically thick, and progressively obscures the central source and the regions of high-temperature dust, reddening the SED.

- The decrease in the upper range of spectral indices for $\dot{M}_{\rm env}/M_\star > 5\times10^{-5}\,{\rm yr}^{-1}$ is an artefact due to the signal-to-noise requirements for computing a spectral index: models with heavily embedded sources have very few or no energy packets emerging at near-infrared wavelengths, leading to a poor signal-to-noise at these wavelengths. The majority of models with high accretion rates for which the reference spectral index can be calculated are pole-on or close to pole-on. For these SEDs the star is not heavily obscured by the envelope since one is looking down the cavity, and the spectral index is bluer. For models with $\dot{M}_{\rm env}/M_\star > 10^{-4}\,{\rm yr}^{-1}$, 98 % of SEDs for the pole-on viewing angle have sufficient signal-to-noise at near- and mid-infrared, as opposed to only 23 % of SEDs for the edge-on viewing angle

- The choice of boundary values for the 'Stage' classification seems to be appropriate, since most Stage I models have $\alpha > 0$, most Stage II models have $-2 < \alpha < 0$, and a large fraction of Stage III models have $\alpha < -2$. This means that for the majority of models, the 'Stage' is roughly equivalent to the 'Class' classification.

The two top panels of Figure 3.11 show the spectral indices computed over a narrower wavelength range ($\alpha_{[\rm IRAC3.6\&8.0]}$ and $\alpha_{[J\,\&\,\rm IRAC8.0]}$). These show a similar pattern, albeit the spread in spectral indices is much larger for a given disk mass or envelope accretion rate. This shows that including a longer wavelength flux measurement ($\sim 20\,\mu$m) in the spectral index calculation provides a better indication of evolutionary stage.

The dependence of the spectral index of disk-only sources on stellar temperature, disk inner radius, and disk flaring power

As discussed in the previous section, the spectral indices of the SEDs for disk-only models with $M_{\rm disk}/M_\star > 10^{-5}$ are independent of $M_{\rm disk}/M_\star$. For these models, the spread in spectral

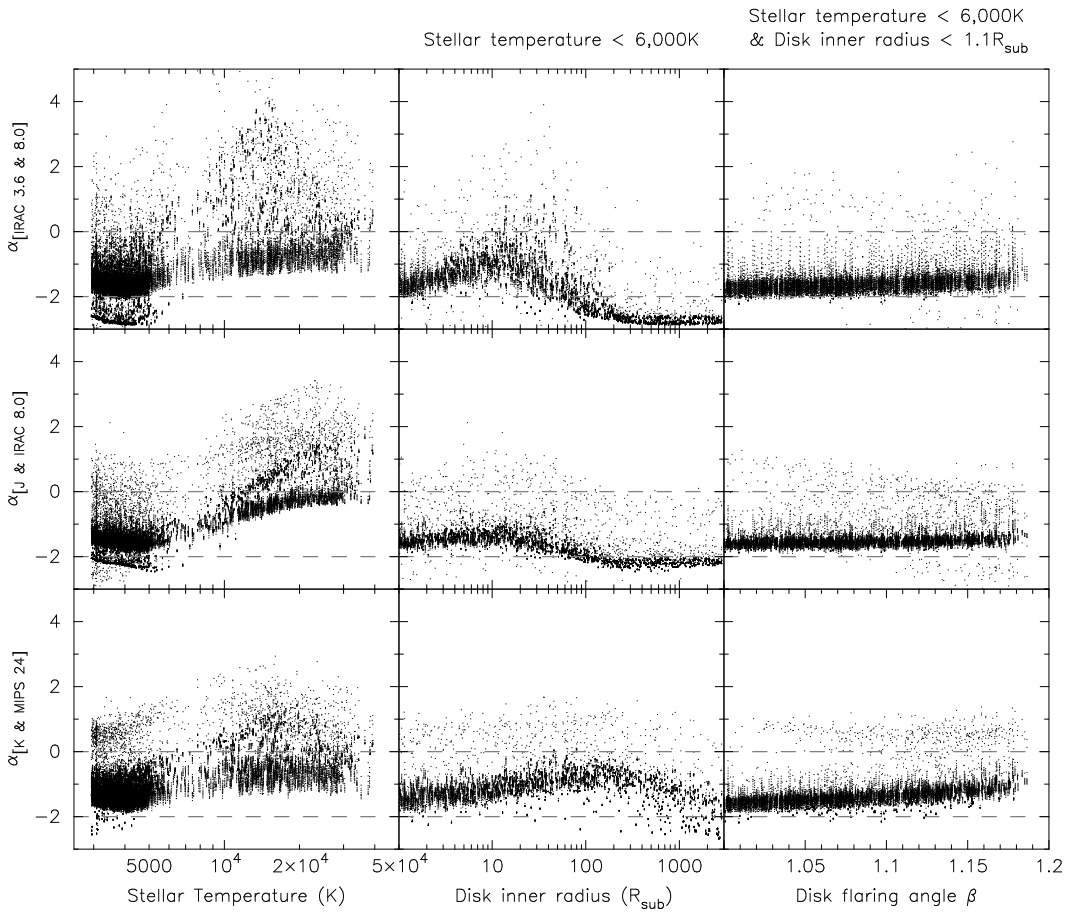

Figure 3.12: *Left* – spectral indices versus the stellar temperature $T_\star$ for all disk-only models with $M_{\rm disk}/M_\star > 10^{-5}$. *Centre* – spectral indices versus the disk inner radius $R_{\rm disk}^{\rm min}$ for all disk only models with $M_{\rm disk}/M_\star > 10^{-5}$ and with $T_\star < 6,000\,{\rm K}$. *Right* – spectral indices versus the disk flaring power for all disk only models with $M_{\rm disk}/M_\star > 10^{-5}$, with $T_\star < 6,000\,{\rm K}$, and with $R_{\rm disk}^{\rm min} = 1 R_{\rm sub}$. The spectral indices were calculated as for Figure 3.11. The dashed horizontal lines are identical to those shown in Figure 3.11.

indices for a given $M_{\rm disk}/M_\star$ is due mainly to the spread in stellar temperatures, disk inner radii, and disk flaring powers; this is illustrated in Figure 3.12, which shows the dependence of the spectral index of these SEDs on the stellar temperature $T_\star$, the disk inner radius $R_{\rm disk}^{\rm min}$, and the disk flaring power β.

The left-hand panels shows all disk-only models with $M_{\rm disk}/M_\star > 10^{-5}$. For low temperatures ($\sim 3,000 - 5,000\,$K), the $\alpha_{[\rm IRAC3.6\&8.0]}$ and the $\alpha_{[J\,\&\,\rm IRAC8.0]}$ spectral indices are separated into two distinct groups. The largest group, centred between spectral index values of -2 and -1 is the bulk of the disk models with no large inner holes. The smaller group, centred at lower spectral index values, represent the models which include inner holes large enough that the JHK$_{\rm s}$ and IRAC fluxes are purely photospheric. In the case of the $\alpha_{[J\,\&\,\rm IRAC8.0]}$ spectral index, and to a lesser extent the $\alpha_{[\rm IRAC3.6\&8.0]}$ spectral index, the average value of these two groups decreases as the temperature increases from $3,000\,$K to $5,000\,$K. This is expected, as the colours of stellar photospheres at near-infrared wavelengths for these temperatures are still dependent on the stellar temperature, and become bluer for larger temperatures.

Beyond $5,000\,$K, the spectral indices increase with stellar temperature, at least in the case of the $\alpha_{[\rm IRAC3.6\&8.0]}$ and the $\alpha_{[J\,\&\,\rm IRAC8.0]}$ spectral indices. This is due to a lower contribution of the stellar flux compared to the infrared dust spectrum at these wavelengths (Whitney et al., 2004b). For models with a $5,000\,$K central source, this central source contributes significantly to the emergent spectrum, making the emission less red. For a $10,000\,$K stellar source, the relative fraction of stellar flux to emission from the disk at near- and mid-infrared wavelengths is much lower, leading to a more pure dust spectrum that is red at near- and mid-infrared wavelengths. This can be seen in the SEDs for the Stage II and III models in Figures 3.7 and 3.8: although the general shape of the contribution to the SED from the disk does not change significantly between the low-, intermediate-, and high-mass models, the change in the stellar spectrum leads to redder colours at near- and mid-infrared wavelengths for the high-mass (and therefore higher temperature) model.

The apparent gap in the models between $6,000\,$K and $10,000\,$K is due to the sampling of the model parameters using evolutionary tracks. For $\alpha_{[\rm IRAC3.6\&8.0]}$ and the $\alpha_{[J\,\&\,\rm IRAC8.0]}$, the average spectral index values are different on either side of this gap. This leads to the bimodal distribution seen in Figure 3.11 for these spectral indices.

The central panels in Figure 3.12 show the detailed variations of the spectral index with

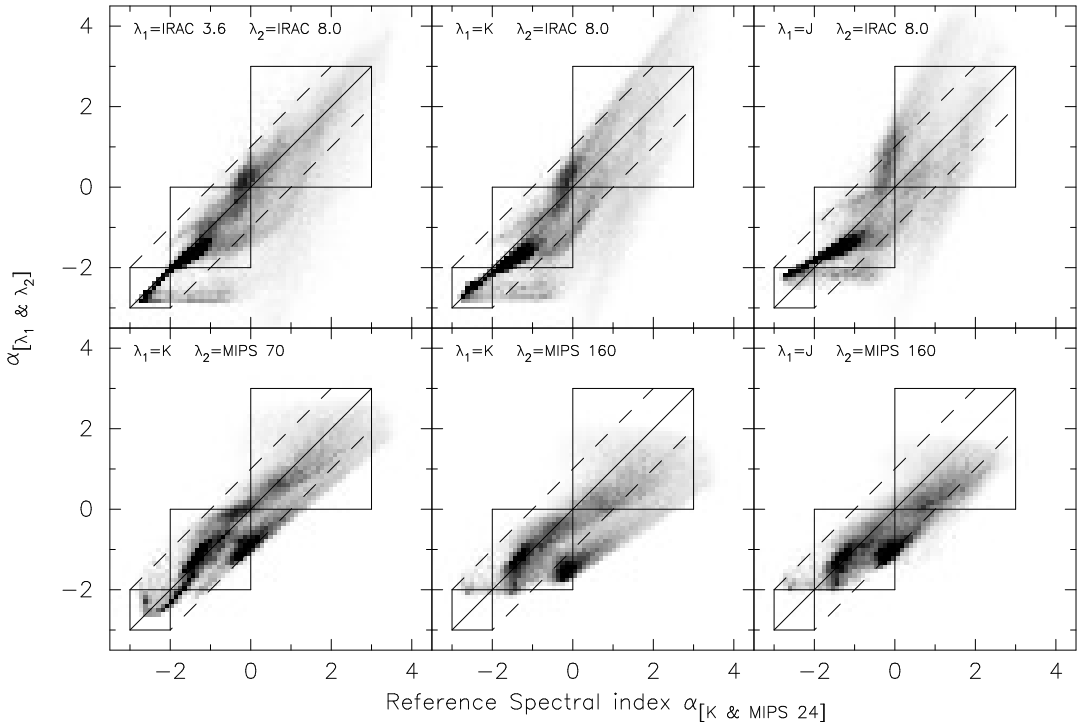

Figure 3.13: The spectral indices for all the models calculated using a $\alpha_{[\lambda_1\,\&\,\lambda_2]}$ spectral index (where the values of λ_1 and λ_2 are shown in the panels) versus the reference spectral index $\alpha_{[K\,\&\,\mathrm{MIPS}\,24]}$. The greyscale shows the number of models on a linear scale. The solid diagonal line represents the line along which the spectral indices are equal. The dashed lines encompass the region within which the difference between the spectral indices in less than 1. The boxes represent regions where the 'Class' assigned to a model is the same for the two spectral indices (in each panel, the boxes are from left to right: Class III, Class II, and Class I models).

disk inner radius for all the disk-only models with $M_{\mathrm{disk}}/M_\star > 10^{-5}$, and with stellar temperatures below 6,000 K. To avoid overcrowding of the plot, models with $R_{\mathrm{disk}}^{\mathrm{min}} = 1R_{\mathrm{sub}}$ are not shown. In all three cases, the spectral index first increases, then decreases to reach photospheric levels. The initial increase is due to removal of the hottest dust from the inner disk and redistribution of the SED to slightly longer wavelengths. As the inner radius increases further, the amount of circumstellar material emitting at mid-infrared wavelengths is reduced, and the mid-infrared emission decreases.

Finally, the right-hand panels of Figure 3.12 show all the disk-only models with $M_{\mathrm{disk}}/M_\star > 10^{-5}$, with stellar temperatures below 6,000 K and with $R_{\mathrm{disk}}^{\mathrm{min}} = 1R_{\mathrm{sub}}$, versus the disk flaring power. A larger flaring power in a disk leads to an increasing surface intercepting the starlight, and therefore an increase in reprocessed radiation. This has only a slight effect on the $\alpha_{[\mathrm{IRAC}3.6\,\&\,8.0]}$ and the $\alpha_{[J\,\&\,\mathrm{IRAC}8.0]}$ spectral indices, but has a more pronounced effect on the reference spectral index $\alpha_{[K\,\&\,\mathrm{MIPS}\,24]}$.

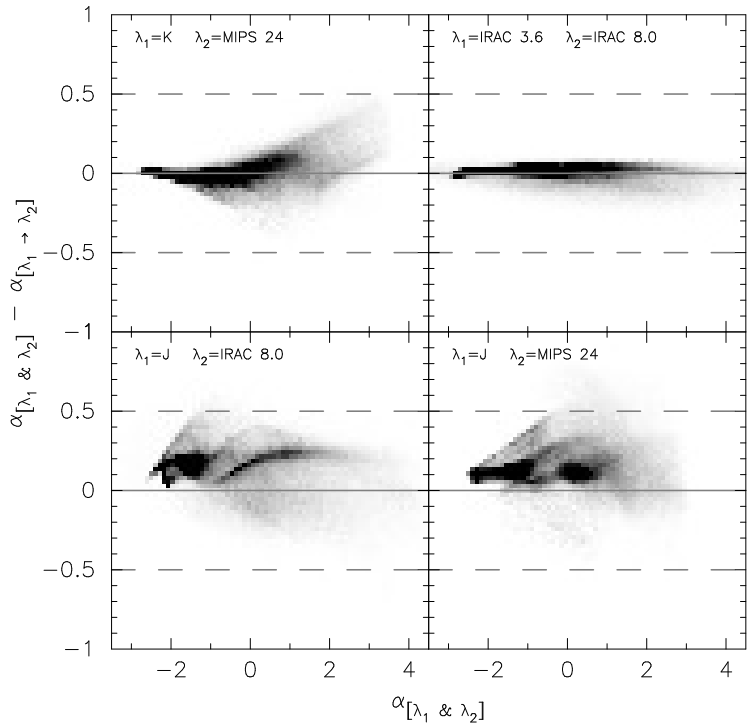

Figure 3.14: The difference between the spectral indices for all the models calculated using only two photometric points ($\alpha_{[\lambda_1 \& \lambda_2]}$) and the spectral indices for the same models calculated by fitting a line to more than two data points in the same range ($\alpha_{[\lambda_1 \rightarrow \lambda_2]}$), versus the spectral indices calculated using only two photometric points. The broadband fluxes used to calculate the $\alpha_{[\lambda_1 \rightarrow \lambda_2]}$ spectral indices are: K+IRAC+MIPS 24 μm ($\alpha_{[K \rightarrow \mathrm{MIPS\,24}]}$), all IRAC fluxes ($\alpha_{[\mathrm{IRAC\,3.6} \rightarrow \mathrm{8.0}]}$), JHK_s +IRAC fluxes ($\alpha_{[J \rightarrow \mathrm{IRAC\,8.0}]}$), and JHK_s +IRAC+MIPS 24 μm ($\alpha_{[J \rightarrow \mathrm{MIPS\,24}]}$). The greyscale shows the number of models on a linear scale. The solid line shows the line along which the spectral indices are equal. The dashed lines show the line along which the two spectral indices differ by ± 0.5.

The dependence of spectral index on wavelength range and distribution

The wavelength range of the fluxes used to calculate the spectral index of a source is dependent on the observations available for that given source. In most cases, the choice of this range is likely to affect the value of the spectral index itself. For example, as seen in §3.3.3, a spectral index calculated using K and MIPS 24 μm fluxes will in most cases differ from a spectral index calculated using IRAC 3.6 μm and IRAC 8.0 μm fluxes.

Figure 3.13 shows the correlation between six different $\alpha_{[\lambda_1 \& \lambda_2]}$ spectral indices (calculated using various combinations of JHK_s, IRAC, and MIPS broadband fluxes) and the reference spectral index $\alpha_{[K \& \mathrm{MIPS\,24}]}$. As can be seen, the value of the spectral index is highly dependent on the range of data used. In some cases the difference can be larger than 1.0, which could lead to a different 'Class' being assigned to a source depending on what spectral index is used.

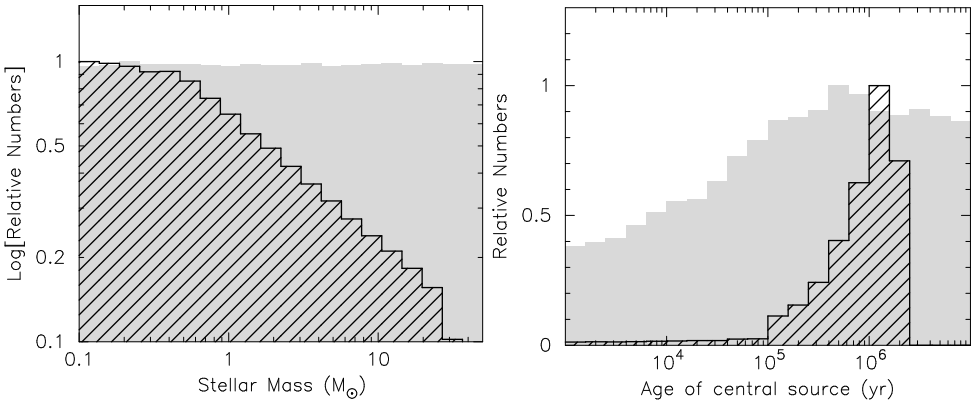

Figure 3.15: The distribution of stellar masses (*left*) and ages (*right*) for the entire set of models (filled grey area) and the virtual cluster before sensitivity cut-offs (hatched area). The stellar masses are sampled logarithmically in the original set of models, and from a Kroupa IMF in the virtual cluster. The ages are sampled close to logarithmically in the original set of models, and linearly in the virtual cluster (with a cut-off at 2×10^6 yr).

The spectral index of a source may also be sensitive to whether it is calculated using only fluxes at two wavelengths ($\alpha_{[\lambda_1 \,\&\, \lambda_2]}$), or whether it is calculated using all fluxes in a given wavelength range ($\alpha_{[\lambda_1 \rightarrow \lambda_2]}$). Figure 3.14 shows the difference between four different $\alpha_{[\lambda_1 \,\&\, \lambda_2]}$ spectral indices (using various combinations of JHK_s, IRAC, and MIPS 24 μm broadband fluxes) versus the equivalent $\alpha_{[\lambda_1 \rightarrow \lambda_2]}$ spectral indices.

The difference between $\alpha_{[\mathrm{IRAC}\,3.6 \rightarrow 8.0]}$ and $\alpha_{[\mathrm{IRAC}\,3.6\,\&\,8.0]}$ is small, typically of the order of 0.1 or less, which is expected, as the wavelength range is fairly narrow and the SED should be close to a straight line. The other three spectral indices, $\alpha_{[K\,\&\,\mathrm{MIPS}\,24]}$, $\alpha_{[J\,\&\,\mathrm{IRAC}8.0]}$, and $\alpha_{[J\,\&\,\mathrm{MIPS}\,24]}$, show a larger difference: in some cases, the spectral index calculated using the two methods differs by up to 0.5.

3.3.4 Colour-colour classification

Virtual Clusters

The parameters of the current models were sampled in order to cover many stages of evolution and stellar masses. However, the distribution of models in parameter space is not meant to be representative of a typical star formation region, since it is meant to encompass outliers as well as typical objects, and since the models are sampled uniformly or close to uniformly in $\log_{10} M_\star$ and $\log_{10} t_\star$.

Therefore, in the current section, colour-colour diagrams for both the whole set of models and a subset of models are shown. This subset, which will be referred to as a *virtual cluster*,

Table 3.2: The bright and faint limits used to create the virtual cluster

Band	Bright limit	Faint limit
J	8.0	16.5
H	7.0	15.5
K	6.5	15.0
[3.6]	6.0	18.0
[4.5]	5.5	17.0
[5.8]	3.0	15.0
[8.0]	3.0	14.0
[24.0]	0.6	10.0

was constructed by re-sampling models from the original set of models in order to produce a standard IMF for the stellar masses (Kroupa, 2001), and to produce a distribution of ages distributed linearly in time, rather than logarithmically. The stellar masses were sampled between 0.1 and 30 $M_{\odot}$, and the ages between 10^3 and 2×10^6 yr. The aim of this procedure is to reproduce the distribution of stellar masses and ages that might be expected from a cluster with the chosen IMF and a continuous star formation rate having switched on 2×10^6 yr ago. The distribution of masses and ages for the original set of models and the virtual cluster are shown in Figure 3.15.

Two different distances were assumed to this cluster: 250 pc to mimic a relatively nearby star formation region (such as the Perseus molecular cloud), and 2.5 kpc to mimic a distant star formation region such as those seen in the GLIMPSE survey (such as the Eagle Nebula). The fluxes integrated in the aperture closest to a $3''$ radius aperture at these distances (i.e. 770 AU and 7130 AU) were used. Sensitivity and saturation limits were then applied, using the bright and faint limits listed in Table 3.2. The JHK_s limits are typical 2MASS values. The IRAC and MIPS 24 μm limits are similar to those quoted for several large-scale surveys, such as the c2d (Harvey et al., 2006; Jørgensen et al., 2006a) and SAGE (Meixner et al., 2006) surveys.

These limits will vary with exposure time and background levels, and the limits given here are just an example of a plausible range. The distribution of masses and ages remaining after applying these limits to the IRAC bands are shown in Figure 3.16: observations of the distant star-forming cluster with these sensitivity and saturation limits would be less sensitive to low-mass YSOs and more sensitive to high-mass YSOs than observations of the nearby cluster. In addition, observations of the distant star-forming cluster would be slightly biased towards

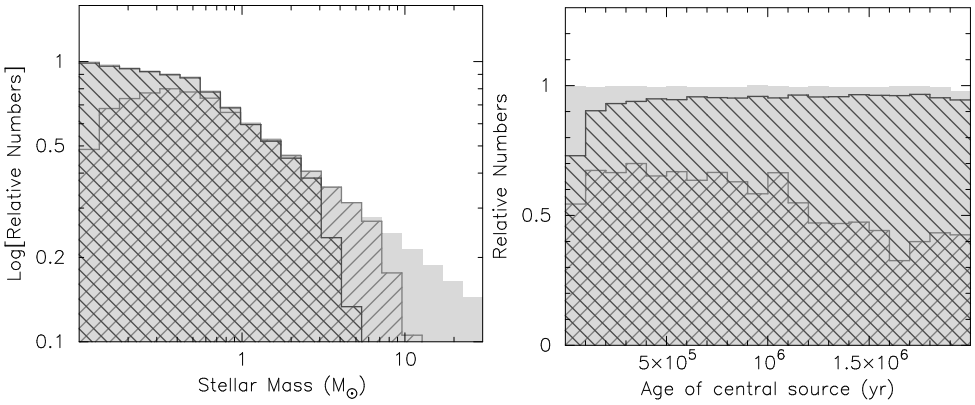

Figure 3.16: The distribution of stellar masses (*left*) and ages (*right*) for the virtual cluster before sensitivity cut-offs (filled grey area), after sensitivity cut-offs at 250 pc (hatched from top-left to bottom-right) and after sensitivity cut-offs at 2.5 kpc (hatched from bottom-left to top-right). Due to the sensitivity and saturation cut-offs, the distribution of models in the 2.5 kpc cluster is more biased towards high mass stars and early evolutionary stages than the 250 pc cluster.

earlier stages of evolution, as the luminosity of PMS stars tends to decrease with age.

Colour-colour diagrams

Colour-colour diagrams have been widely used to classify YSOs, including for example JHK_s and IRAC colour-colour diagrams. In a recent study of this colour-colour space, Allen et al. (2004) proposed that disk-only sources should fall mostly in a box defined by $0.4 < [5.8] - [8.0] < 1.1$ and $0.0 < [3.6] - [4.5] < 0.8$, whereas younger sources with infalling envelopes should fall redward of this location (c.f. Figure 1.9). Although the models used for that work covered a range of temperatures and evolutionary states, the interpretation of the colour-colour diagram was made using only models with a temperature of 4,000 K, an age of 1 Myr, and using only one viewing angle. As shown by Hartmann et al. (2005), this analysis is appropriate for the Taurus star formation region where most sources have stellar temperatures ranging from 3,000 K to 5,000 K (Kenyon & Hartmann, 1995). Further study of this colour-colour space is needed to investigate whether such a classification can apply to more distant and massive star formation regions where the sources seen are likely to have a much wider range of ages and temperatures. In this section, the IRAC colour-colour space is re-examined for the nearby and distant virtual clusters, and results for other colour-colour spaces are also presented.

Figure 3.17 shows the distribution of the entire set of radiation transfer models in J−H vs. H−K_s, $[3.6] - [4.5]$ vs. $[5.8] - [8.0]$, and $[3.6] - [5.8]$ vs. $[8.0] - [24.0]$ colour-colour

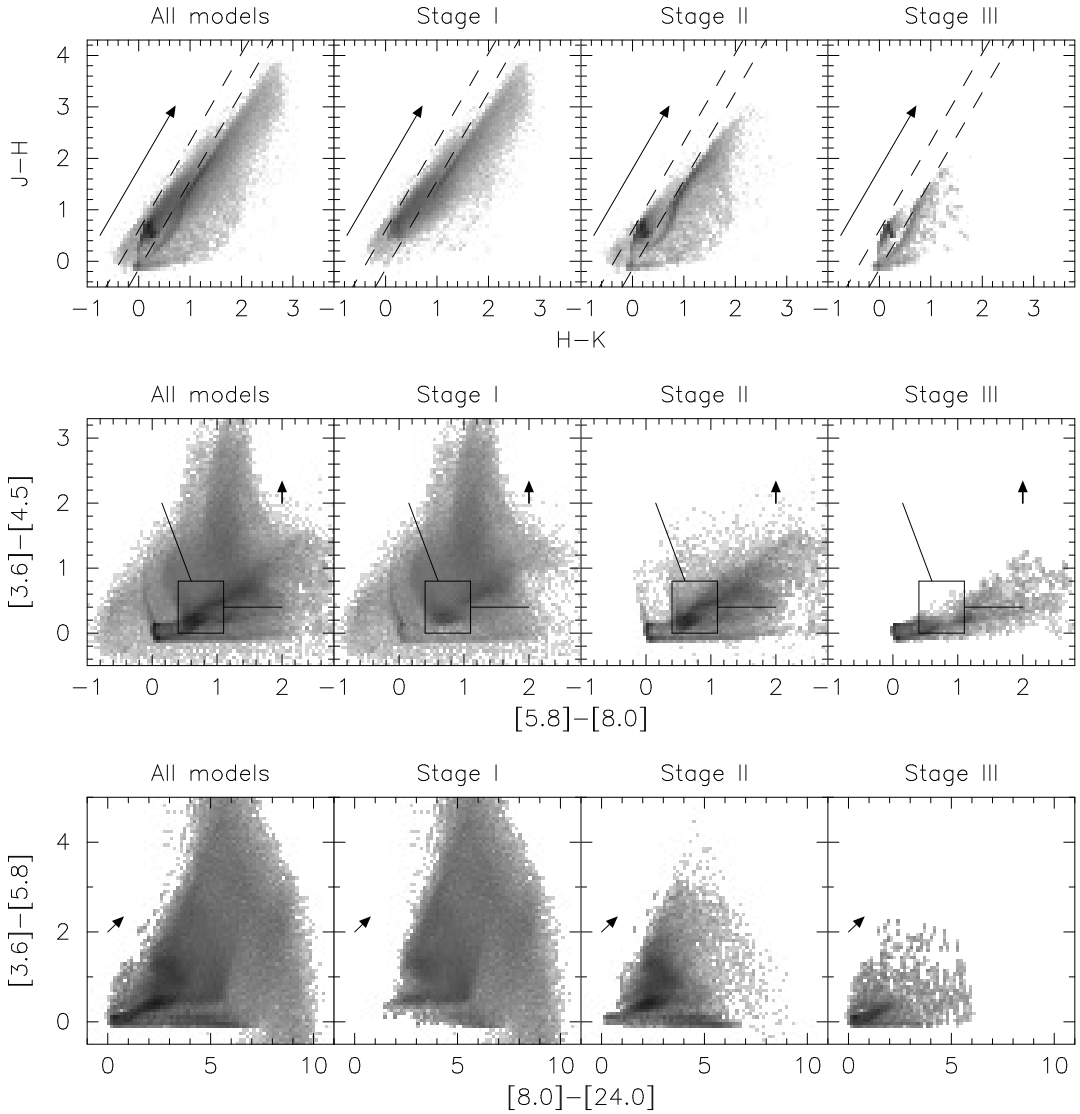

Figure 3.17: JHK_s, IRAC, and IRAC+MIPS 24 μm colour-colour diagrams for all the model SEDs, showing the number of models on a logarithmic greyscale. The greyscale is shown down to 0.01 % of the peak value. The reddening vector shows an extinction of $A_V = 20$, assuming the Indebetouw et al. (2005) extinction law. The dashed lines in the JHK_s colour-colour diagrams show the locus of the reddened stellar photospheres. The solid lines in the IRAC colour-colour diagrams show the "disk domain" and the domain of embedded young objects (redward of the "disk domain") from Allen et al. (2004) and Megeath et al. (2004).

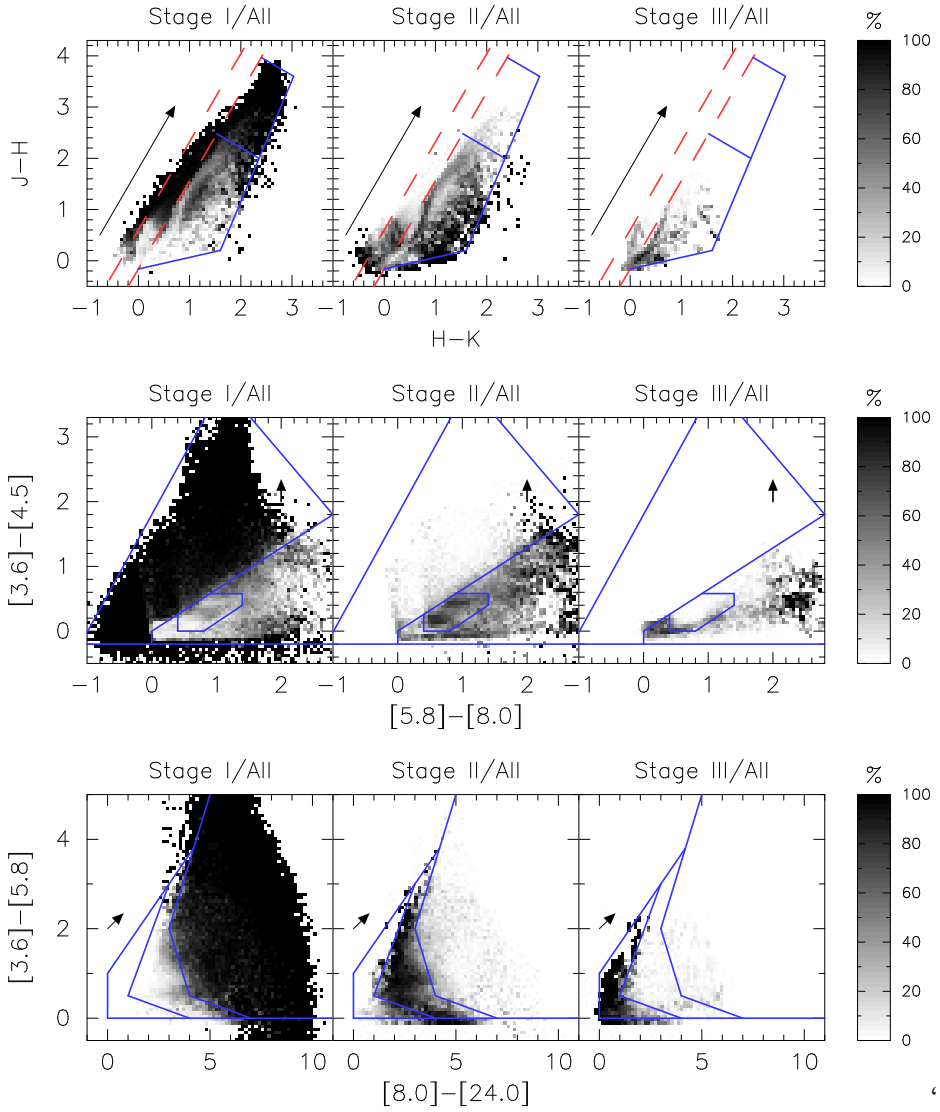

Figure 3.18: Colour-colour diagrams for all the model SEDs showing from left to right: the ratio of the number of Stage I models to all models, the ratio of the number of Stage II models to all models, and the ratio of the number of Stage III models to all models. From top to bottom: JHK_s, IRAC, and IRAC+MIPS 24 μm colour-colour diagrams. The reddening vector shows an extinction of $A_V = 20$, assuming the Indebetouw et al. (2005) extinction law. The red lines in the JHK_s colour-colour diagrams show the locus of the reddened stellar photospheres. The blue lines outline the regions shown in Figure 3.23.

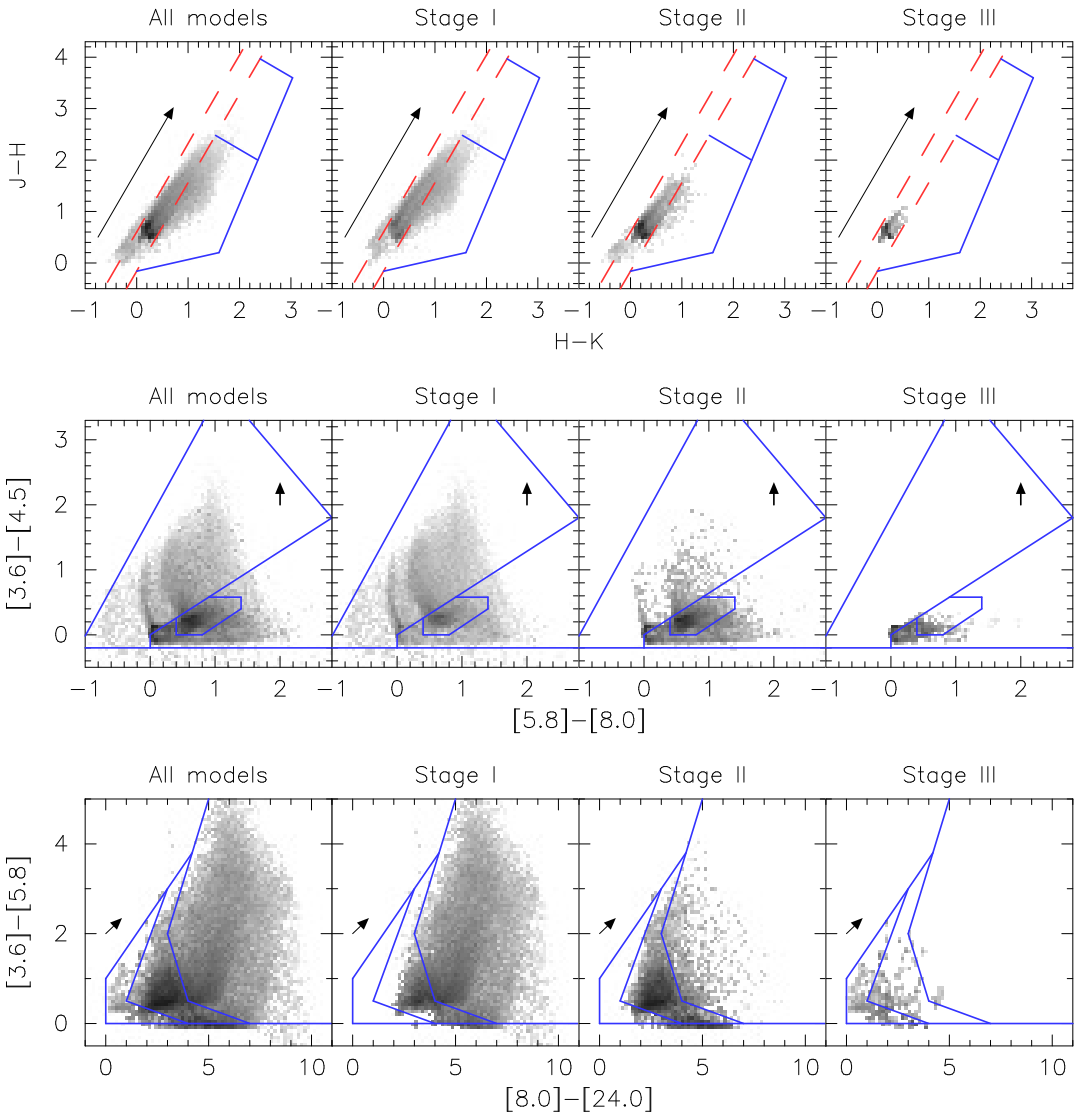

Figure 3.19: As for Figure 3.17 for the virtual cluster at 250 pc including sensitivity and saturation cut-offs.

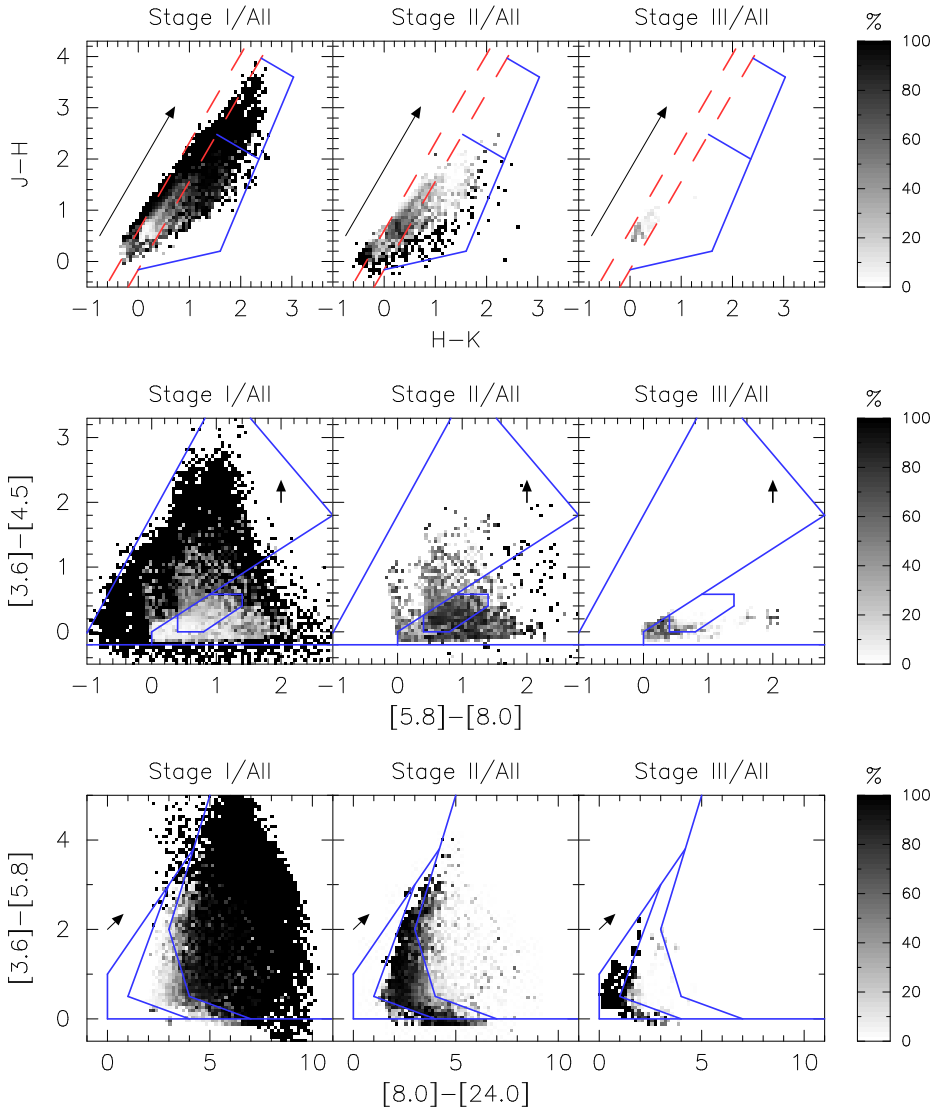

Figure 3.20: As for Figure 3.18 for the virtual cluster at 250 pc including sensitivity and saturation cut-offs.

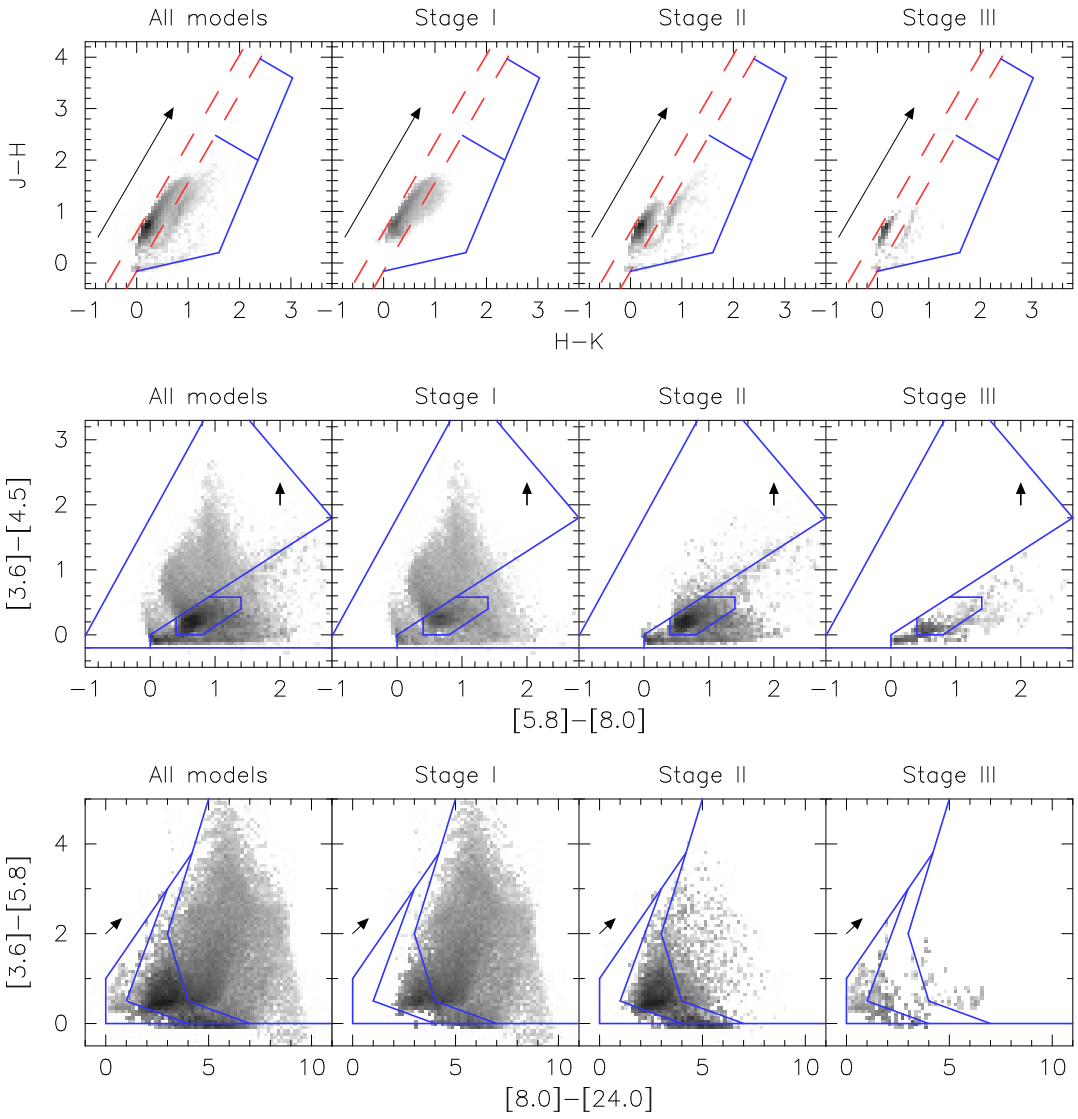

Figure 3.21: As for Figure 3.17 for the virtual cluster at 2.5 kpc including sensitivity and saturation cut-offs.

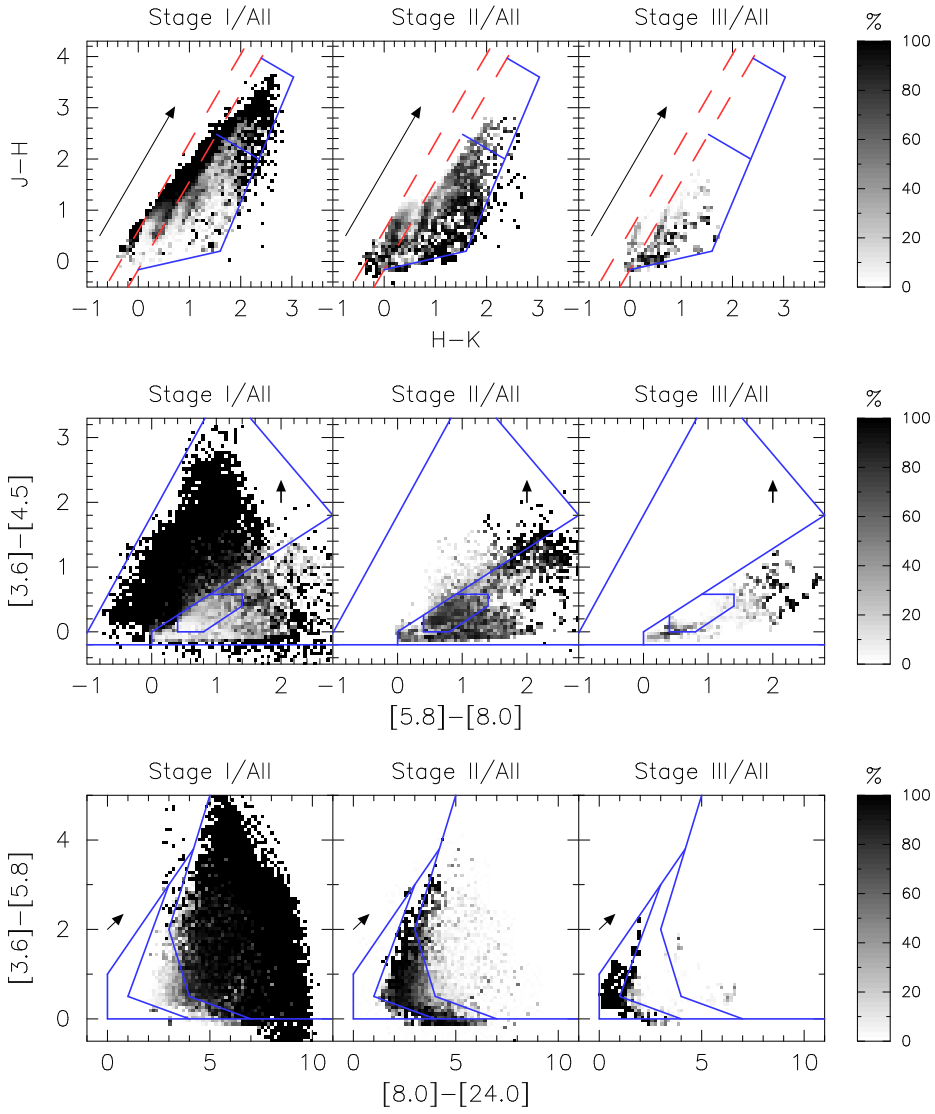

Figure 3.22: As for Figure 3.18 for the virtual cluster at 2.5 kpc including sensitivity and saturation cut-offs.

diagrams. These show the number of models on a logarithmic greyscale for all models, as well as for each individual Stage (I/II/III). Figure 3.18 shows the fraction of models at each Stage relative to the total, for the same colour-colour spaces as Figure 3.17. Dark areas show where most of the models belong to a given Stage: for example a dark area in a 'Stage I/All' ratio plot indicates a region where most models are Stage I models. To ensure that these results are not biased by unrealistic models, the same diagrams are shown for the virtual clusters with sensitivity and saturation limits applied, at 250 pc (Figures 3.19 and 3.20) and 2.5 kpc (Figures 3.21 and 3.22). The main difference between the colour-colour diagrams for the entire set of models and for the virtual clusters is that there are many fewer Stage I models in the virtual cluster plots. This is expected as the ages are distributed logarithmically in the overall set of models, while they are sampled linearly in the cluster. In addition, faint Stage I models will be removed due to the applied sensitivity limits.

JHK$_s$ colour-colour diagrams: The models tend to lie along and redward in H−K$_s$ of the locus for reddened stellar photospheres. For the whole set of models and for the two virtual clusters, a number of Stage I models occupy a small region where no Stage II and III models lie. However the region where only Stage I models are found is different in each case. Stage II models also lie along and redward in H−K$_s$ of the locus for stellar photospheres, while the colours of Stage III models are in most cases identical to stellar photospheres.

Observations of distant star formation regions are likely to be affected by high levels of extinction that would make most YSOs along the locus of reddened stellar photospheres indistinguishable from highly reddened stars. This suggests that there are in fact no regions in J−H vs. H−K$_s$ colour-colour space where only sources at a specific stage of evolution always lie, and therefore that J−H vs. H−K$_s$ colours are not a reliable indicator of the evolutionary stage of a source.

YSOs displaying colours with a redder H−K$_s$ colour than reddened stellar photospheres can still be classified as such, but their evolutionary stage cannot be determined, while many YSOs will be simply be indistinguishable from reddened stellar photospheres.

IRAC colour-colour diagrams: The models lie mostly redward in [3.6] − [4.5] and [5.8] − [8.0] compared to stellar photospheres, which fall mostly at (0,0). The Stage I models occupy a large region of IRAC colour-colour space, which includes a substantial region unoccupied by Stage II and III models. Many Stage I models are fairly red at [3.6] − [4.5], but are not

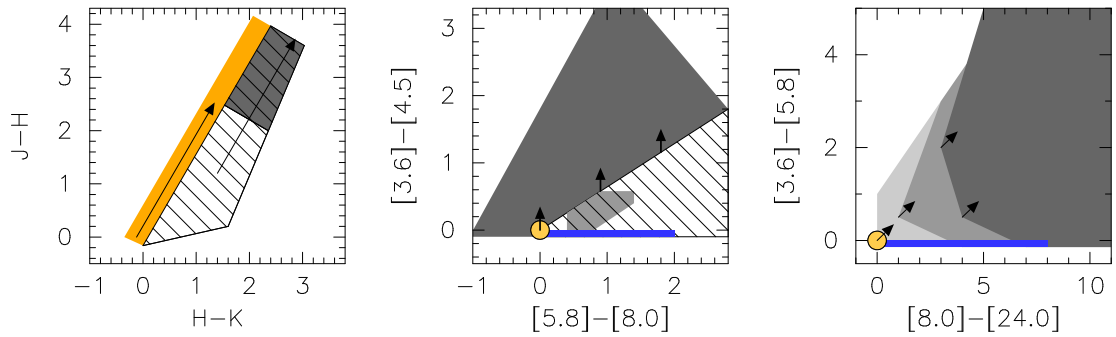

Figure 3.23: Approximate regions of JHK_s (*left*), IRAC (*center*) and IRAC+MIPS 24 μm (*right*) colour-colour space where the different evolutionary stages lie. From dark to light grey: the regions where most models are Stage I, II, and III respectively. The hatched region in the JHK_s and IRAC colour-colour diagrams are regions where models of all evolutionary stages can be present. The dark grey region in the JHK_s colour-colour diagram is also hatched to indicate that this region, although never occupied by Stage II and III models in the absence of extinction, would easily be contaminated by Stage II and III models for high values of extinction. The Stage II area in the IRAC colour-colour diagram is hatched to show that although most models in this region are Stage II models, Stage I models can also be found with these colours. The orange region in the JHK_s colour-colour diagram represents the location of reddened stellar photospheres. The yellow disk in the IRAC and IRAC+MIPS 24 μm colour-colour diagrams represents the approximate location of stellar photospheres in the absence of extinction. The blue rectangles show the approximate regions where only disks with large inner holes lie. The reddening vectors show an extinction of $A_V = 20$, assuming the Indebetouw et al. (2005) extinction law.

always as red at $[5.8]-[8.0]$ as the predictions by Allen et al. (2004). The main difference in the models presented here is that they include bipolar cavities that allow more scattered light to emerge, which tends to make the sources bluer at mid-infrared wavelengths. Furthermore, pole-on Stage I models tend to have bluer colours, as one can view the star unobscured by the envelope, by looking down the cavity. The region where only Stage I models fall is similar for the whole set of models and for the virtual clusters. Most of the Stage II models lie in the same region indicated by Allen et al. as the "disk domain". However, many also lie outside this region, due to variations in disk mass, stellar temperature, and inner hole size, as discussed below. Most regions occupied by Stage II and III models are also occupied by Stage I models. This suggests that although many Stage I sources can be identified uniquely as such, the evolutionary stage of the remaining Stage I sources as well as of most Stage II and Stage III sources cannot be reliably found from the IRAC colours alone. This can be seen in Figures 3.18, 3.20, and 3.22, which shows that the 'Stage I/All' fraction is close to 100 % (black areas) in a large region of IRAC colour-colour space, while the 'Stage II/All' and 'Stage III/All' fractions never reach 100 % (grey areas). Most sources that fall in the Allen et al. "disk domain" are most likely to be Stage II sources, but can in some cases be Stage I sources.

In Figure 3.23 (and over-plotted on the IRAC colour-colour diagrams in Figures 3.18 through 3.22) the approximate regions corresponding to the different evolutionary stages are shown. These should of course be seen only as general trends. For example, one complication for Stage I identification is that the Stage I region lies along the reddening line from the Stage II region. However, as shown by the reddening vector, substantial amounts of extinction ($A_V > 20$) are required to change the colours of a source significantly.

This suggests that unlike JHK_s colour-colour diagrams, IRAC colour-colour diagrams appear to be effective in separating stars with no circumstellar material from most Stage I and II sources (the colours of many Stage III sources are very similar to those of stars in the IRAC bands). Furthermore, very young (Stage I) sources can be distinguished in many cases from Stage II/III sources.

IRAC+MIPS 24 μm colour-colour diagrams: As for IRAC colour-colour diagrams, the models lie mostly redward in $[3.6]-[5.8]$ and $[8.0]-[24.0]$ compared to stellar photospheres, which fall mostly at (0,0). Stage I models cover a very wide range of colours, and a large number fall in regions that are not occupied by Stage II and III models. Furthermore, Stage II and III models also seem to separate into well-defined regions, suggesting that IRAC+MIPS 24 μm colour-colour diagrams may be effective in discriminating between various evolutionary stages.

As before, the approximate regions corresponding to Stage I, II, and III models are shown in Figure 3.23, and are over-plotted on the IRAC+MIPS 24 μm colour-colour diagrams. Even if a source is not detected in MIPS 24 μm, an upper limit on its flux can still provide constraints on its evolutionary stage: for example, if a source has $[8.0]-[24.0] < 2$, it is not likely to be a Stage I source.

As found in §3.3.3, this shows that including data at wavelengths longward of 20 μm is valuable in assessing the evolutionary stage of YSOs.

Colours and physical parameters

Figures 3.24 to 3.28 show how various physical parameters affect the colours of the models.

Envelope accretion rate: Figure 3.24 shows how the colours of the models depend on $\dot{M}_{\rm env}/M_\star$. Interestingly, the models with very high envelope accretion rates are relatively blue in JHK_s, IRAC and IRAC+MIPS colour space compared to models with lower accretion rates. This is

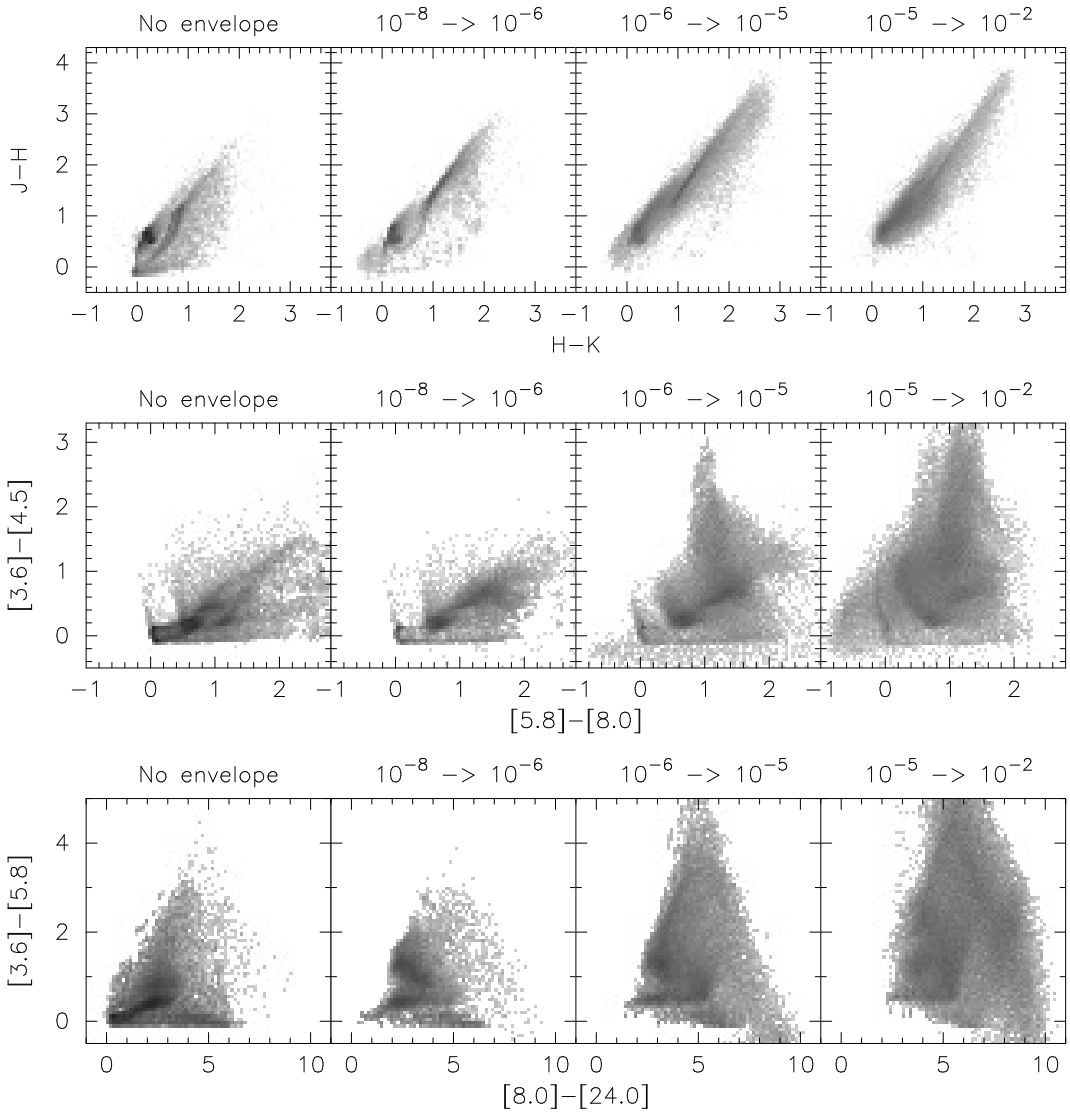

Figure 3.24: The dependence of the JHK_s, IRAC, and IRAC+MIPS 24 μm colours on the envelope accretion rate $\dot{M}_{\rm env}/M_\star$ (the values are shown above each box; the unit is $\rm yr^{-1}$).

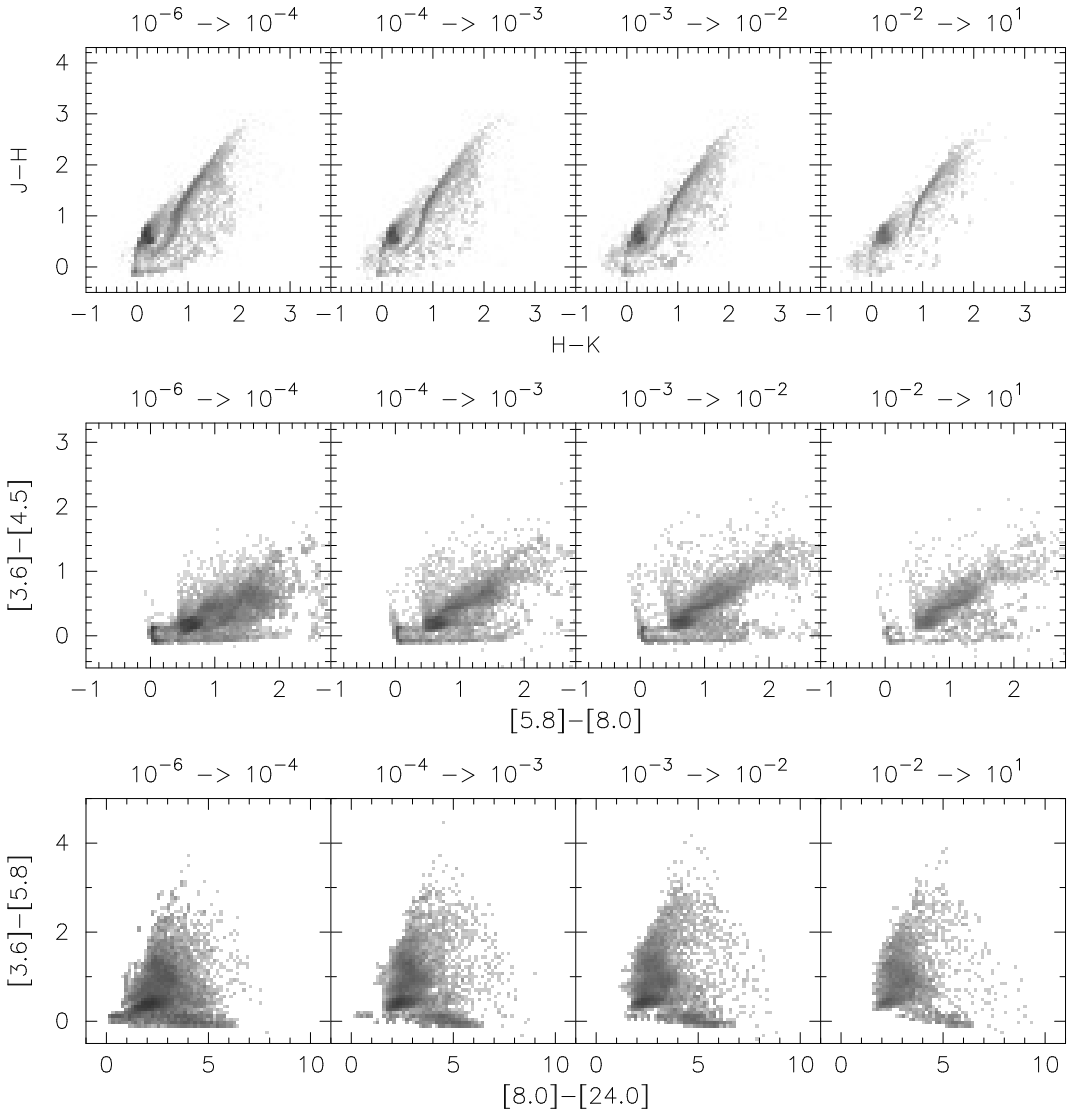

Figure 3.25: The dependence of the JHK$_s$, IRAC, and IRAC+MIPS 24 μm colours on the disk mass $M_{\rm disk}/M_\star$ (the values are shown above each box). All Stage II models are shown.

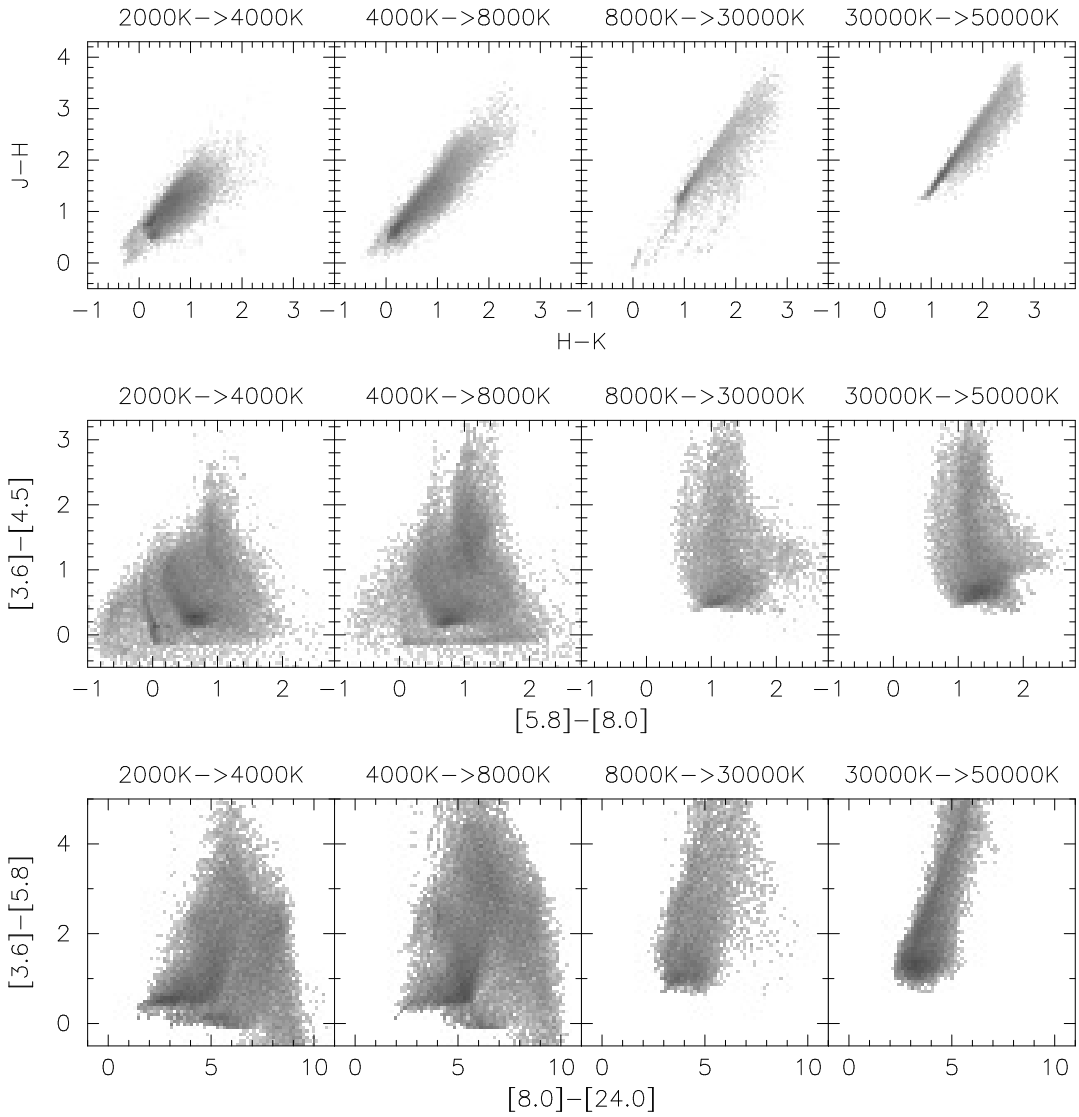

Figure 3.26: The dependence of the JHK$_s$, IRAC, and IRAC+MIPS 24 μm colours on the stellar temperature $T_\star$ (the values are shown above each box). All Stage I models are shown.

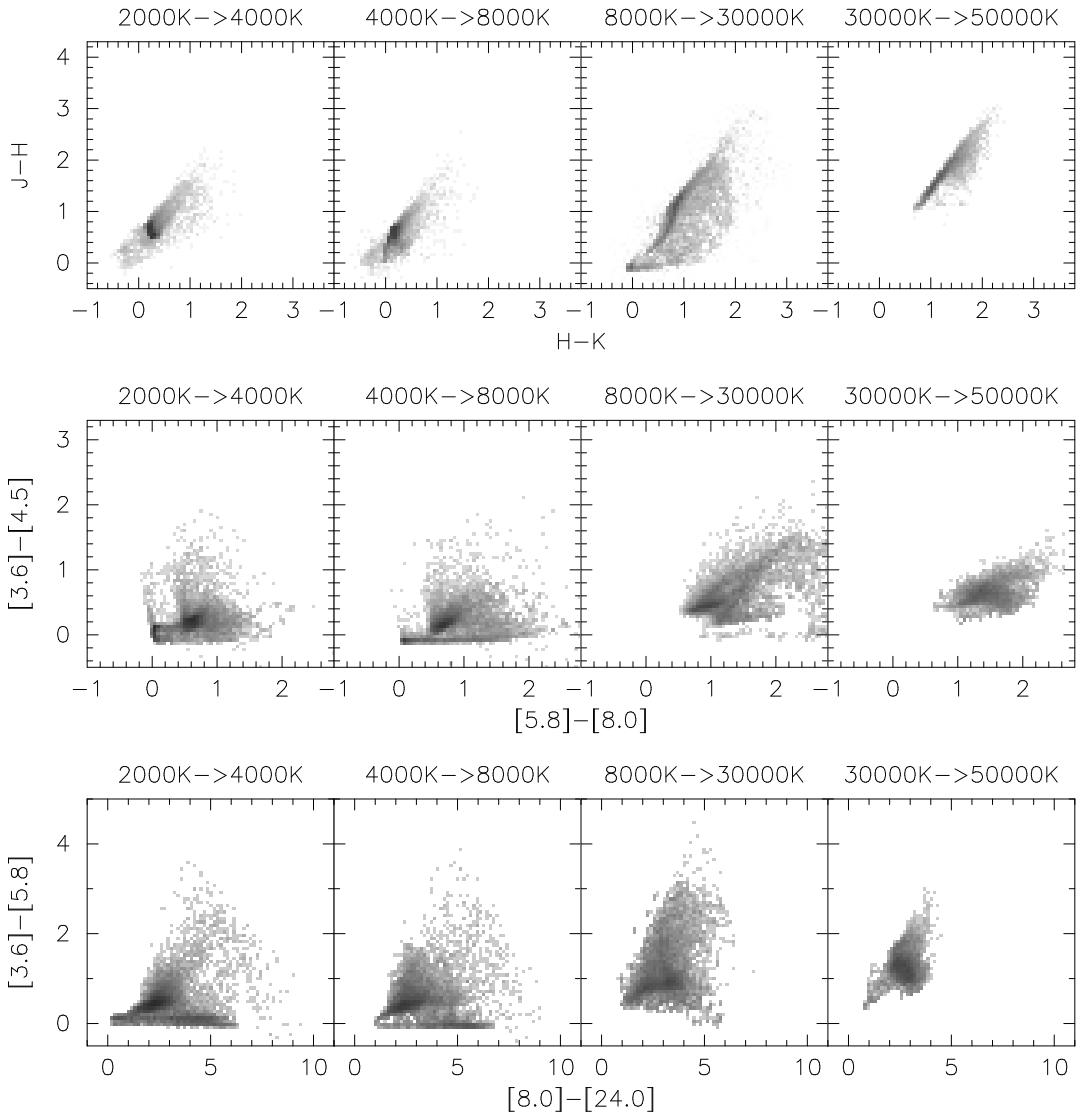

Figure 3.27: The dependence of the JHK$_s$, IRAC, and IRAC+MIPS 24 μm colours on the stellar temperature $T_\star$ (the values are shown above each box). All Stage II models are shown.

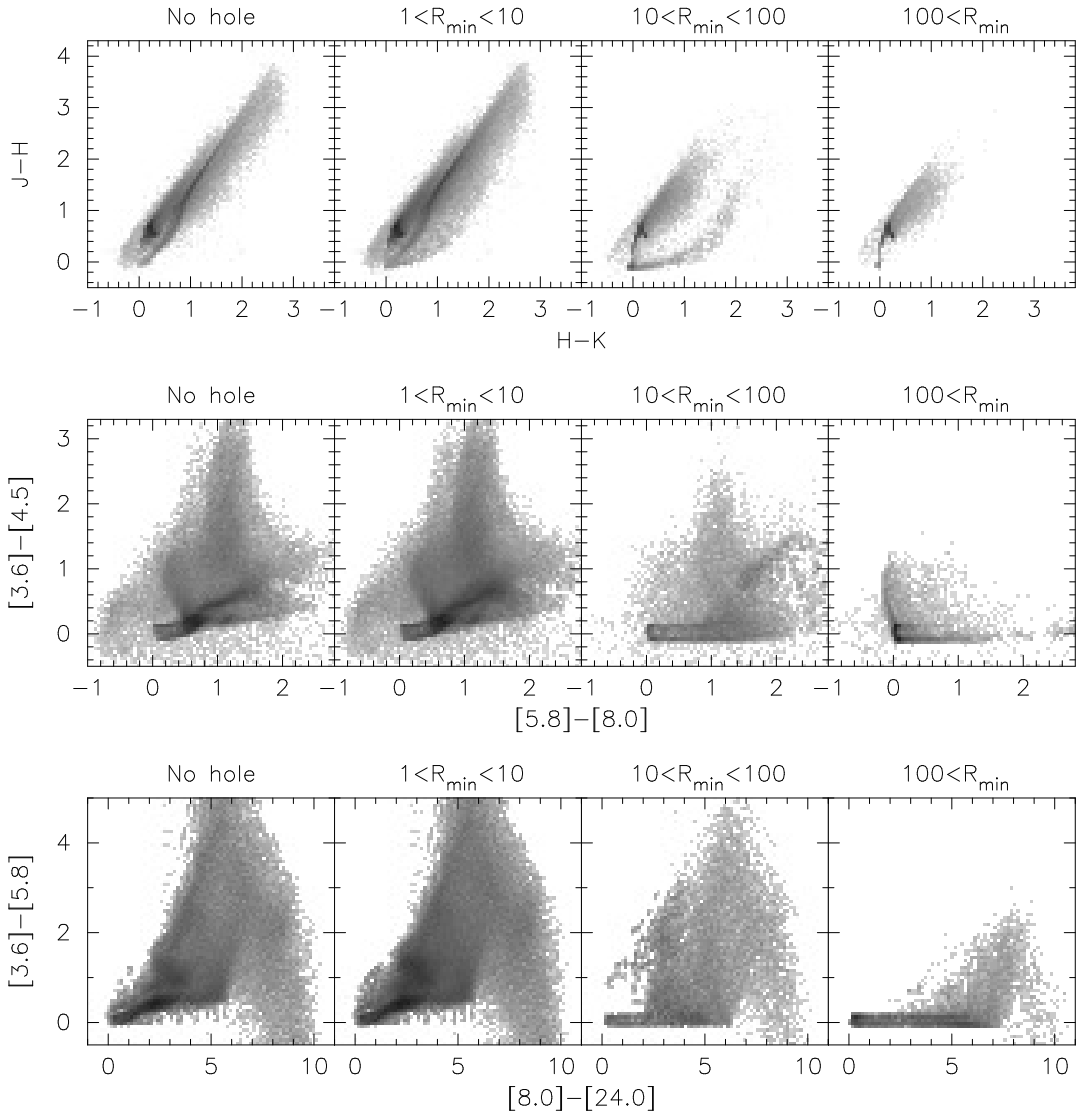

Figure 3.28: The dependence of the JHK$_s$, IRAC, and IRAC+MIPS 24 μm colours on the disk and envelope inner radii $R_{\rm disk}^{\rm min}$ (= $R_{\rm env}^{\rm min}$) (the values are shown above each box, and the unit is the dust sublimation radius $R_{\rm sub}$). All the models are shown.

due to the complete extinction of the stellar and inner disk/envelope radiation, leaving only scattered light that is relatively blue (Whitney et al., 2003a,b). These may however be very faint and thus below detection limits at large distances. For example the bluest models in $[5.8]-[8.0]$ in the IRAC colour-colour diagram for the whole set of models (Figure 3.17) are not present in the same diagram for the virtual cluster at 2.5 kpc after sensitivity limits have been applied (Figure 3.21). However, even in this case the youngest models still display colours bluer than would be expected if bipolar cavities had not been included. In the same way as with spectral indices (c.f. §3.3.3), models with accretion rates $\dot{M}_{\rm env}/M_{\star} < 10^{-6}\,{\rm yr}^{-1}$ have colours similar to disk-only models; i.e. the envelope does not dominate the near- and mid-infrared colours.

Disk mass: Figure 3.25 shows the effect of disk mass on the colours of Stage II models. The effect on the JHK_s, IRAC, and MIPS 24 μm colours is negligible. This is not surprising, since the disk is opaque at these wavelengths, and the near- and mid-infrared radiation originates only from the surface of the disk (as previously found in §3.3.3).

Stellar Temperature: Figures 3.26 and 3.27 show the effect of stellar temperature on the colours of Stage I and Stage II models respectively. Whitney et al. (2004b) showed that the IRAC colours of YSOs become redder for hotter stellar sources. These figures show that this applies more generally to near- and mid-infrared colours. This echoes the result found in §3.3.3 that the spectral index of the models calculated using near-infrared and mid-infrared wavelengths increases with stellar temperature.

Disk and envelope inner radius: Figure 3.28 shows the effect of increasing the inner radius of the disk and envelope on the colours of all the models. Since the inner holes are completely evacuated, this means that as the inner radius of the disk is increased, the temperature of the warmest dust decreases, progressively removing flux from shorter to longer wavelengths; thus only photospheric fluxes remain at shorter wavelengths, where the disk contribution has been removed. The colours of the models in the JHK_s colour-colour diagram tend to the photospheric colours for $10\,R_{\rm sub} < R_{\rm disk}^{\rm min} < 100\,R_{\rm sub}$ (photospheric colours are not necessarily $J-H = 0$ and $H-K_s = 0$ except for high photospheric temperatures). For these values of the inner radius, the $[3.6]-[4.5]$ colours and the $[3.6]-[5.8]$ colours also tend to the photospheric colours (close to or equal to zero), while the $[8.0]-[24.0]$ colours are not significantly affected. For inner radii $R_{\rm disk}^{\rm min} > 100\,R_{\rm sub}$, most models have $[3.6]-[4.5]$ and

$[3.6]-[5.8]$ equal to zero, and the $[5.8]-[8.0]$ colours also tend to zero (as can be seen from the high concentration of models at (0,0) in the IRAC colour-colour diagram). The models with $[3.6]-[4.5]>0$ or $[3.6]-[5.8]>0$ and with $R_{\rm disk}^{\rm min} > 100\,R_{\rm sub}$ are typically embedded sources for which the extinction to the central source produces colours that are redder than stellar photospheres. The regions of colour-colour space where models with holes can be unambiguously identified as such are the regions for which $[3.6]-[4.5]=0$ (e.g. in the IRAC colour-colour diagram) and $[3.6]-[5.8]=0$ (e.g. in the IRAC+MIPS colour-colour diagrams). These regions are shown in Figure 3.23.

3.4 Discussion and Conclusion

A large set of model SEDs has been computed for axisymmetric YSO models using a Monte-Carlo radiation transfer code. These models span a large range of evolutionary stages, from the deeply embedded protostars to stars surrounded only by optically thin disks. The 20,000 models are publicly available on a dedicated web server [4], which is described in more detail in Appendix B. For each model, the following output are available for download:

- The SEDs for 10 inclinations (from pole-on to edge-on) and integrated in 50 different circular apertures (with radii between 100 to 100,000 AU).
- Three separate SEDs, constructed from the energy packets whose last point of origin is the star, the disk, and the envelope respectively (see §3.3.2), for each inclination and aperture. In addition, an SED constructed for each inclination and aperture from photons who last scattered before escaping, and an SED constructed for each inclination from photons which escaped directly from the stellar surface are available.
- A polarisation spectrum for each inclination and aperture.
- Convolved fluxes and magnitudes for each inclination and aperture for a wide range of filters.

The convolved fluxes and the model parameters can be downloaded for all models as single files. These files can be used for example to carry out the analysis of colour-colour spaces or spectral indices not covered in this paper, or to compare the models to data directly (c.f. Chapter 4).

Typical SEDs from the set of models were presented (Figure 3.7), including separate SEDs constructed from the energy packets whose last point of origin are the star, the disk and the envelope (Figure 3.8). Also shown were polarisation spectra for these models in UBVRI and JHK_sL bands (Figure 3.9), including the variation of the K-band polarisation for all of the models with disk mass and envelope accretion rate (Figure 3.10). Stage I sources show a high polarisation ($> 5\,\%$) for envelope accretion rates above $\dot{M}_{\rm env}/M_\star \sim 2 \times 10^{-6}\,{\rm yr}^{-1}$, over a large range of viewing angles ($45-90°$) and a broad wavelength range ($0.5-10\,\mu$m). Stage I sources can show a 90° position angle rotation with wavelength, as discussed by previous authors (Bastien, 1987; Kenyon et al., 1993b; Whitney et al., 1997) due to the dominance of scattering in either the cavity or the disk. Stage II sources show high polarisation ($> 3\,\%$) only when viewed edge-on, but show significant polarisation ($> 0.5\,\%$) over a range of viewing angles.

An analysis of JHK_s, IRAC and MIPS spectral indices and colour-colour diagrams was carried out using the model SEDs, and 'virtual clusters' were simulated in order to understand how a cluster of young stars might look in these colour-colour spaces. The models indicate that:

- How well a given spectral index indicates the evolutionary stage of a source is dependent on the range of wavelengths of the fluxes used to calculate the spectral index (Figure 3.11). The results suggest that the use of fluxes beyond $\sim 20\,\mu$m (e.g. MIPS $24\,\mu$m), in addition to $1-10\,\mu$m fluxes, in calculations of the spectral index of YSOs is valuable for deriving information about the evolutionary stage of these sources.

- For optically thin disks, the traditional 2.0 to $25\,\mu$m spectral index increases with disk mass, while for optically thick disks, the same spectral index is insensitive to disk mass, as the emergent flux at these wavelengths originates only in the surface layers of the disk (Figure 3.11).

- The near- and mid-infrared colours of a disk-only source are sensitive to stellar temperature, disk inner radius, and disk flaring power (Figure 3.12). In particular, for temperatures above $5,000\,$K, these colours become redder as the temperature increases, while the presence of an inner hole decreases the flux at near- and mid-infrared wavelengths. For large enough holes, the near- and mid-infrared colours are the same as those of a stellar photosphere. The effect of a larger disk flaring power is to increase the amount

of flux intercepted by the disk, and thus to increase the amount of reprocessed flux at mid- and far-infrared wavelengths.

- For a given source, the spectral index is sensitive to the wavelength range of the broad-band fluxes used to calculate the spectral index (Figure 3.13), and to a lesser extent is also dependent on whether the spectral index is calculated from the slope of a line joining two points, or as the slope of a least-squares fit line to a larger number of fluxes (Figure 3.14).

- J−H vs. H−K_s colour-colour diagrams can be used to identify sources as YSOs if they lie redward in H−K_s of the locus for reddened stellar photospheres, although their evolutionary stage cannot be reliably found simply from the JHK$_s$ colours. In addition, many YSOs are likely to be indistinguishable from reddened stellar photospheres in regions of high interstellar extinction.

- Stage I models tend to occupy large regions in IRAC and IRAC+MIPS 24 μm colour-colour diagrams, due to inclination effects, scattering in the bipolar cavities (which makes some edge-on sources blue), and variations in stellar temperature.

- [3.6]−[4.5] vs. [5.8]−[8.0] colour-colour diagrams contain a large region that is likely to be occupied only by Stage I sources. The region corresponding to the "disk domain" from Allen et al. (2004) is likely to contain mostly Stage II sources, but also a number of Stage I sources. The remaining regions in this colour-colour space can be occupied by sources at *any* evolutionary stage.

- [3.6] − [5.8] vs. [8.0] − [24.0] colour-colour diagrams provide a good separation of YSOs at different evolutionary stages. Even if a given source is not visible in MIPS 24 μm, an upper limit on the flux can still constrain its evolutionary stage.

Figure 3.23 shows approximate regions in IRAC and IRAC+MIPS 24 μm colour-colour space where models of a given evolutionary stage lie, irrespective of whether the entire set of models or the virtual clusters are used. near-infrared fluxes (such as JHK$_s$ fluxes) can be used to discriminate between reddened stars and many (but not necessarily all) YSOs, but cannot reliably determine the evolutionary stage of a YSO. Mid-infrared fluxes (such as IRAC fluxes) should be efficient in separating YSOs from stellar photospheres, and allow some of the youngest sources to be unambiguously classified as such, although the evolutionary stage of

the remaining YSOs is likely to be ambiguous. Finally, including fluxes at wavelengths beyond $\sim 20\,\mu$m (such as MIPS $24\,\mu$m) in addition to near- and mid-infrared fluxes substantially improves the ability to distinguish between the various evolutionary stages of YSOs.

4

Fitting YSO SEDs using pre-computed models

Adapted from *Robitaille et al., 2007, ApJS,* ***169****, 328*

A method to analyse the SEDs of YSOs is presented. This method consists of fitting data with pre-computed radiation transfer models spanning a large region of parameter space. This allows the entire range of values consistent with the multi-wavelength observations of a given source to be determined rather than a single set of physical parameter values. The aim of this method is to avoid over-interpretation when modelling SEDs. Data from optical to sub-mm wavelengths, including new *Spitzer* IRAC and MIPS photometry, are used to construct SEDs for 30 young and spatially resolved sources in the Taurus-Auriga star-forming region. The SED fitting technique is demonstrated using these sources, and it is shown that the evolutionary stage and physical parameters derived are in agreement with previous independent studies, including disk masses, disk accretion rates, and stellar temperatures. It is shown how fluxes at various wavelengths help constrain physical parameters, and examples of degeneracies that can occur when fitting SEDs are presented. A web-based version of this tool is available to the community.

4.1 Introduction

In Chapter 3, a large set of model SEDs of YSOs was presented. The models were used to determine whether simple observable diagnostics such as spectral indices or colours of observed SEDs could help gain an understanding of the physical conditions in YSOs. However, these methods do not make efficient use of all data available because they cannot easily accommodate arbitrary numbers of broadband fluxes at arbitrary wavelengths. Instead, it is best to model the observed SEDs directly.

If a source has been observed at many different wavelengths from optical to mm wavelengths, it is possible, though not certain, that a unique set of parameters will reproduce the observed SED, provided that all the parameters actually affect the shape of the SED, and that there are no degeneracies. However, many star-forming regions have been observed by a number of infrared surveys, providing flux measurements for thousands of sources in a limited wavelength range typically extending from near- to mid-infrared wavelengths (c.f. §2.3). When studying a large number of YSOs, one wants to know not only *one* set of physical parameters that can explain the data for each source, but *all* the different sets of parameters that can explain the data for each source, in order to avoid any over-interpretation. Manually modelling the SEDs of these many sources is impossible. In particular, it is very likely that there is not a unique set of parameters that can explain the data available for a given source, and it would be extremely time-consuming to explore parameter space manually for each source, let alone thousands of sources. The solution to this problem, presented in the first part of this thesis, is to pre-compute a large set of radiation transfer models that provide a reasonably large coverage of parameter space. The models can then be fit to observed SEDs to find all the combinations of parameters that can explain the data for a given source.

This chapter describes the method used to fit these models to observed SEDs, and presents examples of what can be learned from using such a technique. In §4.2, the technical details of the fitting method are described. In §4.3, the use of the fitting method on Taurus-Auriga sources is demonstrated as a proof-of-concept: the sample of sources and the data used to construct the SEDs are first described (§4.3.1); then the values of a selection of physical parameters is compared with independent estimates (§4.3.2); and finally an analysis showing how different combinations of data points constrain physical parameters for a given source is shown, and degeneracies that can arise are discussed (§4.3.3). Additionally, an example of

a model fit to a resolved source for which fluxes can be measured in apertures smaller than the source itself is shown, demonstrating that fluxes from the different apertures can be fit simultaneously (§4.3.4).

4.2 Technical overview

The SED fitting tool presented in this chapter makes use of the 200,000 YSO model SEDs (20,000 sets of physical parameters and 10 viewing angles) presented in Chapter 3. The models consist of pre-main-sequence stars with different combinations of axisymmetric circumstellar disks, infalling flattened envelopes, and outflow cavities, covering a wide range of parameter space. The main caveat for this work is the assumption that stars of all masses form via accretion through a disk and envelope. However, the set of models covers a large range of parameter space, so that as little as possible is assumed about the specifics of the accretion physics. Details about the models and the ranges of parameters sampled, including caveats, are discussed in Chapter 3.

The models were convolved with common filter band-passes ranging from optical (e.g. UBVRI), to near and mid-infrared (e.g. 2MASS JHK, *Spitzer* IRAC & MIPS), far-infrared, and sub-mm (e.g. IRAS, SCUBA). Details on the convolution procedure are given in Appendix A.

Let us assume that photometry at N wavelengths $\lambda_{i\ (i=1...N)}$ is available for a given source, and that the flux densities are $F_\nu(\lambda_i)$ with uncertainties $\sigma(\lambda_i)$, measured in apertures $A(\lambda_i)$. Let us also assume that the source lies in a distance range $d_{\rm min}$ to $d_{\rm max}$. In order to fit convolved model fluxes to data, the models are first interpolated to the apertures $A(\lambda_i)$ used to perform the photometry, for a number of distances d between $d_{\rm min}$ and $d_{\rm max}$, and are scaled to the appropriate distance. This can easily be done as each SED was computed for 50 apertures between 100 and 100,000 AU. At each of these distances, the convolved model fluxes are fit to the data using optimal scaling, allowing the visual extinction A_V to be a free parameter. Writing the convolved, interpolated, and scaled model fluxes as $M_\nu(\lambda_i)$, the overall pattern $P_\nu(\lambda_i)$ that is being fit to the data is then

$$P_\nu(\lambda_i) = M_\nu(\lambda_i) \times 10^{-0.4 A_V \kappa_{\lambda_i}/\kappa_V} \tag{4.1}$$

where κ_{λ_i} and κ_V are given by an extinction law (c.f. §2.1). In this chapter, an extinction model that fits a typical Galactic ISM curve modified for the mid-infrared extinction properties

derived by Indebetouw et al. (2005) (Wolff, private communication) was calculated with the method of Kim, Martin, & Hendry (1994). Since $P_\nu(\lambda_i)$ is a non-linear function of A_V, it is convenient to work with $\log[F_\nu]$ and $\log[P_\nu]$ rather than F_ν and P_ν so as to transform this into a linear problem. The model that is fit to the data is then:

$$\log_{10}[P_\nu(\lambda_i)] = \log_{10}[M_\nu(\lambda_i)] - 0.4 A_V \frac{\kappa_{\lambda_i}}{\kappa_V} \tag{4.2}$$

where the free parameter A_V can be determined from optimal scaling. The unbiased fluxes and flux variances in $\log_{10}$ space are given by:

$$\langle \log_{10}[F_\nu] \rangle = \log_{10}\langle F_\nu \rangle - \frac{1}{2}\frac{1}{\log_e 10}\frac{1}{\langle F_\nu \rangle^2}\sigma^2(F_\nu) + ... \tag{4.3}$$

$$\sigma^2(\langle \log_{10}[F_\nu] \rangle) = \left[\frac{1}{\log_e 10}\frac{1}{\langle F_\nu \rangle}\right]^2 \sigma^2(F_\nu) + ... \tag{4.4}$$

Once the free parameter A_V has been determined, the χ^2-per-data point value of the fit is computed using:

$$\chi^2 = \frac{1}{N}\sum_{i=1}^{N}\left(\frac{\langle \log_{10}[F_\nu(\lambda_i)] \rangle - \log_{10}[P_\nu(\lambda_i)]}{\sigma(\langle \log_{10}[F_\nu](\lambda_i) \rangle)}\right)^2 \tag{4.5}$$

where N is the number of data points being fit. Throughout this paper, the χ^2 values mentioned are per data point.

This fitting process is repeated for a range of distances between d_{min} and d_{max}, and a best-fit d, A_V, and χ^2 value can be found for each model SED. The process is repeated for all the models in the grid. In this way, all the model SEDs in the grid are compared with the data, and the parameters of the model SEDs that fit a source well can be analysed. The implementation of this algorithm is described in Appendix C.

The process described above does not make any assumptions about the spatial extent of the source. For example the apertures may be smaller than the extent of the source (see §4.3.4 for an example). Usually however, one measures the total flux of a source by using an aperture larger than the source. With the knowledge that the source is not larger than a given aperture, a fraction of models can be eliminated if they are clearly larger than the aperture.

For example, if a source in Taurus is unresolved at a given wavelength λ_i, then models that would have been resolved at that particular wavelength should not be fit to the data. More generally, if the apparent extent of a source is known to always be smaller than the

apertures that the fluxes were measured in, then all models whose apparent extent is larger than the aperture in at least one wavelength are eliminated. Note that not all models that are *physically* larger than the aperture should be eliminated, but only those that *appear* larger (the apparent size can be smaller than the physical size). To use this information, the wavelength-dependent outermost radius $R_{\lambda_i}(\Sigma = \Sigma_0/2)$ at which the surface brightness Σ of the model is equal to half of the peak surface brightness Σ_0 is computed for all models. All models that have $R_{\lambda_i}(\Sigma = \Sigma_0/2) > A(\lambda_i)$ in at least one wavelength λ_i are then rejected.

4.3 Proof-of-concept using known Taurus-Auriga sources

4.3.1 The data

This section presents an analysis that aims to determine whether fitting model SEDs to observed SEDs can correctly identify the evolutionary stage of YSOs and a selection of physical parameters. This was done by fitting the SEDs of well studied and resolved YSOs in the Taurus-Auriga star-forming region. Over the last few decades, Taurus has been one of the best studied star-formation regions, and is in that respect one of the regions for which the most data are available. A sample of 30 sources was constructed by selecting those from Kenyon & Hartmann (1995) that have been spatially resolved as of mid-2006[1]. The latter requirement ensures that good a-priori knowledge of the evolutionary stage of the objects from direct observations is available (e.g. young protostars with infalling envelopes, or disks). FS Tau and FS Tau B were not included due to their small angular separation, which makes it difficult to construct separate SEDs, and UZ Tau E was not included because of insufficient SED coverage. DG Tau and DG Tau B were included, despite their small angular separation, as IRAC and MIPS data were available, allowing the construction of two separate well defined SEDs.

A few sources are known from direct imaging to be more complex than axisymmetric objects (e.g. IRAS 04016+2610; Padgett et al. 1999 ; Wood et al. 2001), but it is interesting to see what can be derived from fitting the SEDs of such sources. Indeed, when looking at more distant star-forming regions, no a-priori knowledge of the complexity of the geometry of an unresolved source is available, and it is interesting to know what can be learned using 2-D models

The SEDs for these 30 sources were compiled using optical (UBVRI), near- (JHKL) and

[1] according to the list at `circumstellardisks.org` [1]

mid-infrared (MNQ) data from Kenyon & Hartmann (1995), JHK_s fluxes from the 2MASS point-source catalogue (Skrutskie et al., 2006), IRAC data from Hartmann et al. (2005) and Luhman et al. (2006), IRAS data from the IRAS point-source catalogue and from Weaver & Jones (1992) (the latter was used over the former when available), SHARC II 350 μm, SCUBA 450 μm, and 850 μm sub-mm data from the compilation presented in Andrews & Williams (2005), and CSO 624 and 769 μm data from Beckwith & Sargent (1991).

In addition, the IRAC fluxes for the sources not presented in Hartmann et al. (2005) or Luhman et al. (2006) were measured, and the IRAC fluxes of RY Tau and DG Tau, which are saturated in all bands, were re-measured using IRAC (PI Fazio – P00006 & P00037) and MIPS data (PI D. Padgett – P03584) retrieved from the *Spitzer* Science Center (SSC) Archive. The fluxes of sources saturated in IRAC were measured using the publicly available `iracworks` code written by Tom Jarrett [5]. Finally, PSF photometry of MIPS 24 and 70 μm data was carried out using a custom written photometry code. For sources that were mildly saturated in MIPS, the saturated pixels were ignored in the PSF fitting, and the flux was determined by ensuring that the wings of the PSFs were being correctly fit. The list of sources along with the data are given in Tables D.1, D.2, D.3, and D.4 in Appendix D.

When fitting the SEDs, it is technically possible to use all the data available for each source, but in cases where several measurements were available at the same wavelength, the highest quality one was used. For example, if MIPS data were available, these were used instead of IRAS data, since IRAS data have a poorer resolution, and are more prone to confusion. Similarly, space-based IRAC data were preferred over ground based mid-infrared data. The following rules were applied:

- when 2MASS JHK data was available, it was used instead of previous JHK measurements.
- when IRAC 3.6 μm data was available, the L-band flux was not used.
- when IRAC 4.5 and/or 5.8 μm data were available, the M-band flux was not used.
- when MIPS 24 μm data was available, the IRAS 25 μm flux was not used.
- when MIPS 70 μm data was available, the IRAS 60 μm and 100 μm data were not used.
- in general, flux measurements were always preferred over upper limits.

Additionally, the ground-based N and Q-band data were not used when fitting the SEDs, due to large uncertainties in the fluxes, filter profiles, calibration, and zero-magnitude fluxes, but these fluxes are quoted in the tables for reference. A lower limit of 25% was imposed on the flux uncertainties for optical, L & M, IRAS, and sub-mm data, so that any flux measurement with a smaller uncertainty saw its uncertainty increased. This was done to account for variability and uncertainties in the zero-magnitude fluxes in the optical, uncertainties in the filter profiles and zero magnitude fluxes in the L & M bands, and uncertainties in the absolute flux calibration for IRAS and sub-mm wavelengths. A lower limit of 40% was imposed on the flux uncertainties for the CSO sub-mm data, as the transmission profiles for these observations were not available: since the FWHM of the filters used for the 769 μm observations is large (190 μm), differences in the filter profile would be noticeable. For the transmission profiles of these two bands, Gaussian functions centred at 624 and 769 μm with FWHM 67 and 190 μm respectively were used; these were subsequently convolved with the atmospheric transmission profile used in Dowell et al. (2003). Additionally, a lower limit of 10% was imposed on the remaining data points, to account mainly for uncertainties in the absolute calibration and photometry extraction.

4.3.2 Comparison of derived physical properties to other methods

The only assumptions made when fitting the observed SEDs with the model SEDs was that the sources were all situated in a distance range of 120 $\rightarrow$ 160 AU (to rule out too luminous or too faint models), that the foreground interstellar extinction was no more than $A_V = 20$ (Whittet et al., 2001), and that none of the sources appeared larger than the apertures used to measure the fluxes. The aperture radii assumed for the data are listed in Table D.5 in Appendix D.

Figure 4.1 shows the SEDs for all the sources along with the best fitting model for each source, and all the models with $\chi^2 - \chi^2_{\rm best} < 3$ (where $\chi^2_{\rm min}$ is the χ^2 per data point of the best fitting model for each source). Although this cut-off is arbitrary, it provides a range of acceptable fits to the eye. A purely statistical argument would of course be more desirable, but the sampling of the models in 14 dimensional space is too sparse to resolve well enough the shape of the minima in the χ^2 'surface' to derive formal confidence intervals. Using a 'chi-by-eye' approach does carry the risk of overestimating the uncertainties on the various parameters, but this is better than under-estimating the uncertainties, which would lead to over-interpretation. Furthermore, intrinsic variability of the sources, along with the fact that

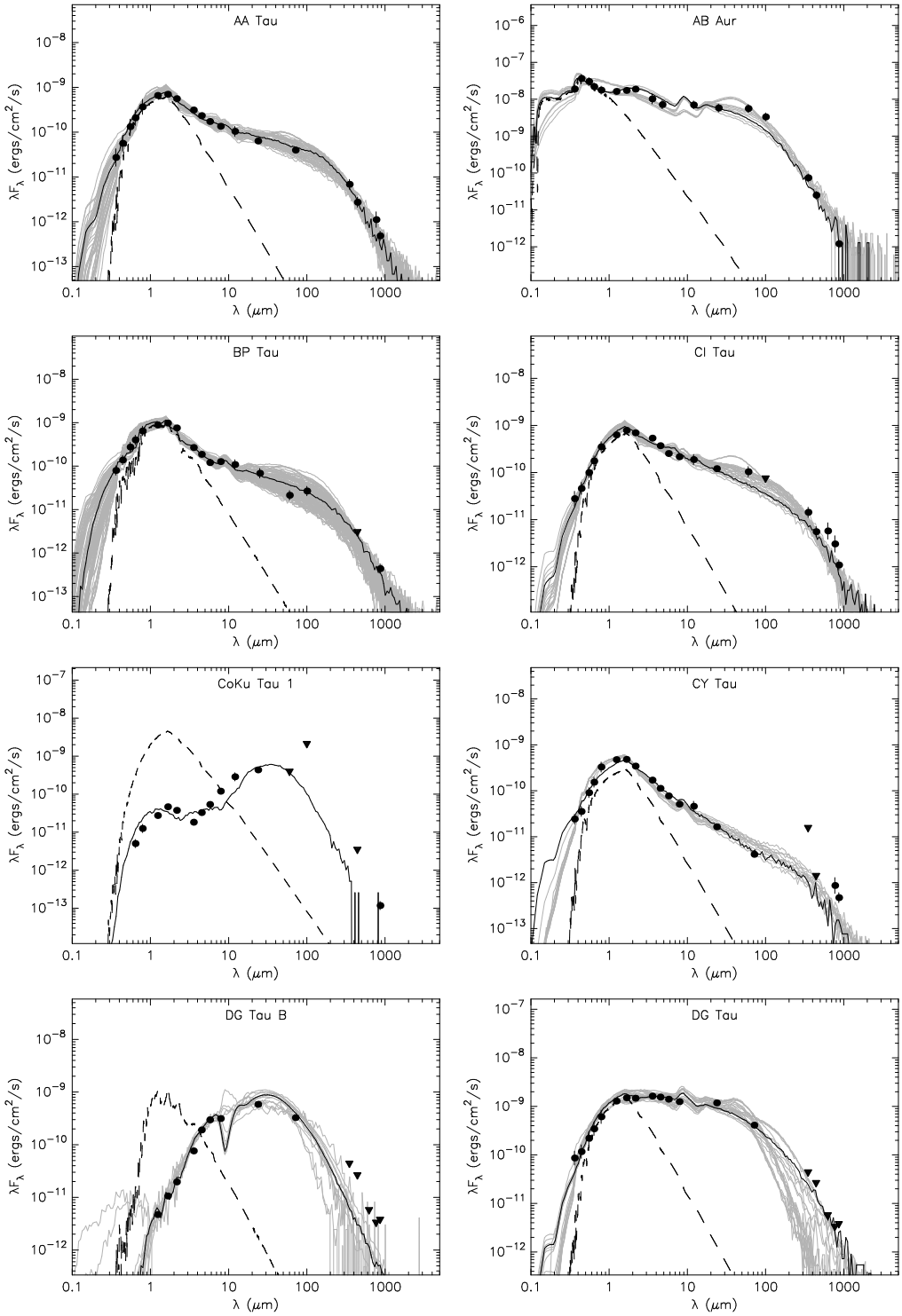

Figure 4.1: SEDs for the 30 Taurus-Auriga sources analysed in this paper. Filled circles are the flux values listed in Tables D.1, D.2, D.3 and D.4. Triangles are upper limits. Error bars are shown if larger than the data points. The solid black line indicates the best fitting model, and the grey lines show all models that also fit the data well (defined by $\chi^2 - \chi^2_{\rm best} < 3$, where χ^2 is the value per data point). The dashed line shows the SED of the stellar photosphere in the best fitting model.

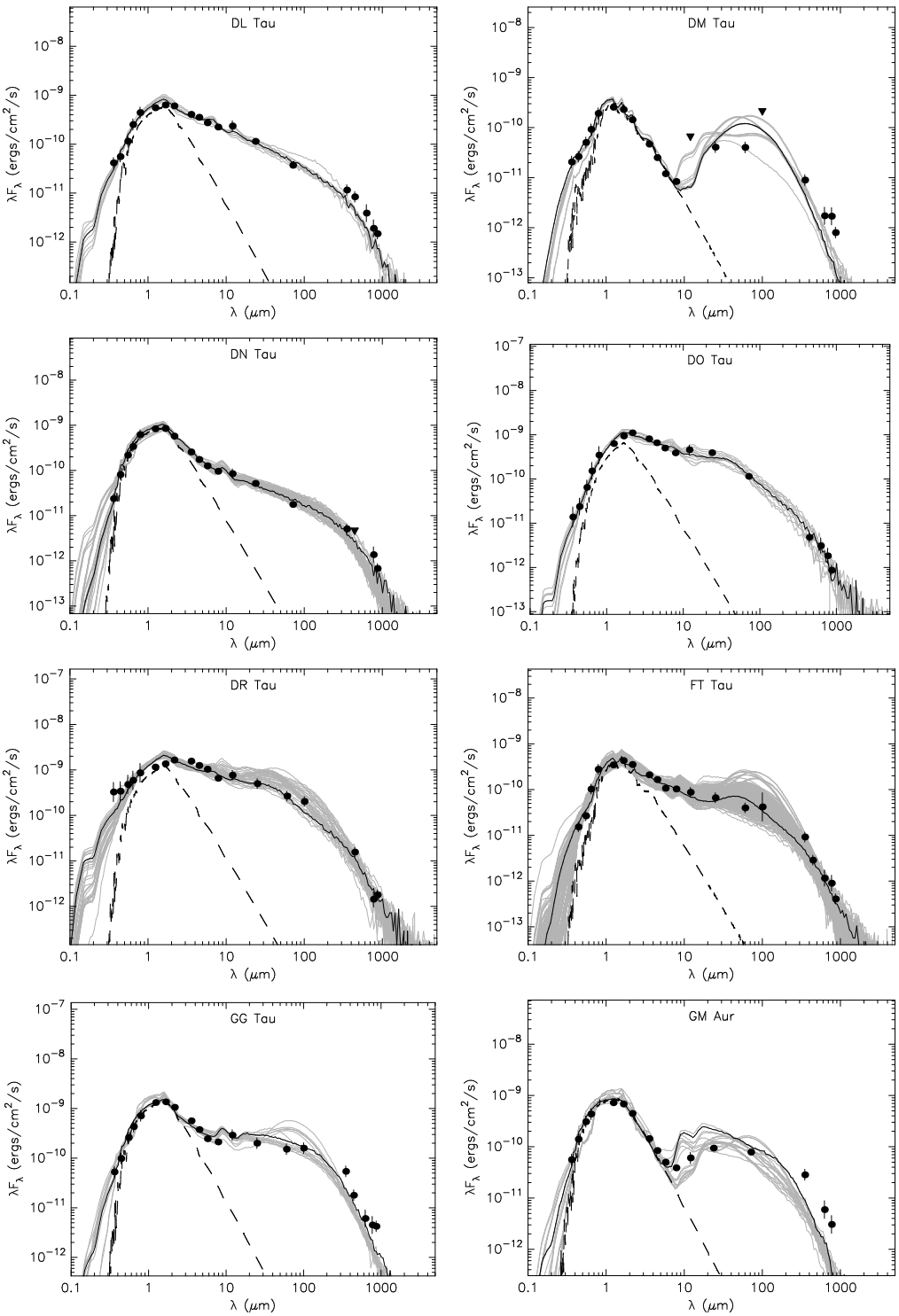

Figure 4.1: Continued

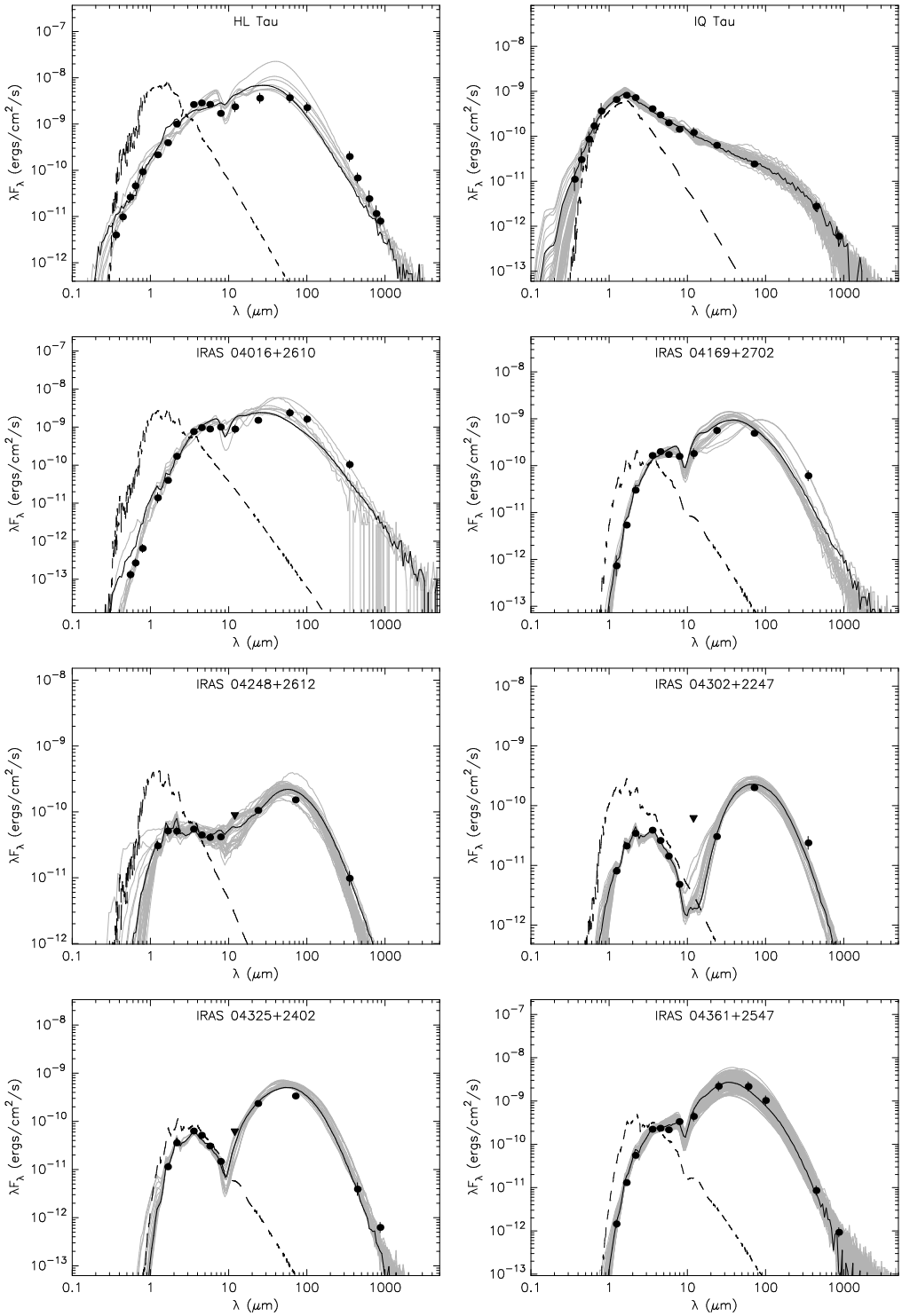

Figure 4.1: Continued

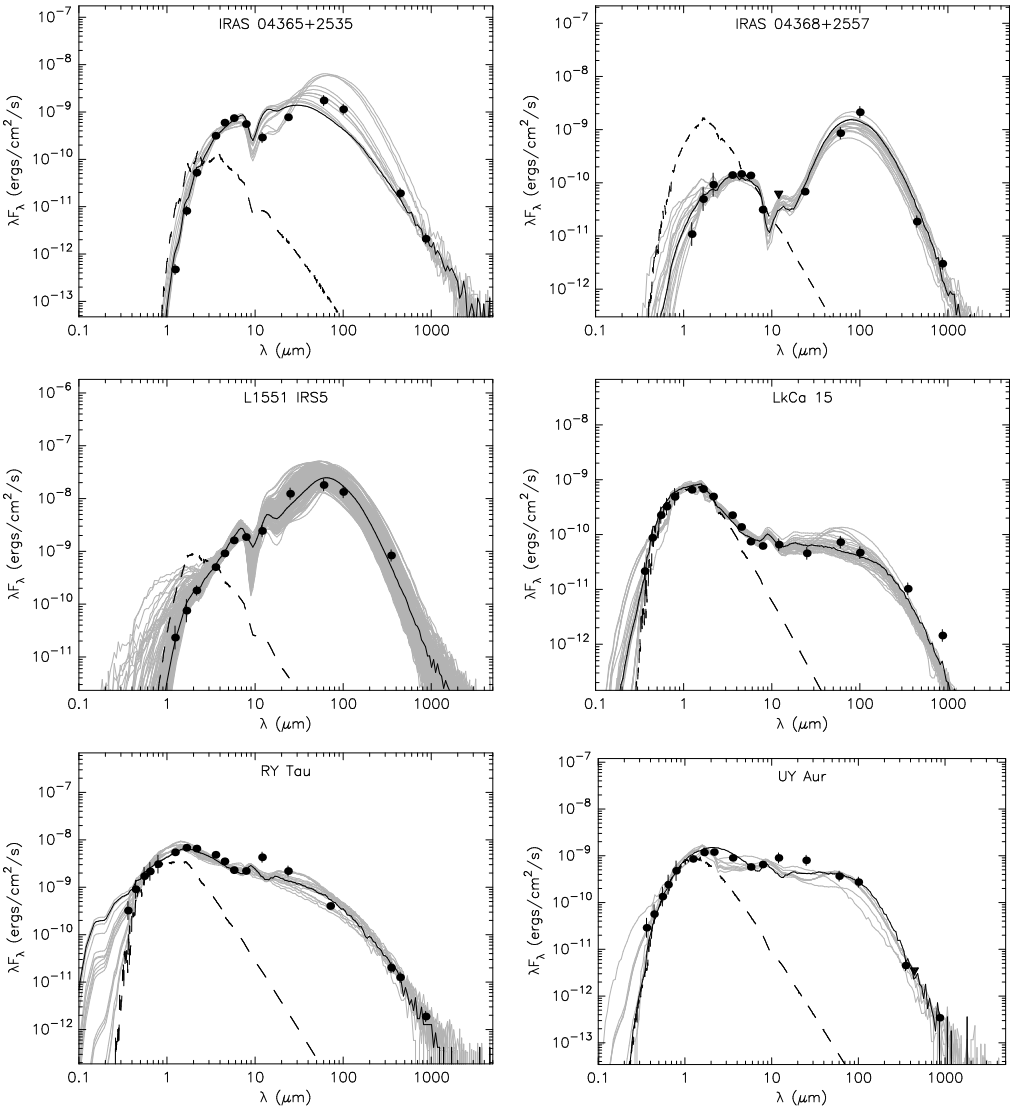

Figure 4.1: Continued

no YSO will be as perfectly symmetrical and well behaved as the models, means that any 'formal' confidence interval would likely be too strict.

All sources except DM Tau and GM Aur have their SED reasonably well fit by the model SEDs. These two sources are known to show a near-infrared deficit in their SEDs (Rice et al., 2003; Calvet et al., 2005), suggesting that the inner region of their disks has been cleared of dust. Although a substantial number of the models used include inner holes, the models systematically over-estimate the observed mid-infrared fluxes. This may be because the models only include completely evacuated holes inside a given radius, rather than having small but non-zero amounts of dust inside the 'holes'.

The SED for CoKu Tau/1 is fit by only one model within the goodness-of-fit constraints. The model that does fit well is that of an edge-on YSO with a remnant accreting envelope (see Table 4.1). Based on the SED fit alone, an edge-on inclination seems reasonable, as the SED is double-peaked, a typical signature of an edge-on disk. Stark et al. (2006) modelled spatially resolved near-infrared images of CoKu Tau/1, and found that it does indeed requires a low-mass envelope, suggesting that CoKu Tau/1 is more evolved than a typical Class I source. However, they find that the images are best-fit using a 64° inclination rather than edge-on. This seems more plausible as the central source is visible in these images (the central source would not be visible in an edge-on system). The central source is a binary system with separation 0.24″ (∼33 AU at 140 pc), which will likely have evacuated some material from the inner disk. The presence of a binary system may help explain why the model SEDs (which only include single central sources) do not fit the data well.

In the remainder of this section, a selection of physical properties of the sources derived from fitting model SEDs to the sources is compared with values quoted in the literature:

Evolutionary Stage and Viewing Angle: The first result that can be compared with known values is whether the correct evolutionary stage is identified, i.e. whether young protostars with infalling envelopes or disks are correctly identified as such (see Table 4.1). To do this, the range of envelope accretion rates that provide a good fit to each source is examined, in particular the lower value of the range of good-fitting models. If this lower value is greater than zero, then this suggests that the SED of the source *cannot* be explained by a disk-only source within the goodness-of-fit constraints applied. Conversely, if the lower value is zero, then this suggests that the SED of the source can be explained by a disk with no infalling en-

Table 4.1: Comparison of values of the envelope accretion rate found from SED fitting with the evolutionary stage of the object determined from resolved observations.

		SED Fitting values			i ($\dot{M}_{\rm env} = 0$)		i ($\dot{M}_{\rm env} > 0$)	
Source Name	Evol. Stage	Min	Best	Max	Min	Max	Min	Max
AA Tau	Disk	0	0	7.69×10^{-8}	18	81	18	63
AB Aur	Hae	0	0	1.41×10^{-6}	32	63	32	57
BP Tau	Disk	0	5.18×10^{-8}	7.69×10^{-8}	18	81	18	81
CI Tau	Disk	0	0	5.72×10^{-8}	18	76	18	63
CoKu Tau 1	Embedded/Disk	6.88×10^{-8}	6.88×10^{-8}	6.88×10^{-8}	···	···	87	87
CY Tau	Disk	0	0	0	18	81	···	···
DG Tau	Disk	0	5.48×10^{-9}	1.11×10^{-7}	18	81	49	81
DG Tau B	Embedded	0	1.00×10^{-6}	1.00×10^{-6}	87	87	18	87
DL Tau	Disk	0	0	0	18	63	···	···
DM Tau	Disk	7.08×10^{-9}	6.19×10^{-7}	8.89×10^{-6}	···	···	18	49
DN Tau	Disk	0	0	5.18×10^{-8}	18	81	18	63
DO Tau	Disk	0	7.22×10^{-9}	7.22×10^{-9}	32	41	18	81
DR Tau	Disk	0	7.22×10^{-9}	5.67×10^{-7}	18	76	18	76
FT Tau	Disk	0	4.73×10^{-8}	7.21×10^{-6}	18	81	18	76
GG Tau	Disk	0	0	2.31×10^{-6}	18	57	18	41
GM Aur	Disk	0	0	1.01×10^{-6}	18	57	18	41
HL Tau	Embedded	1.87×10^{-6}	2.13×10^{-6}	1.59×10^{-5}	···	···	18	32
IQ Tau	Disk	0	0	5.18×10^{-8}	18	81	18	81
IRAS 04016+2610	Embedded	0	9.28×10^{-7}	4.86×10^{-6}	81	87	18	41
IRAS 04169+2702	Embedded	3.70×10^{-7}	1.52×10^{-6}	2.78×10^{-5}	···	···	32	76
IRAS 04248+2612	Embedded	0	1.73×10^{-6}	5.10×10^{-6}	81	81	18	87
IRAS 04302+2247	Embedded	1.65×10^{-6}	1.23×10^{-5}	1.23×10^{-5}	···	···	18	81
IRAS 04325+2402	Embedded	1.20×10^{-6}	1.20×10^{-6}	1.51×10^{-5}	···	···	32	76
IRAS 04361+2547	Embedded	8.51×10^{-7}	1.46×10^{-6}	3.00×10^{-5}	···	···	18	81
IRAS 04365+2535	Embedded	7.16×10^{-7}	9.28×10^{-7}	2.64×10^{-5}	···	···	18	76
IRAS 04368+2557	Embedded	9.11×10^{-6}	2.82×10^{-5}	5.05×10^{-5}	···	···	41	81
L1551 IRS5	Embedded	5.54×10^{-6}	6.47×10^{-5}	2.96×10^{-4}	···	···	18	76
LkCa 15	Disk	0	0	3.76×10^{-7}	18	70	18	63
RY Tau	Disk	0	0	9.52×10^{-8}	18	76	57	76
UY Aur	Disk	0	0	5.88×10^{-7}	70	70	57	81

Notes — All accretion rates are $M_\odot\,{\rm yr}^{-1}$. 'Embedded' refers to sources that are still surrounded by an infalling envelope, and 'Disk' refers to sources that are surrounded only by a circumstellar disk. The last four columns show the ranges of inclinations i for the disk-only models ($\dot{M}_{\rm env} = 0$) which provide a good fit as well as the range of inclinations i for the embedded models ($\dot{M}_{\rm env} > 0$) which provide a good fit. In the models (c.f. Chapter 3), photons are binned into ten viewing angles. The values quoted here correspond to the central value of the bins. The central values of the bins are, from face-on to edge-on respectively: 18°, 32°, 41°, 49°, 57°, 63°, 70°, 76°, 81°, and 87° (to the nearest degree)

velope. In most cases where the lower value is zero, the upper value is non-zero, which means that it is impossible to rule out that there may be very optically thin envelopes surrounding the disks. The ranges of inclinations to the line-of-sight that provide a good fit are also listed, as there is in some cases a degeneracy between evolutionary stage and inclination. Several remarks about the results can be made:

- All known disk sources (marked as 'Disk' in Table 4.1) except DM Tau are well fit by models with no infalling envelope. Furthermore, the maximum value of the accretion rate providing a good fit for these sources does not exceed $10^{-6}\,M_\odot\,{\rm yr}^{-1}$. This is expected, as envelopes with accretion rates lower than $\sim 10^{-6}\,M_\odot\,{\rm yr}^{-1}$ do not contribute

significantly to the SED (c.f. Chapter 3)

- Most sources that are known to have infalling envelopes (marked as 'Embedded' in Table 4.1), cannot be fit by disk-only models.

- The exceptions to the above are DG Tau B, IRAS 04016+2610 and IRAS 04248+2612, which are also known to have infalling envelopes, but can be fit by disk-only models as well as models with infalling envelopes. However, for all three sources, the disk-only models that provide good fits are all viewed edge-on (the lower limit on the range of inclinations for disk-only models, i.e. models for which $\dot{M}_{\rm env} = 0$, which fit these sources well is larger than 80°). This demonstrates that even SEDs with data ranging from optical or near-infrared to sub-mm do not always allow various geometries to be unambiguously determined once viewing angle is taken into account.

In practice, some model fits can be rejected based on statistical arguments. For example, in a star-forming cluster, observing a source with an edge-on disk has a low probability both because one is less likely to observe a disk with an edge-on inclination, and because such a source would be much fainter. As discussed further in this section, the edge-on disk models that fit the observed SEDs well require the luminosity of the central star to be larger than $100 L_{\odot}$, which is unrealistic, as in this case one would expect to observe many more non edge-on sources with such luminosities.

In most cases, the inclination of the line of sight is not well determined. The only constraints found are that none of the disk-only sources are seen exactly edge-on (87° in Table 1), and that CoKu Tau/1 cannot be fit by any non edge-on models, as discussed previously.

Stellar Temperature: In Table 4.2 and in Figure 4.2, the temperatures derived from SED fitting are compared to those corresponding to the spectral types listed in Kenyon & Hartmann (1995). The latter were determined from spectroscopic observations, and therefore provide an independent and more accurate measure of the temperature. For all sources but one, the best-fit value is close to the known value. The exception to this is UY Aur, but the *range* of temperatures for this source (3540 → 8090 K) is consistent with the literature value (4060 K).

AB Aur is the only source in this sample that is known to have a high temperature ($\sim 10,500$ K), and it is also the source for which the best-fit model has the highest temperature (11,767 K). Overall, the temperatures of the sources are correctly identified to better than

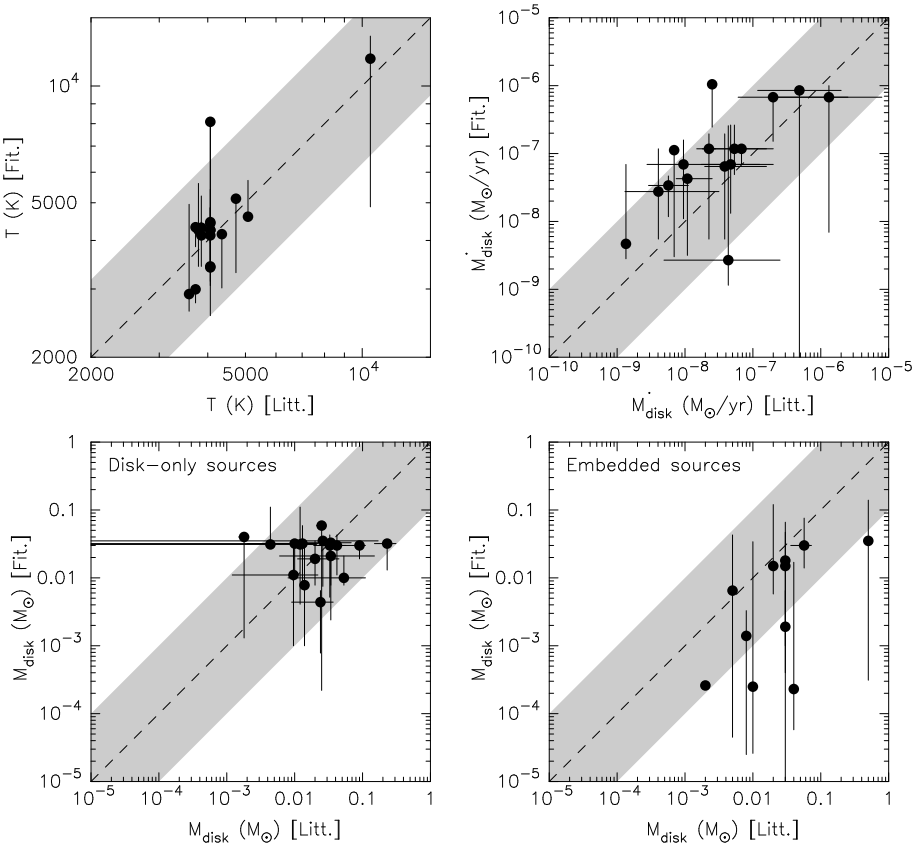

Figure 4.2: Comparison of the values of stellar temperature (*top left*), disk accretion rate (*top right*), and disk mass (*bottom left and right*) found from SED fitting with values quoted in the literature and derived from different methods. The dashed line shows where the values would be equal, and the grey area shows where the agreement is better than ±0.2 orders of magnitude for the temperature, and ±1 order of magnitude for the disk mass and accretion rate. Error bars in the y-direction indicate the range of values of the models shown in Figure 4.1. Error bars in the x-direction show the range between the lowest value and the highest value quoted in the literature. For the stellar temperature, only one reference (Kenyon & Hartmann, 1995) was used, and therefore no uncertainties are shown on the x-axis. The likely uncertainty quoted by the authors is ±1 spectral class, corresponding roughly to ±100K.

±0.2 orders of magnitude.

Disk Mass: The disk masses derived from SED fitting are compared to values listed in Dutrey et al. (1996), Kitamura et al. (2002), and Andrews & Williams (2005). These values were determined from sub-mm and mm observations. In Table 4.3, the various literature values are listed, including an average value, a minimum value defined to be the smallest value of $M_{\rm disk} - \sigma(M_{\rm disk})$ quoted, and a maximum value defined to be the largest value of $M_{\rm disk} + \sigma(M_{\rm disk})$ quoted. This range is compared to the range found from SED fitting (this is also shown graphically in Figure 4.2). The disk masses for the models assume a gas-to-dust ratio of 100. As can be seen from Figure 4.2, for the very young sources (marked 'Embedded' in

Table 4.2: Comparison of values of the central source temperatures from the literature with those found from SED fitting.

		SED Fitting values		
Source Name	$T_{\rm star}$	$T_{\rm min}$	$T_{\rm best}$	$T_{\rm max}$
AA Tau	4060	3060	4458	4859
AB Aur	10500	4881	11767	13452
BP Tau	4060	3138	3427	5415
CI Tau	4060	3486	4255	4859
CoKu Tau 1	···	4826	4826	4826
CY Tau	3720	3855	4329	4329
DG Tau	4350→5080	4314	4549	10722
DG Tau B	···	2580	2706	13618
DL Tau	4060	4255	4255	4458
DM Tau	3720	2762	2993	3045
DN Tau	3850	3427	4314	4458
DO Tau	3850	4123	4123	5209
DR Tau	4060	3935	4123	8061
FT Tau	···	2783	3060	5013
GG Tau	4060	3320	4430	4859
GM Aur	4730	3303	5126	5126
HL Tau	4060	2561	3409	4030
IQ Tau	3785	3427	4255	5612
IRAS 04016+2610	···	2552	2847	13587
IRAS 04169+2702	···	2585	2718	4152
IRAS 04248+2612	3580	2627	2909	4956
IRAS 04302+2247	···	2762	2986	3241
IRAS 04325+2402	···	2586	2741	3616
IRAS 04361+2547	···	2585	3225	4064
IRAS 04365+2535	···	2637	2847	4228
IRAS 04368+2557	···	2932	3855	3869
L1551 IRS5	4060→6030	3070	3651	4900
LkCa 15	4350	3017	4150	4204
RY Tau	5080	4604	4604	5713
UY Aur	4060	3540	8090	8090

Notes — All temperatures are in K.

References — All literature spectral types were taken from Kenyon & Hartmann (1995), except that for DG Tau, which is from White & Hillenbrand (2004). Table A5 in Kenyon & Hartmann (1995) is used to convert the spectral types to temperatures.

Table 4.1) the disk masses are not well constrained. For example IRAS 04361+2547 could, on the basis of the SED, have a disk mass between $2.5 \times 10^{-5}\,M_{\odot}$ and $3.2 \times 10^{-2}\,M_{\odot}$. This is because, in the early stages of evolution, when the disk is deeply embedded inside the infalling envelope, the relative contributions of the disk and envelope to the SED are difficult to disentangle. For disk-only sources (marked 'Disk' in Table 4.1), the fitted masses generally agree with the literature values to within less than an order of magnitude. This is fairly accurate considering that the disk masses in the entire set of models range over nine orders of magnitude, and that literature values often rely on assuming that the emission arises from optically thin isothermal regions of the disk (e.g. Eq. [2.4]). Furthermore, the choice of a dust opacity law will also affect the disk mass obtained.

Table 4.3: Comparison of values of the disk mass from the literature with those found from SED fitting.

	Literature values						SED Fitting values		
Source Name	D96	K02	A05	Mean	Min	Max	Min	Best	Max
AA Tau	−1.8	−1.6 ± 0.3	−1.9 ± 0.1	−1.7	−2.0	−1.3	−2.1	−1.7	−1.5
AB Aur	···	···	−2.4 ± 0.1	−2.4	−2.4	−2.3	−1.5	−1.5	−1.0
BP Tau	−2.9	···	−1.8 ± 0.1	−2.0	−2.9	−1.7	−3.0	−1.9	−1.4
CI Tau	−1.2	···	−1.6 ± 0.1	−1.4	−1.7	−1.2	−2.0	−1.5	−1.4
CoKu Tau 1	···	···	∼ −2.7	−2.7	−2.7	−2.7	−3.6	−3.6	−3.6
CY Tau	−1.8	−1.3 ± 0.4	∼ −2.2	−1.5	−2.2	−0.8	−2.1	−1.7	−1.7
DG Tau	−1.6	···	−1.6 ± 0.1	−1.6	−1.7	−1.6	−3.7	−1.2	−1.2
DG Tau B	···	···	···	···	···	···	−3.7	−2.6	−1.1
DL Tau	···	···	−1.1 ± 0.1	−1.0	−1.2	−1.0	−1.7	−1.5	−1.5
DM Tau	−1.6	−1.7 ± 0.3	−1.6 ± 0.1	−1.6	−2.0	−1.4	−3.1	−2.4	−2.2
DN Tau	−1.6	−9.0 ± 2.5	−1.5 ± 0.1	−1.6	···	−0.8	−2.1	−1.5	−1.5
DO Tau	−1.7	−2.7 ± 0.5	−2.2 ± 0.1	−2.0	···	−1.7	−1.9	−1.5	−1.5
DR Tau	···	−2.3 ± 0.3	−1.7 ± 0.1	−1.9	−2.7	−1.7	−2.0	−1.5	−1.2
FT Tau	−1.9	···	−1.9 ± 0.1	−1.9	−1.9	−1.8	−3.0	−2.1	−1.5
GG Tau	···	···	−0.7 ± 0.2	−0.6	−0.8	−0.5	−1.9	−1.5	−1.5
GM Aur	−1.4	−1.5 ± 0.3	−1.6 ± 0.1	−1.5	−1.9	−1.2	−2.6	−1.5	−1.4
HL Tau	···	−1.3 ± 0.1	−1.2 ± 0.1	−1.2	−1.4	−1.1	−1.9	−1.5	−1.1
IQ Tau	···	−1.4 ± 0.2	−1.7 ± 0.1	−1.5	−1.7	−1.2	−2.3	−1.5	−1.4
IRAS 04016+2610	···	···	∼ −1.7	−1.7	−1.7	−1.7	−2.2	−1.8	−0.9
IRAS 04169+2702	···	···	∼ −1.5	−1.5	−1.5	−1.5	−3.0	−1.8	−1.3
IRAS 04248+2612	···	···	∼ −2.3	−2.3	−2.3	−2.3	−4.3	−2.2	−1.4
IRAS 04302+2247	···	···	∼ −1.5	−1.5	−1.5	−1.5	−5.5	−2.7	−2.2
IRAS 04325+2402	···	···	∼ −2.1	−2.1	−2.1	−2.1	−4.6	−2.8	−2.5
IRAS 04361+2547	···	···	∼ −2.0	−2.0	−2.0	−2.0	−4.6	−3.6	−1.5
IRAS 04365+2535	···	···	∼ −1.5	−1.5	−1.5	−1.5	−3.4	−1.8	−1.2
IRAS 04368+2557	···	···	∼ −1.4	−1.4	−1.4	−1.4	−4.2	−3.6	−1.8
L1551 IRS5	···	···	∼ −0.3	−0.3	−0.3	−0.3	−3.5	−1.5	−0.9
LkCa 15	···	−1.4 ± 0.4	−1.3 ± 0.1	−1.3	−2.1	−1.0	−2.1	−2.0	−1.7
RY Tau	···	−3.4 ± 1.0	−1.8 ± 0.1	−1.9	···	−1.7	−2.4	−1.5	−1.0
UY Aur	···	···	−2.8 ± 0.1	−2.7	−2.8	−2.7	−2.9	−1.4	−1.4

Notes — All disk masses are in $\log[M_\odot]$.

References — D96: Dutrey et al. (1996), K02: Kitamura et al. (2002), A05: Andrews & Williams (2005).

Disk Accretion Rates: In Table 4.4 and in Figure 4.2 the disk accretion rates derived from SED fitting are compared to values listed in Valenti et al. (1993), Hartigan et al. (1995), Hartmann et al. (1998), and Mohanty et al. (2005). Most of these literature values were derived from UV and optical spectroscopy, by modelling Hα line profiles or measuring the amount of blue veiling (c.f. §1.2.2), and therefore represent an independent and more direct and accurate estimate of the disk accretion rate than SED fitting. The agreement between values derived from SED fitting and literature values is reasonable over the three orders of magnitude spanned.

The values obtained from SED fitting appear to be slightly larger than those taken from the literature. This could be due to a small inconsistency in the models where the accretion luminosity inside the dust destruction radius but outside the magnetic truncation radius is, for simplicity, being emitted as stellar photons, with a resulting stellar spectrum. Thus, to match

Table 4.4: Comparison of values of the disk accretion rate from the literature with those found from SED fitting.

	Literature values							SED Fitting values		
Source Name	V93	H95	H98	M05	Mean	Min	Max	Min	Best	Max
AA Tau	−8.15	−6.90	−8.48	−8.56	−8.02	−8.56	−6.90	−7.96	−7.16	−6.8
AB Aur	···	···	···	···	···	···	···	−7.13	−6.92	−5.88
BP Tau	−7.61	−6.80	−7.54	−7.71	−7.42	−7.71	−6.80	−8.26	−7.19	−6.71
CI Tau	−7.83	−6.80	−7.19	···	−7.27	−7.83	−6.80	−7.31	−6.93	−6.58
CoKu Tau 1	···	···	···	···	···	···	···	−10.08	−10.08	−10.08
CY Tau	···	−8.20	−8.12	−8.16	−8.16	−8.20	−8.12	−8.52	−6.95	−6.95
DG Tau	···	−5.70	···	−6.93	−6.32	−6.93	−5.70	−11.2	−6.07	−6.07
DG Tau B	···	···	···	···	···	···	···	−9.98	−6.98	−5.64
DL Tau	−7.63	−6.70	···	···	−7.17	−7.63	−6.70	−7.16	−6.93	−6.93
DM Tau	−8.54	···	−7.95	···	−8.24	−8.54	−7.95	−7.93	−7.47	−7.33
DN Tau	−8.89	−7.50	−8.46	−8.72	−8.39	−8.89	−7.50	−8.26	−7.56	−6.93
DO Tau	−7.22	−5.60	−6.84	−7.15	−6.70	−7.22	−5.60	−6.82	−6.17	−6.17
DR Tau	···	−5.10	···	−6.66	−5.88	−6.66	−5.10	−8.16	−6.17	−6
FT Tau	···	···	···	···	···	···	···	−8.56	−7.29	−6.79
GG Tau	−7.52	−6.70	−7.76	···	−7.33	−7.76	−6.70	−7.88	−7.16	−6.58
GM Aur	−8.13	−7.60	−8.02	−8.11	−7.97	−8.13	−7.60	−8.5	−7.37	−7.37
HL Tau	···	···	···	···	···	···	···	−6.53	−5.99	−5.29
IQ Tau	−7.74	···	−7.55	···	−7.65	−7.74	−7.55	−8.26	−6.93	−6.71
IRAS 04016+2610	···	···	···	···	···	···	···	−7.22	−6.26	−5.41
IRAS 04169+2702	···	···	···	···	···	···	···	−7.76	−6.73	−6.12
IRAS 04248+2612	···	···	···	···	···	···	···	−10.41	−7.57	−6.89
IRAS 04302+2247	···	···	···	···	···	···	···	−11.2	−9.3	−7.33
IRAS 04325+2402	···	···	···	···	···	···	···	−11.1	−8.88	−7.28
IRAS 04361+2547	···	···	···	···	···	···	···	−11.97	−8.56	−5.55
IRAS 04365+2535	···	···	···	···	···	···	···	−8.6	−6.26	−5.68
IRAS 04368+2557	···	···	···	···	···	···	···	−11.01	−11.01	−7.3
L1551 IRS5	···	···	···	···	···	···	···	−9.29	−5.34	−4.93
LkCa 15	···	···	−8.87	···	−8.87	−8.87	−8.87	−8.55	−8.33	−7.16
RY Tau	···	−7.60	···	···	−7.60	−7.60	−7.60	−6.61	−5.98	−5.92
UY Aur	−8.31	−6.60	−7.18	···	−7.36	−8.31	−6.60	−8.94	−8.57	−6.59

Notes — All disk accretion rates are in $\log[M_\odot/\mathrm{yr}]$.

References — V93: Valenti et al. (1993), H95: Hartigan et al. (1995), H98: Hartmann et al. (1998), M05: Mohanty et al. (2005).

a given near-infrared excess, a slightly higher accretion rate is required. For example, RY Tau is the source for which the model estimate deviates the most from literature values; Akeson et al. (2005) found that for this source, the accretion luminosity from the gas disk inside the dust destruction radius contributed significantly to the total disk accretion luminosity.

Disk/Envelope Inner Radius: All the sources in the sample can be fit by disks and envelopes with no inner holes ($R_{\rm disk}^{\rm min} = R_{\rm sub}$ where $R_{\rm sub}$ is defined in Eq. [3.7]), with the exception of DM Tau, GM Aur, IRAS 04302+2247, and IRAS 04325+2402 (see Table 4.5). As described in Chapter 3, the inner radius is the same for the disk and the envelope. For most sources, the upper limit to the disk inner radius is larger than $R_{\rm sub}$, and it is generally not possible to rule out the existence of holes in any of the sources. However, in the case of DM Tau, GM Aur, IRAS 04302+2247, and IRAS 04325+2402, the lower limit being larger than $R_{\rm sub}$ *does* rule

Table 4.5: Range of parameter values providing a good fit from SED fitting for additional disk parameters.

Source Name	$R_{\rm disk}^{\rm min}$ Min ($R_{\rm sub}$)	$R_{\rm disk}^{\rm min}$ Max ($R_{\rm sub}$)	$R_{\rm disk}^{\rm min}$ Min (AU)	$R_{\rm disk}^{\rm min}$ Max (AU)	$R_{\rm disk}^{\rm max}$ Min (AU)	$R_{\rm disk}^{\rm max}$ Max (AU)	h(100 AU) Min (AU)	h(100 AU) Max (AU)
AA Tau	1.0	6.4	0.04	0.51	62.1	168.9	2.33	6.67
AB Aur	1.0	2.7	0.48	1.19	83.1	170.7	2.90	7.28
BP Tau	1.0	6.4	0.05	0.51	19.3	585.8	1.17	9.26
CI Tau	1.0	6.8	0.08	0.62	77.8	198.7	1.17	5.51
CoKu Tau 1	1.0	1.0	0.23	0.23	76.7	76.7	5.02	5.02
CY Tau	1.0	1.0	0.04	0.11	97.5	198.7	1.17	3.79
DG Tau	1.0	6.1	0.21	2.50	78.8	2540.7	2.69	6.81
DG Tau B	1.0	9.5	0.07	6.25	2.3	893.7	2.76	10.37
DL Tau	1.0	1.0	0.10	0.11	101.3	198.7	1.17	3.16
DM Tau	130.2	455.1	3.37	19.68	50.4	178.3	3.53	11.64
DN Tau	1.0	6.4	0.06	0.51	49.6	163.1	2.33	5.77
DO Tau	1.0	1.5	0.16	0.26	103.7	190.6	2.42	2.91
DR Tau	1.0	5.8	0.21	1.39	72.4	158.5	2.26	7.61
FT Tau	1.0	12.1	0.04	1.01	24.8	489.3	1.17	17.42
GG Tau	1.0	6.8	0.06	0.62	55.0	133.0	3.14	12.47
GM Aur	12.1	265.8	1.01	23.93	69.3	352.2	2.30	5.84
HL Tau	1.0	2.9	0.17	0.43	2.2	39.0	4.80	19.30
IQ Tau	1.0	6.4	0.07	0.51	49.6	415.8	1.17	5.77
IRAS 04016+2610	1.0	2.9	0.09	2.46	2.2	3651.1	3.35	30.16
IRAS 04169+2702	1.0	3.9	0.07	0.42	3.6	150.7	5.28	27.90
IRAS 04248+2612	1.0	48.9	0.03	2.20	27.0	211.5	2.74	13.97
IRAS 04302+2247	77.9	1700.5	3.25	58.85	36.2	1215.0	3.31	10.12
IRAS 04325+2402	95.6	497.5	4.29	21.55	22.8	393.5	3.69	14.99
IRAS 04361+2547	1.0	11.3	0.07	1.63	2.2	1296.0	3.43	24.36
IRAS 04365+2535	1.0	9.3	0.09	1.60	2.7	176.7	5.11	15.54
IRAS 04368+2557	1.0	2.5	0.05	0.24	33.8	1303.3	3.18	9.67
L1551 IRS5	1.0	30.0	0.17	12.10	1.2	731.2	2.81	21.12
LkCa 15	1.0	2.7	0.04	0.12	62.1	195.5	4.42	9.84
RY Tau	1.0	4.7	0.29	1.38	37.9	124.1	1.92	5.76
UY Aur	1.0	10.1	0.27	1.94	51.5	1159.7	3.47	10.44

out disks or envelopes with *no* inner holes. GM Aur has previously been found to require an inner hole of order ~ 4 AU in order to explain its SED (Rice et al., 2003). More recently, *Spitzer* IRS spectroscopy has confirmed that both GM Aur and DM Tau show a near-infrared deficit, suggesting inner hole sizes of 24 AU and 3 AU respectively (Calvet et al., 2005). Here, the SED of GM Aur is well fit by models having an inner hole size between ~ 1 and 24 AU, and DM Tau with models having an inner hole size between ~ 3.4 and 20 AU: these values are consistent with the values found by Calvet et al..

The above comparisons show that in most cases, the parameters of the best fit model agree well with previously published values. Even in cases where the best-fit parameters does not agree with the published values, the *range* of parameter values providing a good fit is consistent with previously published values.

In addition to the parameters presented above, the ranges of values providing a good

Table 4.6: Range of parameter values providing a good fit from SED fitting for the stellar mass and total bolometric luminosity.

Source Name	$M_\star$ Min ($M_\odot$)	$M_\star$ Max ($M_\odot$)	$L_{\rm bol}$ Min ($L_\odot$)	$L_{\rm bol}$ Max ($L_\odot$)
AA Tau	0.20	1.74	0.44	3.32
AB Aur	2.57	3.62	42.64	181.47
BP Tau	0.22	1.74	0.59	4.48
CI Tau	0.35	1.78	1.60	5.12
CoKu Tau 1	2.68	2.68	11.44	11.44
CY Tau	0.57	1.08	0.40	3.01
DG Tau	1.10	3.07	9.63	42.02
DG Tau B	0.11	3.70	0.67	249.65
DL Tau	0.99	1.29	2.53	3.01
DM Tau	0.10	0.20	0.16	0.44
DN Tau	0.33	1.29	0.82	2.70
DO Tau	0.80	1.49	5.40	7.59
DR Tau	0.63	2.13	7.53	14.36
FT Tau	0.11	2.03	0.36	7.01
GG Tau	0.28	1.63	0.82	3.01
GM Aur	0.28	1.62	0.65	3.16
HL Tau	0.10	0.91	3.46	15.05
IQ Tau	0.33	1.94	1.04	5.16
IRAS 04016+2610	0.10	3.73	2.00	249.21
IRAS 04169+2702	0.11	0.90	0.73	5.87
IRAS 04248+2612	0.10	2.84	0.27	11.30
IRAS 04302+2247	0.10	0.25	0.15	0.67
IRAS 04325+2402	0.10	0.41	0.46	1.54
IRAS 04361+2547	0.11	0.85	1.20	9.37
IRAS 04365+2535	0.11	1.25	2.00	14.43
IRAS 04368+2557	0.15	0.59	0.64	3.84
L1551 IRS5	0.21	4.70	6.88	72.40
LkCa 15	0.18	0.91	0.42	1.39
RY Tau	1.64	3.34	18.75	40.65
UY Aur	0.37	2.04	2.11	14.22

fit for the stellar mass, bolometric luminosity, disk outer radius, and disk scaleheight h at 100 AU are presented in Tables 4.5 and 4.6. The disk outer radii are generally fairly uncertain, and range from tens to hundreds of AU. The stellar masses are likely to be constrained because temperatures are well determined, and the stellar temperatures are related to the stellar masses through evolutionary tracks (c.f. Chapter 3). No literature values are available for the disk scale-heights. However the derived values should be consistent with the true values: as shown in Chapter 3, the disk flaring power does have an effect on the SED, meaning that the SEDs should be somewhat sensitive to the disk scale-height. The values are poorly constrained for embedded sources, where the disk does not contribute significantly to the SED, as expected. Finally, the main uncertainty in the bolometric luminosity is due to uncertainties in the viewing angle. For example the sources for which the luminosity is very poorly constrained (from a few $L_\odot$ to over $100 L_\odot$), such as DG Tau B or IRAS 04016+2610, are those for which both edge-on disks and young protostars with infalling envelopes provide

a good fit. These two possibilities would result in two very different bolometric luminosities. If the inclination can be constrained, then the true bolometric luminosity of the sources can be accurately determined from SED modelling.

4.3.3 Parameter constraints versus wavelength coverage

As mentioned in §4.1, when fitting model SEDs to multi-wavelength observations of a source, it is important to have a grasp not only of which set of parameters provides a good fit, but also whether it is the *only* set of parameters that does so. For example, a source may be well fit by a model with a $1\,M_{\odot}$ central source and a 300 AU disk with a mass of $M_{\rm disk} = 0.01\,M_{\odot}$ disk, but it may be that the radius of the disk does not actually have an effect on the SED at the wavelengths of the available data, and that any disk radius would provide a suitable fit. Furthermore, two completely different sets of parameters may fit data equally well (e.g. the sources from §4.3.2 that can be fit by SED models of young protostellar objects or older edge-on disks).

The aim of the approach presented in this chapter is not to *determine* all of the parameter values, but to find *how well constrained* each parameter is. This section presents an analysis which shows how the YSO model SED fitting tool can be used to analyse how well various parameters are constrained when using different combinations of data points. In addition, examples of degeneracies that can arise in parameter space are shown.

The first example shown is AA Tau, which is a known T-Tauri source with optical variability. Figure 4.3 shows the model SED fits to the data, and a selection of parameters for these fits (disk mass and accretion rate, envelope accretion rate, and stellar temperature). For each combination of data points, all models with $\chi^2 - \chi^2_{\rm min} < 3$ are shown, as in §4.3.2. As before, a distance range of 120 → 160pc is assumed. The SED is first fit using only IRAC points, with 11,674 model SEDs satisfying the goodness of fit criterion ($\sim$ 5% of all model SEDs). The disk mass, disk accretion rate and envelope accretion rate are not at all constrained apart from very high values of the temperature being ruled out (this is because models with very high temperatures would be too luminous to explain the IRAC fluxes). This suggests that using IRAC fluxes alone does not necessarily provide a good estimate of the evolutionary stage of an object. Adding JHK data reduces the number of good fits to 2,826 model SEDs, but does not provide any significant improvement in the determination of the four parameters shown here. Adding IRAS 12 μm, MIPS 24 μm and MIPS 70 μm does have an important

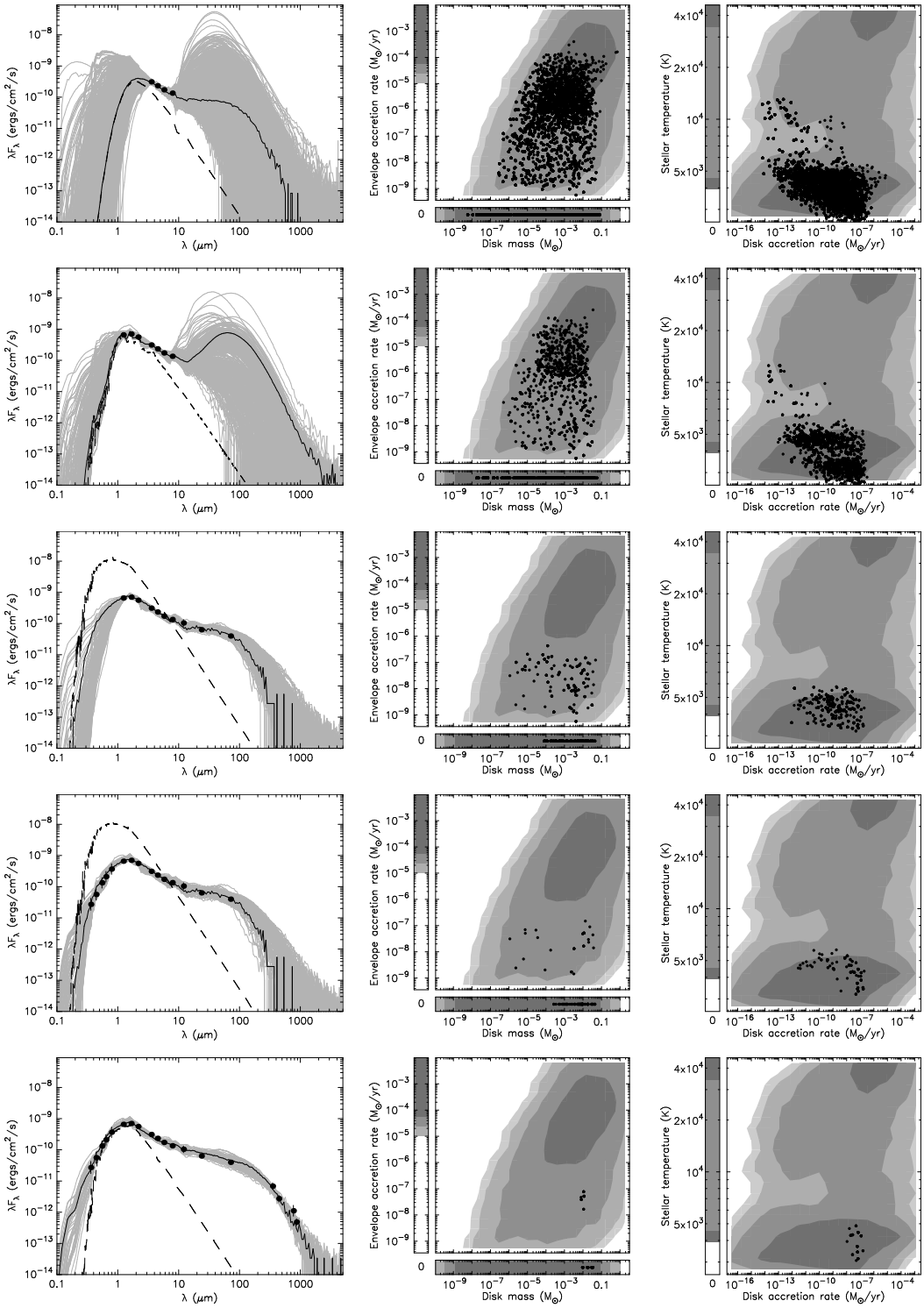

Figure 4.3: *Left* – model SED fits to the observed SED of AA Tau using from top to bottom: IRAC points only, JHK + IRAC points, JHK + IRAC + MIPS 24 μm + MIPS 70 μm, UBVRI + JHK + IRAC + MIPS 24 μm + MIPS 70 μm, and UBVRI + JHK + IRAC + MIPS 24 μm + MIPS 70 μm + sub-mm points (when more than 200 model SEDs fit the data well, the 200 best fit SEDs are shown, and one in ten SEDs beyond this). *Centre and Right* – a selection of parameters for the model fits. Filled circles are the good fits shown in the SED plots. The greyscale shows the parameter space of the grid of models (smoothed). Each shade of grey shows an increase in a factor of 10 in the density of models.

effect which is to provide a much more strict upper limit on the envelope accretion rate ($\sim 10^{-7}\,M_\odot\,\mathrm{yr}^{-1}$), and also provides a lower limit on the disk mass of $10^{-6}\,M_\odot$. Furthermore, the disk accretion rate and the central source temperature are better determined. This echoes the findings presented in Chapter 3 that data beyond $\sim 20\,\mu$m are very helpful in constraining the evolutionary stage of a source. Adding the optical data rules out models that have both low central source temperatures and low disk accretion rates, leaving a degeneracy between the optical data being explained by a higher temperature or a higher disk accretion rate. Finally, adding the sub-mm data has the predictable effect of providing a strong constraint on the disk mass, placing it at $\sim 10^{-2}\,M_\odot$. The degeneracy between central source temperature and disk accretion rate is resolved, and the disk accretion rate is estimated at $\sim 10^{-8} - 10^{-7}\,M_\odot\,\mathrm{yr}^{-1}$.

The second example is IRAS 04361+2547, which is a known protostar surrounded by an infalling envelope and with molecular outflows, as shown by spatially resolved observations (e.g. Terebey et al., 1990; Tamura et al., 1991). Figure 4.4 shows the model SED fits to the data, and a selection of parameters for these fits (disk mass, envelope accretion rate, and stellar mass and temperature). As for AA Tau, all models with $\chi^2 - \chi^2_{\mathrm{min}} < 3$ are shown. The SED is first fit using only IRAC points, with 1,959 model SEDs satisfy the goodness of fit criterion. As before, the disk mass and envelope accretion rate are not at all constrained. Stellar mass and temperature are also very poorly constrained. Adding JHK data reduces the number of good fits to 183, and does provide an improvement in the determination of the envelope accretion rate. However, there is a bimodal distribution of models in $(\dot{M}_{\mathrm{env}}, M_{\mathrm{disk}})$, with one peak centred at fairly high accretion rates ($\sim 10^{-5}\,M_\odot\,\mathrm{yr}^{-1}$), and one centred at zero accretion rates (mostly edge-on disk-only models). A bimodal distribution is also seen in $(T_\star, M_\star)$. The models with high temperatures correspond to the edge-on disk-only models, which require on average a larger central source luminosity to match the observed fluxes, while the models with lower temperatures correspond to the young models with large envelope infall rates. This is a good example of a young protostar/edge-on disk degeneracy. The addition of IRAS 12 μm and IRAS 25 μm reduces the number of edge-on disk models that fit well, but does not rule them out. Adding IRAS 60 μm and IRAS 100 μm rules out all edge-on disk models, and in the process rules out all models with $M_\star > 1\,M_\odot$. Finally, adding the sub-mm data further constrains the parameters, albeit not much. By this stage, the SED fit is fairly well constrained. The envelope accretion rate is constrained to within an order of magnitude, the disk mass is determined to within three orders of magnitude, the temperature

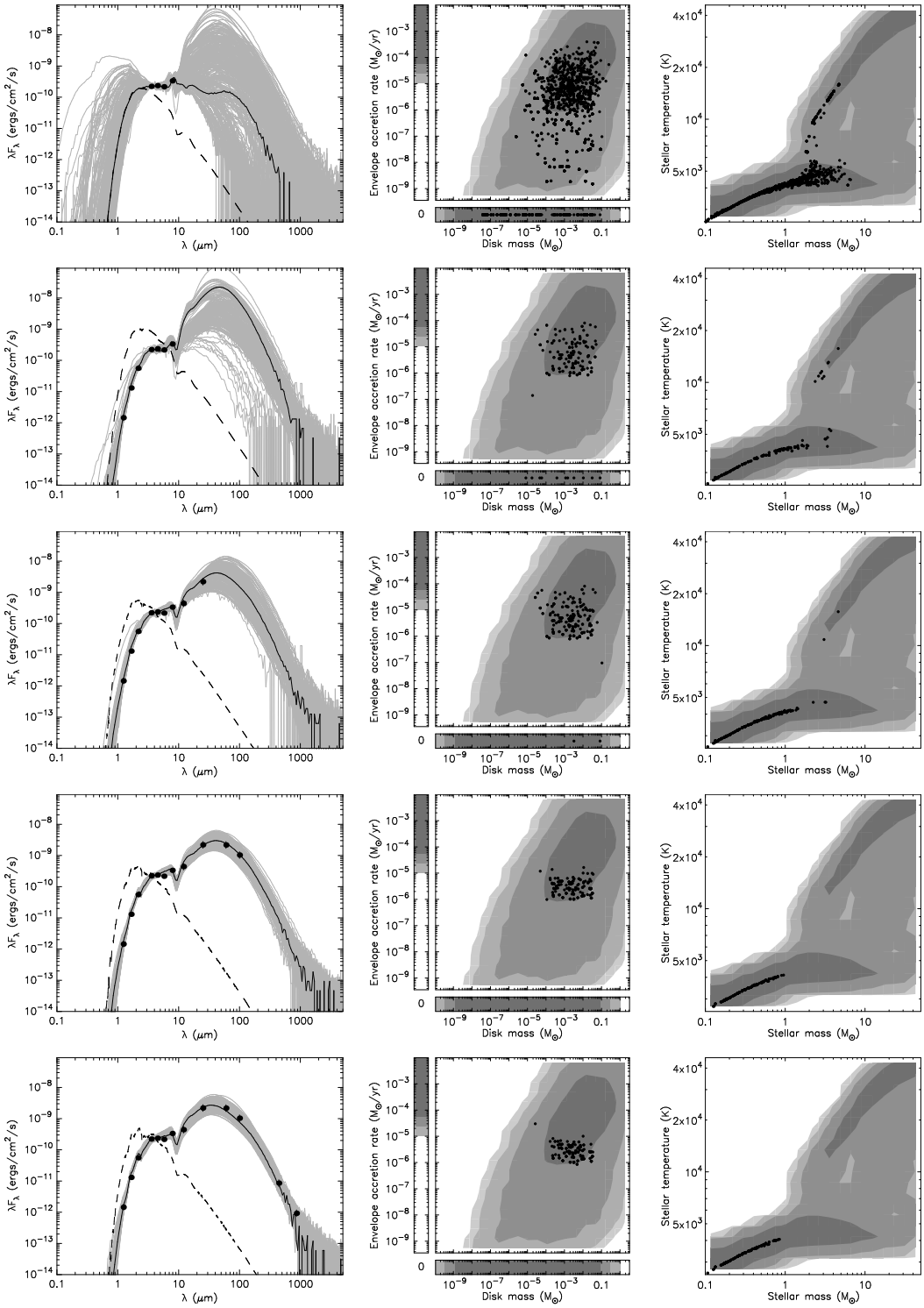

Figure 4.4: *Left* – model SED fits to the observed SED of IRAS 04361+2547 using from top to bottom: IRAC points only, JHK + IRAC points, JHK + IRAC + IRAS 12 & 25 μm, JHK + IRAC + All IRAS bands, and JHK + IRAC + All IRAS bands + sub-mm points (when more than 200 model SEDs fit the data well, the 200 best fit SEDs are shown, and one in ten SEDs beyond this). *Centre and Right* – a selection of parameters for the model fits. Filled circles are the good fits shown in the SED plots. The greyscale shows the parameter space of the grid of models as in Figure 4.3. The alignment of all the fits along a curve in the $T_\star$ vs $M_\star$ plots (right) is due to the sampling of the models using evolutionary tracks, i.e. for a given $M_\star$ and $t_\star$, $T_\star$ is obtained using evolutionary tracks (c.f. Chapter 3).

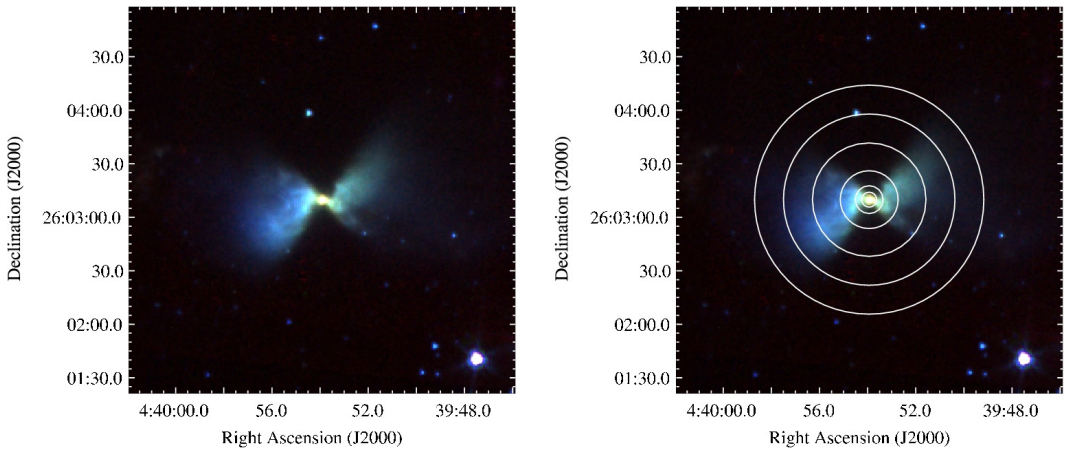

Figure 4.5: *Left* – Three colour image of IRAS 04368+2557 using IRAC 3.6 μm (blue – 0 to 3 MJy/sr), IRAC 4.5 μm (green – 0 to 6 MJy/sr), and IRAC 8.0 μm (red – 0 to 12 MJy/sr). *Right* – The same image with the six photometry apertures over-plotted (4″, 8″, 16″, 32″, 48″, and 64″).

is determined to be no more than 4,000 K, and the stellar mass is determined to be no more than 1 $M_{\odot}$.

4.3.4 Analysis of resolved sources

As mentioned in §4.2, when analysing the SED of a resolved object, it is possible to specify apertures smaller than the apparent extent of the source. In this section, this is demonstrated by modelling IRAS 04368+2557 using solely IRAC photometry in different circular apertures.

In order to model IRAS 04368+2557, the total fluxes in the four IRAC bands were measured in six different apertures: 4″, 8″, 16″, 32″, 48″, and 64″. A composite colour image of the source is shown in Figure 4.5, along with the position of the six apertures. A distance range of 120 → 160 pc to the object was assumed, as well as an A_V range of 0 to 20 mag. No further constraints such as an inclination of the object to the line of sight, nor the cavity size, were applied, as the aim was to find out whether the fitting tool can determine such parameters solely from the SED.

The left plots in Figure 4.6 show the fluxes for the six apertures along with the best fitting aperture-dependent model SED. Also shown are the near-infrared, far-infrared, and sub-mm data points, but these are initially not used in the fitting process. Using the parameters of the best fit, a model image was computed by rerunning this model with a higher number of 'photons' to achieve a higher signal-to-noise. The model image is shown in Figure 4.7. The model SED fitter correctly finds an SED that matches the data adequately in all apertures,

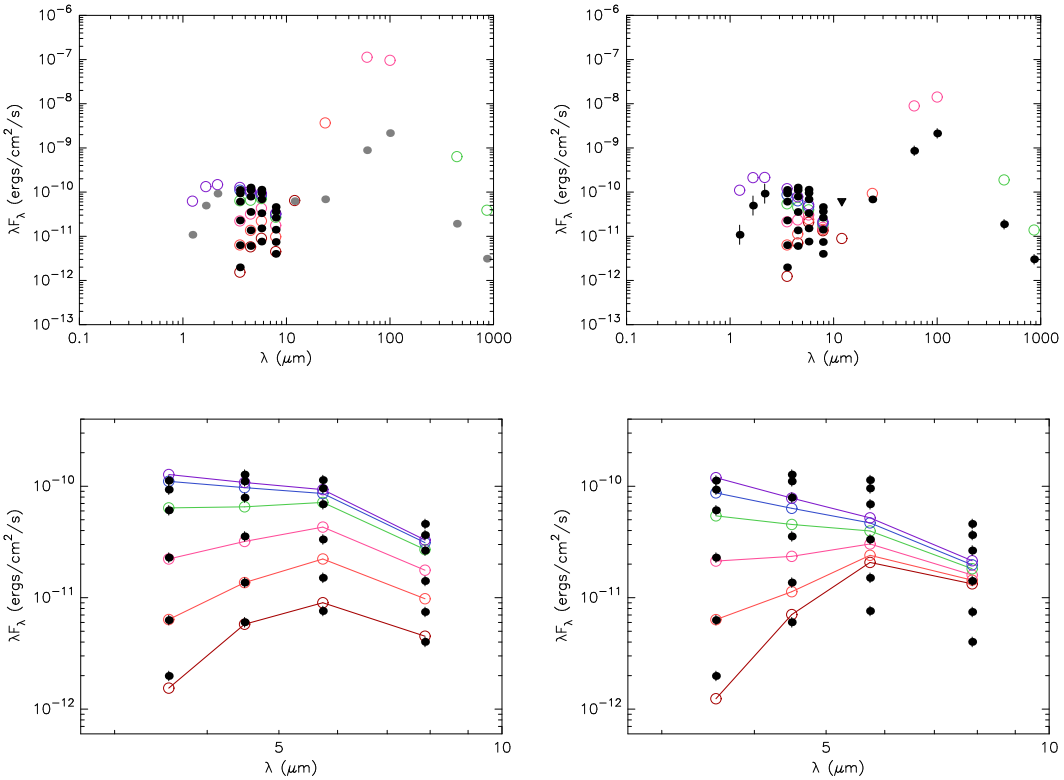

Figure 4.6: *Top left* – best-fit model to the IRAC data in the six apertures for IRAS 04368+2557 (only the IRAC data are used). The IRAC data points are shown as filled black circles. The other data points are shown as grey circles to indicate that these were not used in the fitting. The apertures assumed for these points are those listed in Table D.5 as before, i.e. 100″ for JHK, 10″ for MIPS 24 μm, 60″ for IRAS 12 & 25 μm, 120″ for IRAS 60 & 100 μm, and 30″ for the sub-mm data. For the IRAC data points, the fluxes in six apertures are shown (4″, 8″, 16″, 32″, 48″, and 64″), with the faintest fluxes corresponding to the smallest apertures, and the brightest fluxes corresponding to the largest apertures. The model SED in the different apertures is shown as open circles. The different colours correspond to the different apertures. *Top right* – best-fit model using the near-infrared, far-infrared, and sub-mm data in addition to the IRAC data in the six apertures. *Bottom* – as above, but showing only the IRAC wavelength range. The solid lines show the best-fit models in the different apertures.

determines the type of object (embedded protostar), the inclination to the line of sight (edge-on), and the colours of the object. The cavity angle is not a perfect match, but this is not surprising since only circularly averaged fluxes were used.

However, all the models that fit the resolved IRAC data well systematically overestimate fluxes at far-infrared wavelengths (as seen in the top left plot of Figure 4.6). The plots on the right of Figure 4.6 show that fitting the data at other wavelengths simultaneously deteriorates the fit at IRAC wavelengths. Furthermore, the models do not reproduce the peak in luminosity at the centre of the object (as seen in Figure 4.7). It has recently been found (Loinard et al., 2002) that the central source of IRAS 04368+2557 is a binary star with a projected separation of 25 AU, meaning that a large cavity can be expected at the centre of the infalling envelope.

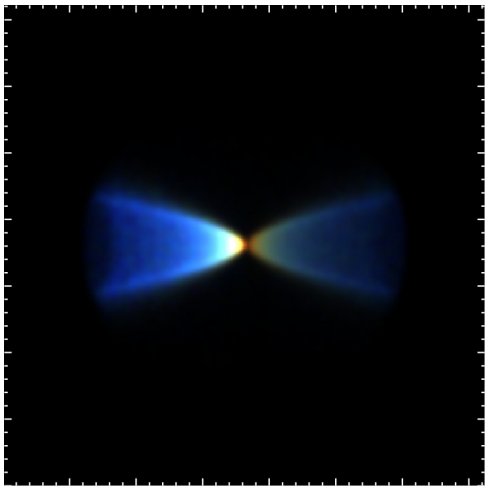

Figure 4.7: Image of the best-fit model to the IRAC data only for IRAS 04368+2557, shown in the same bands (IRAC 3.6, 4.5, and 8.0 μm) and with the same scaling as the image in Figure 4.5.

As mentioned previously, although the models include inner holes, these holes are completely evacuated, rather than having low levels of dust. A small but non-zero amount of dust inside an inner hole may be enough to provide the IRAC fluxes observed, while decreasing the amount of far-infrared flux. The parameters of the best-fitting models for the IRAC data only, and for the full SED, are listed in Table 4.7. As well as demonstrating SED fitting of resolved sources, this is an illustration of how detailed modelling of an individual source can be used to improve the models in future.

Since this work was carried out, Tobin et al. (2008) have suggested that both the SED and the IRAC images can be well reproduced by a model in which a 'double' bipolar cavity is present, with a large scale bipolar cavity corresponding to that seen in the IRAC images, and a smaller-scale cavity with a smaller opening angle in the inner hundred AU. The smaller opening angle of the 'inner' cavity intercepts more radiation, scattering more stellar light at mid-infrared wavelengths, and therefore increasing the amount of mid-infrared emission relative to the longer wavelengths, and producing a central peak of emission as seen in the IRAC images. Near-infrared HST or ground-based adaptive optics observations could verify whether this is indeed the case.

4.4 Summary and Conclusions

A method to fit observed YSO SEDs using a pre-computed set of models was presented. Although the values of 14 physical parameters were varied in the models from Chapter 3, the

Table 4.7: The main parameters for the best-fitting models to IRAS 04368+2557

Parameter	IRAC data only	Full SED
Stellar Mass	$4.07\,M_{\odot}$	$1.46\,M_{\odot}$
Stellar Radius	$21.57R_{\odot}$	$8.21R_{\odot}$
Stellar Temperature	4,360 K	4,260 K
Envelope accretion rate	$2.63\times10^{-4}\,M_{\odot}\,\mathrm{yr}^{-1}$	$1.37\times10^{-4}\,M_{\odot}\,\mathrm{yr}^{-1}$
Envelope outer radius	9,120 AU	16,200 AU
Cavity opening angle	16°	43°
Viewing angle	75°	81°
Bolometric Luminosity	$155L_{\odot}$	$20L_{\odot}$

Notes — These are the main parameters of the best-fit model SEDs to the SED of IRAS 04368+2557, first fitting only the IRAC data simultaneously in six apertures, then fitting the full SED including the multi-aperture IRAC data.

aim of this method is not to determine all of these parameters from fitting observed SEDs, but to determine *which* parameters can be constrained, if any, and if so, what range of values provide acceptable fits. Data from UBVRI to sub-mm wavelengths were compiled for 30 YSOs in the Taurus-Auriga star-forming region. The evolutionary stages, stellar temperatures, disk masses, and disk accretion rates derived from fitting the model SEDs to the data are in good agreement with independently determined values (for example from spectroscopy). In cases where the best fitting model is not in agreement with the literature value, the *range* of parameter values of the model SEDs that provide a good fit is in general still consistent with this value. An analysis was also presented to show how adding fluxes at various wavelengths helps constrain different parameters. For example it was found, as in Chapter 3, that data in the range $20-100\,\mu$m in addition to shorter wavelength data are very useful in constraining parameters such as the envelope accretion rate, and thus the evolutionary stage of a source. An online fitting tool making use of this method is available to the community [4]. In future, this method will be extended to fit spectra (e.g. *Spitzer* IRS data) and polarisation measurements simultaneously with the broadband SED, in order to place further constraints on the geometry and the chemistry of the circumstellar environment of YSOs.

5

Red Sources in the Galactic Mid-Plane

Adapted from *Robitaille et al., 2008, accepted for publication in AJ*

A highly reliable flux-limited census of 18,949 point sources in the Galactic mid-plane that have intrinsically red mid-infrared colours is presented. These sources were selected from the *Spitzer* GLIMPSE I and II surveys of 274 deg^2 of the Galactic mid-plane, and consist mostly of high- and intermediate-mass YSOs and AGB stars. The selection criteria were carefully chosen to minimise the effects of position-dependent sensitivity, saturation, and confusion. The distribution of sources on the sky and their location in IRAC and MIPS 24 μm colour-magnitude and colour-colour space are presented. Using this large sample, it is shown that YSOs and AGB stars can be mostly separated by simple colour-magnitude selection criteria into approximately $50-70$ % of YSOs and $30-50$ % of AGB stars. Planetary nebulae and background galaxies together represent at most $2-3$ % of all the red sources. 1,004 red sources in the GLIMPSE II region, mostly AGB stars with high mass-loss rates, show significant ($\geq$0.3 mag) variability at 4.5 and/or 8.0 μm. With over 11,000 likely YSOs and over 7,000 likely AGB stars, this is to date the largest uniform census of AGB stars and high- and intermediate mass YSOs in the Milky-Way Galaxy.

5.1 Introduction

The *Spitzer Space Telescope* has recently completed a number of surveys of the Galactic mid-plane using the IRAC (3.6, 4.5, 5.8, and 8.0 μm) and MIPS (24 and 70 μm) instruments. In the context of star formation, the GLIMPSE surveys – which to date includes GLIMPSE I, GLIMPSE II, and GLIMPSE 3D – and the MIPSGAL surveys – which include the MIPSGAL I and II surveys – have so far been used for studies of individual star formation regions (e.g. Whitney et al., 2004a; Indebetouw et al., 2007; Mercer et al., 2007; Shepherd et al., 2007; Povich et al., 2008). However, the full potential of these surveys is that they provide a uniform view of the Galactic mid-plane – not only do they cover large and well-studied star formation regions, but they also show the distributed star formation between these regions. Therefore, in addition to focusing on specific regions, a whole continuum of star formation environments can now be studied. When seen in this light, these observations have the potential to revolutionise our view of Galactic star formation.

As previously described in §2.3, these surveys are not the first of their kind at mid- and far-infrared wavelengths. Previous major surveys covering the Galactic plane include the IRAS all-sky survey in 1983 at 12, 25, 60, and 100 μm, the ISO Galactic plane survey (Omont et al., 2003) at 7 and 15 μm, and the MSX survey of the Galactic plane (Price et al., 2001) at 8.28, 12.13, 14.65, and 21.3 μm. However, the combination of coverage, sensitivity and resolution of the *Spitzer* observations is unprecedented: the FWHM of the PSF is 2″ at 8 μm, and 6″ at 24 μm, compared to the detector resolution of 18.3″ for MSX 8.28 and 21.3 μm and a FWHM of approximately 3-5′ for IRAS 12 and 25 μm. The point source sensitivity at 8 μm is 100 and 1,000 times better than MSX 8.28 μm and IRAS 12 μm respectively, and the sensitivity at 24 μm is also approximately 100 and 1,000 times more sensitive than MSX 21.3 μm and IRAS 25 μm respectively. At 7 μm, the sensitivity and resolution of the ISOGAL observations (9 mJy and 6″ respectively) approach those of the *Spitzer* GLIMPSE survey, but the coverage of the ISOGAL survey is only 6 % of that of the GLIMPSE and MIPSGAL surveys (16 deg^2 for ISOGAL versus 274 deg^2 for GLIMPSE).

These three previous surveys have been used to search for YSOs, which are brighter and redder at infrared wavelengths than field stars due to thermal emission from circumstellar dust. Wood & Churchwell (1989) selected 1,717 candidate embedded massive stars with UCHII regions from the IRAS data, 1,646 of which are associated with the Galactic plane; Felli

et al. (2002a) used the ISOGAL survey in conjunction with radio observations to compile a list of 715 YSO candidates; and the MSX survey was used to compile a Galaxy-wide sample of candidate massive YSOs which were followed up to eliminate contaminants via the Red MSX Source (RMS) survey (Hoare et al., 2004). However, the increased sensitivity of the recent *Spitzer* observations of the Galactic mid-plane will allow many intermediate mass YSOs and more distant massive YSOs to be seen.

This chapter describes the compilation of a red source catalogue which is photometrically very reliable, and is affected as little as possible by any biases due for example to position-dependent sensitivity or saturation limits. In addition to YSOs, a number of AGB stars, which are also red at mid-infrared wavelengths due to the dust that surrounds them, are present in the red source catalogue presented here. Because interstellar extinction is low at mid-infrared wavelengths, and because of the selection criteria used for this catalogue, these are amongst the reddest and most distant AGB stars in the Galaxy.

In future (c.f. §6.2), this catalogue will be used to study the distribution of star formation regions in the Galaxy, the environments in which stars form, and to estimate the present rate of star formation in the Galaxy. §5.2 describes the GLIMPSE observations that are used to compile the red source catalogue, the various issues that affect the completeness of the GLIMPSE Catalogs, and the complementary surveys that are used to construct SEDs from 1.25 to 24 μm. §5.3 describes the selection of the red sources from the GLIMPSE Catalogs, including the procedure used to increase the reliability and improve the uniformity of the selection across the Galaxy. In §5.4, the angular distribution and colours of the red sources are shown, red variable sources are identified, and the composition of the red source catalogue is studied. Finally, in §6.1, the main findings are summarised.

5.2 Observations

5.2.1 Description of the IRAC observations

In this chapter, observations taken with the *Spitzer* IRAC camera are used to select intrinsically red sources. The IRAC data used are from the GLIMPSE I survey (PI: Churchwell; PIDs 146, 186, 187, 188, 189, 190, 191, 192, and 195), the GLIMPSE II survey of the inner region of the Galactic plane (PI: Churchwell; PID 20201), and observations of the Galactic centre (PI: Stolovy; PID 3677). GLIMPSE I covers $10^\circ \leq |\ell| \leq 65^\circ$ and $|b| \leq 1^\circ$. GLIMPSE II fills in the

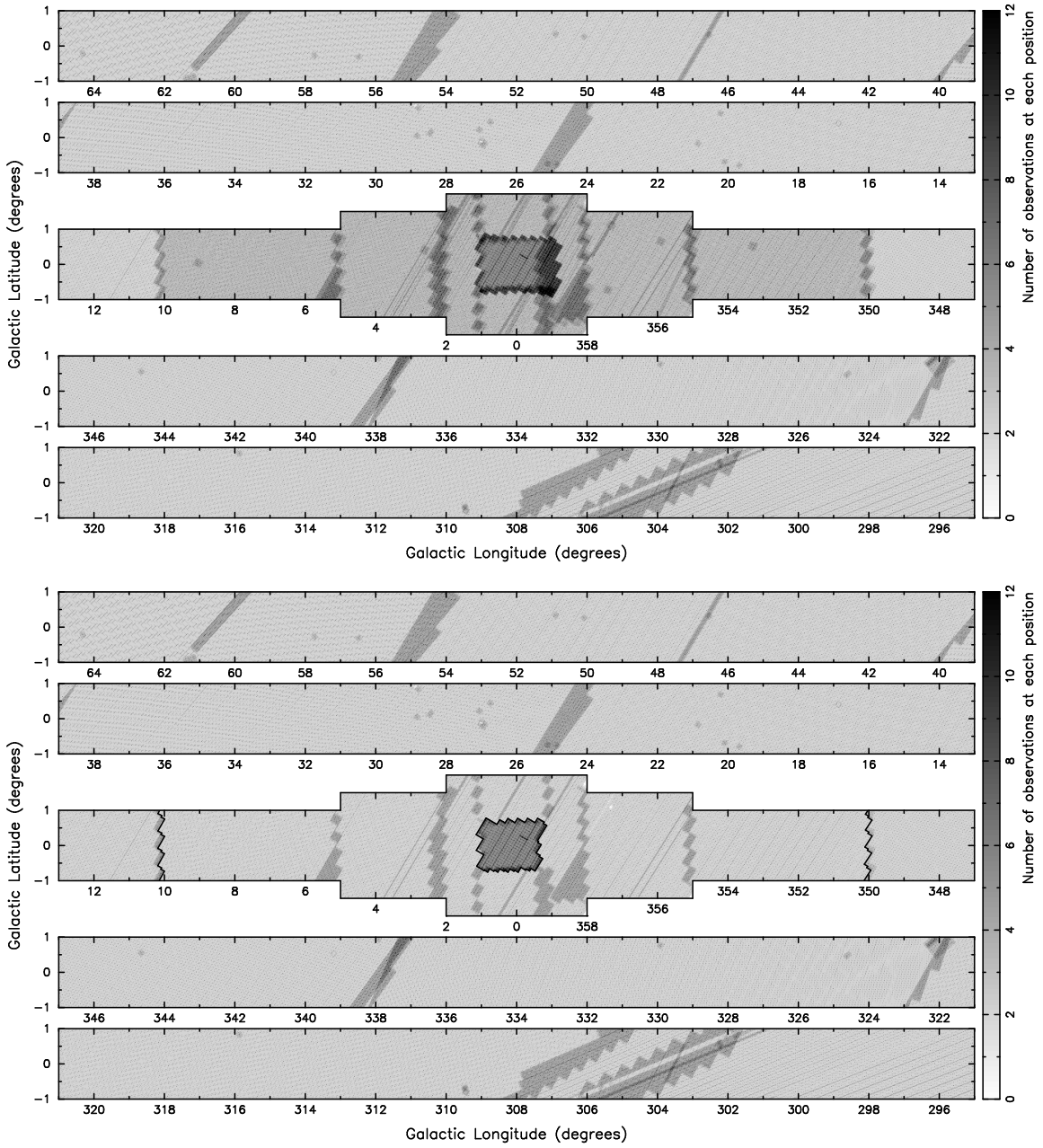

Figure 5.1: Coverage of the GLIMPSE I and II surveys, and the Galactic centre data. The top panel shows the coverage using all available GLIMPSE observations, while the bottom panel shows the coverage if only the first epoch data are used inside the GLIMPSE II region. This region is enclosed by the thick lines at $\ell = 10^{\circ}$ and $\ell = 350^{\circ}$, and excludes the Galactic centre region, also enclosed by a thick line. The scale used is shown on the right in each case: darker shades of grey indicate areas that have been observed a larger number of times.

region for $|\ell| < 10°$, with $|b| \leq 1°$ for $|\ell| > 5°$, $|b| \leq 1.5°$ for $2° < |\ell| \leq 5°$, and $|b| \leq 2°$ for $|\ell| \leq 2°$. The total area surveyed is thus 274 deg^2. In reality, due to the observing strategy, the surveys extend slightly beyond these limits; however throughout the remainder of this chapter only sources inside this 'official' survey area are considered, as this makes calculations of surface densities of sources and the analysis of clustering more straightforward. The coverage of all the IRAC observations is shown in the top panel of Figure 5.1.

All IRAC observations consist of frames with 1.2 s effective exposure times. In principle, GLIMPSE I has one epoch of observations, with two exposures at each position, GLIMPSE II has two epochs of observations (separated by six months), with three exposures at each position (two during the first epoch, and one during the second), and the Galactic centre data have a single epoch of observations, with five exposures at each position. In practice, a given position can be covered more often than this because of re-observed missing or bad frames, and overlap between the individual frames, between the observing campaigns, and between the different surveys. This can be seen in Figure 5.1.

The GLIMPSE I and II v2.0 all-epoch enhanced data products consist of highly reliable Point Source Catalogs, more complete Point Source Archives, and mosaic images with both 0.6″ and 1.2″ pixel resolutions. This processing of the all-epoch GLIMPSE II data includes all GLIMPSE I basic calibrated data (BCD) frames for $|\ell| < 11°$, and includes all of the Galactic centre data, and therefore supersedes the GLIMPSE I v2.0 data products for $9° < |\ell| < 11°$. Since the GLIMPSE II survey is two epoch, single-epoch data products are also available for the whole GLIMPSE II area. For example, the first-epoch enhanced data products include only GLIMPSE II BCD frames from the first epoch (and exclude GLIMPSE II second-epoch, GLIMPSE I, or Galactic centre data).

For this work, the Point Source Catalogs were used, as they have a higher reliability than the Point Source Archives. The Catalogs are high-quality subsets of the Archives: for example, one of the main differences between the Catalogs and the Archives is that a source can be included in the Archives if it is detected only in one IRAC band, whereas it is required to be detected in at least two neighbouring bands in order to be included in the Catalogs. In addition, some fluxes present for a given source in the Archives may be nulled in the Catalogs, for example if the fluxes approach the saturation levels. More details on the GLIMPSE data products, such as the selection criteria for the Archives and Catalogs, are provided in the GLIMPSE I and

II Science Data Products Documents [6][7] and the GLIMPSE Quality Assurance Document [8]. As will be described in §5.2.2, highly variable sources will be missing from the all-epoch Catalogs in the GLIMPSE II survey area in particular, so the GLIMPSE II first-epoch Catalog was used instead of the all-epoch Catalog to select sources from the GLIMPSE II region.

5.2.2 Completeness of the IRAC observations

In this section, the effects of position dependent saturation and sensitivity, variability, and confusion on the completeness of the GLIMPSE I and II surveys are reviewed. As will be discussed in §5.3.1, only IRAC 4.5 and 8.0 μm fluxes were used for the source selection. Therefore, the following discussions refer mostly to these two bands.

Saturation

Since all IRAC observations used the same effective exposure time of 1.2 s, the *pixel* saturation level is independent of position across the whole survey. However, the maximum flux a point source can have without being saturated will depend on the background emission. For instance, if the background is very bright, and close to saturation, only faint point sources will avoid saturation. Since the level of diffuse emission is a strong function of position in the survey area, the *point source* flux saturation level will be position-dependent. Using the equation for point source saturation from the *Spitzer Observer's Manual* [9], the equation for the saturation flux at 4.5 μm is

$$\frac{F_{\rm sat}}{\rm mJy} = \frac{1}{11.09}\left(3621 - \frac{B}{\rm MJy/sr}\right), \tag{5.1}$$

and for 8.0 μm, the equation is

$$\frac{F_{\rm sat}}{\rm mJy} = \frac{1}{4.79}\left(5878 - \frac{B}{\rm MJy/sr}\right), \tag{5.2}$$

where $F_{\rm sat}$ is the point source saturation flux and B is the background level. In the ideal case of a zero background level, the point source saturation levels in these two bands are therefore 327 and 1228 mJy respectively. These are conservative 'worst-case' values, which assume for example that the sources are perfectly aligned with the centre of pixels. In reality, it was found in the GLIMPSE processing that fluxes up to 450 and 1,590 mJy could be extracted reliably at 4.5 and 8.0 μm respectively, i.e. 30-40 % higher than the SSC 'worst case' values. However,

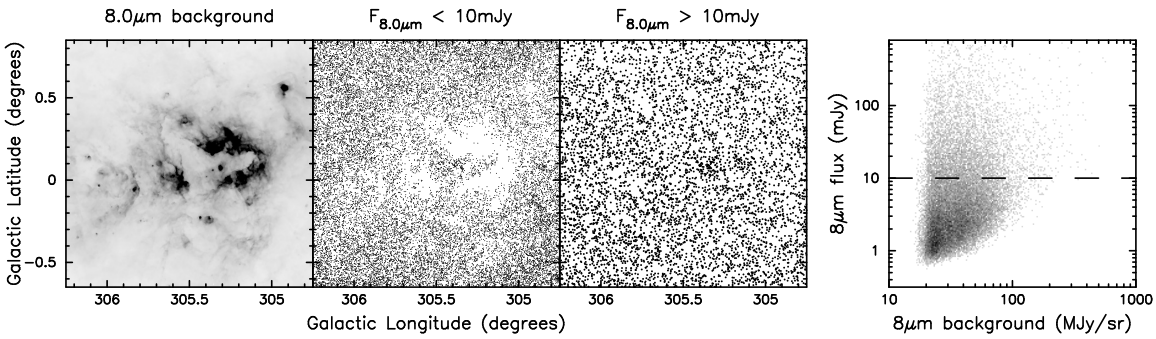

Figure 5.2: The dependence of sensitivity on the diffuse emission brightness. From left to right: 8.0 μm diffuse emission intensity for a 1.5° ×1.5° field centred on $(\ell,b) = (305.5°,0.1°)$ (where a darker shade of grey indicates brighter diffuse emission); point sources (shown as black points) extracted with 8.0 μm flux densities less than 10 mJy; point sources (shown as black points) extracted with 8.0 μm flux densities more than 10 mJy; flux density versus diffuse emission brightness for all the sources in this field (shown on a greyscale where darker shades of grey indicate more sources). The horizontal dashed line corresponds to $F_\nu = 10$ mJy. Only point sources satisfying the brightness and quality selection criteria from Eqs. (5.3) and (5.4) are used in this figure.

the dependence of the point source saturation limit is essentially correct: as the background level increases, the point source saturation flux decreases.

At 4.5 μm, the diffuse emission (excluding the zodiacal light) almost never exceeds 25 MJy/sr, which means that in practice, the point source saturation flux will change by less than 1 % as a function of position. The only notable exceptions where the diffuse emission is brighter than this (and exceeds 100 MJy/sr) are the Galactic centre and the Omega Nebula (M17) star formation region.

At 8.0 μm, in regions where the diffuse emission is as high as 1,000 MJy/sr, all sources fainter than ∼1,000 mJy should still be detectable. In practice, such a high background value is very rare: the fraction of the survey for which the diffuse emission brightness is above 1,000 MJy/sr is approximately 0.015 % (approximately 0.04 deg^2). Furthermore, only very few sources (135) in the final red source catalogue (0.7 %) are brighter than 1,000 mJy at 8.0 μm. Therefore, the probability of a bright (>1,000 mJy) source being in a region of bright (>1,000 MJy/sr) diffuse emission is very low. This means that the dependence of the saturation limit on the diffuse emission brightness is likely to remain unnoticed for this work. The exception to this is the M17 star formation region, which is so bright at 8 μm that the diffuse emission saturates in places; thus the point source saturation flux in this region decreases substantially, and reaches zero where the diffuse emission saturates.

Sensitivity

Although different regions of the survey were observed a different number of times, the photometry for the GLIMPSE I and II Catalogs was always done on 1.2 s BCD frames, meaning that the number of observations at a given position should not in principle affect the sensitivity limit (this would be different if the source detection and photometry were both carried out on mosaics). In practice, the more a source is observed, the more likely it is to be detected enough times to satisfy the Catalog selection criteria, but this effect is not found to be dominant: for example, there is no jump in the number of sources at $\ell = 10°$ or $\ell = 350°$ between the all-epoch GLIMPSE I and II Catalogs, despite the fact that the all-epoch GLIMPSE II Catalogs use three observations at each position instead of two.

The main factor that determines the sensitivity limit, in particular at 8.0 μm, is the brightness of the diffuse emission. The brighter the background emission, the larger the Poisson noise, and therefore the poorer the sensitivity. This has a strong effect on the detectability of sources, mainly for sources fainter than 10 mJy at 8 μm. To illustrate this, the distribution of sources around the ℓ=305° region is shown in Figure 5.2, distinguishing between sources brighter and sources fainter than 10 mJy (only sources satisfying the data quality criteria outlined in §5.3.2 are shown). The right hand panel clearly shows the dependence of the faintest source detected as a function of background flux. To ensure that the angular distribution of sources in the red source catalogue is not affected by the variations in the sky background, lower limits on the 4.5 and 8.0 μm fluxes of 0.5 and 10 mJy respectively ([4.5]=13.89 and [8.0]=9.52) will be imposed in §5.3.2.

Variability

The issue of variability between the various epochs of observations is important, as the entire survey area is constructed from BCD frames taken at different epochs, separated in some cases by over a year. The bandmerger in the GLIMPSE pipeline, a modified version of the SSC bandmerger [10], makes uses of the positions, fluxes, and flux uncertainties of detections within the same band, but in different BCD frames, in order to determine whether to combine the detections. The larger the positional offset between two detections, the more the fluxes have to agree for the detections to be combined, and vice-versa. Thus, two detections with differing fluxes are most likely to be matched if they are positionally coincident. In this case,

to be combined, the fluxes can differ by up to $4.5\sigma_{\rm total}$, where $\sigma^2_{\rm total} = \sigma^2_1 + \sigma^2_2$, and σ_1 and σ_2 are the flux uncertainties of the two detections respectively. The threshold of 4.5σ was determined empirically by running the GLIMPSE bandmerger with various combinations of nearby detections and a range of different fluxes. Therefore, detections with fluxes differing by more than $4.5\sigma_{\rm total}$ are never combined by the GLIMPSE pipeline regardless of their positional offset. Not combining two detections results in the detections being treated as two separate sources, which in turns decreases the chance of either of these sources making it to the final Archives or Catalogs. No constraints are placed on the fluxes when deciding to consider detections in *different bands* as belonging to the same source (that decision is based on close positional coincidence only).

For the work presented here, sources are only selected from the Catalogs if the standard deviation of the fluxes from the different BCD frames is less than 15 % of the mean flux, as will be described in §5.3.2. Therefore, although it is not straightforward to know whether a given variable source will be included in the GLIMPSE Catalogs due to the merging of detections in the GLIMPSE pipeline, the requirement for the standard deviation to be less than 15 % does remove any sources that are significantly variable from regions covered at several epochs in the all-epoch Catalogs. No variable stars are removed in regions covered only at a single epoch (i.e. most of GLIMPSE I and the Galactic centre).

In Figure 5.3, the maximum difference in epochs between BCD frames is shown as a function of position. The top panel shows this using all BCD frames available, and is therefore a map of where variable sources are likely to be missing when using the all-epoch v2.0 Catalogs. The GLIMPSE I area is mostly single epoch, as the two exposures at each position were taken 20 seconds apart. GLIMPSE I was observed in segments of 15° of longitude, separated by intervals of weeks to months, so the regions of overlap between these segments are effectively multi-epoch (the epoch difference is 15 to 20 days at $\ell = 55°$ and 322°, and is 130 to 170 days at $\ell = 40°$, 25°, 337°, and 307°). A small fraction of the survey was re-observed to fill in gaps in the coverage, resulting in small multi-epoch patches. The largest re-observed region is the region between ℓ=302° and 306°, which was re-observed 611 days after the original survey. The Galactic centre observations are single-epoch, as the entire set of observations was completed within 16 hours. Finally, the GLIMPSE II area is two-epoch by design, with the two epochs separated by 215 to 225 days. Since the two GLIMPSE II epochs were observed after GLIMPSE I and after the Galactic centre observations, the regions of overlap between

GLIMPSE II, GLIMPSE I and the Galactic centre data were observed at three different epochs, with a maximum epoch difference of 597 days at the overlap region between GLIMPSE I and II (at $|\ell| = 10°$), and 396 days at the overlap region between GLIMPSE II and the Galactic centre observations (at $|\ell| = 1°$ and $|b| < 0.75°$, and at $|b| = 0.75°$ and $|\ell| < 1°$). The bottom panel of Figure 5.3 shows the same as the top panel with the exception that wherever first-epoch GLIMPSE II BCD frames are available, only those are used; this region is outlined in the bottom panel of Figure 5.1. This dramatically reduces the area in which variable sources will be missing.

To summarise, a large fraction of significantly variable stars is likely to be absent from the GLIMPSE all-epoch Catalogs in regions covered at several epochs (for epochs sufficiently far apart). These regions occur (a) within each individual survey, in regions of overlap between different observing campaigns, or where re-observations have been carried out, (b) in the entire GLIMPSE II survey region, since this survey was two-epoch by design, and (c) in the regions of overlap between GLIMPSE I and II, and between GLIMPSE II and the Galactic centre data. However, by using the GLIMPSE II first-epoch Catalog instead of the all-epoch Catalog wherever possible, the number of excluded variables sources can be minimised.

Confusion

As described in the GLIMPSE Quality Assurance document [8], photometry can become unreliable when two sources are separated by less than $2.4''$. In this situation, 'flux stealing' – splitting the flux incorrectly between two sources – becomes important. This is most likely to happen in dense clusters and in the GLIMPSE II survey area as one approaches the Galactic centre. All sources in the GLIMPSE Catalogs are assigned a *close source flag* that indicates whether another source is closer than $2.5''$ (flag set to 2), closer than $3.0''$ (flag set to 1), or whether there is no other source within $3.0''$ (flag set to 0). Since photometric accuracy is very important for this work, only sources that have no neighbour closer than $3.0''$ are kept (as described further in §5.3.2). However, this means that the red source catalogue will be incomplete in regions of very high stellar densities such as dense clusters or towards the Galactic centre.

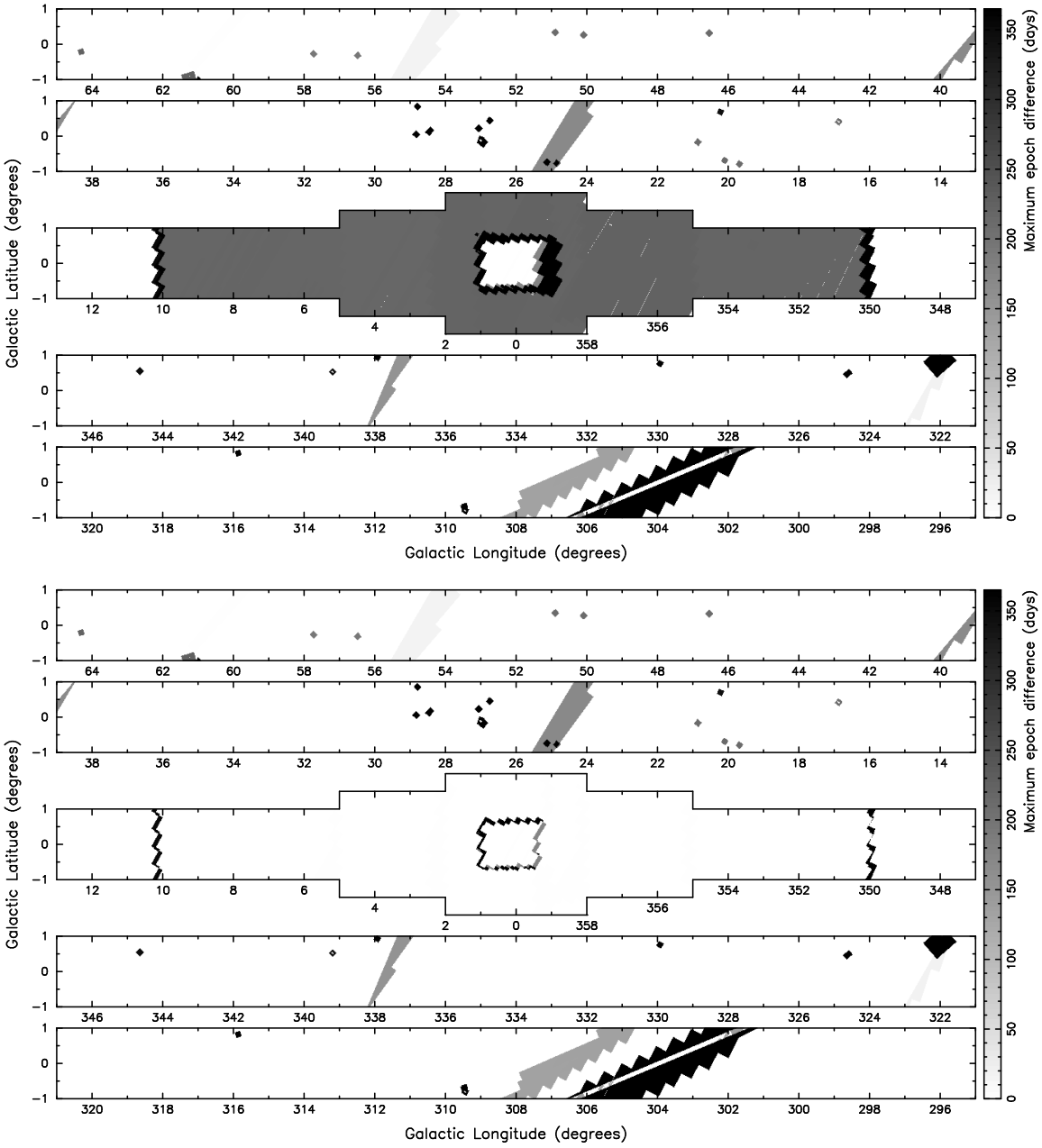

Figure 5.3: Maximum epoch difference between BCD frames as a function of position. The top panel shows the epoch difference in the BCD frames used for the all-epoch data products, while the bottom panel uses exclusively the GLIMPSE II first epoch BCD frames where available, and all BCD frames elsewhere. The scale used is shown on the right in each case: darker shades of grey correspond to larger epoch differences, with differences of a year and above shown in black. Therefore, white corresponds to areas covered effectively at a single epoch.

5.2.3 Description of the complementary observations

For this work, complementary observations were used to construct SEDs from 1.25 to 24 μm for the sources selected as intrinsically red. These complementary observations are:

- The 2MASS Point Source Catalog (Skrutskie et al., 2006), which includes photometry in JHK_s filters for the whole area covered by the GLIMPSE surveys. The 2MASS photometry is merged with the IRAC data in the GLIMPSE pipeline, and is listed in the GLIMPSE I and II Catalogs. The 10-σ sensitivity limits are typically 15.8, 15.1, and 14.3 mag for J, H, and K_s respectively.

- *Spitzer* MIPS data from the MIPSGAL I survey of the GLIMPSE I area, (PI: Carey; PID 20597), the MIPSGAL II survey of the GLIMPSE II area (PI: Carey; PID 30594), and observations of the Galactic centre (PI: Yusef-Zadeh; PID 20414). Since Point Source Catalogs are not available at the time of publication, the post-basic calibrated data (PBCD) mosaics were used to perform the photometry.

- MSX band E (21.3 μm) data for sources saturated at MIPS 24 μm.

5.3 Source selection and catalogue compilation

5.3.1 Definition of an intrinsically red source

Due to the difficulty in separating YSOs, AGB stars, planetary nebulae (PNe), and other red sources at mid-infrared wavelengths, the decision was made to first create a catalogue of all intrinsically red sources, and to leave the separation of the various populations until after compiling the catalogue. The definition of an *intrinsically red source* adopted here is one that is intrinsically redder at IRAC wavelengths than field stars (such as main sequence or red giant stars), and would therefore still be red in the absence of interstellar extinction.

One option to select red sources would be to remove sources that could be well fit by reddened stellar photosphere models, allowing interstellar extinction to be a free parameter, and considering the remaining sources to be intrinsically red (e.g. Indebetouw et al., 2007; Poulton et al., 2008). However, while SED modelling can usually provide unique insights into the properties of objects by making the best use of multi-wavelength data, such a procedure would not be suitable for generating a red source catalogue for several reasons. Firstly, the

goodness of fit is quantified by a χ^2 value, which not only depends on the fluxes of a source, but also the flux errors, meaning that the number of sources selected is very sensitive to the χ^2 threshold and the choice of flux errors. In addition, the number of sources badly fit by reddened photospheres strongly depends on the specific stellar photosphere models used. For example, using Castelli & Kurucz (2004) models resulted in approximately twice as many remaining red sources as the Brott & Hauschildt (2005) models for a same χ^2 cut-off. Finally, such a selection is not easily reproducible. Undoubtedly, the models will improve in the future, and might result in yet a different number of red sources given the same selection criterion. Reproducing the selection criterion would require using the same version of the models as was used in this thesis.

Instead, the decision was made to extract intrinsically red sources using a colour selection. A multi-colour selection criterion – combined with different sensitivity and saturation limits at different wavelengths – would make it difficult to understand selection biases. Therefore, a very simple single-colour selection criterion was chosen, namely that the colour between IRAC 4.5 μm and IRAC 8.0 μm be above a certain threshold for a source to be considered as red. While this selection may appear simplistic at first, it allows a much better understanding of selection biases, and is easily reproducible. A cut-off value of $[4.5]-[8.0] \geq 1$ was used to select red sources, and this choice is justified in §5.3.3.

The choice of IRAC 4.5 μm (rather than 3.6 μm) as the lower wavelength was motivated by recent results which suggest that the interstellar extinction law is approximately flat between 4.5 μm and 8.0 μm (Lutz, 1999; Indebetouw et al., 2005; Flaherty et al., 2007). Using the selective extinction values from Indebetouw et al. and Flaherty et al., one finds $E([4.5]-[8.0])/A_K = 0.000 \pm 0.040$ and $E([4.5]-[8.0])/A_K = 0.041 \pm 0.020$ respectively, where the uncertainties are the standard deviations of the values for the different lines of sight, and effectively represent the region to region variations. Therefore, a star with an intrinsic colour of $[4.5]-[8.0] = 0$ would need to be seen through an extinction of at least $A_{\rm K} = 25$ to have $[4.5]-[8.0] \geq 1$, that is $A_{\rm V} \approx 190-220$ assuming $A_V/A_K \approx 7.5-8.8$ (Cardelli et al., 1989). Even if the intrinsic colour of a source was $[4.5]-[8.0] = 0.5$ (for example due to an absorption line or band at 4.5 μm), this would still require $A_{\rm V} \approx 100$ to obtain $[4.5]-[8.0] \geq 1$. While such high extinctions can occur through dark clouds for example, the vast majority of GLIMPSE sources will not be subjected to such high interstellar extinctions.

5.3.2 Initial selection criteria

As described in §5.2.2, the variations in the diffuse emission throughout the survey translate into a different point source sensitivity as a function of position. Since the aim was to produce a complete catalogue within colour and magnitude selection criteria, only sources that had 4.5 μm fluxes equal to or larger than 0.5 mJy, and 8.0 μm fluxes equal to or larger than 10 mJy were selected.

The issue of contamination by bad photometry and erroneous detections required the most attention when compiling the catalogue. The source detection reliability for the GLIMPSE Catalogs is required to be at least 99.5 %, and the overall accuracy of the photometry is also very high. However, applying a colour selection can lead to a bias towards selecting sources with erroneous fluxes: for example, if a given source has either its 4.5 or the 8.0 μm flux erroneously estimated, this source will have non-stellar colours; in particular, sources with over-estimated 8.0 μm fluxes or underestimated 4.5 μm fluxes have a higher likelihood of being selected by a criterion such as $[4.5]-[8.0] \geq 1$ than sources with accurate photometry. Therefore, it is important for this work to ensure that the photometry is as accurate as possible.

There are a number of reasons why fluxes might be wrongly estimated for a given source, one of which – 'flux stealing' by close neighbours – was already mentioned in §5.2.2. Since close neighbours can lead to uncertain photometry, only sources with a close source flag set to zero were selected (no Archive source within 3″).

Another possible source of unreliable photometry is low signal-to-noise detections. One common cause of over-estimation of fluxes occurs when a spurious local peak in the background emission (due to noise or cosmic rays) is mistaken for a point source, or when a source that should not have been detected becomes bright enough to be detected due to Poisson fluctuations in the number of photons from that source (Malmquist bias). In addition, genuine sources with low signal-to-noise may also have their fluxes wrongly estimated. Assuming that the photometric errors are correctly computed, the reliability of the Catalogs can be increased by applying signal-to-noise cuts. For the purposes of the work, only sources with fractional flux errors below 15 % were selected.

For a small fraction of sources, photometric uncertainties may be under-estimated, and unreliable photometry may remain. Spurious detections are not likely to happen twice at the

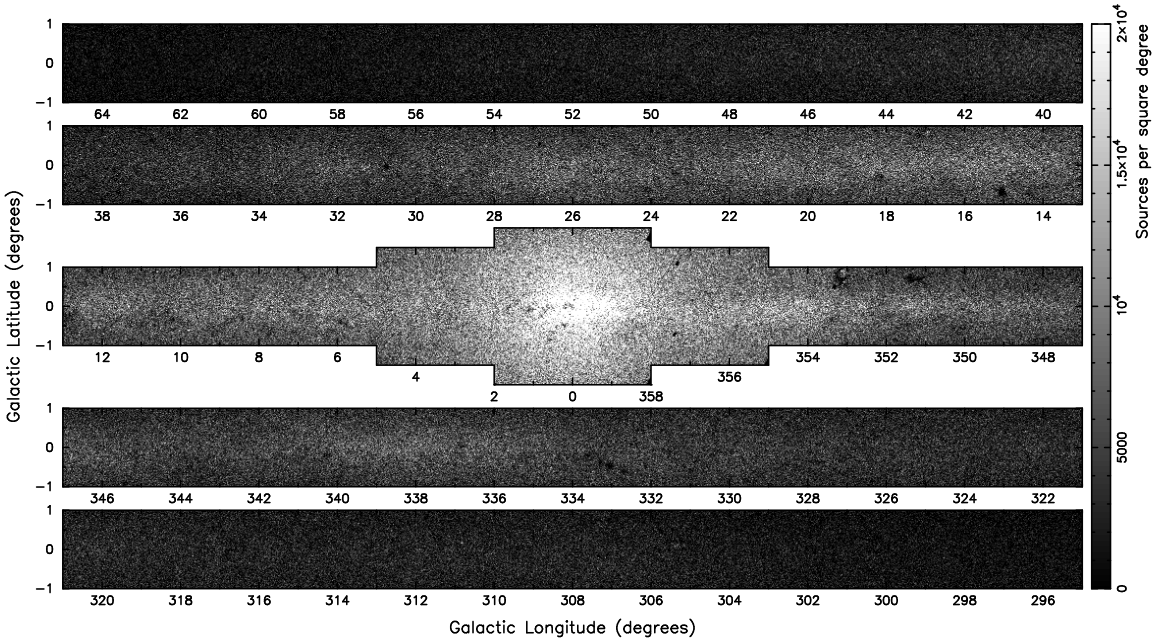

Figure 5.4: Angular distribution of the GLIMPSE I and II Catalog sources satisfying Eqs. (5.3) and (5.4). The scale used is shown on the right: lighter shades of grey correspond to a higher stellar density.

same position in two different observations, and can therefore be identified by looking for sources detected only in one BCD frame, in regions covered by multiple BCD frames. In order to eliminate such sources, only sources detected at least twice at 4.5 and 8.0 μm were selected. For genuine faint sources with low signal-to-noise, one can use the standard deviation of the fluxes from the multiple detections to check whether the flux is reliable. For this reason, the standard deviation of detections was required to be less than 15 % of the fluxes.

As discussed in §5.2.2, in order to eliminate as few variable stars as possible, the GLIMPSE II first-epoch Catalog was used for the GLIMPSE II first epoch survey area, and the GLIMPSE I and II all-epoch Catalogs were used for the remaining area, i.e. most of the GLIMPSE I and Galactic centre regions. The initial selection criterion applied to these Catalogs can be summarised into two criteria: *brightness* criteria, and *quality* criteria. The brightness criteria are

$$\begin{cases} 0.5\,\mathrm{mJy} \leq F_{4.5\,\mu\mathrm{m}} \leq 450\,\mathrm{mJy}, & \text{i.e. } 13.89 \geq [4.5] \geq 6.50 \\ 10\,\mathrm{mJy} \leq F_{8.0\,\mu\mathrm{m}} \leq 1,590\,\mathrm{mJy}, & \text{i.e. } 9.52 \geq [8.0] \geq 4.01 \end{cases} . \tag{5.3}$$

Table 5.1: Numbers of sources in the GLIMPSE Catalogs after selection criteria.

Selection criteria	GLIMPSE I + GC[a] all-epoch	GLIMPSE II first epoch	Total
Eq. (5.3)	908,748	591,772	1,500,520
Eqs. (5.3) and (5.4)	828,795	526,587	1,355,382
Eqs. (5.3), (5.4) and (5.5)	17,104	4,995	22,099

a — Excluding sources that lie in the GLIMPSE II first epoch survey area

Notes — Only sources inside the 'official' survey area are included, as described in §5.2.1

and the quality criteria are

$$\begin{cases} \text{csf} = 0 & \\ dF_i/F_i \leq 15\,\% & i = 2,4 \\ M_i \geq 2 & i = 2,4 \\ F_i\_\text{rms}/F_i \leq 15\,\% & i = 2,4 \end{cases} \tag{5.4}$$

using the notation from the GLIMPSE Science Data Products Documents [6][7]: csf is the close source flag, F_i and dF_i are the fluxes and 1σ errors, M_i is the number of detections, F_i_rms is the RMS or standard deviation of individual detections from F_i, and i is the IRAC band number, where $i = 2$ corresponds to 4.5 μm, and $i = 4$ corresponds to 8.0 μm.

The number of sources selected from the GLIMPSE I and II all-epoch Catalogs (excluding the GLIMPSE II first epoch area) and from the GLIMPSE II first-epoch Catalog after each requirement are listed in Table 5.1. The distribution of the sources after applying the brightness and quality selection criteria is shown in Figure 5.4. A few regions show a decrease in the surface density of sources due to the diffuse emission (e.g. M17 at ℓ=15°, and the regions at ℓ=333, 351, and 353°) despite removing all 8.0 μm fluxes below 10 mJy, but the distribution of sources seems otherwise unaffected by diffuse emission.

5.3.3 Selection of red sources

In this section, only the sources that satisfy Eqs. (5.3) and (5.4), i.e. the brightness and quality selection criteria, are used. Figure 5.5 shows a [8.0] vs. [4.5] − [8.0] colour-magnitude diagram for all these sources (on a linear and logarithmic greyscale respectively). The large majority of sources lie close to, but not at [4.5] − [8.0] = 0. This is likely due to the CO

fundamental absorption feature in the spectrum of giants and dwarfs which decreases the 4.5 μm flux. Also shown are the distribution of sources in a $[3.6]-[4.5]$ vs. $[4.5]-[8.0]$ and a $[3.6]-[4.5]$ vs. $[5.8]-[8.0]$ colour-colour diagram. Most sources fall around $[3.6]-[4.5] \approx -0.1$, $[4.5]-[8.0] \approx +0.2$, and $[5.8]-[8.0] = 0$. The slightly negative values for the $[3.6]-[4.5]$ colour, the slightly positive value for $[4.5]-[8.0]$, and the zero value for $[5.8]-[8.0]$ are all consistent with the presence of an absorption feature at 4.5 μm.

The top panel of Figure 5.6 shows the sources selected if the selection criterion for red sources is chosen to be $[4.5]-[8.0] \geq 0.75$. Two populations of sources are seen, the bluest of which contains the tail of the distribution of bright stars. The bottom two panels of Figure 5.6 show sources with $0.75 \leq [4.5]-[8.0] < 1$ and $[4.5]-[8.0] \geq 1$ respectively. The two populations separate well in colour-colour space. The $[3.6]-[4.5]$ vs. $[4.5]-[8.0]$ also clearly shows that one of the populations is in fact outliers from the main concentration of sources in colour-colour space. For this reason, the final *colour* selection criterion for intrinsically red sources was chosen to be

$$[4.5]-[8.0] \geq 1. \tag{5.5}$$

This selection criterion corresponds to selecting all sources with a spectral index $\alpha \geq -1.2$ (as originally defined by Lada 1987). Adopting the 'Class' definition of Greene et al. (1994), this means that all Class I sources ($\alpha \geq 0.3$), all 'flat spectrum' sources ($-0.3 \leq \alpha < 0.3$), and a large number of Class II sources ($-1.6 \leq \alpha < -0.3$) will be included in the red source catalogue. However, it should be stressed that the spectral index values discussed here are only calculated over a very small wavelength range, and are therefore not as good an indicator of evolutionary stage as spectral index values calculated over a larger wavelength range (c.f. Chapter 3). The numbers of sources selected using this criterion are listed in Table 5.1. In total 22,099 sources were selected.

5.3.4 Validation of the GLIMPSE photometry

The quality selection criteria in Eq. (5.4) removed a large fraction of, but not all false red sources. For example, 8.0 μm fluxes can be over-estimated because of the spatially complex nature of the strong diffuse PAH emission: if a source lies on a sharp peak of diffuse emission, the background level can be under-estimated, and the flux over-estimated. Therefore,

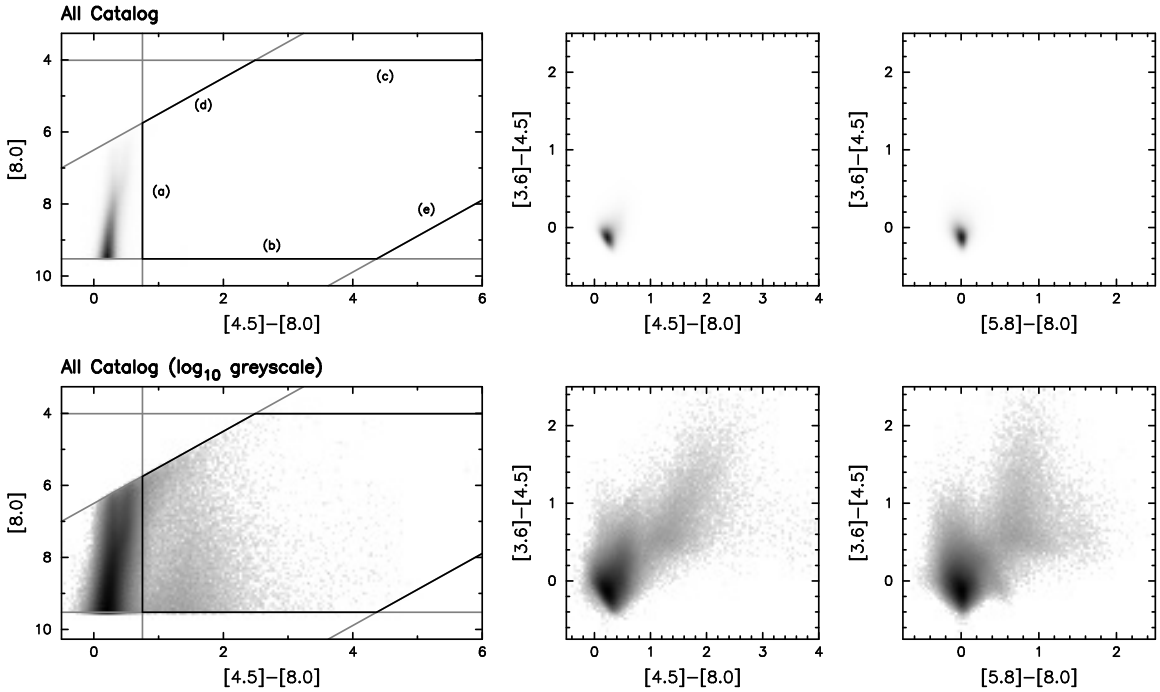

Figure 5.5: All GLIMPSE I and II Catalog sources satisfying Eqs. (5.3) and (5.4) shown on a linear greyscale (*top*), and the same sources shown on a logarithmic greyscale (*bottom*). The grey lines in the left panels show (as labelled in the top left panel): (a) a $[4.5]-[8.0]>0.75$ colour selection, (b) the [8.0] sensitivity limit, (c) the [8.0] saturation limit, (d) the [4.5] saturation limit, and (e) the [4.5] sensitivity limit. The black lines show the boundaries of the resulting completeness region.

a foreground or background star superimposed on clumpy PAH emission can produce a false red star in the GLIMPSE Catalogs. In order to achieve close to 100 % reliability, the following procedure was carried out:

1. For each red source from §5.3.3, the 4.5 and 8.0 μm fluxes were calculated independently using a custom written aperture and PSF photometry program (c.f. Appendix E), and using the final v2.0 mosaics rather than the BCD frames. For the sources extracted from the GLIMPSE II first-epoch Catalog, first-epoch only v2.0 mosaics were used. The point response functions (PRFs) were computed for the mosaics, as these differ slightly from BCD PRFs, and these were used to determine the appropriate IRAC aperture corrections, which were found to be in good agreement with the official SSC aperture corrections.

2. The mosaic images were examined by eye for every source, to determine whether the aperture photometry could be trusted, based on the radial profile of the source, by determining whether the sky background was correctly estimated, and whether there was any contamination inside the source aperture.

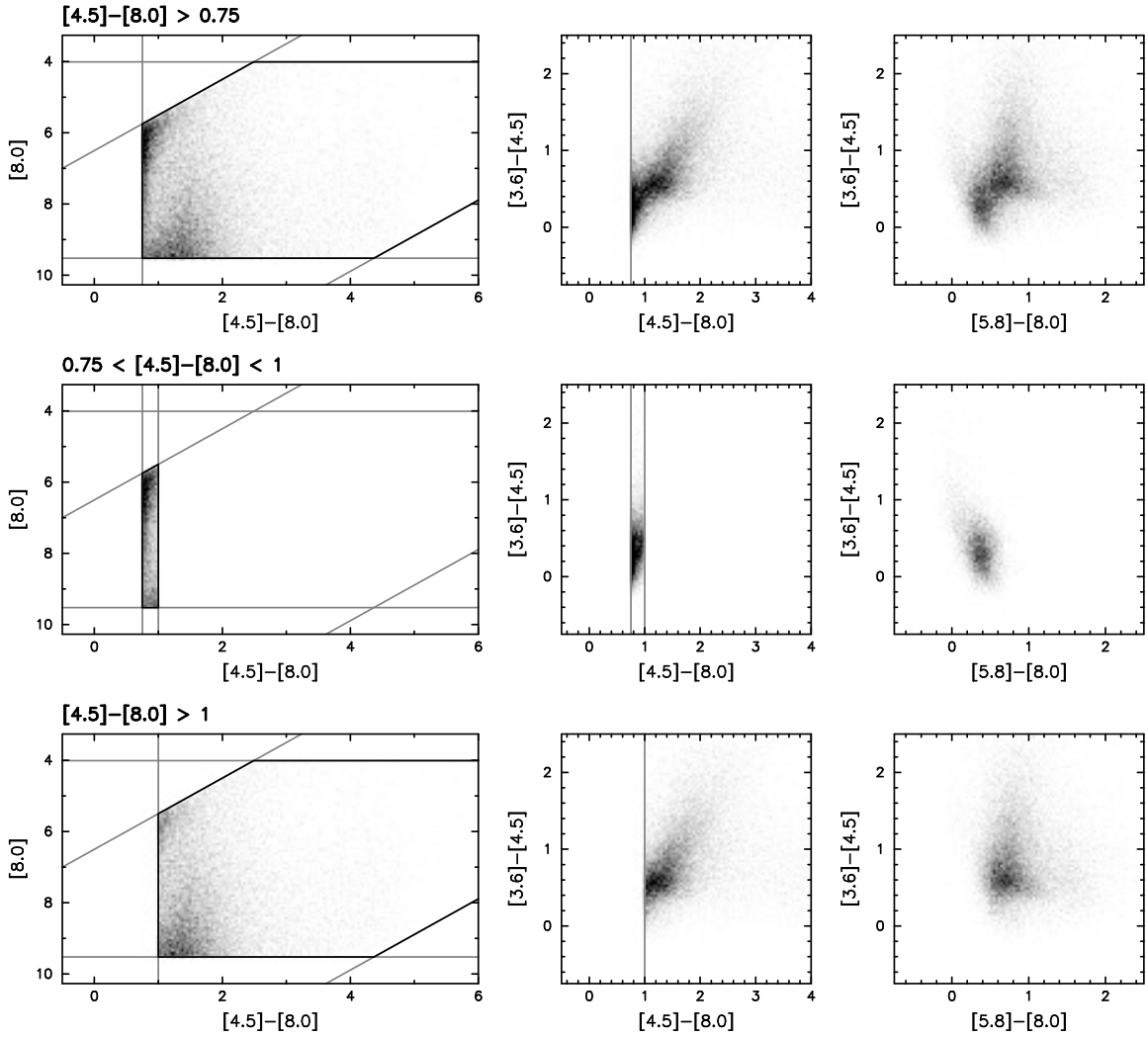

Figure 5.6: As for Figure 5.5, but showing only sources with $[4.5] - [8.0] > 0.75$ (*top*), only sources with $0.75 < [4.5] - [8.0] < 1$ (*centre*), and only sources with $[4.5] - [8.0] \geq 1$ (*bottom*). All panels show the density of sources on a linear greyscale. The grey vertical lines in the central panels show the colour selection criterion used in each case.

3. If the aperture photometry flux could not be trusted, a flux was determined by fitting the appropriate PSF to the source, and a residual image made by subtracting the scaled PSF from the mosaic. The residual image was inspected to determine whether this automated PSF photometry was reliable.

4. If the automated PSF photometry did not provide a clean residual, the position and flux of the scaled PSF were adjusted until the source was correctly subtracted.

5. In cases where this could not be achieved, the source was marked as unreliable. This includes extended sources, slightly diffuse sources, blended sources, and sources with low signal-to-noise detections.

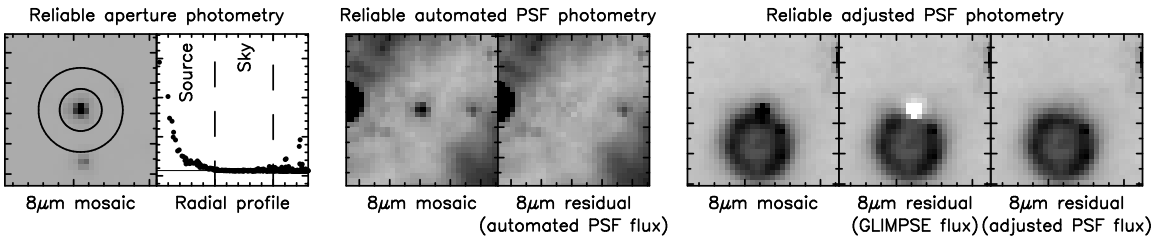

Figure 5.7: Examples of methods used to derive independent mosaic photometry fluxes. *Left:* a source for which a flux could be reliably measured using aperture photometry. The source aperture and the annulus for the sky determination are over-plotted on the image. The radial profile shows that the sky background (indicated by a horizontal solid line) is accurately determined, and the source aperture (indicated by the left vertical dashed line) contains no contamination. *centre:* a source for which automated PSF photometry provided a reliable mosaic flux. *Right:* a source for which both the GLIMPSE and the independently determined flux over-estimated the flux of the source, but where the flux was reliably determined after adjusting it to obtain a clean residual.

Figure 5.7 shows examples of the independent flux determinations for three sources. The first is one for which aperture photometry was reliable based on the radial profile of the source, the second is one for which the independent automated PSF photometry was reliable, and the third is one for which GLIMPSE's and the independent automated photometry were not reliable, but for which a reliable independent flux was obtained after manual adjustments. The independent photometry is likely to be on average more reliable than the GLIMPSE Catalog fluxes, not because of the flux determination algorithms, but because each source was visually inspected to decide which method produced the most reliable flux, and in some cases *manual* adjustments were made to improve the PSF fit. In addition, using the mosaics rather than the original BCD frames means that outlying pixels such as cosmic rays do not affect the photometry as they were removed in the mosaicking process.

For sources that had either a reliable independent aperture or PSF (automated or adjusted) flux, these fluxes were compared with the original GLIMPSE fluxes, and all GLIMPSE fluxes that differed from the independent value by less than 15 % of the GLIMPSE flux were considered to be trustworthy. For sources with fluxes disagreeing by a larger fraction, such as the source shown in the right-hand panel of Figure 5.7, it was found that the independently determined fluxes were always the most reliable, which is expected since their photometry was verified, and in some cases improved, manually. In total, only 1,098 and 302 sources (5.0 % and 1.4 % of all red sources respectively) had 4.5 μm and 8.0 μm fluxes respectively for which the GLIMPSE flux differed from the independent mosaic flux by more than 15 %. In these cases, the independent flux was used instead of the original GLIMPSE flux. The brightness and colour selection criteria from Eqs. (5.3) and (5.5) were then re-applied.

Of the 22,099 red sources selected in §5.3.3, 3,055 (13.8 %) were rejected because reliable independent photometry could not be performed in one or both of the bands (1,050 at 4.5 μm only, 1,171 at 8.0 μm only, and 834 at both 4.5 and 8.0 μm). Of those with reliable photometry, 58 were rejected as no longer red, and 59 were rejected as no longer bright enough or too bright (including 22 both no longer red and no longer bright enough or too bright). The source shown in the right hand panel of Figure 5.7 is an example of a source that was only present in the original red source list because the 8.0 μm flux was overestimated. After computing reliable fluxes, it was found to have $[4.5] - [8.0] = 0.38$ instead of 1.41. Finally, 18,949 sources (85.7 %) had reliable photometry, and satisfied the brightness and colour selection criteria from Eqs. (5.3) and (5.5), and these are the sources that constitute the final red source catalogue; these sources are listed in Table F.1.

5.3.5 Constructing SEDs

By default, the red source catalogue contains JHK_s, 3.6, and 5.8 μm data when available, since these are all in the GLIMPSE Catalogs, although none of these were *required* for the selection. Of the 18,949 sources in the red source catalogue, 13,011 have a K_s-band flux available, 9,740 have an H-band flux available, and 6,817 have a J-band flux available. Therefore, any JHK_s diagrams in subsequent sections will be incomplete as they only contain approximately one third of all sources. The JHK_s, 3.6, and 5.8 μm photometry was not manually checked, but to ensure the high reliability of these fluxes, 3.6 and 5.8 μm fluxes were rejected if they did not satisfy the stringent quality criteria from Eq. (5.4), and 2MASS fluxes were rejected if the quality flags in the 2MASS Catalog were set to E, F, or X (indicating unreliable fluxes).

To determine MIPS 24 μm fluxes, PSF photometry was performed at the positions of the 18,949 red sources on the MIPSGAL 24 μm PBCD mosaics. Similarly to the independent IRAC fluxes, a custom-written PSF photometry program that allows adjustments in flux and position was used to manually improve the PSF fit for each source. Therefore, the MIPS photometry should also be reliable, modulo the uncertainties resulting from carrying out photometry onPBCD frames.

For sources saturated in the MIPS 24 μm observations, the MIPS 24 μm images were used to assess whether the MSX 21.3 μm flux would suffer from contamination from other sources. In cases where the MSX 21.3 μm emission originated solely from a single source, the MSX 21.3 μm flux is listed in Table F.1 instead of the MIPS 24 μm flux. The MSX images were

inspected to remove any unreliable MSX 21.3 μm fluxes. For sources saturated at MIPS 24 μm where a reliable MSX 21.3 μm flux could not be used, PSF photometry was performed on the MIPS 24 μm data by fitting the unsaturated wings of the PSF whenever possible. In total, MIPS 24 μm fluxes were measured for 16,480 sources, MSX 21.3 μm fluxes were used for 112 sources, and 2,181 sources were either not covered by MIPS observations, not detected, were saturated, or could not have fluxes reliably measured (e.g low signal-to-noise, artefacts, blending), and the MSX 21.3 μm flux could not be used.

In the remainder of this chapter, sources with MSX 21.3 μm data points instead of MIPS 24 μm are shown in colour-colour and colour-magnitude plots as if they were MIPS 24 μm data points. Using the models from Chapter 3, it was found that the MIPS 24 μm to MSX 21.3 μm flux ratio is most likely to be between 0.7 and 3 for YSOs, meaning that by using the MSX 21.3 μm instead of MIPS 24 μm data in colour-colour or colour-magnitude diagrams, the MIPS 24 μm magnitude is likely to be at most overestimated by 0.3 mag and underestimated by 1.2 mag. Compared to the range in $[8.0]-[24.0]$ shown in colour-colour diagrams in the remainder of this chapter, and considering the small fraction of sources for which MSX 21.3 μm was used in place of MIPS 24 μm (<1 %), this substitution is unlikely to be noticeable.

5.3.6 Extended sources

While the red source catalogue presented in this chapter aims to be as complete as possible within the colour and brightness selection criteria imposed, it can only be complete for point sources, as it does not include YSOs that may be extended. While these are clearly of great importance, the GLIMPSE Point Source Catalog fluxes are measured using PSF photometry, and therefore are only reliable for point sources. Furthermore, extended sources have a lower probability of being found by the point source detection algorithm. For this reason, only a fraction of extended sources are likely to make it to the Point Source Catalogs, and in cases where they do, their fluxes are not likely to be reliable. Therefore, all extended sources were removed from the red source catalogue for consistency, as described in §5.3.4.

In particular, massive YSOs that appear extended at 4.5 μm due to H_2 and CO bandhead emission from outflows are likely to be excluded; however, a number of these are identified in the recent work by Cyganowski et al. (2008) who found over 300 such objects in the GLIMPSE I survey. In addition, the brightest extended YSOs at IRAC wavelengths may be detected as point sources in the MIPSGAL or MSX surveys, and may therefore be present in

the MIPSGAL or MSX Point Source Catalogs (such as the massive YSO candidates identified by the RMS survey).

5.3.7 Completeness and Reliability

In this section, estimates of the completeness and reliability of the red source catalogue are presented. The completeness – i.e. the fraction of red point sources in the survey area that are present in the final catalogue – is not straightforward to estimate, as it depends on several factors, such as the initial completeness of the GLIMPSE Catalogs and the fraction of genuine sources rejected by the quality selection criteria in Eq. (5.4). Rather than estimate the change in completeness at each step in the selection process, the completeness was estimated using sources from the GLIMPSE Point Source Archives, which are more complete (albeit less reliable) than the Point Source Catalogs used in this chapter. In total, 39,505 sources from the Point Source Archives satisfied Eqs. (5.3) and (5.5). These were selected in the same way as the Catalog sources, i.e. using the GLIMPSE II first epoch data where available. By examining a random sample of 400 of these sources and performing independent mosaic photometry, it was found that 27.0 % were unambiguously not present in the mosaics, extended, not red enough, or too faint or bright. The remaining 73.0 % included well-defined point sources, and sources for which no reliable photometry could be performed (e.g. blended sources or sources in areas of complex diffuse emission). Therefore, a conservative upper limit on the number of genuine red point sources was determined to be 39,505×73.0 % =28,839, assuming that the Archives themselves are complete. In comparison, 18,949 sources are present in the final red source catalogue, suggesting a conservative lower limit on the completeness of 65.7 %.

The reliability of the red source catalogue, i.e. the fraction of sources that are genuine red point sources, should be virtually 100 %, as all red sources in the catalogue were examined individually to reject any sources that could not be confirmed as red. The 4.5 μm, 8.0 μm, and 24.0 μm photometry of all the red sources in the final catalogue should be accurate to better than 15%, since all fluxes were verified independently through mosaic photometry, and erroneous fluxes were corrected. For sources close to $[4.5]-[8.0]=1$, the photometric and calibration uncertainties mean that some sources may in fact have an intrinsic $[4.5]-[8.0]$ colour slightly below 1. However, a fraction of sources with a measured $[4.5]-[8.0]$ colour slightly below 1 are likely to have an intrinsic $[4.5]-[8.0]$ colour slightly above 1. The effect is likely to be similar in both directions, so that the total number of sources in the red source

catalogue should not be significantly affected by this.

The most stringent criterion in the selection procedure used in this chapter was the requirement that the 8.0 μm fluxes should be larger than 10 mJy. Although this was done in part to obtain a homogeneously sensitive sample of sources over the whole survey area, it also removed a large fraction of erroneous fluxes from faint and spurious sources, meaning that the subsequent quality selection criteria from Eq. (5.4) only removed a further 10 % of sources. However, the quality selection criteria would have been much more critical for fainter sources. As an example, approximately 40,000 of the sources in the GLIMPSE Catalogs that have $[4.5] - [8.0] \geq 0.75$ only have a single detection at 8.0 μm. The SEDs of these sources typically resemble 'transition disk' SEDs, with photospheric fluxes for the first three IRAC bands, and an excess at 8.0 μm. However, upon closer inspection, it was clear that for the large majority of these sources, the colour excess was not real, and in some cases the source was not present in the mosaic image at 8 μm. Most of these sources had 8.0 μm fluxes below 10 mJy, meaning that below this flux level, requiring two detections in each band would have been much more important. This suggests that when searching for red sources fainter than 10 mJy at 8 μm in the GLIMPSE I or II Catalogs, one should make a careful assessment of the quality of the data and of the photometry. In particular, any source in the GLIMPSE Catalogs with an SED resembling that of 'debris' or 'transition disks', i.e. with only an excess at 8 μm should not be trusted unless at least two detections are present at 8 μm, and the images are inspected visually to confirm the source. As previously mentioned in §5.3.2, erroneous photometry is only an issue for this work because the red colour selection used here preferentially selects sources with unreliable photometry from the Catalogs, due to their unusual colours; but the GLIMPSE Catalogs are overall very reliable.

5.4 Analysis

5.4.1 Observable properties of the red sources

Angular distribution of sources

Figure 5.8 shows the angular distribution of all intrinsically red sources in the final catalogue. The distribution of sources shows a large number of clusters, and a more diffuse component that can be seen for example at latitudes $|b| > 1^\circ$ in the GLIMPSE II region. The strong clustering of sources suggests that a significant fraction of the red sources are YSOs, as clustering

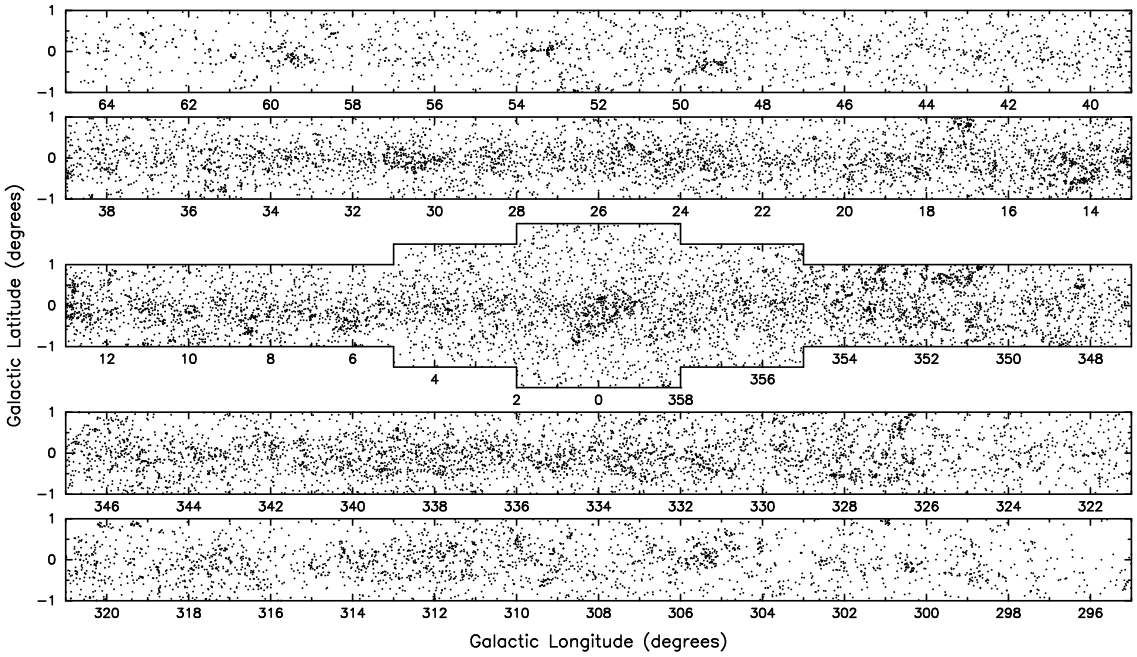

Figure 5.8: Angular distribution of all the sources in the final red source catalogue.

is not expected for AGB stars or PNe, and galaxies are shown to contribute less than 0.5% of the sources in the red source catalogue (§5.4.2). The red sources do not show a strong increase in source density for $|\ell| < 2^\circ$ as was visible in the distribution of GLIMPSE Catalog sources in Figure 5.4.

Colour and magnitude distribution

Figure 5.9 shows the colour-colour and colour-magnitude distribution of the red sources. It is clear from these diagrams that the red sources span a large region of colour-colour and colour-magnitude space. In the colour-magnitude diagrams, the red sources appear to separate into two populations: one redder and fainter, peaking at $[8.0] > 8$ and $1 < [4.5] - [8.0] < 2$, and one bluer and brighter, peaking at $[8.0] < 6.5$ and $[4.5] - [8.0] < 1.4$. The latter appears to be an extension of the sources removed in §5.3.3. These two populations are identified in §5.4.2 and separated in §5.4.3.

Variability

As shown in Table 5.1, 4,987 of the initially selected red sources were extracted from the GLIMPSE II first epoch Catalog. Of these, 4,472 are present in the final red source catalogue after removal of unreliable sources, and 4,455 also fall in the GLIMPSE II second epoch observations. The GLIMPSE II second epoch Point Source Archives were used to assign second

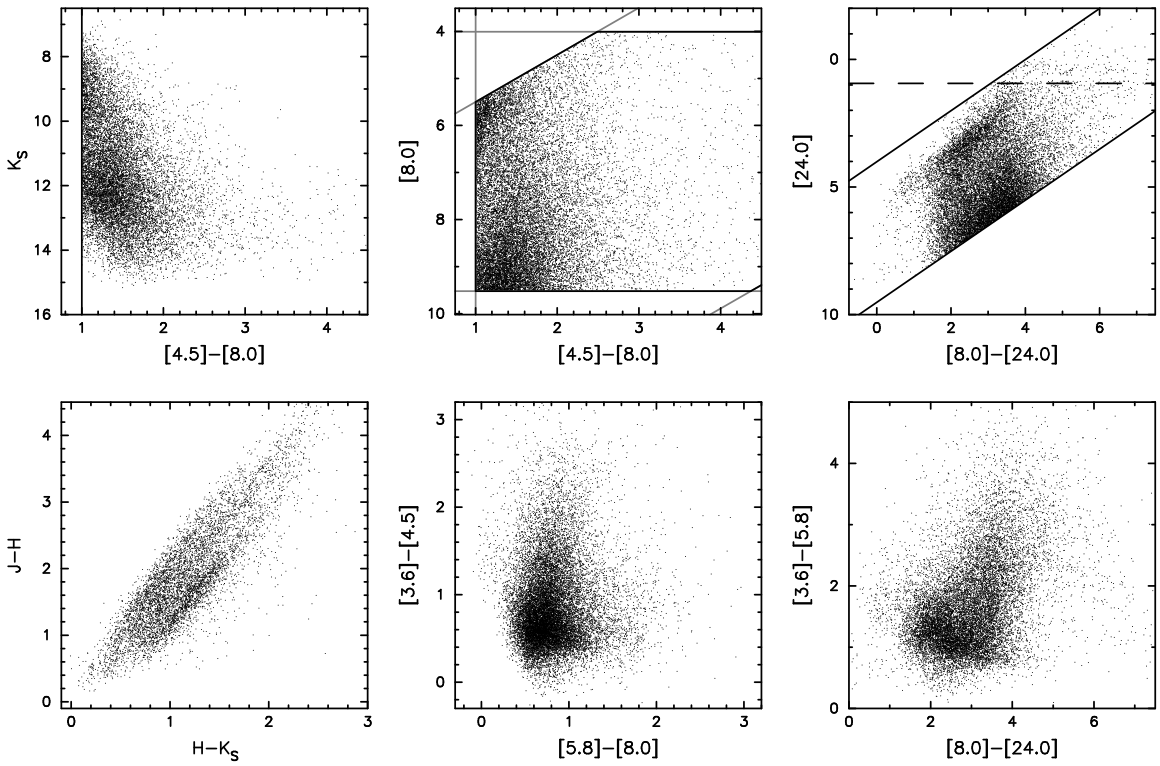

Figure 5.9: Colour/magnitude distribution of all the sources in the final red source catalogue. The solid lines outline the selection criteria from Eqs. (5.3) and (5.5). The horizontal dashed line in the top right panel shows the [24.0] magnitude limit above which MSX photometry is used if possible.

epoch fluxes[1]. The same procedure as described in §5.3.4 was carried out to ensure that these fluxes were reliable, namely computing independent mosaic fluxes and visually inspecting all sources to determine whether the second epoch fluxes were reliable. Reliable second epoch fluxes were available for 3,980 sources at 4.5 μm and for 4,331 sources at 8.0 μm. Most of the sources flagged as unreliable at 4.5 μm were above the saturation limit. The 4,455 sources with two-epoch photometry are listed in Table F.2.

The top panels in Figure 5.10 show the change in [4.5] between the two epochs, the change in [8.0], and the correlation between the change in [4.5] and [8.0]. In total, 1,004 sources (22.5 % of GLIMPSE II sources with photometry at both epochs) show a change of at least 0.3 mag at either (or both) 4.5 μm and 8.0 μm. At 4.5 μm, 308 become fainter, 298 brighter, and 398 do not have a reliable second epoch flux; at 8.0 μm, 242 sources become fainter, 586 brighter, and 176 do not have a reliable second epoch flux. The large number of unreliable fluxes at 4.5 μm is due to sources that brighten above the saturation limit in the

[1]No second epoch Point Source Catalog exists at the time of writing, because the current GLIMPSE Catalogs rely on the fact that each position is observed at least twice to increase the point source detection reliability, but GLIMPSE II second epoch observations only consist of one observation for each position

second epoch. For sources that do have reliable fluxes at both wavelengths and epochs, the top right panel of Figure 5.10 shows that in most cases the change in magnitude between the two bands is equal, and that the $[4.5]-[8.0]$ colour does not change in most cases, although there are a few outliers.

Thus, it appears that approximately 2/3 of the variable sources increase in brightness between the first and second epoch, of which half saturate at $4.5\,\mu$m in the second epoch, while only 1/3 of sources become fainter. This clear asymmetry is a selection artefact rather than a physical effect: the variable sources tend to be close to the $4.5\,\mu$m saturation limit. Therefore sources that would have become fainter in the second epoch are more likely to have been saturated during the first epoch, and therefore are less likely to be present in the red source catalogue.

The colours and magnitudes of the variables and non-variables are shown in the middle and bottom panels of Figure 5.10. The variable sources are clearly not simply a random subset of all the red sources. Instead, it appears that the variable sources represent an important fraction of the population of bluer and brighter sources seen previously in Figure 5.9. As will be discussed further in §5.4.2, these sources are likely to be AGB stars that are long period variables (LPVs). As shown by Marengo et al. (2008), AGB stars with semi-regular type variability do not have IRAC amplitudes as large as AGB stars with Mira variability, and therefore the variable sources presented here are most likely to be Mira variables. A fraction of variable stars may be mistakenly classified as non-variable if they happen to be at a similar light-curve phase at the two epochs, and therefore the fraction of variable sources should be considered a lower limit.

5.4.2 Populations

In this section, the composition of the red source catalogue is determined qualitatively and quantitatively. It is expected to contain YSOs, AGB stars, PNe, and background galaxies.

Planetary Nebulae

The colours of PNe – that is, including both the central source and the diffuse emission – are known to be very red at IRAC and MIPS wavelengths, mainly due to varying contributions from H_2, PAH, dust, and ionised gas line emission, at $8\,\mu$m (Hora et al., 2004, 2008). Therefore, distant PNe are expected to be present in the red source catalogue. Resolved PNe will

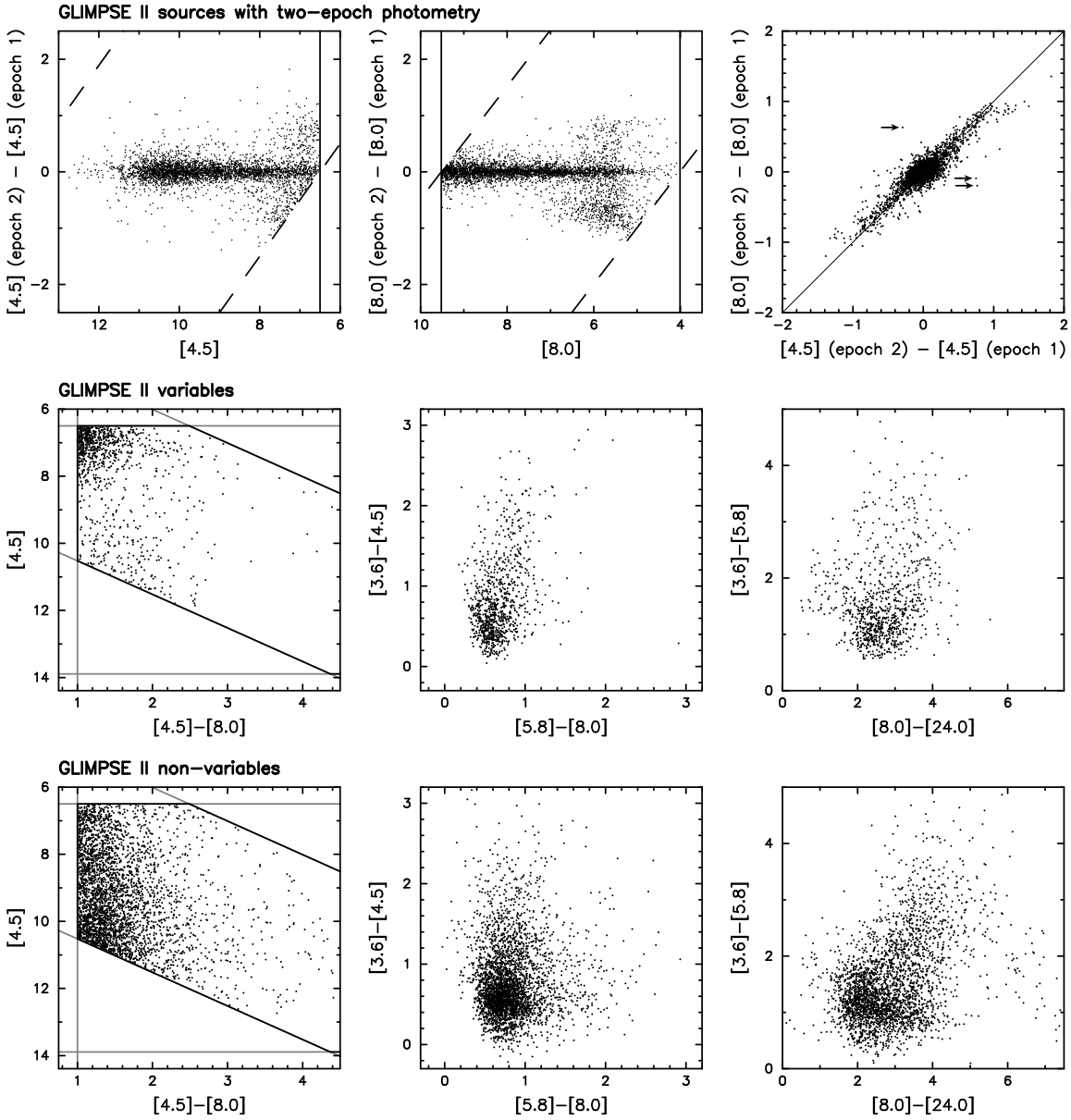

Figure 5.10: *Top* – Magnitude changes between the GLIMPSE II epoch 1 and 2 data for the red sources where observations were available at both epochs. The solid and dashed lines in the top left and top centre panels show the [4.5] and [8.0] sensitivity and saturation limits, and the solid diagonal line in the top right panel shows where the change in magnitude in equal in [4.5] and [8.0]. Most sources do not appear to change colour significantly, i.e. the magnitude change is approximately equal in both bands. However, there are exceptions to this: for example for three extreme outliers from the distribution indicated by the arrows, the colour change is so strong that it is clearly visible in 3-colour GLIMPSE images. The cause of this is not clear, but this could simply be due to blending of a variable source with a foreground or background source. *Centre* – colour/magnitude distribution of the sources which show variability by at least 0.3 mag in one or both bands. The lines are as in Figure 5.9. *Bottom* – colour/magnitude distribution of the sources which vary by less than 0.3 mag in both bands between the two epochs .

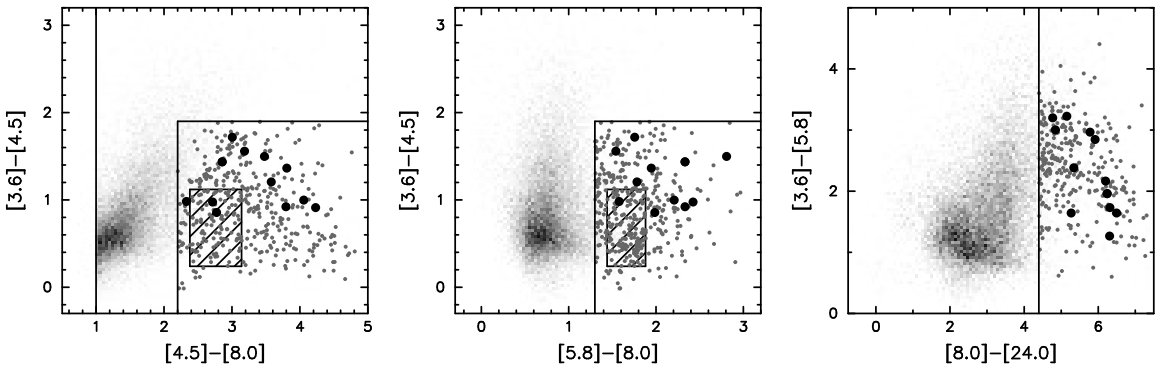

Figure 5.11: IRAC and MIPS 24 μm colour-colour diagrams of all the red sources (greyscale), those that are known PNe (filled circles), and those that have similar colours to known PNe (dark grey points). The hatched rectangle shows the location of the Galactic PNe from Cohen et al. (2007), and the solid lines show the selection criteria to select sources with colours similar to those of the known PNe.

not be present, as extended sources are excluded.

The red source catalogue was cross-correlated with the Strasbourg-ESO Catalogue of Galactic Planetary Nebulae (Acker et al., 1992), the sample of southern PNe from Kimeswenger (2001), and the sources in the RMS survey confirmed as PNe (Hoare et al., 2004), which contain 1143, 995, and 76 sources respectively. Of these, only 2, 5, and 6 are present in the final red source catalogue respectively. Figure 5.11 shows the location of these PNe in colour-magnitude and colour-colour space relative to all the sources in the red source catalogue. The PNe are clearly amongst the reddest sources in $[4.5]-[8.0]$, $[5.8]-[8.0]$ and $[8.0]-[24.0]$. The colours in $[3.6]-[4.5]$ vs. $[5.8]-[8.0]$ are in good agreement with the colours of PNe reported by Hora et al. (2004), Cohen et al. (2007), and Hora et al. (2008).

It is likely that previously unknown distant PNe are missing from the three catalogues used for the cross-correlation. An upper limit on the number of PNe in the red source catalogue can be estimated by counting all red sources that fall within the same region of colour-colour space as the known PNe. To do this, all sources satisfying:

$$\begin{cases} [3.6]-[4.5] & < & 1.9 \\ [4.5]-[8.0] & > & 2.2 \\ [5.8]-[8.0] & > & 1.3 \\ [8.0]-[24.0] & > & 4.4 \end{cases} \tag{5.6}$$

were selected. For any given source, only the selection criteria that could be applied based on the data available were used: for example, for sources with no $[3.6]$ magnitude, only the last

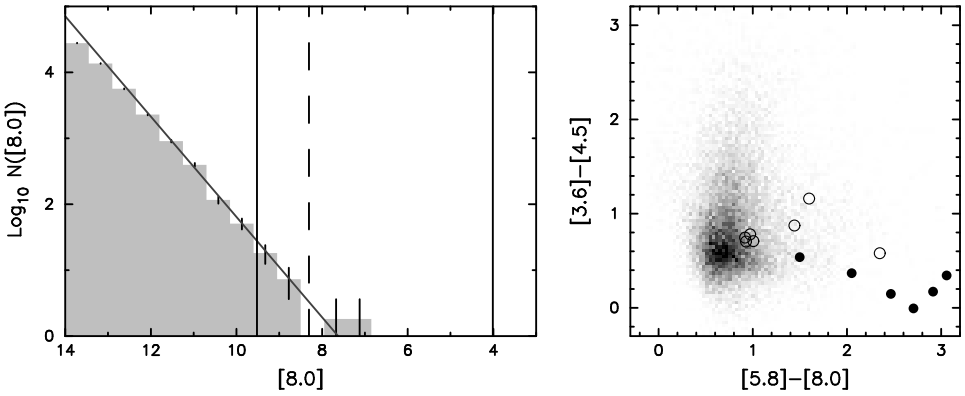

Figure 5.12: *Left* – the grey histogram shows the number density of SWIRE galaxies as a function of [8.0] magnitude. The vertical solid lines show the range of magnitudes used to select the red sources in this chapter, and the vertical dashed line shows the approximate SWIRE saturation level. The solid grey line shows the best fit to the source counts below the SWIRE saturation level. This line is used to extrapolate the expected number of galaxies above the saturation level. *Right* – IRAC colour-colour diagram of all red sources (greyscale), and the SWIRE galaxies which would have satisfied the brightness criterion in the absence of interstellar extinction. The empty circles show AGN, which have dust-dominated SEDs at IRAC wavelengths, and the filled circles show 'normal' galaxies, which have PAH-dominated SEDs in the same wavelength range.

three criteria were used. In total, 458 sources were selected. These selection criteria will also include objects which are not PNe (such as YSOs), but provide an *upper limit* of 2.4 % on the fraction of PNe in the red source catalogue.

Galaxies and AGNs

In order to estimate the fraction of galaxies and dusty active galactic nucleis (AGNs) present in the red source catalogue, data from the *Spitzer* Wide-Area Infrared Extragalactic Survey (SWIRE; Lonsdale et al. 2003) were used. These data consists of IRAC and MIPS observations of six patches of sky covering in total 63.2 deg^2 (at IRAC wavelengths). The Spring 2005 Catalogs for the Lockman, ELAIS N1, ELAIS N2, and XMM_LSS fields, and the Fall 2005 Catalogs for the CDFS and ELAIS S1 fields were used.

Sources detected at both 4.5 and 8.0 μm were selected from the SWIRE Catalogs. Since the red source catalogue only includes point sources, only sources with an extended source flag of -1, 0, or 1 at both these wavelengths (i.e. point-like, indeterminate, or slightly extended) were selected, and the IRAC aperture fluxes were used. Foreground stars were removed by selecting only sources with $[5.8]-[8.0] > 0.5$. The [8.0] distribution of the sources satisfying these criteria is shown in Figure 5.12 along with the approximate saturation limit for SWIRE and the brightness criteria from Eq. (5.3). Only 13 sources would have been bright enough to

be selected, in the absence of interstellar extinction, of which 6 are known 'normal' galaxies with PAH-dominated mid-infrared colours, and the remaining 7 are known active galaxies (specifically QSOs and Seyfert II galaxies), with dust-dominated mid-infrared colours. The IRAC colours of these sources are shown in Figure 5.12.

Extrapolating the distribution of sources above the SWIRE saturation level (as shown in Figure 5.12) suggests that approximately 16±4 sources might have been 'detected' in total in the absence of saturation. The GLIMPSE survey area is 274 deg^2, so the number of 'detected' galaxies should be scaled accordingly, assuming that the density of extra-galactic sources in the six SWIRE patches is similar to that in the GLIMPSE survey area (in the absence of interstellar extinction). This results in an estimated 70 ± 17 galaxies in the red source catalogue. This number is an upper limit, as for a large fraction of the GLIMPSE area, the extinction through the Galaxy is likely to make these sources too faint to be included in the red source catalogue. Therefore, *at most* 0.4 % of sources in the red source catalogue are likely to be background extragalactic sources. This upper limit applies only to the red source catalogue presented in this chapter, so the fraction of galaxies in the entire GLIMPSE Catalogs is likely to be different if for example the 8 μm flux is not required to be larger than 10 mJy.

AGB stars

In order to understand where various types of AGB stars should lie in IRAC and MIPS 24 μm colour-colour and colour-magnitude space, the red source catalogue was initially cross-correlated with catalogues of known C- and O-rich AGB stars (e.g. Lindqvist et al., 1992; Chengalur et al., 1993; Sjouwerman et al., 1998; Alksnis et al., 2001). However, no previously known C-rich, and only 16 previously known O-rich AGB stars were found. Instead, the colours and magnitudes of AGB stars were analysed using known AGB stars in the 'Surveying the Agents of a Galaxy's Evolution' (SAGE) survey of the LMC (Meixner et al. 2006; PID 20203).

The SAGE IRAC and MIPS magnitudes for AGB stars from Srinivasan et. al (2008, in preparation) were used. These include 'standard' C- and O-rich AGB stars as well as 'extreme' AGB stars[2]. The latter, sometimes referred to as 'obscured' AGB stars, are also C- and O- rich AGB stars, but with very high mass-loss rates, and therefore large amounts of circumstellar dust. In the remainder of this chapter, 'Extreme' AGB stars will be referred to as 'xAGB stars',

[2]Red sources that were excluded in their analysis (Srinivasan, private communication, 2008) are used here, and 29 'extreme' AGB stars that were likely LMC YSOs were removed following a visual inspection

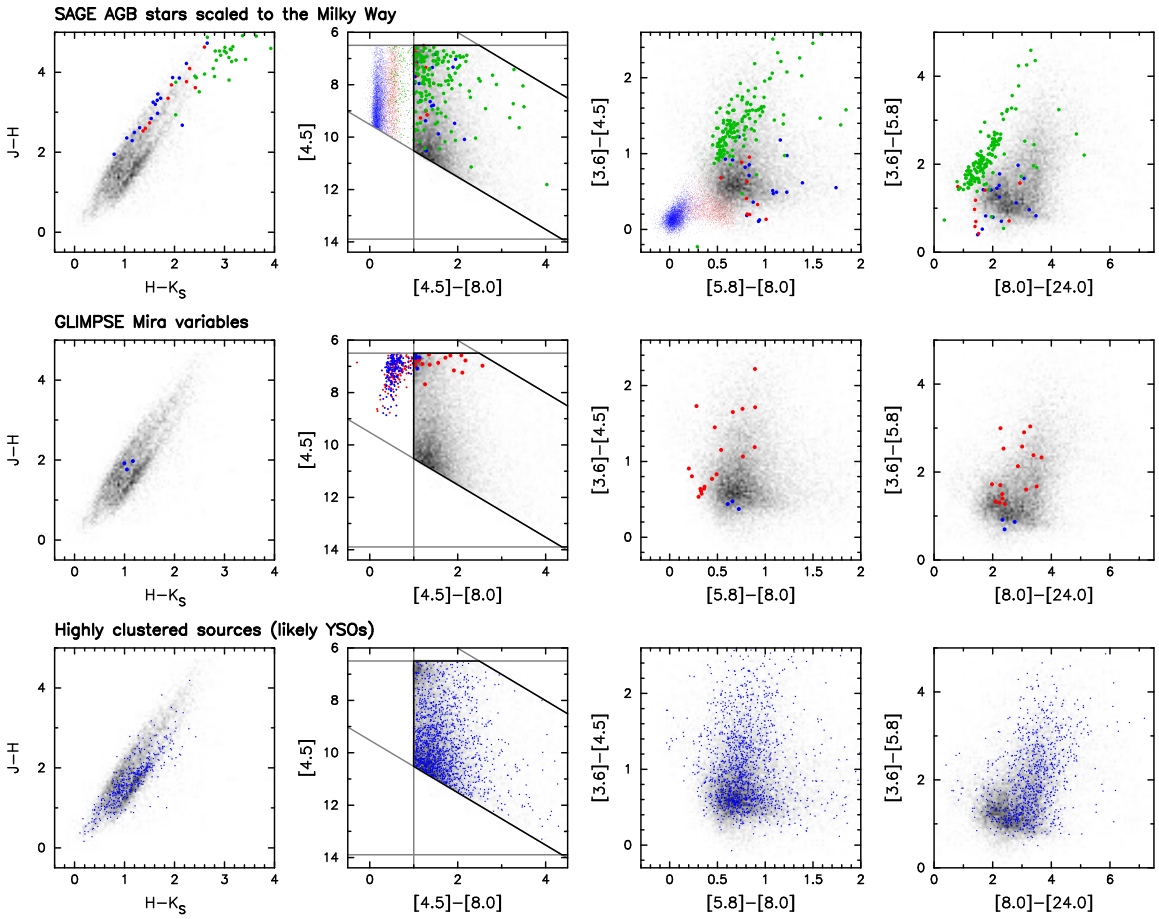

Figure 5.13: Location of AGB stars and likely YSOs in IRAC and MIPS colour-magnitude and colour-colour space. In all plots, the background greyscale shows all red sources, and the solid lines are as in Figure 5.9. *Top:* location of the SAGE LMC AGB stars, scaled to random locations in the Milky-Way, that satisfy the brightness and colour selection criteria from Eqs. (5.3) and (5.5). C-rich sAGB stars are shown in red, O-rich sAGB stars in blue, and xAGB stars in green. The smaller points in the [4.5] vs. [4.5] − [8.0] and the [3.6] − [4.5] vs. [5.8] − [8.0] diagrams are the sources that do not satisfy the colour selection criterion. *centre:* Mira variables from the GCVS (red) and OGLE (blue), identified amongst the GLIMPSE sources that satisfy the brightness, quality, and colour selection criteria. The smaller points in the [4.5] vs. [4.5] − [8.0] diagram are the sources that do not satisfy the colour selection criterion. *Bottom:* highly clustered red sources (blue). In all of the JHK$_s$ plots, sources that are not detected in J, H, or K$_s$ are not shown.

and 'Standard' AGB stars as 'sAGB stars'. The term 'AGB stars' will be used when referring to both xAGB and sAGB stars.

The LMC AGB stars were assumed to be situated at a distance of 50.1 kpc (Alves, 2004, and references therein). Using GLIMPSE data, Benjamin et al. (2005) showed that red giant stars in the Milky-Way are distributed in an exponential disk with a scale length of 3.9 kpc. The AGB stars were assumed to be similarly distributed, and their positions were randomly sampled in such a disk, with an exponential vertical distribution that had a scaleheight of 300 pc. Using this 3-D distribution, 41 % of AGB stars fell inside the GLIMPSE survey area (as defined in §5.2.1). The magnitudes were scaled appropriately, and interstellar extinction was applied using an approximate extinction-distance relation of 1.9 mag/kpc (Allen, 1973), using the extinction law derived by Indebetouw et al. (2005) for JHK_s and IRAC wavelengths, and assuming $A_{24\mu m}/A_V \sim 0.04$, by extrapolation of the mid-infrared interstellar extinction law found by Lutz (1999). Only sources that matched the selection criteria described in §5.3.2 were selected.

The SAGE sensitivity limits (17.47 and 14.23 at 4.5 and 8.0 μm respectively) are 3-4 magnitudes lower than the flux requirements from §5.3.2, so that the faintest SAGE sources were still fainter than the sensitivity requirements from Eq. (5.3) after placing the synthetic AGB stars at positions in the Milky-Way and applying extinction, except for the few sources that were placed at distances very close to the Sun. Therefore, this method should be sensitive to AGB stars in all of the colour-magnitude space covered by the red source catalogue. For the remainder of this section, these re-scaled and reddened LMC AGB stars will be referred to as the *synthetic* AGB stars. The main caveat of this approach is that it is not clear whether the intrinsic IRAC and MIPS 24 μm colours of AGB stars are identical in the LMC and the Milky-Way. However, any differences between the intrinsic colours between the LMC and Milky-Way are likely to be much less important than the uncertainty in the extinction-distance relation and in the extinction law assumed.

The location of the synthetic AGB stars that fall in the survey area in colour-magnitude and colour-colour space is shown in Figure 5.13: just under half (46 %) satisfy the brightness selection criteria in Eq. (5.3), of which 72 % are O-rich sAGB stars, 24 % are C-rich sAGB stars, and 4 % are xAGB stars. Under 1 % of all AGB stars that fall in the survey area and that satisfy the brightness selection criteria further satisfy the colour selection criterion from Eq. (5.5). Of

these, 83 % are xAGB stars, 10 % are O-rich sAGB stars, and 7 % are C-rich sAGB stars. These account for 24 %, 0.1 %, and 0.4 % of all xAGB, O-rich sAGB, and C-rich sAGB stars that fall inside the survey area respectively. Therefore, xAGB stars are likely to represent the majority of AGB stars in the red source catalogue, as they are much redder on average than sAGB stars. The xAGB stars that are present in the catalogue likely represent a quarter of all xAGB stars that fall in the survey area, while the sAGB stars only represent a very small fraction (< 0.5 %) of those in the survey area, because most are bluer than $[4.5] - [8.0] = 1$.

Since xAGB stars are luminous, they are more likely to be present at the bright end of the red source sample. In fact, a large fraction of xAGB stars appear to share the same region of [4.5] and [8.0] colour-magnitude space as the variable stars shown in Figure 5.10, which can be explained if the variable stars in this region are AGB stars with Mira variability. Evidence that this is the case is shown in the central panel of Figure 5.13, which shows the location of 274 GLIMPSE Mira variables, identified amongst the GLIMPSE sources satisfying Eqs. (5.3) and (5.4) using the Combined General Catalog of Variable Stars v4.2 (Samus et al., 2004) and the OGLE Catalog of Mira variables in the Galactic Bulge (Groenewegen & Blommaert, 2005). Of these, 25 also satisfy the colour selection from Eq. (5.5) and therefore are in the red source catalogue. Only three of the 25 fall in the region covered by the two epoch GLIMPSE II observations, but all three are classified as variable at 4.5 and 8.0 μm based on the analysis in §5.4.1.

In J−H vs. H−K_s colour-colour space, the synthetic sAGB stars tend to occupy bluer colours of H−K_s. The xAGB stars tend to have large J−H values, suggesting very high values of the interstellar extinction. In IRAC colour-colour space, the AGB stars are not easily distinguishable from the whole population of red sources. However, once MIPS 24 μm data are included, the AGB stars tend to have bluer $[8.0] - [24.0]$ colours on average than the overall red population (e.g. only very few synthetic AGB stars are seen to have $[8.0] - [24.0] > 3$).

In order to roughly estimate the fraction of AGB stars in the red source catalogue, it is necessary to know the ratio of the total number of AGB stars in the Milky-Way to the total number of AGB stars in the LMC. Assuming that the ratio of AGB to all stars is approximately the same for both galaxies, and that both have similar star formation histories, this ratio can be derived from the ratio of the total stellar mass in each galaxy (excluding the gas and dark matter mass). The total stellar mass of the Milky-Way is of the order of $4.8 - 5.5 \times 10^{10}\,M_\odot$

(Flynn et al., 2006), and that of the LMC is of the order of $2.7 \times 10^9\,M_\odot$ (van der Marel et al., 2002), implying a ratio in stellar masses and therefore in the number of AGB stars of approximately 20. Since 177 synthetic AGB stars are 'selected' according to the brightness and colour selection criteria in Eqs. (5.3) and (5.5), this suggests that approximately $177 \times 20 = 3,540$ AGB stars may be present in the red source catalogue (i.e. 19 % of all red sources).

Young stellar objects

In order to understand where YSOs lie in near- and mid-infrared colour and magnitude space, sources that are highly likely to be YSOs need to be identified in the red source catalogue. However, catalogues of well known Galactic YSOs, such as confirmed massive YSOs from the RMS survey, cannot be used, as these surveys are not as deep as GLIMPSE and would appear to show that YSOs are more likely to be present at the bright end of the red source catalogue.

Instead, a method involving only the red sources presented in this chapter was used. As described in §5.4.1, a large number of clusters are present in the red source catalogue. However, AGB stars and PNe are not expected to be clustered in this way, and galaxies represent less than 0.5% of the sources (§5.4.2). Therefore clustered objects have a high probability of being YSOs. By requiring the second closest neighbour of a source to be less than $2'$, only sources in the regions of highest source density were selected. These include for example a number of sources in the NGC 6611 cluster in the Eagle Nebula (M16; e.g. Indebetouw et al., 2007).

The distribution of these sources in colour-colour and colour-magnitude diagrams is shown in the bottom panel of Figure 5.13. In the J−H vs. H−K_s diagram, the probable YSOs appear to occupy preferentially redder values of H−K_s. In the [4.5] vs. [4.5] − [8.0] colour magnitude diagram, the distribution of probable YSOs matches that of the overall distribution of red sources, with the exception of the bright blue peak where AGB stars are expected to lie. In [3.6] − [4.5] vs. [5.8] − [8.0] colour-colour space, the clustered sources are virtually indistinguishable from the overall red source sample. Finally, in [3.6] − [5.8] vs. [8.0] − [24.0] colour-colour space, the clustered sources do not match the distribution of all the red sources, as there is a deficit of clustered sources for $[8.0] - [24.0] \lesssim 2.5$.

5.4.3 Separation of YSOs and AGB stars

In this section, the relative fraction of AGB stars and YSOs in the red source catalogue is estimated, using simple colour-magnitude selection criteria to separate the two populations as much as possible. The purpose of this analysis is not to provide reliable selection criteria for the two populations, but simply to estimate the relative importance of each population. Therefore, the separation is only approximate, and there is likely to be contamination in both directions. A reliable separation of the two populations would require additional data, such as spectroscopic observations, which are not available here.

As shown in Figure 5.13, xAGB stars account for the brighter and bluer peak seen in $[8.0]$ or $[4.5]$ vs. $[4.5]-[8.0]$ colour-magnitude diagrams. Therefore, all sources with $[4.5] \leq 7.8$ are classified as xAGB star candidates, although it should be noted that this criterion will inevitably include a fraction of luminous YSOs. The angular distribution of these sources is shown in the top panel of Figure 5.14, and does not show any clustering, suggesting that the fraction of YSOs with $[4.5] \leq 7.8$ is small. The number density of sources increases towards the Galactic centre, and a clear peak is seen at the Galactic centre itself, suggesting that this population of sources is intrinsically very luminous, and is seen out to at least 8.5 kpc. In the GLIMPSE II region, 52 % of sources selected as xAGB stars are variable, and 68 % of variable stars are xAGB stars.

Sources with $[4.5] > 7.8$ are likely to consist mostly of sAGB stars and YSOs. After removal of most of the xAGB stars as described above, both distributed and clustered sources remain. A small sample of the distributed sources was extracted by selecting sources seen at high latitudes ($|b| > 1.5°$) in the GLIMPSE II region, where there is no indication of ongoing star formation. These are most likely to be sAGB stars. After examining the colours of these sources, it was apparent that a number of these had IRAC and MIPS colours consistent with the peak of sources seen in Figure 5.13 for $[8.0]-[24.0] < 2.5$, where there was also a deficit of YSO candidates (c.f. §5.4.2). Since the red sources were all required to have $[4.5]-[8.0] \geq 1$ (Eq. [5.5]), sources with $[8.0]-[24.0] < 1.9$ have SEDs with spectral indices that are lower between 8 and 24 μm than between 4.5 and 8 μm. This behaviour is not typical of YSO SEDs, and it indicates that the majority of the dust lies very close to the photosphere of the central source, as is more likely to be the case for AGB stars. A number of the high latitude stars also appeared to have $1.9 < [8.0]-[24.0] < 2.5$. Therefore, a cut-off value of $[8.0]-[24.0] = 2.5$

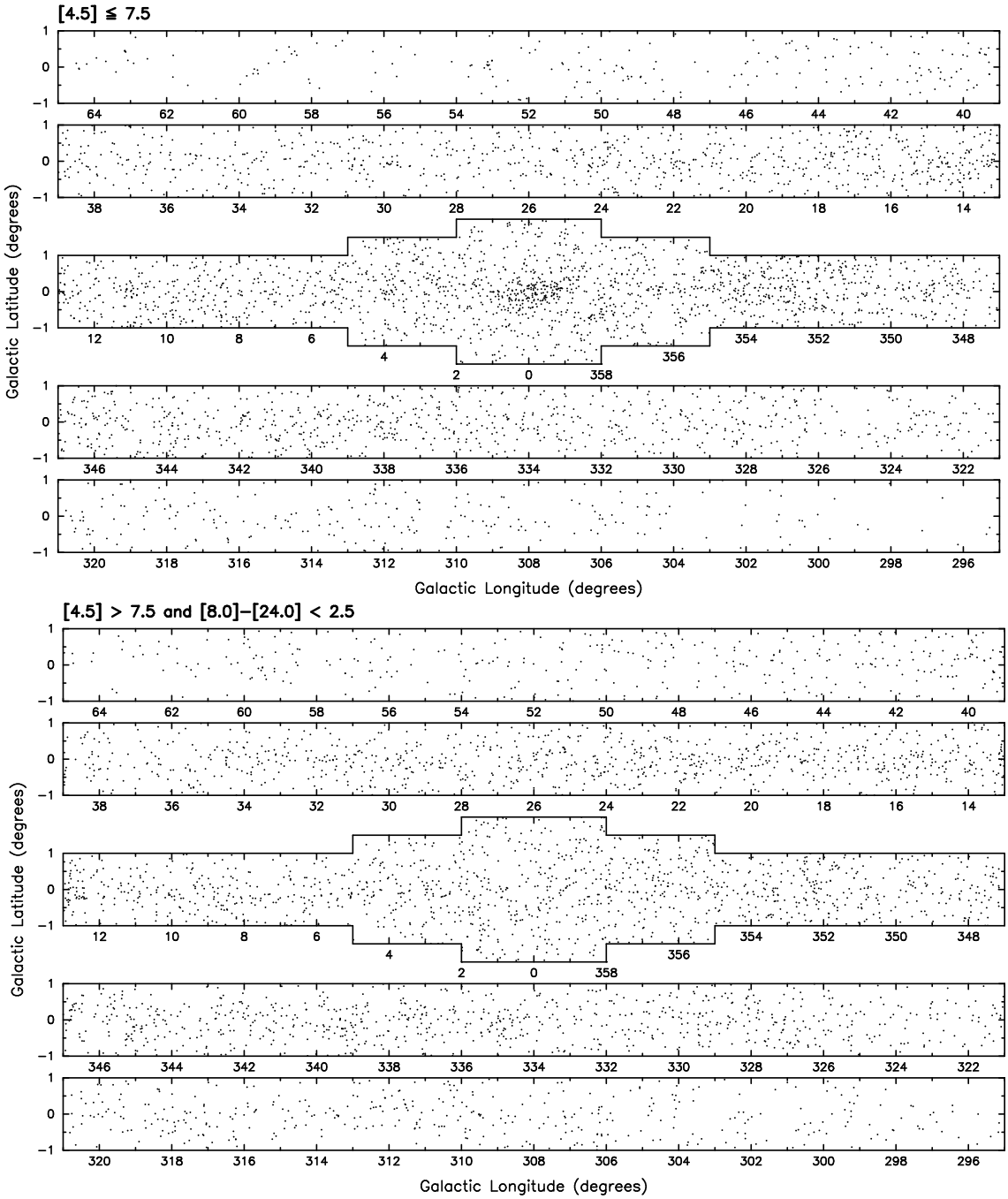

Figure 5.14: Angular distribution of the colour selected populations consisting mostly of xAGB stars (*top*), and sAGB stars (*bottom*).

was chosen to separate candidate sAGB stars from candidate YSOs. The angular distribution of red sources detected at 24 μm and with $[8.0] - [24.0] < 2.5$ is shown in the bottom panel of Figure 5.14. These sources appear to be uniformly distributed in the Galactic plane, confirming that these are likely to be mostly sAGB stars. The number density of these sources falls off somewhat slower with Galactic longitude than the xAGB star candidates, consistent with their lower luminosity and consequently closer distance. In contrast, the distribution of red sources with $[8.0] - [24.0] \geq 2.5$, shown in the top panel of Figure 5.15, shows more clustering, in agreement with their classification as candidate YSOs. The absence of a peak at the Galactic centre for sAGB stars can be explained if these are not seen as far out as the Galactic centre. However, while they are indeed fainter than xAGB stars, the analysis in §5.4.5 shows that they should still be detectable beyond 8.5 kpc, so it is likely that this is instead an artefact due to the requirement for a valid MIPS 24 μm magnitude to carry out the $[8.0] - [24.0]$ colour selection (see below).

This criterion used to separate sAGB stars from YSOs is similar to the $[8.0] - [24.0] > 2.2$ criterion suggested by Whitney et al. (2008, equation (3)) for a stringent removal of AGB stars. This simple colour selection only approximately separates AGB stars and YSOs, so that there is likely to be contamination in both directions. For example, an examination of the IRAC and MIPS colours of spectroscopically confirmed AGB stars in Serpens suggests that the $[8.0] - [24.0] < 2.5$ criterion does appear to be successful in selecting a large fraction of AGB stars, but inevitably also selects a small fraction of YSOs (Paul Harvey and Neal Evans, 2008, private communication). Nevertheless, as the angular distributions of the various populations show, this separation is likely to be sufficient for the purpose of estimating the relative fraction of AGB stars and YSOs in the red source catalogue.

Sources with $[4.5] > 7.8$ and with no fluxes at MIPS 24 μm cannot be separated into sAGB stars and YSOs as suggested above. These sources show very strong clustering, as shown in the bottom panel of Figure 5.15. The two main reasons that some red sources do not have fluxes at 24 μm are either that they lie on top of very bright (and in some cases saturated) diffuse emission, which lowers the point source sensitivity, or that the photometry could not be carried out due to blending of multiple sources, since MIPS 24 μm has a lower angular resolution than IRAC. High stellar densities and bright 24 μm diffuse emission are most likely to occur in massive star formation regions and towards the Galactic centre. Thus, it seems likely that most of the clustered sources that do not have MIPS 24 μm fluxes are YSOs, with

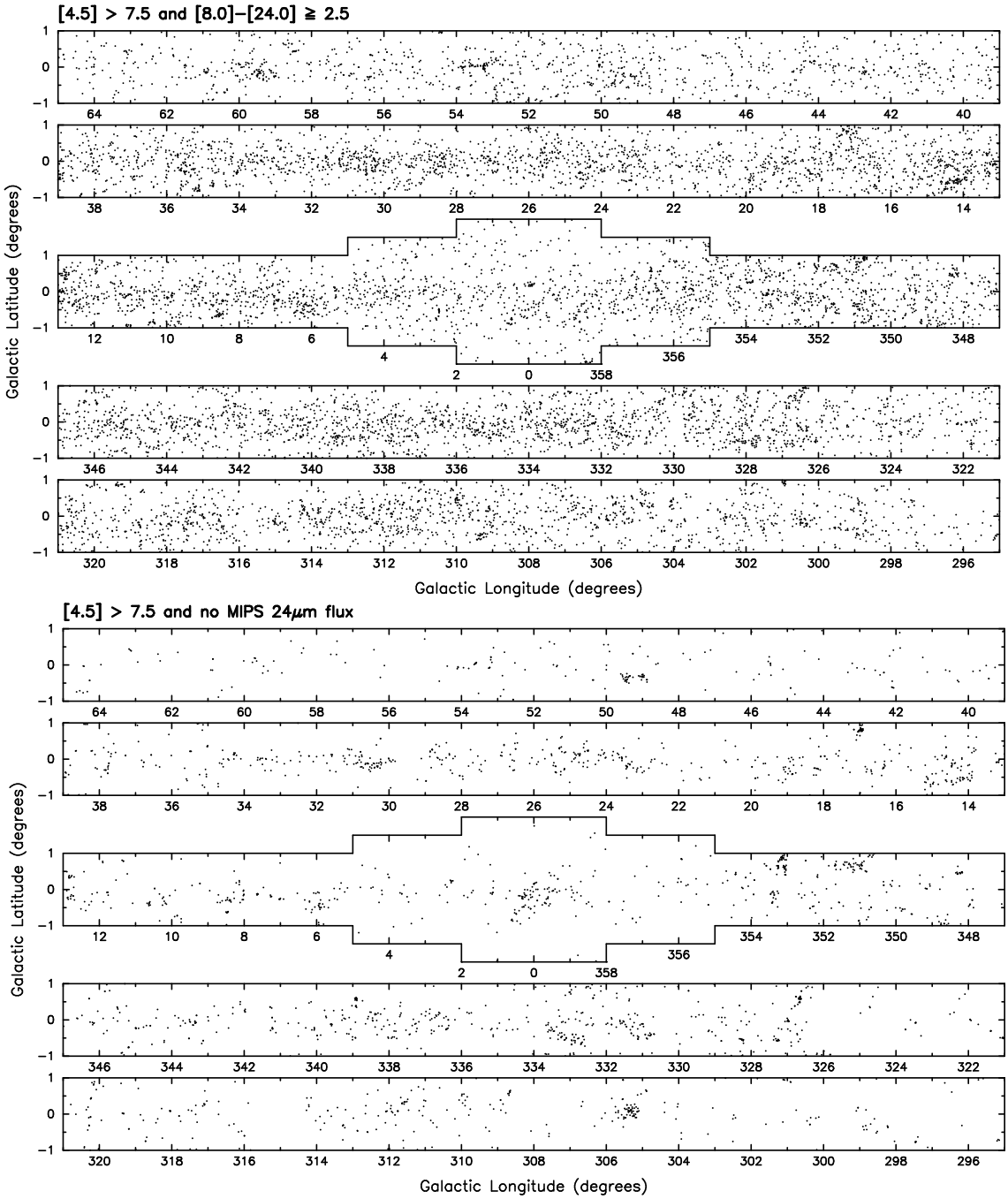

Figure 5.15: Angular distribution of the colour selected populations consisting mostly of YSOs (*top*), and the sources with no MIPS 24 μm photometry (*bottom*), which also consist mostly of YSOs.

the exception of the concentration of sources at the Galactic centre, which may be the missing peak of sAGB stars mentioned previously.

To summarise, sources with

$$[4.5] \leq 7.8 \tag{5.7}$$

are classified as candidate xAGB stars, sources with

$$[4.5] > 7.8 \text{ and } [8.0] - [24.0] < 2.5 \tag{5.8}$$

are classified as candidate sAGB stars, and sources with

$$[4.5] > 7.8 \text{ and } [8.0] - [24.0] \geq 2.5. \tag{5.9}$$

are classified as candidate YSOs. Sources with $[4.5] > 7.8$ and no MIPS 24 μm detections cannot be separated using the above criteria, but are likely to be dominated by highly clustered YSOs in massive star formation regions. Therefore, for the remainder of this section, these are classified as candidate YSOs.

Figure 5.16 shows the colour-colour and colour-magnitude distributions of the candidate xAGB stars, the candidate sAGB stars, and the candidate YSOs. The J−H vs. H−K_s diagrams show that the majority of sources in the three populations appear to have different near-infrared colours. The candidate xAGB stars have a larger extinction, consistent with the fact that these sources are on average more luminous than sAGB stars and are therefore seen out to larger distances. The candidate sAGB stars have a bluer H−K_s colour than the candidate YSOs. In fact, the JHK_s colours of these three populations are in good agreement with those of the synthetic xAGB stars, sAGB stars, and the clustered YSOs shown in Figure 5.13. The [4.5] magnitude distribution of the sAGB stars and YSOs also differs: these show a quasi-uniform distribution of sources as a function of [4.5], while the candidate YSOs show a clear increase in the number of sources towards fainter values of [4.5]. Finally, the distributions of the three populations in IRAC colour-colour space overlap, but are nevertheless distinctly different.

Both the angular distribution and the colours of the various populations suggest that these are indeed mostly composed of xAGB stars, sAGB stars, and YSOs. In total, 7,300 and 11,649 sources are classified as candidate AGB stars and YSOs respectively, although it should be stressed that the above separation is very approximate, and there is likely to be contamination

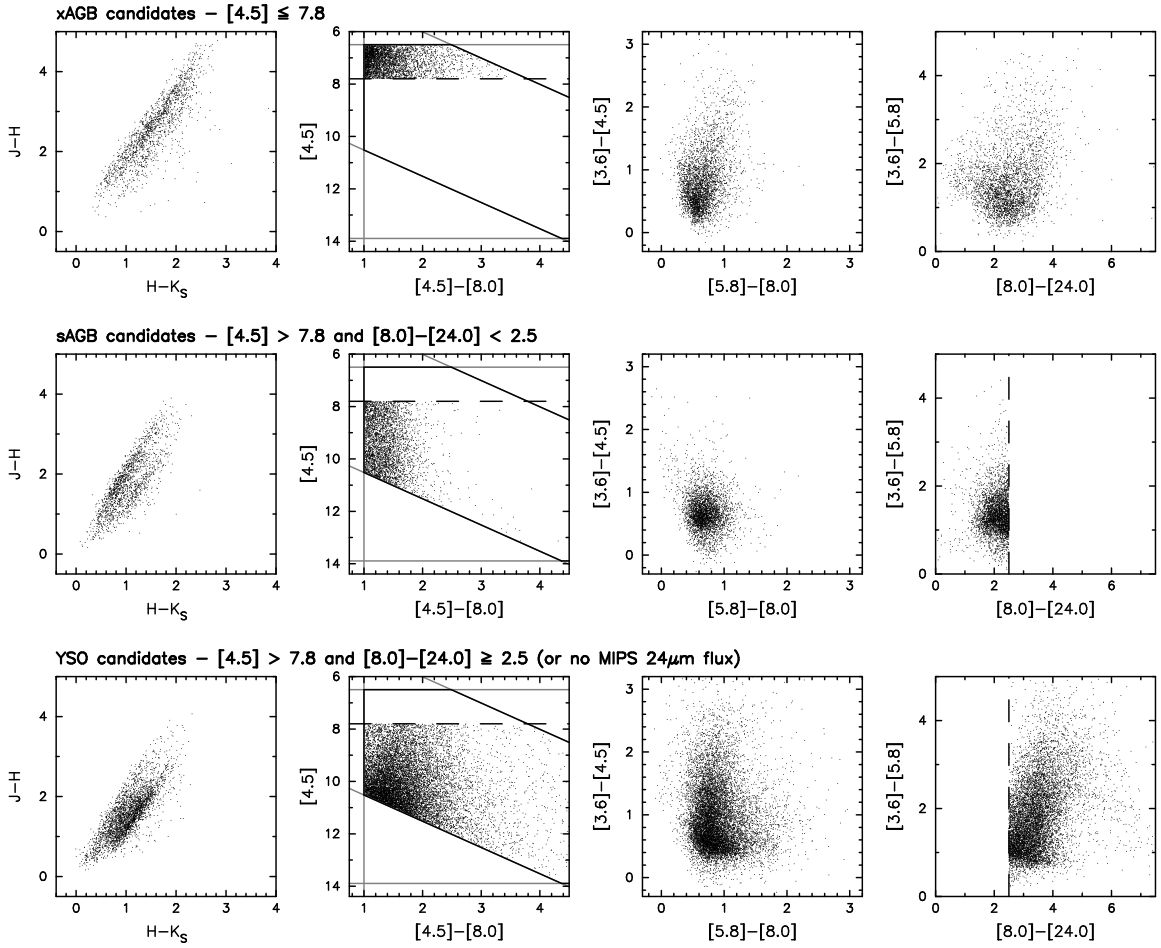

Figure 5.16: Colour-magnitude and colour-colour diagrams for the populations consisting mostly of xAGB stars (*top*), sAGB stars (*centre*), and YSOs (*bottom*). The solid lines are as in Figure 5.9. The dashed lines show the selection criteria used to separate the populations.

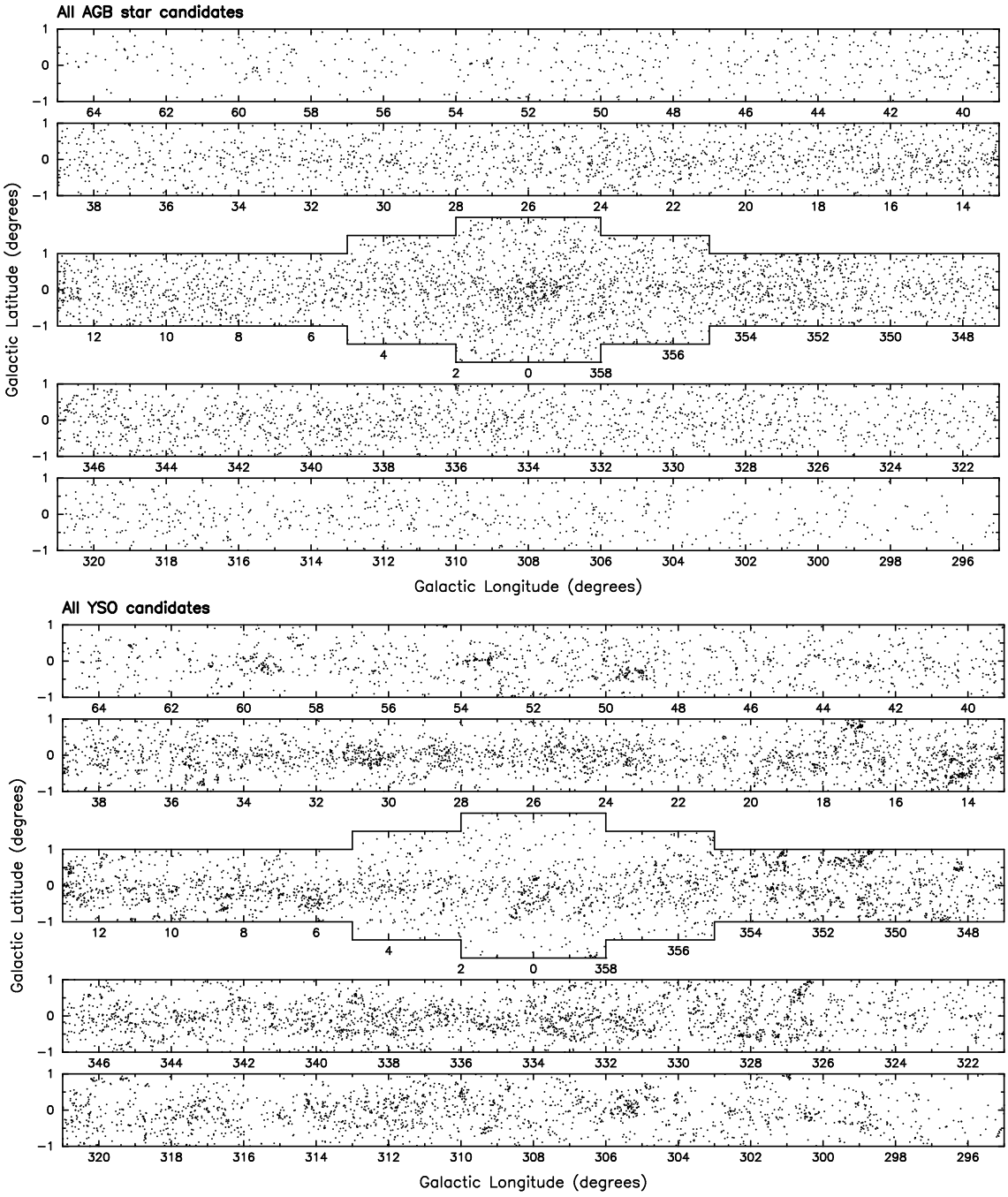

Figure 5.17: Angular distribution of all the AGB candidates (*top*) and YSO candidates (*bottom*).

in both samples. Taking into account that the separation is uncertain, especially for sources with no MIPS 24 μm fluxes, approximately 30 to 50 % in the red source catalogue are likely to be AGB stars, and 50 to 70 % are likely to be YSOs. Figure 5.17 shows the angular distribution of all the AGB and YSO candidates, and shows that the two populations are reasonably well separated by the simple criteria provided in this section.

5.4.4 Angular Distribution of AGB stars

While the angular distribution of candidate YSOs appears highly clustered, the distribution of candidate AGB stars appears to be fairly smooth. In fact, the longitude and latitude distribution can be well approximated by a simple function of the form:

$$\Sigma(\ell, b) = \Sigma_0 \exp\left(-|\ell|/\ell_0\right) \exp\left(-|b|/b_0\right) \tag{5.10}$$

To fit this function to the distribution of sources, the surface density of all candidate AGB stars was estimated in 130 longitude bins (1° wide) and 9 latitude bins (0.33° high), and Poisson uncertainties were calculated for each bin. The distribution of AGB stars is shown in Figure 5.18, with the best fit over-plotted. The best fit parameters were found to be $\Sigma_0 = 100 \pm 3\,\mathrm{deg}^{-2}$, $\ell_0 = 14.1 \pm 0.3°$, and $b_0 = 0.418 \pm 0.014°$, and the reduced χ^2 of the fit was found to be 1.479. This fit is therefore a good statistical description of the surface density of the AGB stars inside the GLIMPSE area. However, the fit tends to underestimate the surface density of AGB stars for $|b| > 1.33°$. In addition, the central peak in the density of AGB stars seen in Figure 5.17 cannot be explained by such a simple function. Finally, this function is only an approximation to the surface density of AGB stars that are present in the red source catalogue presented in this chapter, rather the surface density of all AGB stars in the GLIMPSE Catalogs, which is likely to be much higher due to the large number of sAGB stars that are likely to have $[4.5] - [8.0] < 1$.

5.4.5 Distance-Luminosity sensitivity

In order to determine the distance range in which the different types of AGB stars in the red source catalogue might lie, the average [4.5] and [8.0] magnitudes of xAGB and sAGB stars in the LMC with $[4.5] - [8.0] \geq 1$ were computed, as well as their standard deviation. The distance range where these 'average' AGB stars would satisfy the brightness criteria for

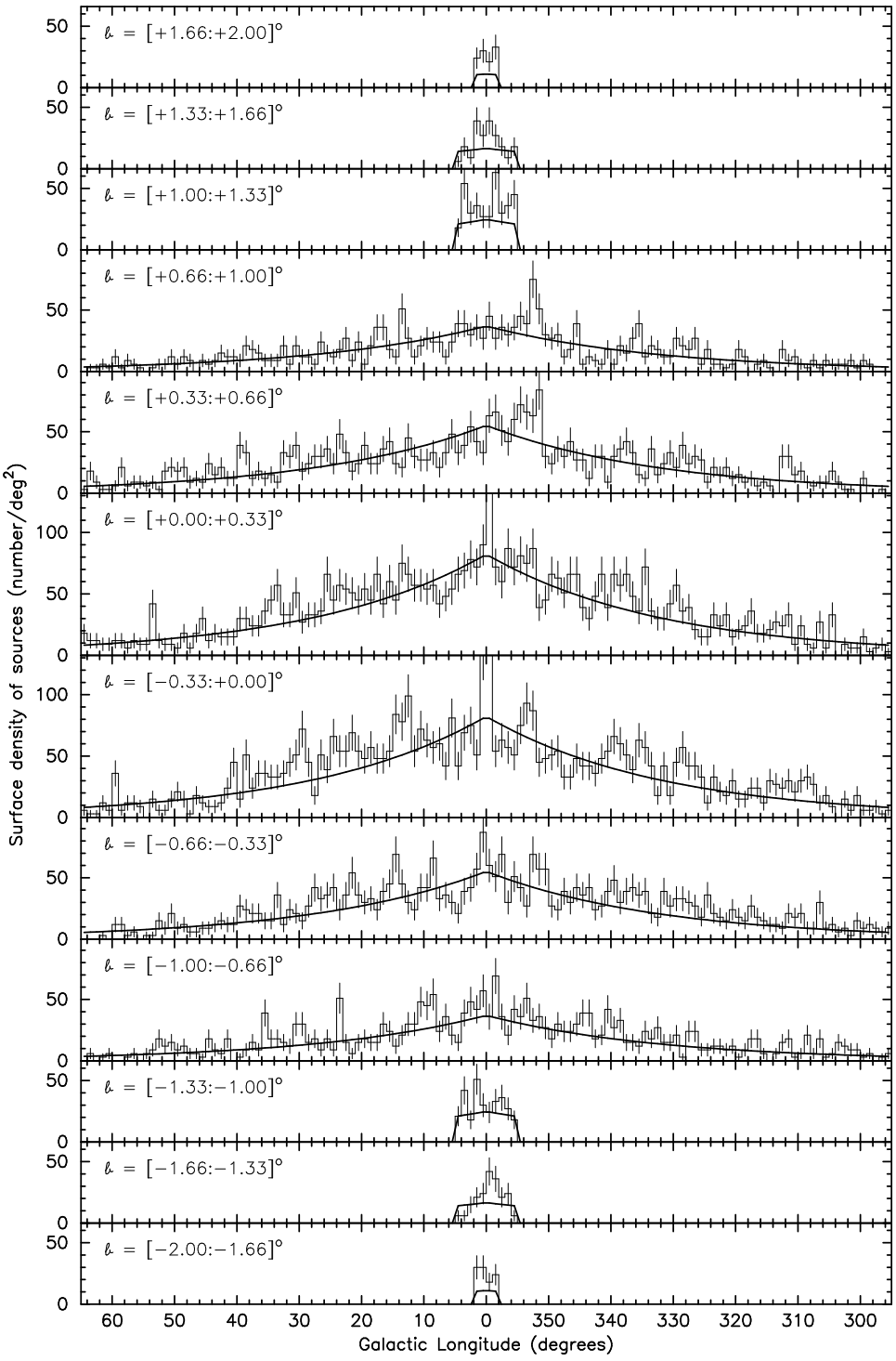

Figure 5.18: Surface density of the candidate AGB stars as a function of Galactic longitude and latitude (histogram) with the best fit analytical distribution shown (solid line). The error bars are Poisson uncertainties. The analytical form of the best fit as well as the best fit parameters are given in §5.4.4.

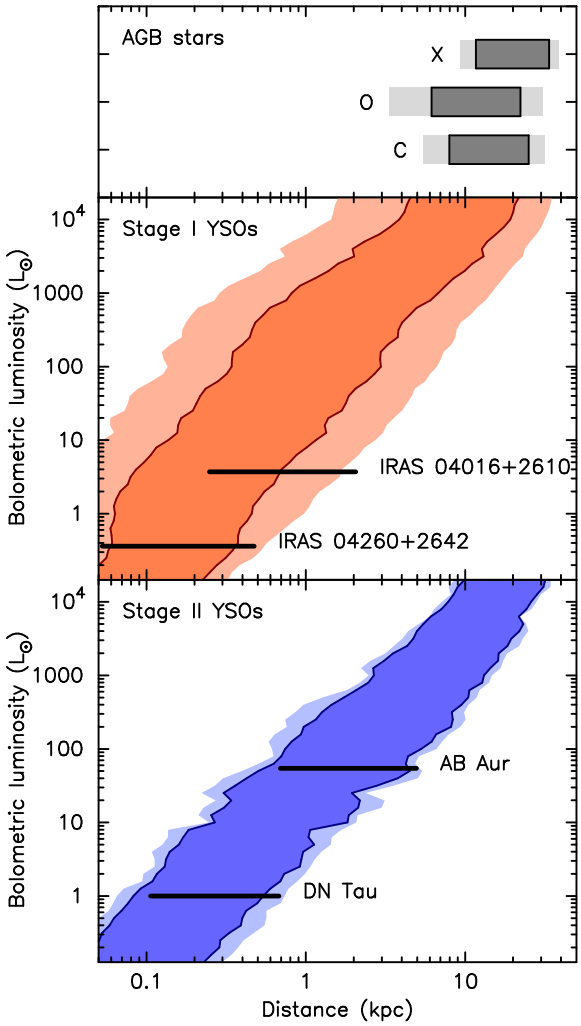

Figure 5.19: *Top* – The region surrounded by the solid line is the distance range in which an AGB star with average [4.5] and [8.0] magnitudes would need to be in order to be present in the red source catalogue. The average magnitudes were derived for LMC AGB stars with $[4.5] - [8.0] \geq 1$. X indicates xAGB stars, C indicates C-rich sAGB stars, and O indicates O-rich sAGB stars. The lighter region outside this corresponds to the 1-σ standard deviation in the average magnitudes. *Bottom* – The luminosity limit as a function of distance for embedded YSOs (Stage I), and for non-embedded YSOs with protoplanetary disks (Stage II). The solid lines enclose the distance ranges corresponding to the average [4.5] and [8.0] magnitudes, and the lighter region outside this corresponds to the 1-σ standard deviation in the average magnitudes. The distance ranges in which a few known objects would be detectable are also shown.

inclusion in the red source catalogue (Eq. [5.3]) was then determined, assuming an approximate extinction-distance relation of 1.9 mag/kpc (Allen, 1973) and the visual to mid-infrared extinction conversion described in §5.4.2. The resulting distance ranges are shown in dark grey in Figure 5.19, while the light grey ranges show the variation in the distance ranges corresponding to the standard deviations on the average magnitudes.

For YSOs, the models from Chapter 3 were used. Average [4.5] and [8.0] magnitudes and standard deviations on these were determined as a function of bolometric luminosity for two evolutionary stages: the embedded phase and the protoplanetary disk phase, or typical Stage I and II models using the 'Stage' definition from Chapter 3. The typical Stage I models were taken to be those with $\dot{M}_{\rm env}/M_\star = 5 \times 10^{-5} \rightarrow 2 \times 10^{-4}\,{\rm yr}^{-1}$, and the typical Stage II models were taken to be those with no infalling envelope and $M_{\rm disk}/M_\star = 0.005 \rightarrow 0.02$. Only models with viewing angles between 30° and 60° were used, and the fluxes were taken to be those inside a $\sim 15,000$ AU aperture. The resulting distance ranges are shown encompassed by the solid lines in Figure 5.19.

For the Stage I models, the standard deviations in the [4.5] and [8.0] magnitudes were typically less than 2.5 mag (or a factor of 10 in flux). These standard deviations are large because mid-infrared wavelengths are very sensitive to geometrical effects, such as viewing angle (Whitney et al., 2003b). For Stage II models, the standard deviations are less than 1 mag. In Figure 5.19, the scatter in the distance range corresponding to the standard deviations on the average [4.5] and [8.0] magnitudes are shown in lighter colour outside the solid lines.

This analysis shows that the faintest AGB stars should be detectable no closer than 3 kpc (closer AGB stars would exceed the saturation level), while the brightest AGB stars should be visible even at the far-side of the Galaxy. xAGB stars should be visible further away on average than sAGB stars. YSOs should also be visible throughout the Galaxy: for example, $1 L_\odot$ YSOs should be visible up to $\sim 0.8 - 1$ kpc; $100 L_\odot$ Stage I YSOs should be visible from 200 pc to nearly 10 kpc, while Stage II YSOs of the same luminosity (such as AB Aur) should be visible from 0.5 to 5 kpc; and $10^4 L_\odot$ YSOs should be visible at the far side of the Galaxy.

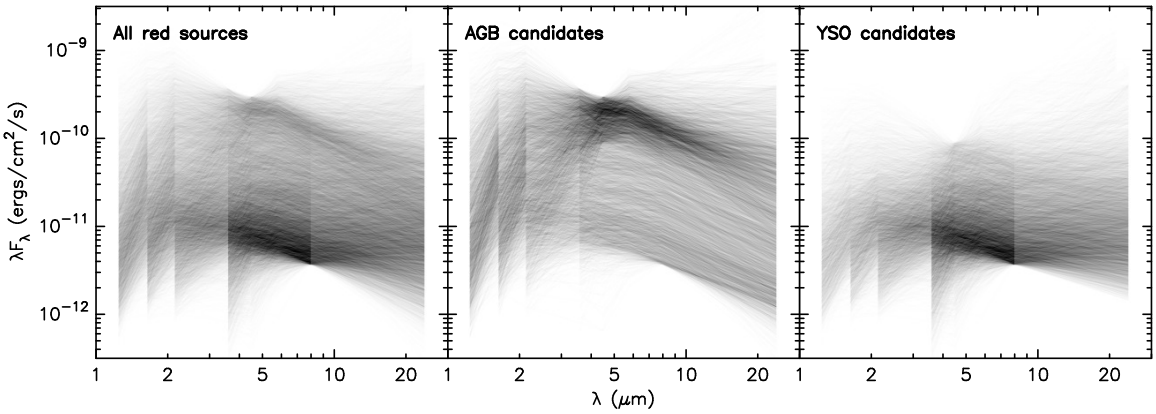

Figure 5.20: *Left* – stacked SEDs for all sources in the red source catalogue. *Centre* – stacked SEDs for all AGB candidates. *Right* – stacked SEDs for all YSO candidates.

5.4.6 Spectral Energy Distributions

Figure 5.20 shows the stacked SEDs of all sources in the red source catalogue. A higher density of sources is present both at the bright and the faint end, consistent with the colour-magnitude diagrams in Figure 5.9. Also shown are the stacked SEDs of only the AGB star candidates, and only the YSO candidates. Figure 5.21 shows typical SEDs for sources in the xAGB, sAGB, and YSO categories. The YSO SEDs show a much larger variation in SED shape than the AGB stars.

5.5 Summary

This chapter has described the compilation of a flux-limited catalogue of nearly 19,000 sources in the Galactic plane that are intrinsically red at mid-infrared wavelengths, using data from the *Spitzer* GLIMPSE I and II surveys and IRAC observations of the Galactic centre. The sources were required to satisfy the brightness and quality selection criteria from Eq. (5.3) and (5.4) to improve the reliability of the red source catalogue (§5.3.2), and were required to have $[4.5]-[8.0] \geq 1$ to be considered 'red' (§5.3.3). The latter criterion was determined to be the most straightforward and reproducible way of selecting red sources (§5.3.1). In particular, the interstellar extinction law is mostly flat between 4.5 and 8.0 μm, meaning that any red colour between the two bands is likely to be intrinsic rather than due to interstellar extinction.

Independent mosaic photometry was performed on all sources selected by these criteria to validate the GLIMPSE 4.5 and 8.0 μm photometry, and each source was visually examined to ensure that the independent flux could be trusted. Sources for which reliable independent

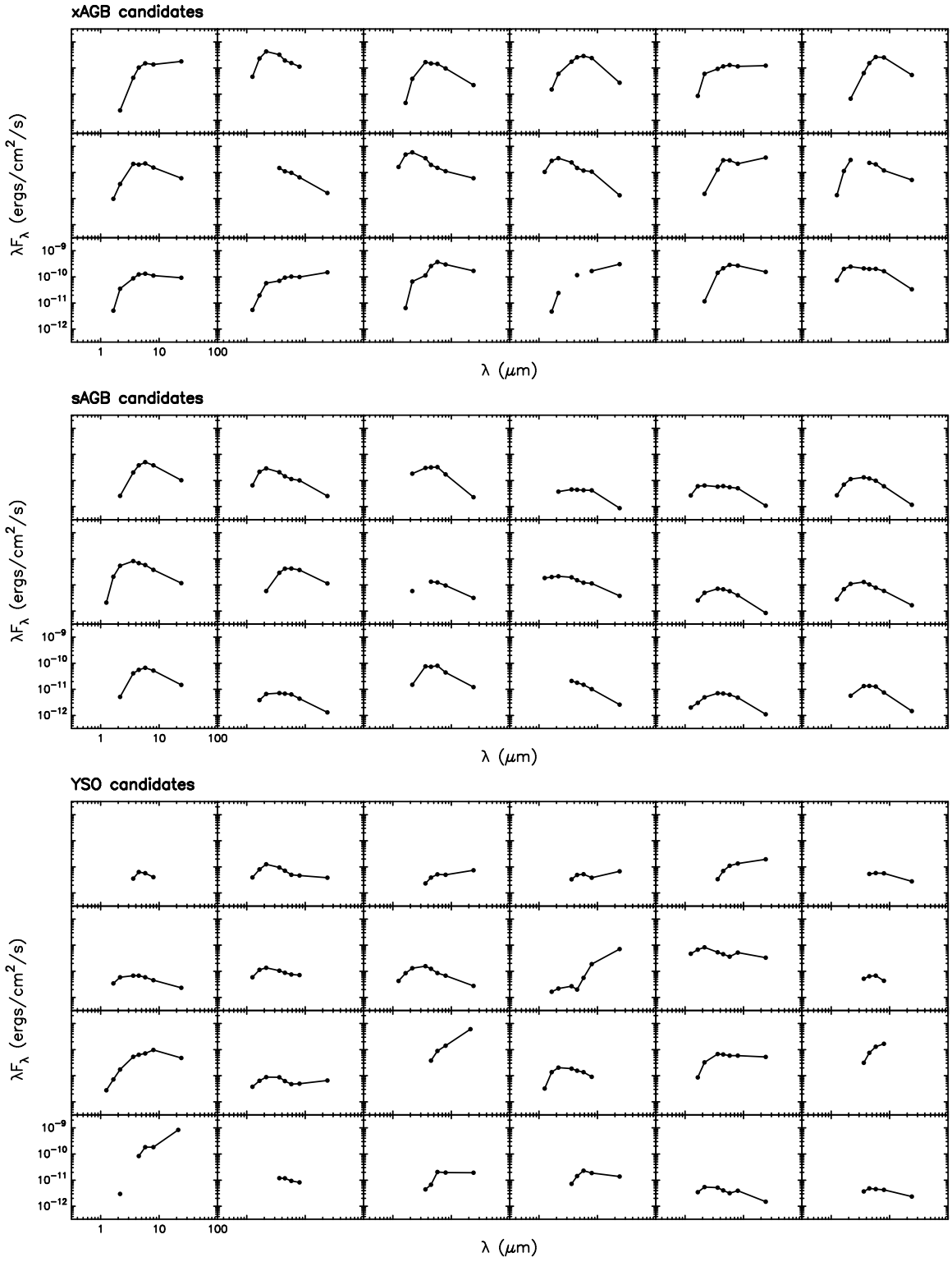

Figure 5.21: Example SEDs of sources selected randomly from the xAGB, sAGB, and YSO candidates.

photometry could not be performed were rejected from the red source catalogue. In addition, sources for which the independent flux was more reliable than the original GLIMPSE flux and for which the new fluxes no longer satisfied the brightness and colour selection criteria from Eqs. (5.3) and (5.5) were rejected from the red source catalogue. In total, 18,949 red sources satisfied all the selection criteria and were determined to have reliable photometry. The final catalogue is given in Table F.1, and includes JHK_s, IRAC, and MIPS 24 μm magnitudes. It is at least 65 % complete (for point sources) and close to 100 % reliable, meaning that every source in the catalogue is a genuine red source.

The near- and mid-infrared colour-magnitude and colour-colour distribution of the red sources was presented (§5.4.1). One particular feature of the IRAC colour-magnitude distribution of the red sources was the presence of two distinct populations, one peaking at bright [4.5] and [8.0] magnitudes ([8.0] $<$ 6.5 and [4.5] $<$ 8.0), and one peaking at faint [4.5] and [8.0] magnitudes ([8.0] $>$ 8 and [4.5] $>$ 8.5). The bright peak consists mostly of bright AGB stars, while the remaining sources consist mostly of fainter AGB stars and YSOs. Using simple colour and magnitude selection criteria, the red sources were separated into three distinct populations (§5.4.3): 'extreme' or 'obscured' C- and O-rich AGB stars (xAGB stars), 'standard' C- and O- rich AGB stars (sAGB stars), and YSOs.

The angular distribution, near- and mid-infrared colours, and magnitudes of these three populations were found to differ. The xAGB stars appear to be seen at least as far as the Galactic centre, show a rapid drop-off with Galactic longitude, and as expected for distant sources, their near-infrared colours therefore suggest higher values of interstellar extinction than the other populations. The sAGB stars show a somewhat shallower drop-off with Galactic longitude, and show less reddening than the xAGB stars, consistent with their closer distance. While they are also expected to be seen at least as far as the Galactic centre (§5.4.5), no concentration of sources is seen at the Galactic centre itself, but this could be an artefact due to the requirement for a valid MIPS 24 μm flux for the classification (§5.4.3). Finally, the YSOs show a shallow drop-off with Galactic longitude, and their distribution is highly clustered, unlike the two populations of AGB stars. The approximate separation of the three populations suggests that approximately $30-50$ % of sources in the red source catalogue are likely to be AGB stars, and approximately $50-70$ % are likely to be YSOs. The fraction of red sources that are galaxies and PNe was found to be very small, on the order of a few % at most (§5.4.2).

The AGB stars in the red source catalogue are likely to form one of the largest samples of mid-infrared selected AGB stars in the Galaxy to date, with over 7,000 AGB star candidates. In particular, the coverage of the GLIMPSE II region at two epochs has allowed us to uncover over a thousand sources with significant variability (> 0.3 mag) at 4.5 and/or 8.0 μm, which are identified as xAGB stars with Mira variability. These represent one fifth of all red sources in the GLIMPSE II region. Of all the AGB stars in the Galaxy that fall in the GLIMPSE survey area (but are not necessarily detected by *Spitzer*), the red source catalogue is likely to only contain a small fraction (~ 1 %) of all sAGB stars, but may contain up to a quarter of all xAGB stars.

In parallel, over 11,000 YSO candidates have been uncovered. These do not provide a *complete* picture of Galactic star formation as seen by *Spitzer*. For example, the red source catalogue does not include blended sources, extended sources, point source YSOs for which excess emission at 4.5 μm due to H_2 and CO bandhead emission from outflows makes the $[4.5] - [8.0]$ too blue for the selection criterion used in this chapter, and sources that are so embedded that they are not detected at IRAC wavelengths. Nevertheless, it is a first step towards a study of star formation – as seen by *Spitzer* – on a Galactic scale, and is to date the largest consistently selected sample of YSOs in the Milky-Way. These thousands of YSOs trace many previously known and some previously unknown sites of star formation, including large star formation complexes, smaller star formation regions, and dark clouds. From this perspective, the red source catalogue can be thought of not only as a large sample of AGB stars and YSOs, but as the most detailed map to date of the birth sites of intermediate and massive stars in the Galactic plane.

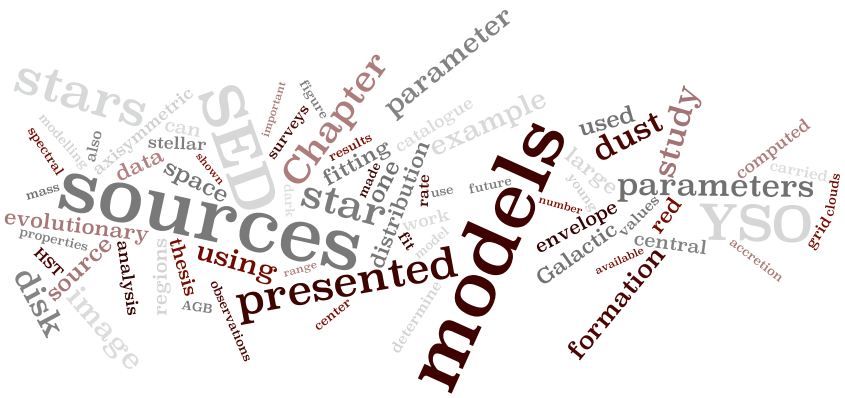

6

Summary and Future Work

At the start of this thesis, an overview of our current understanding of star formation was presented, and it was suggested that both the study of nearby resolved sources and of distant unresolved sources was essential for improving our understanding of star formation on Galactic scales. The work presented in this thesis has concentrated on the study of large numbers of unresolved sources, both from a modelling and an observational point of view. A large set of models and an SED analysis technique were developed, allowing efficient modelling of large numbers of sources with arbitrary wavelength coverage. In parallel, a census of intrinsically red sources was carried out using *Spitzer* observations of the Galactic mid-plane to search for thousands of previously unknown YSOs. In this chapter, I summarise the main results presented in this thesis (§6.1), and I provide an overview of the future avenues of research building on the work presented in this thesis (§6.2).

6.1 Main results

Detailed results of the work presented in Chapters 3, 4, and 5 were described at the end of each chapter. The main results are summarised here:

1. A large set of 200,000 model SEDs for YSOs was computed using a Monte-Carlo radiation transfer code. The parameter space explored was designed to span a wide range of evolutionary stages, from embedded protostars to PMS stars with optically thin disks, and to include sub-stellar to high-mass stars. The SEDs can be separated into components arising from the star, disk, or envelope, and into direct, scattered, or thermal emission components (§3.2)

2. A detailed analysis was carried out to study the relation between spectral index values, colours, and the physical properties of YSOs. In particular, the dependence of spectral indices and colours on evolutionary stage – specifically disk mass and envelope infall rate – was shown, as was the dependence on stellar temperature, disk inner radius, and disk flaring power. The effect of using different wavelength ranges and spectral index calculation techniques was also studied. Finally, it was shown that data redward of 20 μm in addition to near- and mid-infrared data are essential to determining the evolutionary stage of a YSO (§3.3).

3. An efficient fitting algorithm making use of the large set of models was developed and presented, with the primary aim to determine the stellar, disk, and envelope properties of YSOs. This is done by finding the ranges of parameter values that are consistent with observed SEDs. This algorithm is efficient, and should allow the rapid modelling of large numbers of sources in star formation regions, making use of all data available for all sources, while avoiding as much as possible over-interpretation within the assumptions made, such as those relating to the dust properties or infall model (§4.2 and Appendix C).

4. An analysis of 30 sources in Taurus was carried out and presented, showing that fitting SEDs using a large set of pre-computed models allows one to reliably estimate whether any parameters can be constrained, and correctly determines physical parameters such as the evolutionary stage, stellar temperatures, or the disk accretion rate, provided that sufficient data are available (§4.3.2).

5. An analysis was carried out to determine how well physical parameters, in particular the envelope infall rate, the disk mass, the disk accretion rate, and the stellar temperature were constrained as a function of the wavelength range of available data, for both an embedded protostar and a T Tauri star with a protoplanetary disk. As for Chapter 3, it was found that data longward of 20 μm in addition to shorter wavelength data are crucial for estimating the evolutionary stage of a given YSO (§4.3.3).

6. A web interface to browse the models and interactively fit data was developed, allowing the community to easily search for models in a given parameter value range, and to fit the SEDs of individual sources (Appendix C).

7. A highly reliable census of 18,949 intrinsically red sources was carried out in the *Spitzer* GLIMPSE survey. The red sources were colour-selected by requiring $[4.5]-[8.0] \geq 1$, and these consist mostly of YSOs and AGB stars. A detailed review of the effects of position-dependent sensitivity and saturation, confusion, and variability on the completeness of the GLIMPSE Point Source Catalogs was presented, and the selection criteria for the intrinsically red sources were chosen to minimise these effects (Chapter 5).

8. An analysis of the stellar content of this red source catalogue was carried out, showing that while galaxies are virtually absent from the catalogue and planetary nebulae only represent at most 2 to 3% of sources, AGB stars and YSOs were found to represent approximately 40% and 60% of sources respectively (§5.4.3).

9. Over 1,000 variable sources with changes in [4.5] or [8.0] magnitudes of at least 0.3 mag were discovered in the GLIMPSE II region. These are most likely to be 'extreme' AGB stars exhibiting Mira type variability (§5.4.1).

Perhaps the figures which best summarise the work presented in this thesis are Figures 4.3 and 4.4, which show that the SED fitting technique can be useful to find out how well constrained various parameters are as a function of the data available, and Figure 5.17, which shows the angular distribution of over 11,000 YSO candidates and just over 7,000 AGB star candidates, spread out over 274 $\deg^2$ of the Galactic mid-plane.

The models presented in Chapter 3 have already been used by the community. In particular, Harvey et al. (2007, 2008), Alcalá et al. (2008), and Merin et al. (2008) have made use of the 'virtual cluster' concept developed in Chapter 3 to compare the synthetic colours of

YSOs to sources in the *Spitzer* c2d surveys. The SED fitting algorithm described in Chapter 4 – whether via the web or the command-line tools described in Appendix C – has also been used for a number of studies, to determine evolutionary stages, bolometric luminosities, envelope infall rates, and central source properties. These include the study of many sources in the LMC (Whitney et al., 2008), the Eagle Nebula (Indebetouw et al., 2007), the Rosette Nebula (Poulton et al., 2008), in a region of the SMC (Simon et al., 2007), in various regions of the Galactic Plane (Shepherd et al., 2007; Watson et al., 2008), and the study of smaller number of sources by the Astronomy community (Birkmann et al., 2007; Vig et al., 2007; Bujarrabal et al., 2008; Caulet et al., 2008; Deharveng et al., 2008; Goicoechea et al., 2008; Hennemann et al., 2008; Persi et al., 2008; Sahai et al., 2008; Seale & Looney, 2008; Yun et al., 2008).

6.2 Future work

6.2.1 Improving the models

The set of model SEDs for YSOs presented in this thesis is the largest to date, both in terms of the number of models, and of the parameter space explored. However, there are many improvements that will be made in future to improve the science that is carried out using these models, in addition to the caveats described in §3.2.3.

While the models cover a large region of parameter space, the way in which parameter space is sampled is complex (c.f. Chapter 3). The various stellar parameters are linked by evolutionary tracks, and the parameters relating to the circumstellar material are often correlated. For example, since the envelope accretion rate is sampled from a range defined in terms of $\dot{M}_{\rm env}/M_\star$, models with higher mass central sources have on average higher envelope accretion rates. Another example is that the range of values used to sample the envelope accretion rate decreases with the age of the central source, while that used for the bipolar cavity angle increases. Therefore, it would be difficult to use the models to search for any correlation between envelope accretion rate and stellar mass or cavity opening angle, as these correlations are essentially built into the parameter space covered. However, as discussed in Chapter 3, producing a completely unbiased grid would be computationally prohibitive. For example, if 14 parameters were to be varied, with 10 different values for each parameter, this would result in 10^{14} models. Assuming that one model takes on average an hour to be computed, this would corresponds to 11 Gyr of computing time (on a single CPU), and this is

far beyond available computing resources!

Nevertheless, an unbiased grid of models is the next logical step for this work. Clearly, the main problem is to reduce the number of models that will need to be computed. As previously mentioned in Chapter 3, not all parameters are important at all evolutionary stages. For example, for deeply embedded sources, most of the disk properties are unlikely to be of great importance. However, it would be dangerous to decide *a priori* which parameters matter at each evolutionary stage. Instead, one can make use of a concept that is popular in hydrodynamics and radiation transfer, namely *adaptive mesh refinement*. This is usually used to provide high resolution in a simulation only where it is needed. In a similar way, one could envisage computing models in parameter space only where certain parameters appear to be important. To do this, an initial grid of models could be computed, with only two values in each parameter space dimension, where these values represent the extreme values that would be present in the final grid. Each pair of neighbouring models would then be compared, and intermediate models would only be computed in cases where the two extreme models differed significantly. The process could then be iterated to provide finer and finer coverage of parameter space. In addition to this technique, one could envisage improvements to the radiation transfer algorithm or code that would allow it to compute these models more efficiently.

Besides a less biased exploration of parameter space, there are other improvements that can be made. For example, the properties of cosmic dust are becoming better known, through detailed spectroscopy of young stars and through laboratory experiments. Models including opacity due to ices should be included, because these, along with silicates, can help the determination of evolutionary stages. For example, Crapsi et al. (2008) recently computed a grid of model SEDs, and found that for non-edge-on YSOs, these spectral features along with the broadband SED could be used to accurately determine the evolutionary stage of a YSO.

As mentioned in §1.3, while studying unresolved sources such as those catalogued in Chapter 5 is important, resolved sources are also essential to the study of star formation. Chapter 4 described an example of the analysis of *Spitzer* IRAC observations of a resolved source in a basic but automated fashion. This type of work can be extended further by allowing proper 'image fitting', i.e. not only fitting circularly averaged fluxes, but the full image itself. Pinte et al. (2008) recently computed a small grid of models to study the T Tauri star

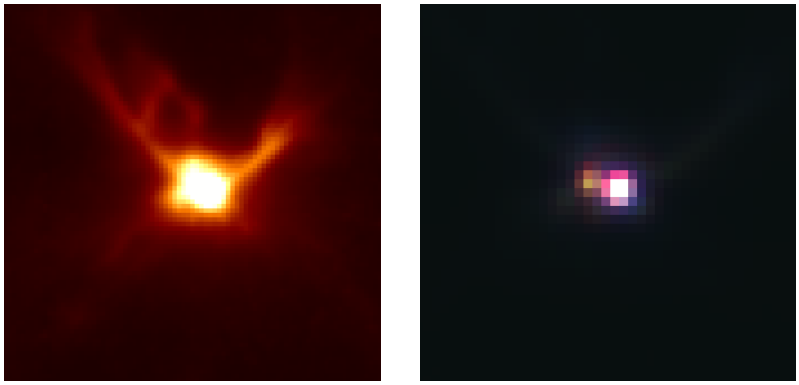

Figure 6.1: *Left* – HST NICMOS H-band image of the young stellar object CoKuTau/1 (Padgett et al., 1999). The distribution of dust is clearly clumpy. *Right* – HST NICMOS JHK colour composite of the central region of CoKuTau/1, showing that the central source is in fact a binary system. These images were taken from the MAST archive.

IM Lupii, and fit not only the SED, but also an HST image, by binning the image flux into a polar grid and fitting this image and the broadband SED simultaneously. In future, it will therefore be important to compute model multi-wavelength images and polarisation maps in addition to SEDs and to develop efficient automated multi-wavelength image fitting algorithms. One could also consider computing interferometric visibilities from the images, as infrared interferometry is more and more commonly used to study emission from the inner regions of disks.

6.2.2 Analysing the underlying assumptions

As well as improving the models, both in terms of parameter space exploration and in terms of physics, it will also be of crucial importance to study to what extent the assumptions made for the modelling work presented in this thesis, such as single central sources and axisymmetric dust distributions, are suitable for the analysis of YSOs.

For over a decade, it has been suggested that 'the usual product of a star formation event is a multiple-star system' (Mathieu, 1994), at least for solar-mass and higher-mass stars. Indeed, the fraction of stars in multiple systems is at least 50% for low-mass stars, and recent results suggest this value may be close to 100% for high-mass stars (e.g. Preibisch et al., 2001). Despite this, the models presented in this thesis, and indeed most models of young stars, often assume a single central object, unless evidence is present for a multiple system. For example, as mentioned in Chapter 4, CoKuTau/1 is in fact a binary system, as shown in Figure 6.1.

One way to study the effects of multiplicity on YSO SEDs would be to run models similar to

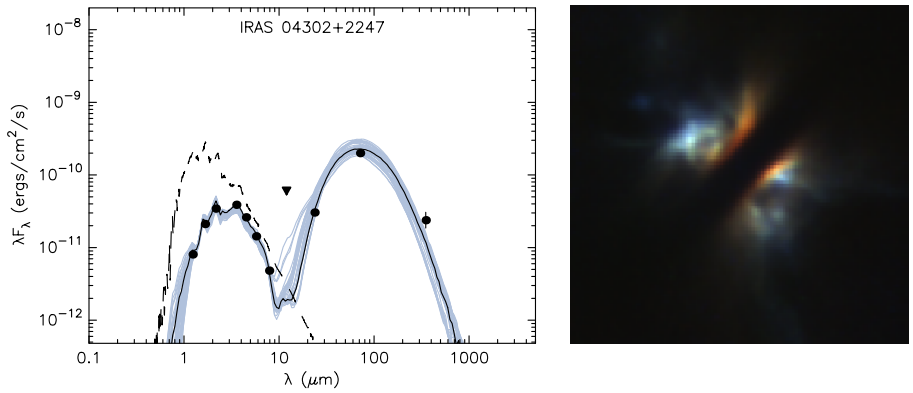

Figure 6.2: *Left* – broadband spectral energy distribution for the protostar IRAS 04302+2247 (black circles) shown with models providing a good fit (solid lines). The models used to fit the observed SED assume a 2-dimensional axisymmetric dust distribution. *Right* – HST NICMOS JHK colour composite image showing the appearance of the central regions of this source at high spatial resolution (Padgett et al., 1999). The dust distribution appears very approximately axisymmetric, and is clearly clumpy. The SED plot is the same as in Chapter 4, and the HST data was extracted from the MAST archive.

those presented in Chapter 3 (or future improved models) but including two central sources, and to predict emergent SEDs. For example, one could compute models with close binaries surrounded by a circumbinary disk, or more complex geometries such as a wider binary with each star surrounded by a disk, and the whole binary by a large circumbinary disk. The emergent SEDs could then be modelled using for example the SED fitting technique presented in Chapter 4 using the models from Chapter 3, which contain only single sources. Comparing the modelled to the 'true' parameters would allow one to determine which physical parameters can be correctly estimated by assuming that only one source is present.

Another avenue of research will be to find out to what extent 2-D analytically described axisymmetric dust distributions are suitable for modelling real sources. Rotational collapse and bipolar outflows give rise to approximately 2-D circumstellar geometries, but clumps and gravitational instabilities cause 3-D variations. Figures 6.2 and 6.3 show broadband SEDs and high resolution observations of the Class I source IRAS 04302+2247 and the Herbig Ae/Be star AB Aur as examples of sources for which deviations from a 2-D axisymmetric dust distribution are clearly visible in resolved images. Furthermore, recent observations of 'disks' around high-mass stars suggest that these, far from being smooth axisymmetric and flared, may be large warped and clumpy transient objects with spiral arm instabilities. It will therefore be important to study to what extent the parameters estimated from SED fitting with 2-D models are still meaningful for realistic 3-D dust distributions. For example, one would expect that the total dust mass around a protostar should still be recoverable

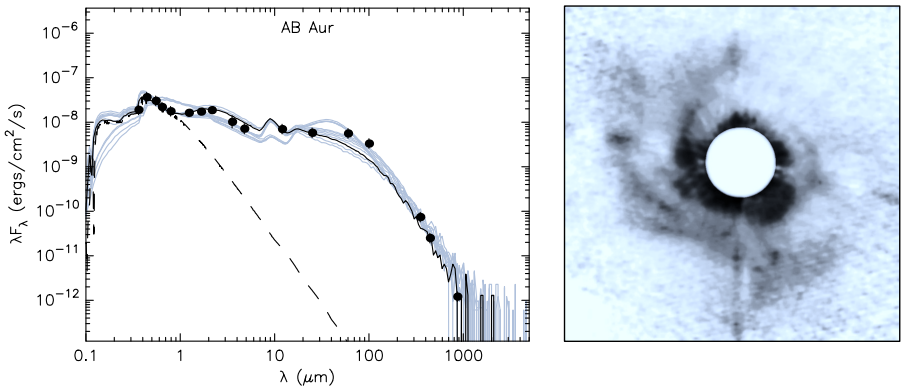

Figure 6.3: *Left* – broadband spectral energy distribution for the Herbig Ae/Be star AB Aur (black circles) shown with models providing a good fit (solid lines). The models used to fit the observed SED assume a 2-dimensional axisymmetric dust distribution. *Right* – High resolution H-band Subaru CIAO+AO image of AB Aur (Fukagawa et al., 2004). Spiral arms are clearly visible in the disk. The SED plot is the same as in Chapter 4, and the Subaru image was adapted from a Subaru press release image.

at mm wavelengths where the dust is optically thin, even if the distribution of dust is only approximately axisymmetric, whereas parameters such as the disk flaring power may not be meaningful for 'disks' around high mass stars if these are not actually flared.

This study could be done by running hydrodynamical simulations of disks and accreting protostars using hydrodynamical codes in order to obtain realistic dust density structures at various stages of evolution in YSOs of different masses, and to use these density structures to predict emergent SEDs. As for the study of the effects of binary stars, these synthetic SEDs could be analysed using the SED analysis tool presented in Chapter 4. The results from this modelling would then be compared with the 'true' dust distribution in the simulations to establish which physical parameters can be still be appropriately recovered using 2-D models.

6.2.3 A census of Galactic star formation

The census of red sources presented in Chapter 5 will be a starting point for a number of studies of star formation in the Galactic mid-plane. A first step will be to quantify the clustering of the sources, which may uncover previously unknown embedded clusters, and to compare the location of YSOs with molecular gas tracers (e.g. CO), dark clouds, and HII regions. Simon et al. (2006) compiled a catalogue of dark clouds, and computed kinematic distances to them using radial velocities from the ^{13}CO Boston University-Five College Radio Astronomy Observatory Galactic Ring Survey (BU-FCRAO GRS). By examining the YSO content of these dark clouds and modelling the SEDs of the sources present, and by comparing these with YSOs in

other environments, such as those in HII regions or in isolation, it might be possible to place constraints on the lifetimes of dark clouds, or to look for systematic difference between stars forming in dark clouds and those forming via the collect and collapse process on the borders of HII regions. For example, a prediction of models of star formation triggering via the collect and collapse process is that stars formed in this way may be systematically more massive than those that form in cold dark clouds (Elmegreen & Lada, 1977). The red source catalogue could also be used in conjunction with a catalogue of confirmed massive stars such as those from the RMS survey, to study whether massive stars ever form in isolation, or whether they are always surrounded by a cluster of lower-mass YSOs.

In order to improve the interpretation of the SEDs, longer wavelength data will be needed. Once the MIPSGAL Point Source Catalogs are released, these will be used to assign 70 μm fluxes to as many of the red sources as possible. In addition, surveys at mm wavelengths such as the Bolocam Galactic Plane Survey will provide mm fluxes for the youngest and most massive YSOs. In future, the *Herschel* Galactic plane survey should provide sub-mm fluxes for many of the youngest sources in the sample. Therefore, it seems likely that in less than a decade, most sources in the red source catalogue will have almost complete SEDs from near-infrared to mm wavelengths. At this point in time, modelling techniques such as that presented in Chapter 4 will be indispensable to analyse these data efficiently.

Another interesting path to explore would be to follow-up a random sample of sources using for example near- or mid-infrared spectroscopy, and to determine whether these sources are actually YSOs or AGB stars based on spectroscopic features. This will make it possible to calculate the true fractions of YSOs and AGB stars in the red source catalogue and to understand better where the different populations lie in IRAC and MIPS colour space. Thus, it will be possible to determine how effective the colour-magnitude selection criteria presented in §5.4.3 are, and how they could be improved. Further into the future, one could even envisage using a multi-object spectrograph to rapidly obtain near- and/or mid-infrared spectra for all sources in the sample.

Galactic star formation is of course not confined to the area covered by the GLIMPSE surveys. Most of the well-studied nearby regions such as the TMC, the OMC, Perseus, and others do not fall inside the area covered by the GLIMPSE surveys. However, by merging the catalogue of candidate YSOs presented in this thesis with YSOs from the surveys of nearby

star formation regions, such as the Spitzer c2d surveys, and observations of the TMC or OMC, we will be one step closer to a complete census of star formation throughout the Milky-Way Galaxy.

Before the discovery of T Tauri stars by Alfred Joy a little more than 60 years ago, no young stars had ever been observed or been recognised as such. Thanks to the rapid progress made in infrared observing technology in the last few decades, and the advent of large-scale infrared surveys and powerful computational techniques, we have now entered an era in which both the detailed and ultra-high resolution observations of nearby young stars and the study of tens of thousands of young stars scattered throughout the Milky-Way will pave the way for a statistically robust theory of star formation in the Galaxy.

A

Convolution of SEDs with broadband filters

This appendix describes the procedure used to obtain monochromatic fluxes through broadband filters for the model SEDs presented in this thesis.

In the following, the true spectrum of a source or model SED is defined as $F_\nu[\text{actual}]$. In general, when a broadband flux is measured through a filter, no knowledge of the true underlying spectrum is available, only the integrated flux over the filter. Therefore, to quote a monochromatic flux $F_{\nu_0}[\text{quoted}]$ at a frequency ν_0, one usually makes an assumption about the spectrum of the source. In the following derivations, this spectrum will be written as $F_\nu[\text{assumed}]$. The difference between $F_\nu[\text{assumed}]$ and $F_{\nu_0}[\text{quoted}]$ is that $F_{\nu_0}[\text{quoted}]$ is the value of $F_\nu[\text{assumed}]$ at ν_0.

In the following derivations, the same assumptions are made for the model SEDs as are made for the data taken in the different filters. For example, fluxes from the IRAC pipeline are quoted using $F_\nu[\text{assumed}] \propto 1/\nu$. That is to say, what would the flux at ν_0 be, if the spectrum of the source was proportional to $1/\nu$, such that the observed integrated flux was

identical to what is actually observed? Since the same assumptions are being made as used for the observed fluxes, a direct comparison between the quoted model fluxes and the quoted observed fluxes can be made without the need for any colour-correction.

***Spitzer* - IRAC**

The IRAC monochromatic fluxes assume $F_\nu[\text{assumed}] \propto 1/\nu$, i.e. $\nu F_\nu[\text{assumed}] \propto \text{const}$ (Reach et al., 2005). The total electron "count" detected through the filter with response $R(\nu)$ (in electrons/photon) is

$$E = \int \frac{F_\nu[\text{actual}]}{h\nu}\, R(\nu)\, d\nu = \int \frac{F_\nu[\text{assumed}]}{h\nu}\, R(\nu)\, d\nu. \tag{A.1}$$

Now $\nu F_\nu[\text{assumed}] \propto \text{const} \equiv \nu_0 F_{\nu_0}[\text{quoted}]$, so

$$\nu_0 F_{\nu_0}[\text{quoted}] \int \frac{1}{h\nu^2}\, R(\nu)\, d\nu = \int \frac{F_\nu[\text{actual}]}{h\nu}\, R(\nu)\, d\nu \tag{A.2}$$

which after rearranging gives

$$F_{\nu_0}[\text{quoted}] = \frac{\int F_\nu[\text{actual}]\, (\nu_0/\nu)\; R(\nu)\, d\nu}{\int (\nu_0/\nu)^2\; R(\nu)\, d\nu} \tag{A.3}$$

The values of $R(\nu)$ are taken from the SSC website [11]. The values of ν_0 are given by $\nu_0 = c/\lambda_0$ where $\lambda_0 = 3.550,\ 4.493,\ 5.731,$ and $7.872\,\mu$m are the nominal wavelengths for IRAC (Reach et al., 2005).

***Spitzer* - MIPS**

The MIPS monochromatic fluxes assume a T=10,000 K blackbody spectrum, i.e very close to $F_\nu[\text{assumed}] \propto \nu^2$, i.e. $F_\nu[\text{assumed}]/\nu^2 \propto \text{const}$ (MIPS data handbook [12]). The total electron "count" through the filter with response $R_\nu(\nu) \equiv R(\nu)/\nu$ (in electrons/unit energy) is

$$E = \int F_\nu[\text{actual}]\; R_\nu(\nu)\, d\nu = \int F_\nu[\text{assumed}]\; R_\nu(\nu)\, d\nu. \tag{A.4}$$

Now $F_\nu[\text{assumed}]/\nu^2 \propto \text{const} \equiv F_{\nu_0}[\text{quoted}]/\nu_0^2$, so

$$F_{\nu_0}[\text{quoted}]/\nu_0^2 \int \nu^2\, R_\nu(\nu)\, d\nu = \int F_\nu[\text{actual}]\; R_\nu(\nu)\, d\nu, \tag{A.5}$$

which after rearranging gives

$$F_{\nu_0}[\text{quoted}] = \frac{\int F_\nu[\text{actual}]\, R_\nu(\nu)\, d\nu}{\int \left(\nu/\nu_0\right)^2\, R_\nu(\nu)\, d\nu}. \tag{A.6}$$

The values of $R_\nu(\nu)$ are taken from the SSC website [13]. The values of ν_0 are given by $\nu_0 = c/\lambda_0$ where $\lambda_0 = 23.68,\ 71.42,$ and $155.9\,\mu$m are the effective wavelengths for MIPS.

IRAS

The IRAS monochromatic fluxes use $F_\nu[\text{assumed}] \propto 1/\nu$, i.e. $\nu F_\nu[\text{assumed}] \propto$ const (IRAS Explanatory Supplement - Section VI.C.3 [14]). In the same way as for IRAC, one finds

$$F_{\nu_0}[\text{quoted}] = \frac{\int F_\nu[\text{actual}]\, \left(\nu_0/\nu\right)\, R(\nu)\, d\nu}{\int \left(\nu_0/\nu\right)^2\, R(\nu)\, d\nu}. \tag{A.7}$$

However, the relative system response listed in the IRAS documentation is in electrons per unit energy (as for MIPS). Therefore, writing $R_\nu(\nu) \equiv R(\nu)/\nu$ gives

$$F_{\nu_0}[\text{quoted}] = \frac{\int F_\nu[\text{actual}]\, R_\nu(\nu)\, d\nu}{\int \left(\nu_0/\nu\right)\, R_\nu(\nu)\, d\nu}. \tag{A.8}$$

The values of $R_\nu(\nu)$ are taken from the IRAS documentation (The 'Relative System Response' in the IRAS Explanatory Supplement - Table II.C.5 [15]). The values of ν_0 are given by $\nu_0 = c/\lambda_0$ where $\lambda_0 = 12,\ 25,\ 60,$ and $100\,\mu$m.

UBVRI photometry

The UBVRI observations from Kenyon & Hartmann (1995) are originally from Herbst et al. (1994), and were made in the Johnson/Cousins UBVRI system. The transmission curves for these bands were taken from Bessell (1990). Since flux densities are not commonly used at optical wavelengths, it was not clear what spectrum to assume in order to derive the monochromatic fluxes (although the calibration is usually done using the spectrum of Vega). However, the differences arising from various assumptions do not change the resulting fluxes by more than a few %. Therefore, the choice of the assumption is unimportant for this work. A flat spectrum was therefore assumed, i.e. $F_\nu[\text{assumed}] \propto 1/\nu$, i.e. $\nu F_\nu[\text{assumed}] \propto$ const.

Therefore, as for IRAC, this gives:

$$F_{\nu_0}[\text{quoted}] = \frac{\int F_\nu[\text{actual}]\,(\nu_0/\nu)\;R(\nu)\,d\nu}{\int (\nu_0/\nu)^2\;R(\nu)\,d\nu}. \tag{A.9}$$

The values of ν_0 are given by $\nu_0 = c/\lambda_0$ where $\lambda_0 = 0.36$, 0.44, 0.55, 0.64, and 0.79 μm.

JHK$_s$/2MASS

For the JHK$_s$ filters, the monochromatic fluxes were calculated using the method for the 2MASS all-sky survey (Skrutskie et al., 2006). The 2MASS isophotal fluxes are computed using the relative system response R_ν from Cohen et al. (2003), and are given by

$$F^{\text{iso}}_{\nu_0}[\text{quoted}] = \frac{\int F_\nu[\text{actual}]\;R_\nu(\nu)\,d\nu}{\Delta\nu_{\text{iso}}}. \tag{A.10}$$

The isophotal bandwidths $\Delta\nu_{\text{iso}}$ for the three bands are listed in Cohen et al. (2003). The isophotal wavelengths are $\lambda_0^{\text{iso}} = 1.235,\ 1.662,$ and 2.159 μm.

SHARC II, SCUBA, and CSO observations

The SHARC II and SCUBA instruments are calibrated on planets, whose radiation follows the Rayleigh-Jeans tail of a blackbody curve at sub-mm wavelengths. Therefore, the assumption made was that $F_\nu[\text{assumed}] \propto \nu^2$, i.e. $F_\nu[\text{assumed}]/\nu^2 \propto$ const. As for MIPS, this gives

$$F_{\nu_0}[\text{quoted}] = \frac{\int F_\nu[\text{actual}]\;R_\nu(\nu)\,d\nu}{\int (\nu/\nu_0)^2\;R_\nu(\nu)\,d\nu}. \tag{A.11}$$

The values of $R_\nu(\nu)$ are taken from Dowell et al. (2003) for the SHARC II observations, and the SCUBA website [16] for the SCUBA 450WB and 850WB observations. For the CSO observations, Gaussian functions centred at 624 and 769 μm were used, with FWHM 67 and 190 μm respectively. The SHARC II and CSO filters were convolved with the atmospheric transmission curve used in Dowell et al. (2003), and the SCUBA filters with the atmospheric transmission curve given with the filter profiles on the SCUBA website. The values of ν_0 are given by $\nu_0 = c/\lambda_0$ where $\lambda_0 = 350,\ 443,$ and 863 μm for SHARC II 350 μm and SCUBA 450WB and 850WB respectively, and $\lambda_0 = 624$ and 769 μm for the CSO observations.

B

WWW model access

In order to make the models presented in Chapter 3 available to the community, a website was set up [4]. This website consists mainly of a 'model browser', ASCII files with convolved fluxes and magnitudes, and an online SED fitting program presented in Appendix C.

B.1 Model browser

Access to individual models is done via a 'model browser' which can show models falling within specific parameter value ranges. This is implemented in HTML with PHP scripts, and a MySQL database behind the scenes, whose purpose is to return models falling in the requested range.

A screen capture of the browser is given in Figure B.1. Models can be selected according to an arbitrary number of criteria. In the screen capture, the models are being selected on the basis of the central source mass, the envelope infall rate, and the disk mass. The models can be sorted by any parameters, and the matching models are shown below with a summary

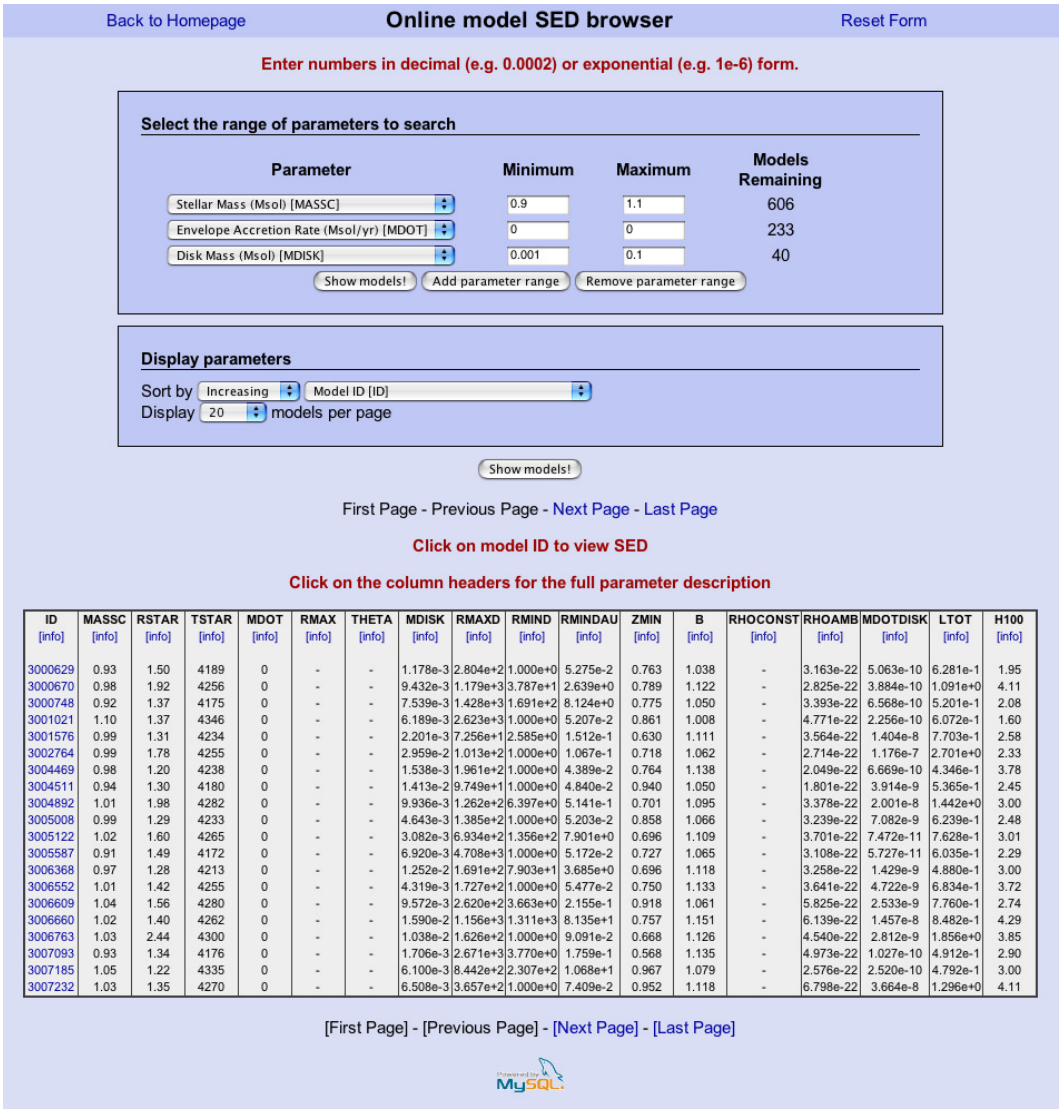

Back to Homepage **Online model SED browser** Reset Form

Enter numbers in decimal (e.g. 0.0002) or exponential (e.g. 1e-6) form.

Select the range of parameters to search

Parameter	Minimum	Maximum	Models Remaining
Stellar Mass (Msol) [MASSC]	0.9	1.1	606
Envelope Accretion Rate (Msol/yr) [MDOT]	0	0	233
Disk Mass (Msol) [MDISK]	0.001	0.1	40

Show models! Add parameter range Remove parameter range

Display parameters

Sort by Increasing Model ID [ID]
Display 20 models per page

Show models!

First Page - Previous Page - Next Page - Last Page

Click on model ID to view SED

Click on the column headers for the full parameter description

ID [info]	MASSC [info]	RSTAR [info]	TSTAR [info]	MDOT [info]	RMAX [info]	THETA [info]	MDISK [info]	RMAXD [info]	RMIND [info]	RMINDAU [info]	ZMIN [info]	B [info]	RHOCONST [info]	RHOAMB [info]	MDOTDISK [info]	LTOT [info]	H100 [info]
3000629	0.93	1.50	4189	0	-	-	1.178e-3	2.804e+2	1.000e+0	5.275e-2	0.763	1.038	-	3.163e-22	5.063e-10	6.281e-1	1.95
3000670	0.98	1.92	4256	0	-	-	9.432e-3	1.179e+3	3.787e+1	2.639e+0	0.789	1.122	-	2.825e-22	3.884e-10	1.091e+0	4.11
3000748	0.92	1.37	4175	0	-	-	7.539e-3	1.428e+3	1.691e+2	8.124e+0	0.775	1.050	-	3.393e-22	6.568e-10	5.201e-1	2.08
3001021	1.10	1.37	4346	0	-	-	6.189e-3	2.623e+3	1.000e+0	5.207e-2	0.861	1.008	-	4.771e-22	2.256e-10	6.072e-1	1.60
3001576	0.99	1.31	4234	0	-	-	2.201e-3	7.256e+1	2.585e+0	1.512e-1	0.630	1.111	-	3.564e-22	1.404e-8	7.703e-1	2.58
3002764	0.99	1.78	4255	0	-	-	2.959e-2	1.013e+2	1.000e+0	1.067e-1	0.718	1.062	-	2.714e-22	1.176e-7	2.701e+0	2.33
3004469	0.98	1.20	4238	0	-	-	1.538e-3	1.961e+2	1.000e+0	4.389e-2	0.764	1.138	-	2.049e-22	6.669e-10	4.346e-1	3.78
3004511	0.94	1.30	4180	0	-	-	1.413e-2	9.749e+1	1.000e+0	4.840e-2	0.940	1.050	-	1.801e-22	3.914e-9	5.365e-1	2.45
3004892	1.01	1.98	4282	0	-	-	9.936e-3	1.262e+2	6.397e+0	5.141e-1	0.701	1.095	-	3.378e-22	2.001e-8	1.442e+0	3.00
3005008	0.99	1.29	4233	0	-	-	4.643e-3	1.385e+2	1.000e+0	5.203e-2	0.858	1.066	-	3.239e-22	7.082e-9	6.239e-1	2.48
3005122	1.02	1.60	4265	0	-	-	3.082e-3	6.934e+2	1.356e+2	7.901e+0	0.696	1.109	-	3.701e-22	7.472e-11	7.628e-1	3.01
3005587	0.91	1.49	4172	0	-	-	6.920e-3	4.708e+3	1.000e+0	5.172e-2	0.727	1.065	-	3.108e-22	5.727e-11	6.035e-1	2.29
3006368	0.97	1.28	4213	0	-	-	1.252e-2	1.691e+2	7.903e+1	3.685e+0	0.696	1.118	-	3.258e-22	1.429e-9	4.880e-1	3.00
3006552	1.01	1.42	4255	0	-	-	4.319e-3	1.727e+2	1.000e+0	5.477e-2	0.750	1.133	-	3.641e-22	4.722e-9	6.834e-1	3.72
3006609	1.04	1.56	4280	0	-	-	9.572e-3	2.620e+2	3.663e+0	2.155e-1	0.918	1.061	-	5.825e-22	2.533e-9	7.760e-1	2.74
3006660	1.02	1.40	4262	0	-	-	1.590e-2	1.156e+3	1.311e+3	8.135e+1	0.757	1.151	-	6.139e-22	1.457e-8	8.482e-1	4.29
3006763	1.03	2.44	4300	0	-	-	1.038e-2	1.626e+2	1.000e+0	9.091e-2	0.668	1.126	-	4.540e-22	2.812e-9	1.856e+0	3.85
3007093	0.93	1.34	4176	0	-	-	1.706e-3	2.671e+3	3.770e+0	1.759e-1	0.568	1.135	-	4.973e-22	1.027e-10	4.912e-1	2.90
3007185	1.05	1.22	4335	0	-	-	6.100e-3	8.442e+2	2.307e+2	1.068e+1	0.967	1.079	-	2.576e-22	2.520e-10	4.792e-1	3.00
3007232	1.03	1.35	4270	0	-	-	6.508e-3	3.657e+2	1.000e+0	7.409e-2	0.952	1.118	-	6.798e-22	3.664e-8	1.296e+0	4.11

[First Page] - [Previous Page] - [Next Page] - [Last Page]

Powered by MySQL

Figure B.1: Screen capture of the 'model browser' for the set of models presented in Chapter 3. The models can be constrained by model parameter values: in this specific case, the models are filtered by stellar mass, envelope infall rate, and disk mass.

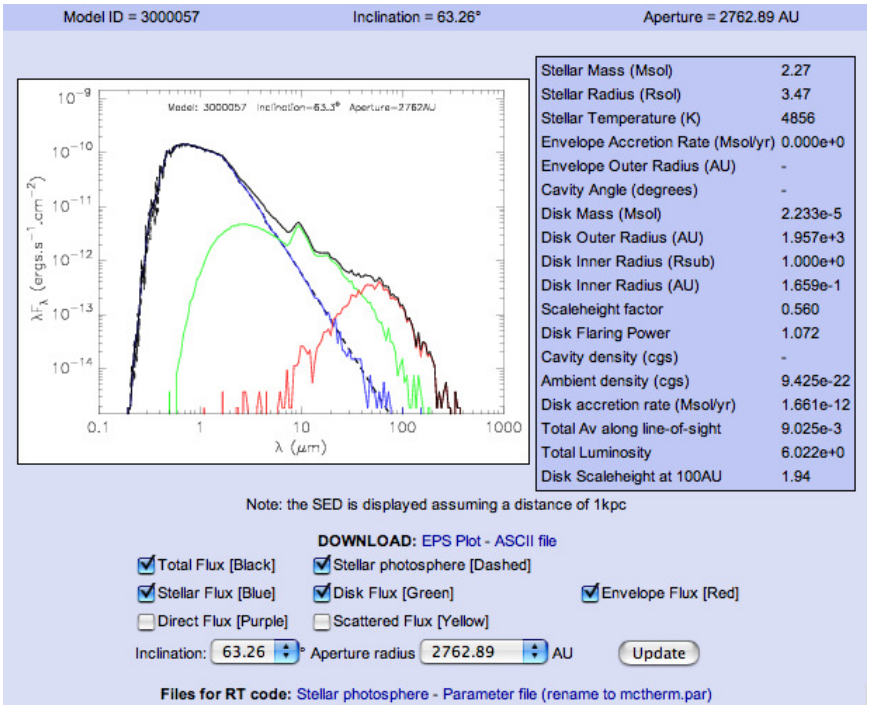

Figure B.2: Screen capture from the online model browser, showing a model of a low-mass disk. This panel shows the total SED, as well as the contributions to the SED from the star, disk, and envelope (which includes the ambient density emission).

of the parameter values. By clicking on the model ID, the corresponding model SED can be viewed. An example is shown in Figure B.2. The SED of the model is shown on the left, and the parameters are summarised on the right. Below are options that allow only certain components to be viewed (total flux, stellar flux, disk flux, envelope flux, etc.). An ASCII file of the SED can be downloaded. The viewing angle and aperture can be changed. Finally, options are available to download files suitable for input to the radiation transfer code, for example for computing images or higher signal-to-noise SEDs.

B.2 ASCII file repository

Also available on the web server are ASCII files containing convolved fluxes and magnitudes for all models, with one file per filter (such as 2MASS JHK$_s$ or IRAC filters.). These were convolved using the equations provided in Appendix A. Also included is a file containing the parameters for all the models. Finally, one file contains the weights to be assigned to each model in order to reproduce the sampling of the IMF and the central source age carried out in §3.3.4.

C

SED fitting code and WWW interface

This appendix briefly describes the implementation of the SED fitting algorithm described in Chapter 4, as well as the public WWW interface [4].

C.1 Implementation

The SED fitting algorithm described in Chapter 4 was implemented as a command-line program written in Fortran 95 using object-orientated and modular techniques. The `PGPLOT` library is used to produce Encapsulated Postscript (EPS) plots, and the `cfitsio` library is used to read and write Flexible Image Transport System (FITS) format files. The source code for the latest version of the fitting code to date, along with a User Manual, is provided in the supplemental DVD included with this thesis.

The SED fitting code can be used with any sets of model SEDs that are functions of wavelength and with fluxes specified in multiple circular apertures, such as those presented in Chapter 3, or functions only of wavelength, such as stellar photosphere models. The models

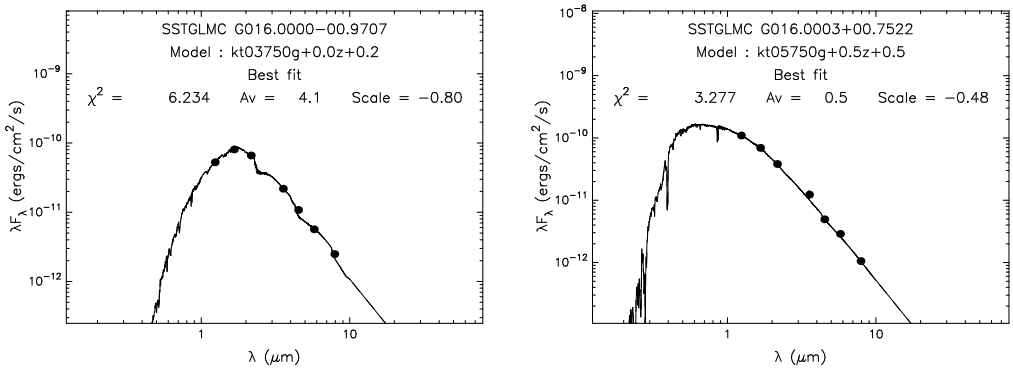

Figure C.1: Examples of model stellar photosphere fits to GLIMPSE sources.

are packaged in FITS table format. The exact table structure used is described by a document included with the SED fitting code. A subset of the models from Chapter 3 and stellar photospheres from Castelli & Kurucz (2004) are included on the DVD in this format.

The analysis of a source or multiple sources is done in several steps:

1. The user prepares the data and writes it to an ASCII file, with one source per line. All sources in a given data file are required to have data specified at the same wavelengths and in the same apertures (although the aperture can change as a function of wavelength), and null fluxes can be specified if data are not available at a given wavelength.

2. The user sets parameters relating to the data (e.g. wavelengths, apertures, etc.) as well as fitting parameters (such as the acceptable range of distances or interstellar extinctions, or the models to use) via parameter files.

3. The fitting code (`fit`) reads in the parameter files and the models. The data file is then read in, source by source. The fitting procedure for each source then depends on whether aperture dependent or independent models are used:

    - For aperture dependent models, the model SEDs are interpolated and scaled to a number of discrete distances inside the range specified, using the apertures specified in the parameter file. The number of distances is typically set to 25 to 100 per decade of distance (e.g. 1 to 10 kpc). All models are fit to the data using optimal scaling, with the interstellar extinction as a free parameter (c.f. Chapter 4). This is repeated for all distances the models are interpolated to. For any given source, a goodness-of-fit χ^2 value is computed for each model/distance combination.

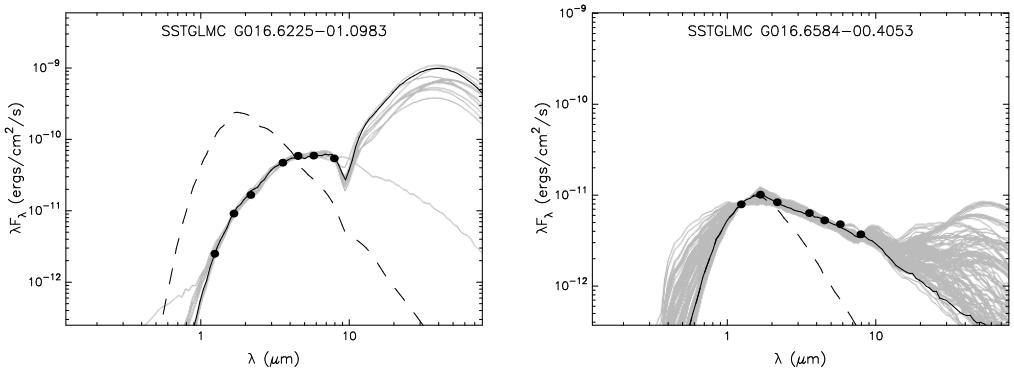

Figure C.2: Examples of model YSO SEDs fits to GLIMPSE sources.

- For aperture independent models, all models are fit to the data using linear regression, with the interstellar extinction and distance as free parameters. For any given source, a goodness-of-fit χ^2 value is computed for each model.

4. For each source, all models (or a subset of models) are output along with their best fit interstellar extinction, best fit distance, and χ^2 value.

5. This output file can then be passed on to secondary analysis programs (e.g. `plot`, `plot_params_1d`, `plot_params_2d`, `generic`, etc.), which can plot SED fits or parameter values, or which can perform any custom analysis such as separating well and badly fit sources, removing model fits inconsistent with a known spectral type, or computing average and standard deviation values for the parameters.

Figure C.1 shows good model stellar photosphere fits to two GLIMPSE sources, and Figure C.2 shows good YSO model SED fits to two GLIMPSE sources. For sources with data specified at seven wavelengths (e.g. 2MASS and IRAC), the current implementation of the fitting code can fit approximately 450 sources per second when using approximately 3,800 stellar photosphere models, and approximately 0.3 sources per second when using approximately 200,000 YSO model SEDs interpolated to 25 distances. Thus, even for thousands of sources, the total time to fit all the model SEDs from Chapter 3 is at most on the order of a few hours.

C.2 WWW interface

While the SED fitting code described in §C.1 is efficient for large numbers of sources, it requires users to download and locally store over 200,000 files totalling several Gb (for the

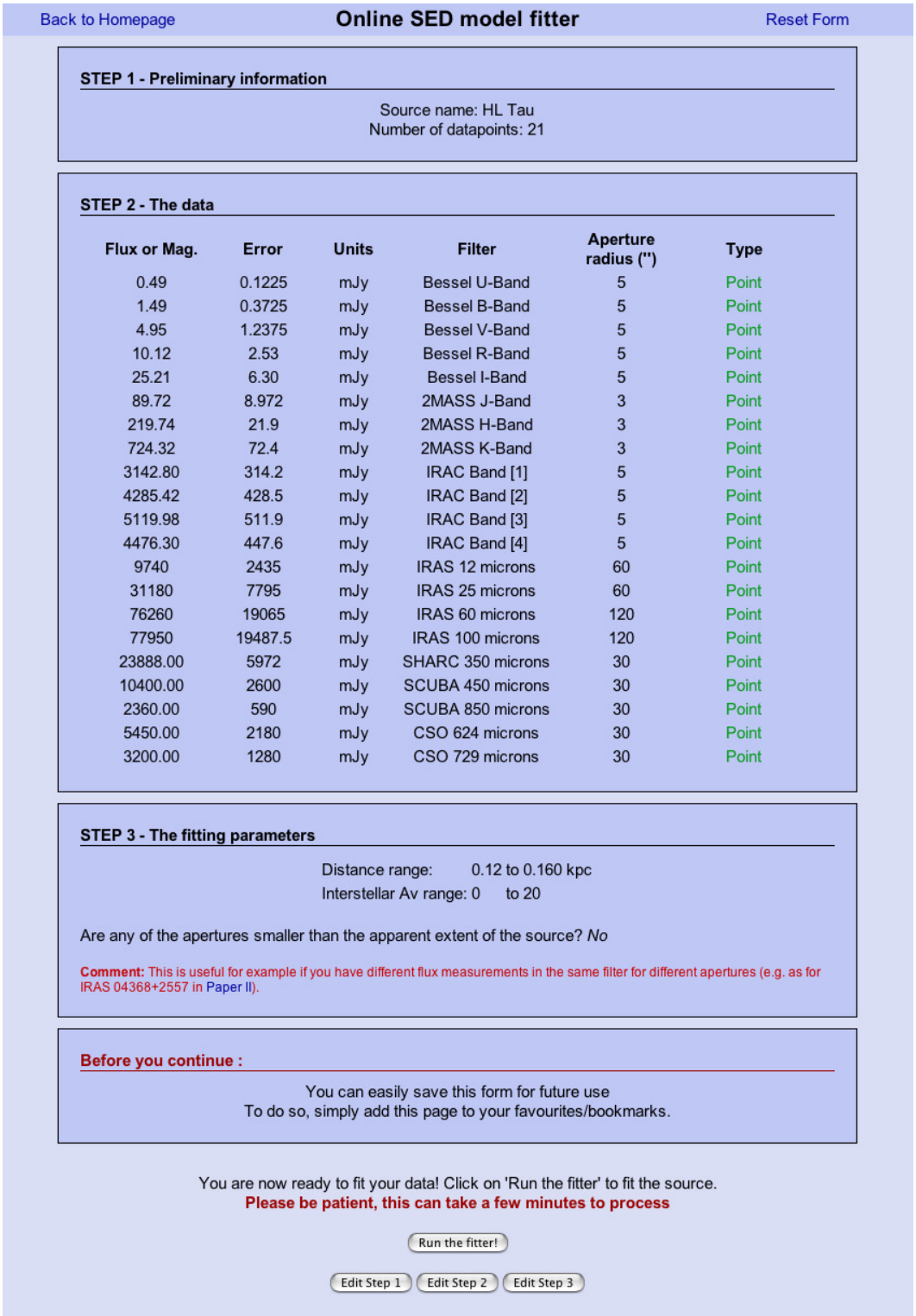

Back to Homepage — **Online SED model fitter** — Reset Form

STEP 1 - Preliminary information

Source name: HL Tau
Number of datapoints: 21

STEP 2 - The data

Flux or Mag.	Error	Units	Filter	Aperture radius (")	Type
0.49	0.1225	mJy	Bessel U-Band	5	Point
1.49	0.3725	mJy	Bessel B-Band	5	Point
4.95	1.2375	mJy	Bessel V-Band	5	Point
10.12	2.53	mJy	Bessel R-Band	5	Point
25.21	6.30	mJy	Bessel I-Band	5	Point
89.72	8.972	mJy	2MASS J-Band	3	Point
219.74	21.9	mJy	2MASS H-Band	3	Point
724.32	72.4	mJy	2MASS K-Band	3	Point
3142.80	314.2	mJy	IRAC Band [1]	5	Point
4285.42	428.5	mJy	IRAC Band [2]	5	Point
5119.98	511.9	mJy	IRAC Band [3]	5	Point
4476.30	447.6	mJy	IRAC Band [4]	5	Point
9740	2435	mJy	IRAS 12 microns	60	Point
31180	7795	mJy	IRAS 25 microns	60	Point
76260	19065	mJy	IRAS 60 microns	120	Point
77950	19487.5	mJy	IRAS 100 microns	120	Point
23888.00	5972	mJy	SHARC 350 microns	30	Point
10400.00	2600	mJy	SCUBA 450 microns	30	Point
2360.00	590	mJy	SCUBA 850 microns	30	Point
5450.00	2180	mJy	CSO 624 microns	30	Point
3200.00	1280	mJy	CSO 729 microns	30	Point

STEP 3 - The fitting parameters

Distance range: 0.12 to 0.160 kpc
Interstellar Av range: 0 to 20

Are any of the apertures smaller than the apparent extent of the source? *No*

Comment: This is useful for example if you have different flux measurements in the same filter for different apertures (e.g. as for IRAS 04368+2557 in Paper II).

Before you continue :

You can easily save this form for future use
To do so, simply add this page to your favourites/bookmarks.

You are now ready to fit your data! Click on 'Run the fitter' to fit the source.
Please be patient, this can take a few minutes to process

Run the fitter!

Edit Step 1 | Edit Step 2 | Edit Step 3

Figure C.3: Input form from the online interface to the SED fitting code.

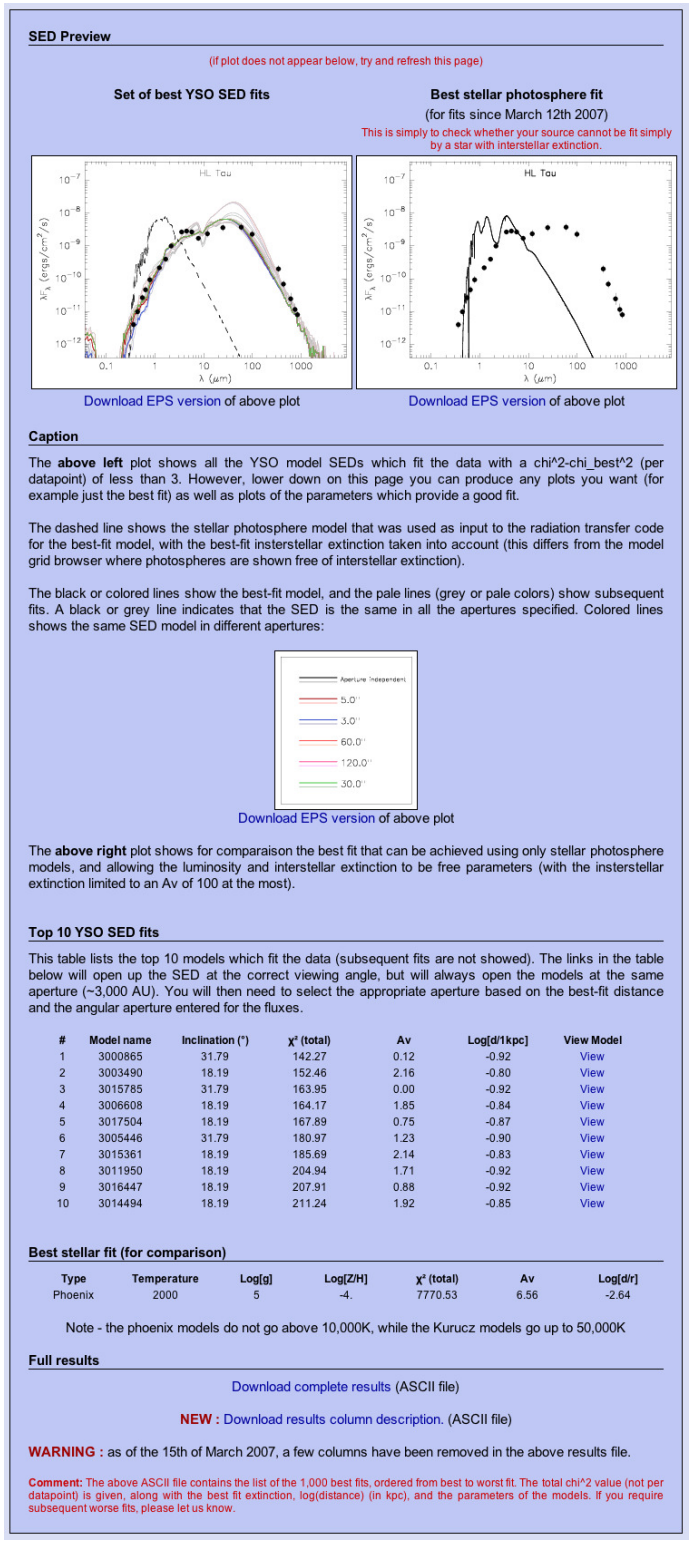

SED Preview

(if plot does not appear below, try and refresh this page)

Set of best YSO SED fits

Best stellar photosphere fit

(for fits since March 12th 2007)

This is simply to check whether your source cannot be fit simply by a star with interstellar extinction.

Download EPS version of above plot

Download EPS version of above plot

Caption

The **above left** plot shows all the YSO model SEDs which fit the data with a chi^2-chi_best^2 (per datapoint) of less than 3. However, lower down on this page you can produce any plots you want (for example just the best fit) as well as plots of the parameters which provide a good fit.

The dashed line shows the stellar photosphere model that was used as input to the radiation transfer code for the best-fit model, with the best-fit insterstellar extinction taken into account (this differs from the model grid browser where photospheres are shown free of interstellar extinction).

The black or colored lines show the best-fit model, and the pale lines (grey or pale colors) show subsequent fits. A black or grey line indicates that the SED is the same in all the apertures specified. Colored lines shows the same SED model in different apertures:

Download EPS version of above plot

The **above right** plot shows for comparaison the best fit that can be achieved using only stellar photosphere models, and allowing the luminosity and interstellar extinction to be free parameters (with the insterstellar extinction limited to an Av of 100 at the most).

Top 10 YSO SED fits

This table lists the top 10 models which fit the data (subsequent fits are not showed). The links in the table below will open up the SED at the correct viewing angle, but will always open the models at the same aperture (~3,000 AU). You will then need to select the appropriate aperture based on the best-fit distance and the angular aperture entered for the fluxes.

#	Model name	Inclination (°)	χ^2 (total)	Av	Log[d/1kpc]	View Model
1	3000865	31.79	142.27	0.12	-0.92	View
2	3003490	18.19	152.46	2.16	-0.80	View
3	3015785	31.79	163.95	0.00	-0.92	View
4	3006608	18.19	164.17	1.85	-0.84	View
5	3017504	18.19	167.89	0.75	-0.87	View
6	3005446	31.79	180.97	1.23	-0.90	View
7	3015361	18.19	185.69	2.14	-0.83	View
8	3011950	18.19	204.94	1.71	-0.92	View
9	3016447	18.19	207.91	0.88	-0.92	View
10	3014494	18.19	211.24	1.92	-0.85	View

Best stellar fit (for comparison)

Type	Temperature	Log[g]	Log[Z/H]	χ^2 (total)	Av	Log[d/r]
Phoenix	2000	5	-4.	7770.53	6.56	-2.64

Note - the phoenix models do not go above 10,000K, while the Kurucz models go up to 50,000K

Full results

Download complete results (ASCII file)

NEW : Download results column description. (ASCII file)

WARNING : as of the 15th of March 2007, a few columns have been removed in the above results file.

Comment: The above ASCII file contains the list of the 1,000 best fits, ordered from best to worst fit. The total chi^2 value (not per datapoint) is given, along with the best fit extinction, log(distance) (in kpc), and the parameters of the models. If you require subsequent worse fits, please let us know.

Figure C.4: A section of the results page from the online interface to the SED fitting code.

models presented in Chapter 3). For researchers wanting to analyse only one or a few sources, this is excessive. Therefore, a WWW interface to the SED fitting code described in §C.1 has been developed, allowing the fitting itself to be done on a central server, and removing the need for researchers to download the models.

The WWW interface was written in HTML with PHP scripts controlling the input of data, the execution of the fitting code behind the scenes, and the presentation of results. An example input form is shown in Figure C.3, and part of the corresponding results page is shown in Figure C.4.

D

The data for the 30 Taurus-Auriga sources

This appendix contains Tables D.1, D.2, D.3, D.4, and D.5, which list the optical to sub-mm data for the 30 Taurus-Auriga sources analysed in Chapter 4 as well as the apertures the fluxes were measured in.

Table D.1: Optical and near-infrared data for the 30 Taurus-Auriga sources.

Source Name	U	B	V	R	I	J	H	K	References
AA Tau	3.60	8.97	26.24	48.11	104.42	271.95	389.67	404.70	1,5
	± 1.61	± 3.62	± 10.20	± 18.80	± 40.92	± 7.76	± 13.28	± 14.53	
AB Aur	2361.72	5547.50	5723.75	4837.74	4797.35	6731.14	9671.64	13549.72	1,5
	± 106.45	± 144.47	± 105.42	± 125.98	± 152.98	± 111.57	± 178.13	± 199.64	
BP Tau	9.87	20.89	51.93	88.44	175.02	366.85	546.39	547.94	1,5
	± 2.01	± 2.83	± 4.76	± 8.73	± 17.93	± 13.18	± 15.60	± 15.64	
CI Tau	3.57	7.05	18.95	38.77	95.68	260.91	438.43	504.35	1,5
	± 1.29	± 2.07	± 3.60	± 7.36	± 18.17	± 6.73	± 17.36	± 13.93	
CoKu Tau 1	···	···	···	1.11	3.41	11.38	25.98	27.18	3,5
	···	···	···	± 0.00	± 0.00	± 0.32	± 0.75	± 0.61	
CY Tau	3.01	5.38	17.20	33.92	89.30	197.01	268.35	249.07	1,5
	± 0.64	± 0.96	± 1.58	± 3.17	± 8.70	± 5.81	± 9.64	± 7.34	
DG Tau	10.93	18.04	42.55	77.27	169.33	532.22	834.64	1064.46	1,5
	± 3.60	± 5.79	± 13.37	± 24.42	± 53.97	± 53.22	± 83.46	± 106.45	
DG Tau B	···	···	···	···	···	1.95	5.91	14.24	5
	···	···	···	···	···	± 0.19	± 0.59	± 1.42	
DL Tau	5.14	8.41	21.80	55.52	120.44	229.13	352.13	438.06	1,5
	± 1.29	± 2.00	± 4.33	± 14.65	± 31.79	± 7.39	± 10.70	± 12.91	
DM Tau	2.57	3.99	9.54	20.30	52.47	106.09	128.20	103.83	1,5
	± 0.69	± 0.80	± 1.56	± 3.62	± 9.38	± 3.03	± 3.42	± 3.16	
DN Tau	2.96	12.29	41.19	74.77	168.34	345.53	474.13	415.27	1,5
	± 0.66	± 1.06	± 3.03	± 5.66	± 13.56	± 17.82	± 21.83	± 12.24	
DO Tau	1.91	3.84	12.75	35.84	101.15	261.39	520.84	801.55	1,5
	± 1.01	± 1.68	± 4.87	± 15.76	± 45.33	± 2.65	± 18.23	± 25.10	
DR Tau	44.27	56.20	98.50	140.72	254.35	476.97	761.20	1192.15	1,5
	± 21.70	± 26.95	± 46.64	± 66.66	± 121.11	± 16.69	± 41.36	± 40.62	
FT Tau	···	2.32	5.03	22.56	75.30	143.12	239.39	255.35	2,5
	···	± 0.46	± 0.00	± 4.48	± 0.00	± 4.22	± 7.27	± 7.29	
GG Tau	6.55	14.88	49.44	94.85	193.02	547.13	757.71	764.07	1,5
	± 0.80	± 0.80	± 2.27	± 4.70	± 11.90	± 27.71	± 25.12	± 30.25	
GM Aur	6.93	21.28	58.29	95.61	···	299.56	379.40	322.06	1,5
	± 0.00	± 0.00	± 0.00	± 0.00	···	± 9.93	± 9.08	± 7.12	
HL Tau	0.49	1.49	4.95	10.12	25.21	89.72	219.74	724.32	1,5
	± 0.11	± 0.23	± 0.72	± 1.49	± 3.71	± 3.47	± 9.31	± 11.34	
IQ Tau	1.59	5.20	17.00	39.34	103.57	270.70	454.46	522.79	1,5
	± 0.94	± 2.93	± 6.24	± 15.46	± 40.78	± 9.72	± 14.23	± 19.26	
IRAS 04016+2610	···	···	0.03	0.06	0.18	5.98	22.24	123.62	1,4
	···	···	± 0.00	± 0.00	± 0.00	± 1.84	± 3.30	± 3.41	
IRAS 04169+2702	···	···	···	···	···	0.34	3.01	21.68	4
	···	···	···	···	···	± 0.17	± 0.10	± 0.40	

Table D.1: Continued

Source Name	U	B	V	R	I	J	H	K	References
IRAS 04248+2612	···	···	···	···	···	12.73	28.83	37.09	4
	···	···	···	···	···	± 2.12	± 4.58	± 5.74	
IRAS 04302+2247	···	···	···	···	···	3.33	11.76	24.88	4
	···	···	···	···	···	± 0.00	± 0.00	± 0.00	
IRAS 04325+2402	···	···	···	···	···	···	6.34	25.82	4
	···	···	···	···	···	···	± 0.00	± 0.00	
IRAS 04361+2547	···	···	···	···	···	0.61	7.28	40.28	4
	···	···	···	···	···	± 0.13	± 0.96	± 2.96	
IRAS 04365+2535	···	···	···	···	···	0.20	4.64	38.51	4
	···	···	···	···	···	± 0.05	± 1.10	± 7.98	
IRAS 04368+2557	···	···	···	···	···	5.05	31.09	75.39	5
	···	···	···	···	···	± 2.52	± 15.55	± 37.69	
L1551 IRS5	···	···	···	···	···	10.88	47.06	133.53	4
	···	···	···	···	···	± 5.48	± 23.21	± 27.67	
LkCa 15	2.75	13.59	43.87	73.39	136.38	270.45	375.58	357.05	1,5
	± 0.97	± 4.73	± 15.13	± 25.57	± 48.12	± 5.73	± 10.03	± 10.52	
RY Tau	42.79	146.36	345.54	507.61	891.41	2255.74	3797.52	4746.03	1,5
	± 18.92	± 64.16	± 150.72	± 221.69	± 390.17	± 66.47	± 220.31	± 122.37	
UY Aur	3.88	9.26	27.51	57.55	141.73	354.89	652.68	866.82	1,5
	± 1.83	± 4.35	± 12.86	± 27.20	± 68.36	± 10.46	± 13.82	± 25.54	

References — 1: UBVRI data from Kenyon & Hartmann (1995), 2: BVRI data from the USNO B-1.0 catalogue, 3: average BVRI data from the USNO B-1.0 catalogue and the NOMAD catalogue, 4: JHK data from Kenyon & Hartmann (1995), and 5: JHK data from the 2MASS all-sky survey (the fluxes for DG Tau, DG Tau B, and IRAS 04368+2557 were measured using aperture photometry)

Notes — Fluxes are in mJy. Values in italics indicate that these are not used when fitting the observed SEDs as higher quality values are available

Table D.2: Mid-infrared data for the 30 Taurus-Auriga sources.

Source Name	L	M	N	Q	IRAC 3.6 μm	IRAC 4.5 μm	IRAC 5.8 μm	IRAC 8.0 μm	References
AA Tau	*426.29*	*297.08*	*456.14*	···	370.55	352.24	331.89	355.82	1,2
	± 77.22	*± 43.31*	*± 101.69*	···	± 13.64	± 12.97	± 12.22	± 9.83	
AB Aur	12758.37	11802.62	*20003.61*	*57313.72*	···	···	···	···	1
	± 4022.34	± 3097.21	*± 4825.28*	*± 13825.24*	···	···	···	···	
BP Tau	*326.75*	*298.13*	*399.26*	*612.71*	318.99	281.25	231.23	335.86	1,4
	± 74.67	*± 30.05*	*± 109.58*	*± 61.76*	± 12.65	± 3.89	± 8.33	± 16.65	
CI Tau	*515.01*	···	*673.23*	···	640.10	558.67	487.90	572.97	1,4
	± 141.56	···	*± 156.72*	···	± 8.08	± 34.11	± 11.14	± 25.35	
CoKu Tau 1	*23.96*	···	···	···	21.72	49.55	102.98	315.60	1,2
	± 1.76	···	···	···	± 0.80	± 2.28	± 1.90	± 5.81	
CY Tau	*213.44*	···	···	···	203.57	170.30	148.89	135.25	1,2
	± 24.47	···	···	···	± 5.62	± 9.40	± 4.11	± 2.49	
DG Tau	*2802.86*	*4800.51*	*7062.90*	*14439.79*	1933.80	2337.04	2697.00	3307.00	1,4
	± 567.96	*± 1152.74*	*± 1696.01*	*± 3642.47*	± 56.63	± 153.35	± 254.70	± 111.03	
DG Tau B	*93.41*	*0.00*	*0.00*	*0.00*	90.62	287.88	571.47	830.28	1,2
	± 0.00	*± 0.00*	*± 0.00*	*± 0.00*	± 5.00	± 15.88	± 21.04	± 22.93	
DL Tau	*604.38*	*628.65*	*621.41*	*641.59*	484.00	533.14	525.85	590.51	1,2
	± 188.70	*± 63.37*	*± 127.81*	*± 64.67*	± 17.82	± 19.63	± 14.52	± 16.31	
DM Tau	*105.50*	···	*400.98*	···	55.72	37.80	23.24	22.13	1,4
	± 36.60	···	*± 126.03*	···	± 0.37	± 1.49	± 3.52	± 2.76	
DN Tau	*312.43*	*324.93*	*261.63*	···	305.50	262.55	242.66	253.06	1,2
	± 72.93	*± 41.55*	*± 42.33*	···	± 14.05	± 14.49	± 8.93	± 6.99	
DO Tau	*951.62*	*1276.84*	*1481.31*	*2480.41*	965.42	988.57	956.89	1026.19	1,2
	± 180.88	*± 120.54*	*± 258.38*	*± 204.91*	± 26.66	± 45.48	± 26.43	± 28.34	
DR Tau	*2315.37*	*2839.78*	*3098.98*	···	1858.72	1890.13	2004.28	1736.27	1,4
	± 866.54	*± 1150.99*	*± 1115.34*	···	± 204.37	± 151.04	± 304.25	± 216.95	
FT Tau	*202.49*	···	···	···	249.53	248.86	205.62	271.85	1,4
	± 0.00	···	···	···	± 2.62	± 2.81	± 1.69	± 10.47	
GG Tau	*746.69*	*722.98*	*945.53*	*420.42*	671.66	567.00	472.32	559.22	1,4
	± 130.07	*± 83.66*	*± 248.12*	*± 46.18*	± 33.22	± 10.93	± 18.54	± 24.92	
GM Aur	*161.34*	···	*461.93*	···	171.63	126.87	95.66	102.42	1,3
	± 25.08	···	*± 67.34*	···	± 2.21	± 0.70	± 0.79	± 2.36	
HL Tau	*1814.08*	*4067.90*	*6150.08*	*21814.62*	3142.80	4285.42	5119.98	4476.30	1,4
	± 623.29	*± 1501.81*	*± 2773.44*	*± 10458.28*	± 232.28	± 41.84	± 306.98	± 47.81	
IQ Tau	*412.46*	···	*403.47*	···	485.54	450.15	384.07	377.29	1,2
	± 82.62	···	*± 65.98*	···	± 8.94	± 3.32	± 8.84	± 2.78	
IRAS 04016+2610	*477.05*	*2149.58*	*2805.75*	*11727.33*	906.78	1453.51	1708.25	2634.31	1,4
	± 13.18	*± 59.37*	*± 77.50*	*± 323.91*	± 69.01	± 66.57	± 95.73	± 133.20	
IRAS 04169+2702	*70.27*	*227.12*	*564.88*	···	195.72	300.10	333.10	417.53	1,4
	± 2.89	*± 4.18*	*± 10.40*	···	± 9.27	± 9.99	± 3.49	± 14.07	

Table D.2: Continued

Source Name	L	M	N	Q	IRAC 3.6 μm	IRAC 4.5 μm	IRAC 5.8 μm	IRAC 8.0 μm	References
IRAS 04248+2612	*28.44*	···	*256.55*	*969.00*	65.22	67.36	78.44	109.88	1,2
	± 8.99	···	*± 39.68*	*± 149.88*	± 5.98	± 6.18	± 7.19	± 10.08	
IRAS 04302+2247	*21.40*	···	···	···	46.25	39.35	27.43	12.68	1,4
	± 0.00	···	···	···	± 0.76	± 0.46	± 0.03	± 1.17	
IRAS 04325+2402	···	···	···	···	74.88	77.34	58.96	38.81	2
	···	···	···	···	± 6.87	± 7.09	± 5.41	± 3.56	
IRAS 04361+2547	*103.71*	*234.08*	*1059.40*	···	264.48	353.50	415.47	880.85	1,4
	± 28.49	*± 17.20*	*± 77.85*	···	± 24.26	± 32.42	± 38.10	± 80.79	
IRAS 04365+2535	*139.33*	*276.58*	*650.91*	*5280.44*	374.30	892.98	1421.88	1469.69	1,2
	± 28.87	*± 57.30*	*± 134.86*	*± 1094.05*	± 20.65	± 32.88	± 39.27	± 40.59	
IRAS 04368+2557	···	···	···	···	166.87	221.00	264.57	82.58	2
	···	···	···	···	± 15.30	± 20.27	± 24.27	± 7.57	
L1551 IRS5	*447.41*	*1422.04*	*5266.47*	*25042.07*	598.89	1375.48	3105.60	4908.54	1,4
	± 179.84	*± 814.78*	*± 1091.15*	*± 5188.44*	± 5.83	± 2.70	± 34.90	± 41.39	
LkCa 15	*253.14*	···	*201.46*	···	267.79	207.04	142.68	163.29	1,4
	± 16.77	···	*± 7.42*	···	± 1.53	± 2.62	± 3.77	± 1.06	
RY Tau	*5677.26*	*7554.89*	*15922.10*	···	5749.96	5298.11	4403.50	5829.60	1,4
	± 1057.69	*± 2110.88*	*± 5629.73*	···	± 72.53	± 57.59	± 157.21	± 161.56	
UY Aur	*1398.63*	···	*2809.14*	*4939.96*	1072.04	···	1106.39	1713.42	1,3
	± 253.34	···	*± 409.52*	*± 720.16*	± 17.77	···	± 8.15	± 4.73	

References — 1: LMNQ data from Kenyon & Hartmann (1995), 2: IRAC data from Hartmann et al. (2005), 3: IRAC data from Luhman et al. (2006), 4: IRAC data measured using data retrieved from the *Spitzer Space Telescope* Archive

Notes — Fluxes are in mJy. Values in italics indicate that these are not used when fitting the observed SEDs as higher quality values are available

Table D.3: Far-infrared data for the 30 Taurus-Auriga sources.

Source Name	MIPS 24 μm	MIPS 70 μm	IRAS 12 μm	IRAS 25 μm	IRAS 60 μm	IRAS 100 μm	References
AA Tau	502.83	950.05	430.00	*610.00*	*1230.00*	*3290.00*	1,2
	± 2.80	± 95.00	± 33.00	± *32.00*	± *96.00*	± *601.00*	
AB Aur	···	···	28950.00	49780.00	115680.00	114470.00	2
	···	···	± 63.00	± 107.00	± 72.00	± 1956.00	
BP Tau	···	···	450.00	590.00	440.00	920.00	2
	···	···	± 35.00	± 36.00	± 2.00	± 226.00	
CI Tau	956.95	···	780.00	*1300.00*	2150.00	< 2540.00	1,2,3
	± 5.70	···	± 25.00	± *46.00*	± 71.00	···	
CoKu Tau 1	3453.61	···	1180.00	*2740.00*	< 7970.00	< 71090.00	1,2,3
	± 38.10	···	± 26.00	± *63.00*	···	···	
CY Tau	130.48	98.86	190.00	*270.00*	*140.00*	···	1,2
	± 1.38	± 9.89	± 45.00	± *35.00*	± *90.00*	···	
DG Tau	9332.72	9824.49	···	···	···	···	1
	± 854.50	± 982.45	···	···	···	···	
DG Tau B	4641.72	7836.02	···	···	···	···	1
	± 99.20	± 783.60	···	···	···	···	
DL Tau	906.17	888.20	970.00	*1320.00*	*1390.00*	*2830.00*	1,2
	± 4.80	± 88.82	± 34.00	± *45.00*	± *84.00*	± *949.00*	
DM Tau	···	···	< 270.00	350.00	830.00	< 7210.00	2,3
	···	···	···	± 33.00	± 104.00	···	
DN Tau	410.03	423.01	350.00	*600.00*	*650.00*	< *5787.00*	1,2
	± 2.60	± 42.30	± 30.00	± *53.00*	± *93.00*	···	
DO Tau	3115.98	2745.71	1880.00	*4070.00*	*6330.00*	*8550.00*	1,2
	± 32.30	± 274.57	± 34.00	± *41.00*	± *106.00*	± *1483.00*	
DR Tau	···	···	3160.00	4300.00	5510.00	6980.00	2
	···	···	± 29.00	± 51.00	± 44.00	± 1144.00	
FT Tau	···	···	360.00	570.00	820.00	1800.00	2
	···	···	± 45.00	± 37.00	± 41.00	± 1287.00	
GG Tau	···	···	1200.00	1720.00	3120.00	5480.00	2
	···	···	± 33.00	± 39.00	± 71.00	± 365.00	
GM Aur	747.62	1877.76	250.00	*1070.00*	*3080.00*	*3440.00*	1,2
	± 6.55	± 17.80	± 31.00	± *42.00*	± *112.00*	± *1969.00*	
HL Tau	···	···	9740.00	31180.00	76260.00	77950.00	2
	···	···	± 31.00	± 73.00	± 810.00	± 1394.00	
IQ Tau	500.09	579.59	500.00	*650.00*	*770.00*	< *1800.00*	1,2,3
	± 3.00	± 57.96	± 29.00	± *30.00*	± *43.00*	···	
IRAS 04016+2610	11992.36	···	3640.00	*15810.00*	48790.00	55690.00	1,2
	± 257.11	···	± 109.20	± *632.40*	± 3903.20	± 7239.70	
IRAS 04169+2702	4519.14	11745.45	750.00	*5210.00*	*17000.00*	*17460.00*	1,2
	± 821.84	± 1174.55	± 52.50	± *312.60*	± *1700.00*	± *2269.80*	

Table D.3: Continued

Source Name	MIPS 24 μm	MIPS 70 μm	IRAS 12 μm	IRAS 25 μm	IRAS 60 μm	IRAS 100 μm	References
IRAS 04248+2612	835.33	3640.03	< 360.00	*1330.00*	*4620.00*	*9260.00*	1,2
	± 4.80	± 364.00	···	± *106.40*	± *415.80*	± *833.40*	
IRAS 04302+2247	241.09	4774.75	< 250.00	*440.00*	*6400.00*	*9430.00*	1,2
	± 1.80	± 477.48	···	± *83.60*	± *640.00*	± *1131.60*	
IRAS 04325+2402	1860.53	8042.05	< 250.00	*2100.00*	*12860.00*	*22350.00*	1,2
	± 11.60	± 804.21	···	± *168.00*	± *1157.40*	± *3576.00*	
IRAS 04361+2547	···	···	1820.00	18870.00	44750.00	35430.00	2
	···	···	± 109.20	± 1132.20	± 5370.00	± 4251.60	
IRAS 04365+2535	6118.02	···	1190.00	*8620.00*	36010.00	39250.00	1,2
	± 399.90	···	± 142.80	± *517.20*	± 4321.20	± 5887.50	
IRAS 04368+2557	542.92	···	< 250.00	*740.00*	17770.00	73260.00	1,2
	± 3.20	···	···	± *66.60*	± 1599.30	± 11721.60	
L1551 IRS5	···	···	10040.00	106200.00	372900.00	457900.00	2
	···	···	± 502.00	± 4248.00	± 18645.00	± 59527.00	
LkCa 15	···	···	270.00	390.00	1500.00	1610.00	2
	···	···	± 30.00	± 33.00	± 48.00	± 200.00	
RY Tau	17862.32	9632.66	17740.00	*26480.00*	*18910.00*	*13500.00*	1,2
	± 4424.47	± 963.27	± 27.00	± *54.00*	± *66.00*	± *2501.00*	
UY Aur	···	···	3710.00	6870.00	7580.00	9400.00	2
	···	···	± 43.00	± 39.00	± 87.00	± 698.00	

References — 1: MIPS data measured using data retrieved from the *Spitzer Space Telescope* Archive, 2: IRAS data from Weaver & Jones (1992), 3: IRAS data from IRAS Point Source Catalog

Notes — Fluxes are in mJy. Values in italics indicate that these are not used when fitting the observed SEDs as higher quality values are available

Table D.4: Sub-mm data for the 30 Taurus-Auriga sources.

Source Name	SHARC 350 μm	SCUBA 450 μm	SCUBA 850 μm	CSO 624 μm	CSO 729 μm	References
AA Tau	825.00	415.00	144.00	···	310.00	1,2
	± 50.00	± 84.00	± 5.00	···	± 60.00	
AB Aur	8930.00	3820.00	359.00	···	···	1
	± 1410.00	± 570.00	± 67.00	···	···	
BP Tau	···	< 456.00	130.00	···	···	1
	···	···	± 7.00	···	···	
CI Tau	1725.00	846.00	324.00	1300.00	850.00	1,2
	± 55.00	± 89.00	± 6.00	± 210.00	± 150.00	
CoKu Tau 1	···	< 522.00	35.00	···	···	1
	···	···	± 7.00	···	···	
CY Tau	< 1839.00	< 210.00	140.00	···	240.00	1,2
	···	···	± 5.00	···	± 40.00	
DG Tau	< 5173.00	< 3950.00	< 1100.00	< 1210.00	< 860.00	1,2
	···	···	···	···	···	
DG Tau B	< 5173.00	< 3950.00	< 1100.00	< 1210.00	< 860.00	1,2
	···	···	···	···	···	
DL Tau	1390.00	1280.00	440.00	880.00	530.00	1,2
	± 180.00	± 170.00	± 40.00	± 140.00	± 90.00	
DM Tau	1077.00	···	237.00	390.00	470.00	1,2
	± 49.00	···	± 12.00	± 130.00	± 80.00	
DN Tau	615.00	< 703.00	201.00	···	380.00	1,2
	± 64.00	···	± 7.00	···	± 80.00	
DO Tau	···	734.00	258.00	700.00	510.00	1,2
	···	± 50.00	± 42.00	± 100.00	± 100.00	
DR Tau	···	2380.00	533.00	···	400.00	1,2
	···	± 172.00	± 7.00	···	± 80.00	
FT Tau	1106.00	437.00	121.00	260.00	250.00	1,2
	± 82.00	± 56.00	± 5.00	± 100.00	± 50.00	
GG Tau	6528.00	2726.00	1255.00	1370.00	1250.00	1,2
	± 153.00	± 250.00	± 57.00	± 170.00	± 8.00	
GM Aur	3419.00	···	···	1340.00	850.00	1,2
	± 133.00	···	···	± 330.00	± 90.00	
HL Tau	23888.00	10400.00	2360.00	5450.00	3200.00	1,2
	± 149.00	± 1400.00	± 90.00	± 290.00	± 100.00	
IQ Tau	···	425.00	178.00	···	···	1
	···	± 26.00	± 3.00	···	···	
IRAS 04016+2610	12477.00	···	···	···	···	1
	± 193.00	···	···	···	···	
IRAS 04169+2702	7344.00	···	···	···	···	1
	± 152.00	···	···	···	···	

Table D.4: Continued

Source Name	SHARC 350 μm	SCUBA 450 μm	SCUBA 850 μm	CSO 624 μm	CSO 729 μm	References
IRAS 04248+2612	1178.00	···	···	···	···	1
	± 30.00	···	···	···	···	
IRAS 04302+2247	2869.00	···	···	···	···	1
	± 21.00	···	···	···	···	
IRAS 04325+2402	···	606.00	186.00	···	···	1
	···	± 185.00	± 11.00	···	···	
IRAS 04361+2547	···	1302.00	275.00	···	···	1
	···	± 168.00	± 8.00	···	···	
IRAS 04365+2535	···	2928.00	622.00	···	···	1
	···	± 230.00	± 13.00	···	···	
IRAS 04368+2557	···	2849.00	895.00	···	···	1
	···	± 222.00	± 11.00	···	···	
L1551 IRS5	100423.00	···	···	···	···	1
	± 812.00	···	···	···	···	
LkCa 15	1235.00	···	428.00	···	···	1
	± 80.00	···	± 11.00	···	···	
RY Tau	2439.00	1920.00	560.00	···	···	1
	± 330.00	± 160.00	± 30.00	···	···	
UY Aur	542.00	< 523.00	102.00	···	···	1
	± 77.00	···	± 6.00	···	···	

References — 1: SHARC II and SCUBA data from the compilation presented in Andrews & Williams (2005), 2: CSO data from Beckwith & Sargent (1991)

Notes — Fluxes are in mJy. Values in italics indicate that these are not used when fitting the observed SEDs as higher quality values are available

Table D.5: Apertures assumed for the SED fitting.

Source Name	UBVRI	JHK	LM	IRAC	MIPS 24 μm	MIPS 70 μm	IRAS 12 & 25 μm	IRAS 60 & 100 μm	Sub-mm
AA Tau	5	3	···	5	10	20	60	···	30
AB Aur	5	3	15	···	···	···	60	120	30
BP Tau	5	3	···	5	···	···	60	120	30
CI Tau	5	3	···	5	10	···	60	120	30
CoKu Tau 1	5	3	···	5	10	···	60	120	30
CY Tau	5	3	···	5	10	20	60	···	30
DG Tau	5	10	···	5	10	20	···	···	30
DG Tau B	···	10	···	5	10	20	···	···	30
DL Tau	5	3	···	5	10	20	60	···	30
DM Tau	5	3	···	5	···	···	60	120	30
DN Tau	5	3	···	5	10	20	60	···	30
DO Tau	5	3	···	5	10	20	60	···	30
DR Tau	5	3	···	5	···	···	60	120	30
FT Tau	5	3	···	5	···	···	60	120	30
GG Tau	5	3	···	5	···	···	60	120	30
GM Aur	5	3	···	5	10	20	60	···	30
HL Tau	5	3	···	5	···	···	60	120	30
IQ Tau	5	3	···	5	10	20	60	···	30
IRAS 04016+2610	5	15	···	5	10	···	60	120	30
IRAS 04169+2702	···	15	···	5	10	20	60	···	30
IRAS 04248+2612	···	15	···	26	10	20	60	···	30
IRAS 04302+2247	···	15	···	26	10	20	60	···	30
IRAS 04325+2402	···	15	···	26	10	20	60	···	30
IRAS 04361+2547	···	15	···	35	···	···	60	120	30
IRAS 04365+2535	···	15	···	5	10	···	60	120	30
IRAS 04368+2557	···	100	···	100	10	···	60	120	30
L1551 IRS5	···	15	···	15	···	···	60	120	30
LkCa 15	5	3	···	13	···	···	60	120	30
RY Tau	5	3	···	5	10	20	60	···	30
UY Aur	5	3	···	5	···	···	60	120	30

Notes — The apertures quoted are in arcseconds. When PSF photometry is done, the apertures were taken to be slightly larger than the FWHM of the PSF. The apertures for the UBVRIJHKLM data from Kenyon & Hartmann (1995) are estimates. The 3″ aperture for the 2MASS data is slightly larger than the 2″ pixel size of 2MASS data. The JHK apertures for DG Tau, DG Tau B and IRAS 04368+2557 are those used to carry out aperture photometry on 2MASS data. An aperture of 5″ was used for the IRAC data from Hartmann et al. (2005) and Luhman et al. (2006) (the latter used PSF photometry, and 5″ is likely an upper limit on the source sizes). The apertures for the IRAC data are those used for aperture photometry by Luhman et al. (2006) or by the authors of this paper. The MIPS PSF full width half maxima are 6 and 18″ for MIPS 24 and 70 μm respectively. Therefore, apertures of 10″ and 20″ were used respectively. The apertures on the IRAS telescope were rectangular, therefore only estimated effective aperture radii are used, specifically 60″ for the 12 and 25 μm data, and 120″ for the 60 and 100 μm data. Finally, Andrews & Williams (2005) used a 30″ aperture to measure the SHARC II 350 μm sub-mm fluxes, but no information concerning the SCUBA and CSO data was available. Since the FWHM of all these instruments is comparable, an aperture of 30″ was assumed for all sub-mm fluxes.

E

Custom photometry program

This appendix gives an overview of the custom-written photometry program used to validate the GLIMPSE photometry in Chapter 5. The large number of sources to perform photometry for (over 20,000), the fact that each of these sources needed to be inspected, and the need to manually adjust the photometry in some cases, meant that a custom interactive photometry tool was needed. The program is written in Fortran 95, and uses the `cfitiso` library for FITS file input/output, and the `PGPLOT` library to display the results of the photometry.

For the PSF photometry described here, it was found that the PRFs provided by the SSC, which are intended for BCD frames, were not adequate for photometry on the GLIMPSE mosaics. This is because the mosaicking tends to make sources less centrally peaked than in the BCD frames. Therefore, approximately 100,000 bright (> 100 mJy) GLIMPSE sources were used in each IRAC band in order to construct PRFs from the mosaics. The resulting PRFs are shown in Figure E.1 on linear and logarithmic greyscales.

The photometry program performs the following for each source:

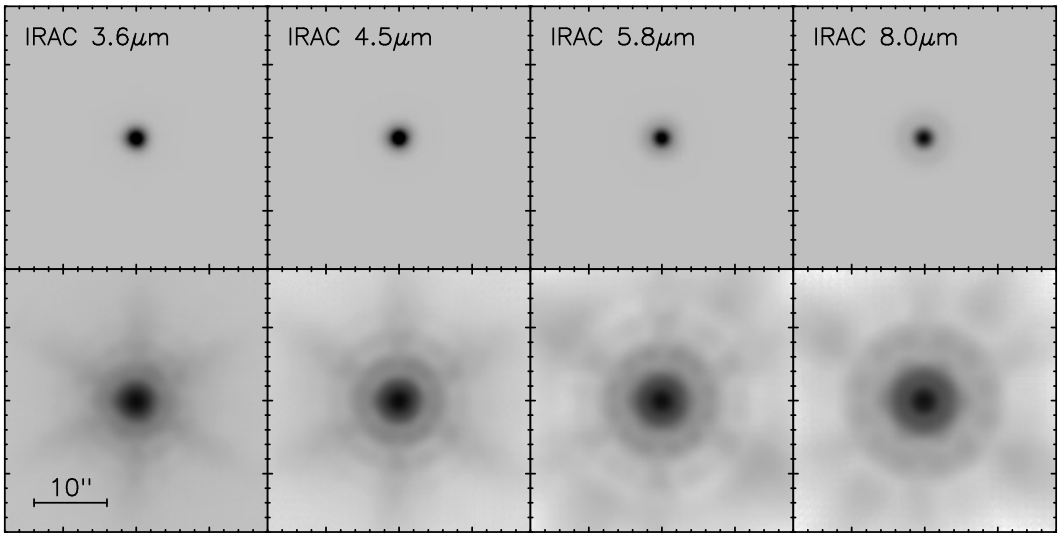

Figure E.1: PRFs for the four *Spitzer* IRAC channels, derived using the 1.2″ resolution mosaics for the GLIMPSE data products. In each case, approximately 100,000 bright stars (> 100 mJy) were used. Each PRF is shown on a linear (*top*) and logarithmic (*bottom*) greyscale.

1. The GLIMPSE source position is read in.

2. Aperture photometry is performed at the position of the GLIMPSE source using three different combinations of source/sky apertures. This is done by searching for all pixels inside the stellar aperture or the sky annulus, and summing the fluxes of these pixels. The uncertainties are estimated as described in Reach et al. (2005), but ignoring the contribution from Poisson noise, which is not expected to be the dominating source of noise.

3. PSF photometry is performed at the position of the GLIMPSE source by fitting a PSF to the source using linear regression. The code varies the position by up to 1″ in order to minimise the χ^2 of the PSF fit.

4. The image of the source is displayed, with apertures overlaid, radial profiles, and the residual image for the PSF fit. Examples of this display are shown in Figures E.2, E.3, and E.4.

5. The user can then interactively adjust the position and flux of the PSF if needed, in order to improve the cleanliness of the residual (c.f. Figure E.4).

6. The user then chooses which estimate is the most reliable. In cases where more than one method is reliable, aperture photometry is given priority over PSF photometry, and automated PSF photometry is given priority over adjusted PSF photometry. That is, the

adjusted PSF photometry is only used as a last resort if all other methods are unreliable. If none of the methods provide reliable photometry (for example in the case of extended sources), the user can flag the photometry as unreliable.

7. The photometry and flags are saved, and the next source is read in.

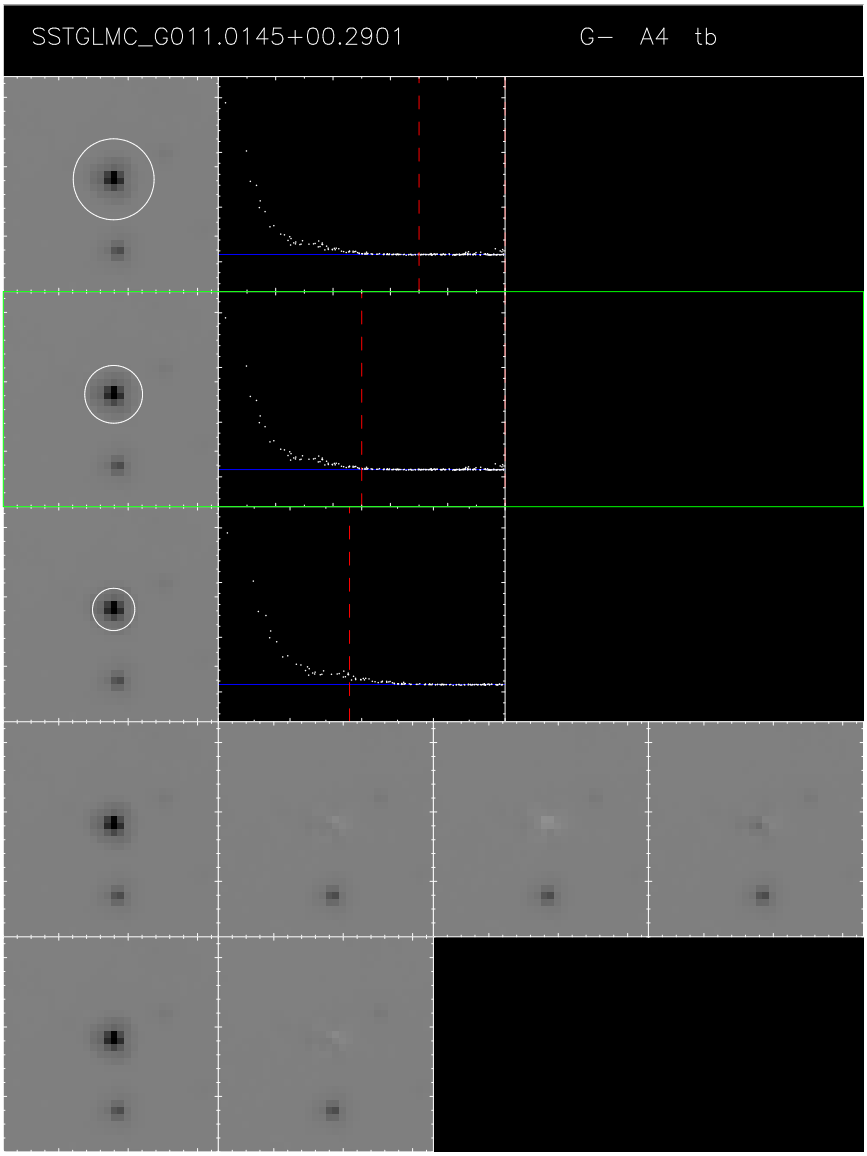

Figure E.2: Screenshot of the program used to inspect the independent photometry. The three top rows show the source with 3.7″, 5″, and 7″ stellar apertures respectively. The fourth row shows, from left to right: the original data, the PRF subtracted data, the PRF subtracted data using the flux value increased by 10%, and the PRF subtracted data using the flux decreased by 10%, the latter two being used to make sure that the flux is accurately determined. The fifth row shows the residual for the custom PRF photometry. By pressing on various keys, one can move and scale the subtracted PSF in the bottom panel interactively. In this specific case, both aperture and PSF photometry appear to be reliable, so aperture photometry was chosen.

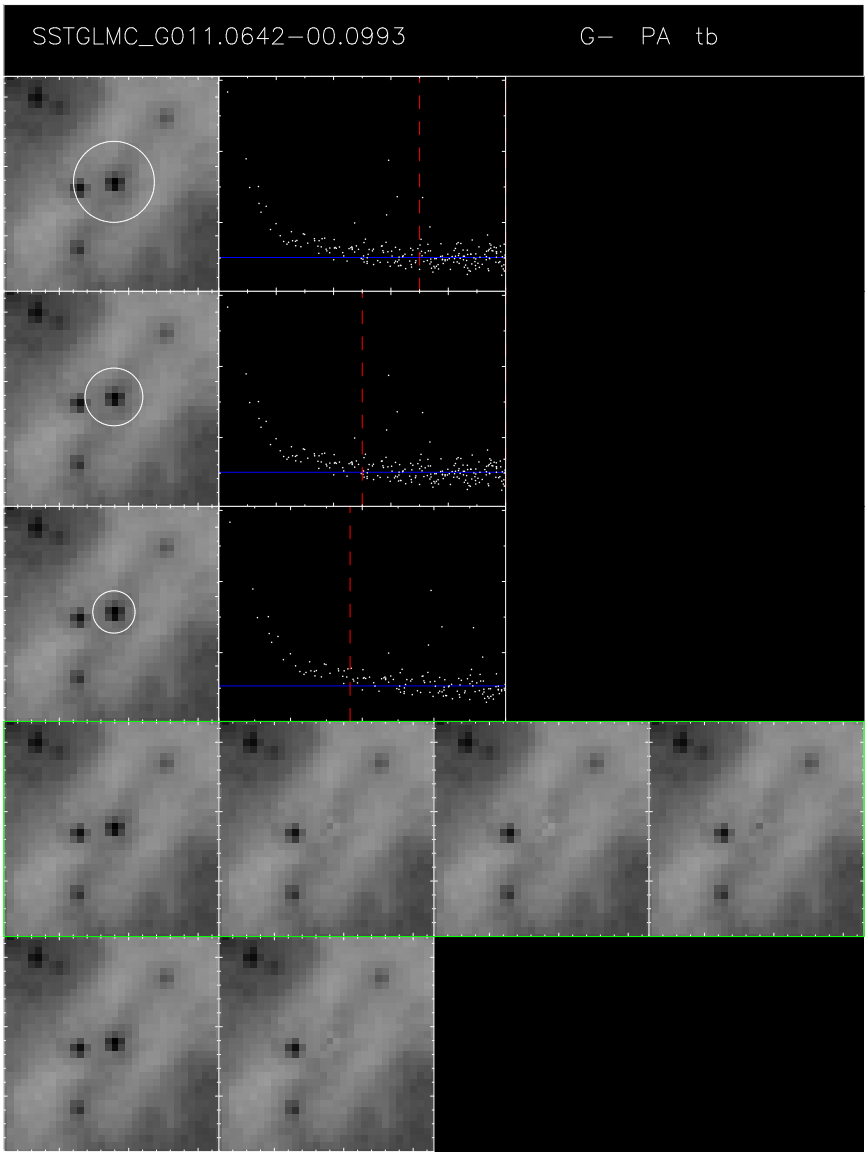

Figure E.3: As for Figure E.2, but this time the automated PSF photometry is prefered over the aperture photometry due to the spatially varying background.

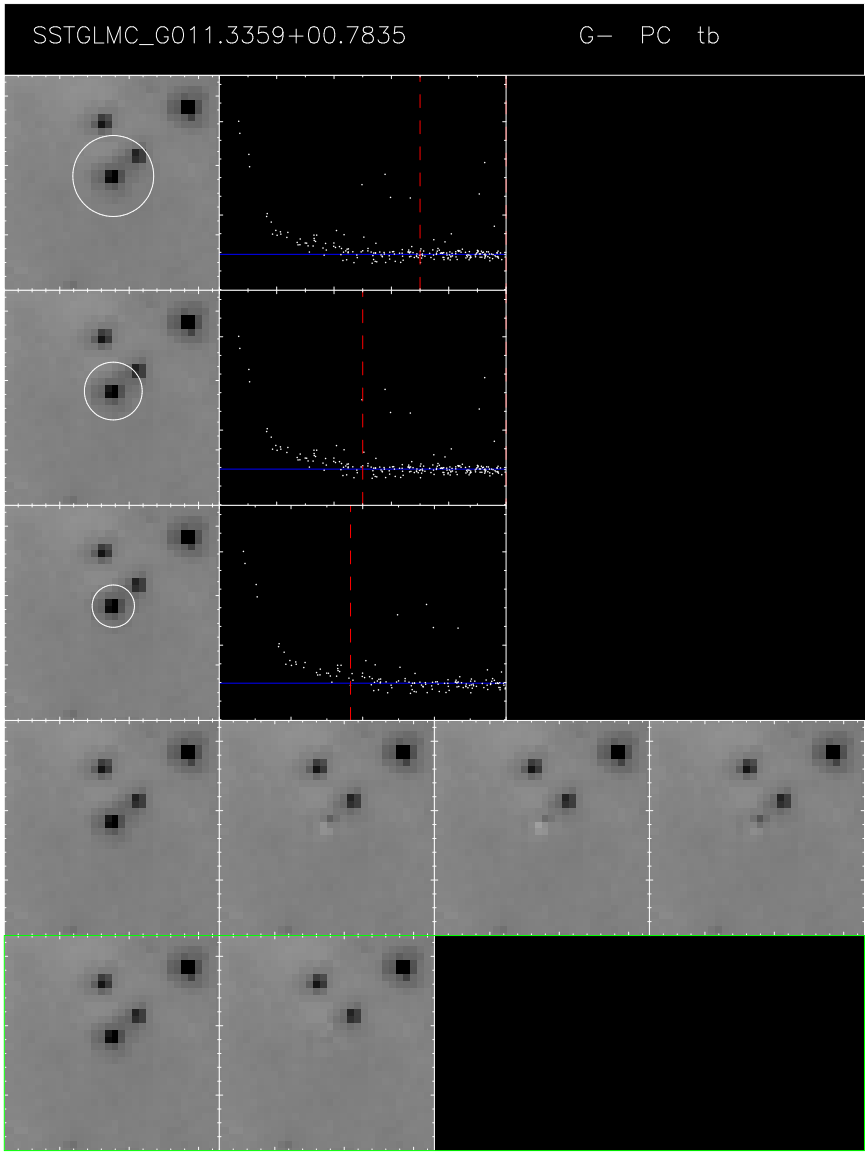

Figure E.4: As for Figure E.2, but this time the adjusted PSF photometry is prefered over the aperture and automated PSF photometry due to the spatially varying background, and the fact that the position of the source can be improved.

F

The red source catalogue

This appendix contains Tables F.1 and F.2, which list all red sources and the subset of red sources with two epoch photometry respectively. However, due to the length of the tables, only the first few lines are shown in each case. The full tables are available in electronic format in the DVD included with this thesis.

Table F.1: Final red source catalogue sources

Source name	Celestial co-ordinates[a]				2MASS			GLIMPSE Catalog				This work				
	ℓ	b	α (J2000)	δ (J2000)	J	H	K_s	[3.6]	[4.5]	[5.8]	[8.0]	[4.5]	[8.0]	MSX E	[24.0]	Flag[b]
SSTGLMC G000.0000+00.1611	0.0000	0.1611	266.2480	−28.8521	···	···	···	9.78	9.19	8.64	8.05	9.13	8.17	···	···	AA
SSTGLMC G000.0000−00.4342	0.0000	−0.4342	266.8295	−29.1617	···	···	11.73	8.29	6.67	5.37	4.30	6.89	4.31	···	0.89	IA
SSTGLMC G000.0031−00.5072	0.0031	−0.5072	266.9029	−29.1969	···	···	···	12.62	10.09	7.60	5.68	10.37	5.69	···	1.41	IA
SSTGLMC G000.0046+01.1431	0.0046	1.1432	265.2992	−28.3321	10.64	9.87	9.40	7.63	6.67	5.78	5.04	6.64	5.03	···	4.50	AA
SSTGLMC G000.0058+00.1527	0.0058	0.1528	266.2596	−28.8516	13.62	11.98	10.73	9.10	8.53	7.85	6.78	8.56	6.76	···	3.59	AA
SSTGLMC G000.0083−00.4818	0.0084	−0.4817	266.8810	−29.1792	···	···	···	9.74	8.79	7.85	7.19	8.88	7.18	···	3.97	AA
SSTGLMC G000.0085+00.1542	0.0085	0.1543	266.2597	−28.8484	···	···	12.57	8.31	6.86	5.78	5.31	6.87	5.29	···	2.94	AA
SSTGLMC G000.0098+00.1625	0.0098	0.1626	266.2525	−28.8430	···	13.39	···	8.34	7.59	7.07	6.32	7.50	6.26	···	2.54	AA
SSTGLMC G000.0106−00.7315	0.0106	−0.7314	267.1274	−29.3063	11.31	8.97	7.77	···	7.18	···	6.07	7.21	6.01	···	2.60	AA
SSTGLMC G000.0110−01.0237	0.0110	−1.0236	267.4151	−29.4564	···	···	···	9.25	8.32	7.27	6.30	8.44	6.24	···	2.15	AA
SSTGLMC G000.0115−01.2781	0.0115	−1.2780	267.6664	−29.5864	11.75	10.50	···	8.81	8.25	7.62	6.84	8.26	6.79	···	5.15	AA
SSTGLMC G000.0127−01.2146	0.0127	−1.2146	267.6045	−29.5529	10.58	8.26	···	···	6.66	6.19	5.53	6.77	5.47	···	2.77	AA
SSTGLMC G000.0164−00.2597	0.0164	−0.2597	266.6684	−29.0572	···	12.67	9.80	7.47	6.94	6.10	5.67	6.98	5.71	···	3.16	AA
SSTGLMC G000.0177−01.8424	0.0177	−1.8423	268.2291	−29.8687	12.14	11.30	10.92	10.53	10.13	9.61	8.04	10.25	8.01	···	4.94	AA
SSTGLMC G000.0196−00.0581	0.0197	−0.0581	266.4735	−28.9497	···	···	···	9.06	8.08	7.31	6.88	8.46	6.97	···	···	IA
SSTGLMC G000.0196−00.1580	0.0197	−0.1579	266.5709	−29.0016	···	···	···	7.29	6.72	5.99	5.65	6.82	5.69	···	3.42	AA
SSTGLMC G000.0226+00.2504	0.0226	0.2505	266.1746	−28.7862	13.38	11.99	11.07	9.56	9.05	8.68	8.00	9.23	7.97	···	4.67	AA
SSTGLMC G000.0311−00.3491	0.0311	−0.3490	266.7645	−29.0910	···	···	12.16	8.88	7.88	7.23	6.80	7.98	6.88	···	3.78	AA
SSTGLMC G000.0321−00.1746	0.0321	−0.1746	266.5946	−28.9996	···	···	···	8.81	7.15	5.75	4.93	7.21	4.90	···	1.69	AA
SSTGLMC G000.0371+01.6473	0.0371	1.6475	264.8339	−28.0370	11.32	10.06	9.11	7.59	6.79	6.06	5.20	6.81	5.19	···	2.84	AA
SSTGLMC G000.0397+00.1519	0.0397	0.1520	266.2806	−28.8230	···	···	12.45	8.19	7.08	6.24	5.94	7.19	6.01	···	4.15	AA
SSTGLMC G000.0408−00.7197	0.0408	−0.7196	267.1336	−29.2744	···	···	···	···	10.80	···	6.00	10.92	5.96	···	0.95	AA
SSTGLMC G000.0419+00.0821	0.0419	0.0822	266.3499	−28.8576	···	···	11.34	8.93	7.24	5.89	5.13	7.39	5.15	···	1.85	AA
SSTGLMC G000.0424−00.2043	0.0424	−0.2042	266.6297	−29.0062	···	···	···	11.23	10.04	9.09	8.41	10.18	8.43	···	···	AA
SSTGLMC G000.0455+00.0699	0.0455	0.0700	266.3639	−28.8609	···	···	···	10.36	8.78	7.58	6.73	8.89	6.74	···	···	AA
SSTGLMC G000.0540−00.7328	0.0540	−0.7327	267.1543	−29.2698	14.04	11.10	9.64	···	7.93	···	6.91	7.98	6.82	···	5.33	AA
SSTGLMC G000.0566−00.7363	0.0567	−0.7363	267.1593	−29.2693	···	12.86	11.79	···	9.42	···	7.90	9.43	7.82	···	3.47	AA
···	···	···	···	···	···	···	···	···	···	···	···	···	···	···	···	

a — These co-ordinates are set to the average position of the source at 4.5 and at 8.0 μm. This position may differ slightly from the 'official' GLIMPSE position in cases where PSF fitting was used to determine the flux of the source if the position of the source was adjusted to obtain a better residual.

b — This column lists two characters, which are flags for 4.5 and 8.0 μm respectively. A = GLIMPSE Catalog magnitudes are in agreement with the independent magnitudes calculated for this work. I = the independent magnitudes calculated for this work should be trusted over the GLIMPSE Catalog magnitudes.

Notes — The zero-magnitude fluxes assumed for this work are: $F_\nu(J) = 1594$ Jy, $F_\nu(H) = 1024$ Jy, $F_\nu(K_s) = 666.7$ Jy, $F_\nu(3.6\mu\text{m}) = 280.9$ Jy, $F_\nu(4.5\mu\text{m}) = 179.7$ Jy, $F_\nu(5.8\mu\text{m}) = 115.0$ Jy, $F_\nu(8.0\mu\text{m}) = 64.13$ Jy, $F_\nu(\text{MSX E}) = 8.75$ Jy, $F_\nu(24.0\mu\text{m}) = 7.14$ Jy.

Table F.2: Red sources from the GLIMPSE II region with photometry at two epochs

	Celestial co-ordinates[a]				Epoch 1		Epoch 2		
GLIMPSE source name	ℓ	b	α (J2000)	δ (J2000)	[4.5]	[8.0]	[4.5]	[8.0]	Variable[b]
SSTGLMC G000.0046+01.1431	0.0046	1.1432	265.2992	−28.3321	6.67	5.04	6.89	5.22	N
SSTGLMC G000.0106−00.7315	0.0106	−0.7314	267.1274	−29.3063	7.18	6.07	···	5.17	Y
SSTGLMC G000.0110−01.0237	0.0110	−1.0236	267.4151	−29.4564	8.32	6.30	8.34	6.32	N
SSTGLMC G000.0115−01.2781	0.0115	−1.2780	267.6664	−29.5864	8.25	6.84	8.30	6.87	N
SSTGLMC G000.0127−01.2146	0.0127	−1.2146	267.6045	−29.5529	6.66	5.53	6.58	5.51	N
SSTGLMC G000.0177−01.8424	0.0177	−1.8423	268.2291	−29.8687	10.13	8.04	10.10	8.04	N
SSTGLMC G000.0371+01.6473	0.0371	1.6475	264.8339	−28.0370	6.79	5.20	···	4.70	Y
SSTGLMC G000.0408−00.7197	0.0408	−0.7196	267.1336	−29.2744	10.80	6.00	10.77	5.99	N
SSTGLMC G000.0540−00.7328	0.0540	−0.7327	267.1543	−29.2698	7.93	6.91	8.09	6.90	N
SSTGLMC G000.0566−00.7363	0.0567	−0.7363	267.1593	−29.2693	9.42	7.90	9.40	7.83	N
SSTGLMC G000.0570+01.2494	0.0571	1.2495	265.2283	−28.2313	10.46	8.88	10.37	8.95	N
SSTGLMC G000.0600+00.7208	0.0600	0.7210	265.7404	−28.5077	7.22	5.76	7.19	5.80	N
SSTGLMC G000.0615−01.1113	0.0616	−1.1113	267.5313	−29.4580	9.75	8.32	9.70	8.36	N
SSTGLMC G000.0745+01.6251	0.0745	1.6252	264.8778	−28.0172	10.09	8.60	10.19	8.73	N
SSTGLMC G000.0865+00.7890	0.0865	0.7891	265.6903	−28.4493	8.17	7.04	8.13	7.01	N
SSTGLMC G000.0965+00.9888	0.0965	0.9889	265.5033	−28.3355	8.71	6.90	8.58	6.87	N
SSTGLMC G000.1051+00.8920	0.1051	0.8921	265.6019	−28.3793	6.63	5.60	6.78	5.72	N
···	···	···	···	···	···	···	···	···	···

a — These co-ordinates are set to the average position of the source at 4.5 and at 8.0 μm, as in Table F.1.

b — Whether the magnitudes for the two epochs differ by at least 0.3 mag at either (or both) 4.5 μm or 8.0 μm.

Online resources

[1] - http://circumstellardisks.org/

[2] - http://stardust.jpl.nasa.gov/

[3] - http://gemelli.colorado.edu/ bwhitney/

[4] - http://www.astro.wisc.edu/protostars/

[5] - http://spider.ipac.caltech.edu/staff/jarrett/irac/

[6] - http://irsa.ipac.caltech.edu/data/SPITZER/GLIMPSE/doc/glimpse1_dataprod_v2.0.pdf

[7] - http://irsa.ipac.caltech.edu/data/SPITZER/GLIMPSE/doc/glimpse2_dataprod_v2.0.pdf

[8] - http://irsa.ipac.caltech.edu/data/SPITZER/GLIMPSE/doc/glimpse_quality_assurance_v1.0.pdf

[9] - http://ssc.spitzer.caltech.edu/documents/som/

[10] - http://ssc.spitzer.caltech.edu/postbcd/bandmerge.html

[11] - http://ssc.spitzer.caltech.edu/irac/spectral_response.html

[12] - http://ssc.spitzer.caltech.edu/mips/dh/

[13] - http://ssc.spitzer.caltech.edu/mips/spectral_response.html

[14] - http://irsa.ipac.caltech.edu/IRASdocs/exp.sup/ch6/C3.html

[15] - http://irsa.ipac.caltech.edu/IRASdocs/exp.sup/ch2/tabC5.html

[16] - http://www.jach.hawaii.edu/JCMT/continuum/background/background.html

Bibliography

Acke, B., & van den Ancker, M. E. 2004, A&A, 426, 151

Acker, A., Marcout, J., Ochsenbein, F., Stenholm, B., & Tylenda, R. 1992, Garching: European Southern Observatory

Adams, F. C., Lada, C. J., & Shu, F. H. 1987, ApJ, 312, 788

Adams, F. C., & Shu, F. H. 1985, ApJ, 296, 655

——. 1986, ApJ, 308, 836

Akeson, R. L. et al. 2005, ApJ, 622, 440

Alcalá, J. M. et al. 2008, ApJ, 676, 427

Alexander, R. D., Clarke, C. J., & Pringle, J. E. 2006a, MNRAS, 369, 216

——. 2006b, MNRAS, 369, 229

Alksnis, A., Balklavs, A., Dzervitis, U., Eglitis, I., Paupers, O., & Pundure, I. 2001, Baltic Astronomy, 10, 1

Allamandola, L. J., Tielens, A. G. G. M., & Barker, J. R. 1985, ApJ, 290, L25

Allen, A., Li, Z.-Y., & Shu, F. H. 2003, ApJ, 599, 363

Allen, C. W. 1973, London: University of London

Allen, L. et al. 2007, Protostars and Planets V, 361

Allen, L. E. et al. 2004, ApJS, 154, 363

Alves, D. R. 2004, New Astronomy Reviews, 48, 659

Ambartsumian, J. A. 1947, in Stellar Evolution and Astrophysics, Erevan: Acad. Sci. Armen. SSR

Andre, P., Ward-Thompson, D., & Barsony, M. 1993, ApJ, 406, 122

Andrews, S. M., & Williams, J. P. 2005, ApJ, 631, 1134

——. 2007, ApJ, 659, 705

Arce, H. G., & Goodman, A. A. 2001, ApJ, 554, 132

Arce, H. G., & Sargent, A. I. 2004, ApJ, 612, 342

——. 2006, ApJ, 646, 1070

Arce, H. G., Shepherd, D., Gueth, F., Lee, C.-F., Bachiller, R., Rosen, A., & Beuther, H. 2007, Protostars and Planets V, 245

Artymowicz, P., & Lubow, S. H. 1994, ApJ, 421, 651

Bachiller, R. 1996, ARA&A, 34, 111

Bachiller, R., & Tafalla, M. 1999, The Origin of Stars and Planetary Systems. Edited by Charles J. Lada and Nikolaos D. Kylafis. Kluwer Academic Publishers, 227

Bacmann, A., André, P., Puget, J.-L., Abergel, A., Bontemps, S., & Ward-Thompson, D. 2000, A&A, 361, 555

Bally, J., Reipurth, B., & Davis, C. J. 2007, Protostars and Planets V, 215

Bastien, P. 1987, ApJ, 317, 231

Bate, M. R., Bonnell, I. A., & Bromm, V. 2003, MNRAS, 339, 577

Beckwith, S., Sargent, A. I., Scoville, N. Z., Masson, C. R., Zuckerman, B., & Phillips, T. G. 1986, ApJ, 309, 755

Beckwith, S., Skrutskie, M. F., Zuckerman, B., & Dyck, H. M. 1984, ApJ, 287, 793

Beckwith, S. V. W., & Sargent, A. I. 1991, ApJ, 381, 250

Beckwith, S. V. W., Sargent, A. I., Chini, R. S., & Guesten, R. 1990, AJ, 99, 924

Beichman, C. A., Myers, P. C., Emerson, J. P., Harris, S., Mathieu, R., Benson, P. J., & Jennings, R. E. 1986, ApJ, 307, 337

Benjamin, R. A. et al. 2003, PASP, 115, 953

——. 2005, ApJ, 630, L149

Bernasconi, P. A., & Maeder, A. 1996, A&A, 307, 829

Bessell, M. S. 1990, PASP, 102, 1181

Beuther, H., Schilke, P., Menten, K. M., Motte, F., Sridharan, T. K., & Wyrowski, F. 2002, ApJ, 566, 945

Beuther, H., & Shepherd, D. 2005, Cores to Clusters: Star Formation with Next Generation Telescopes. Edited by M.S. Nanda Kumar, 105

Birkmann, S. M., Krause, O., Hennemann, M., Henning, T., Steinacker, J., & Lemke, D. 2007, A&A, 474, 883

Bjorkman, J. E. 1997, Stellar Atmospheres : Theory and Observations : lectures held at the Astrophysics School IX, 497, 239

Bjorkman, J. E., & Wood, K. 2001, ApJ, 554, 615

Bless, R. C., & Savage, B. D. 1972, ApJ, 171, 293

Blitz, L. 1993, Protostars and planets III, 125

Bonnell, I. A., Vine, S. G., & Bate, M. R. 2004, MNRAS, 349, 735

Bouvier, J., Cabrit, S., Fernandez, M., Martin, E. L., & Matthews, J. M. 1993, A&A, 272, 176

Brott, I., & Hauschildt, P. H. 2005, Proceedings of the Gaia Symposium "The Three-Dimensional Universe with Gaia" (ESA SP-576). Held at the Observatoire de Paris-Meudon, 576, 565

Bujarrabal, V., Young, K., & Fong, D. 2008, A&A, 483, 839

Burrows, C. J. et al. 1996, ApJ, 473, 437

Calvet, N., D'Alessio, P., Hartmann, L., Wilner, D., Walsh, A., & Sitko, M. 2002, ApJ, 568, 1008

Calvet, N. et al. 2005, ApJ, 630, L185

Calvet, N., & Gullbring, E. 1998, ApJ, 509, 802

Calvet, N., Hartmann, L., Kenyon, S. J., & Whitney, B. A. 1994, ApJ, 434, 330

Calvet, N., Muzerolle, J., Briceño, C., Hernández, J., Hartmann, L., Saucedo, J. L., & Gordon, K. D. 2004, AJ, 128, 1294

Carciofi, A. C., Bjorkman, J. E., & Magalhães, A. M. 2004, ApJ, 604, 238

Cardelli, J. A., Clayton, G. C., & Mathis, J. S. 1989, ApJ, 345, 245

Carpenter, J. M., Wolf, S., Schreyer, K., Launhardt, R., & Henning, T. 2005, AJ, 129, 1049

Cassen, P., & Moosman, A. 1981, Icarus, 48, 353

Castelli, F., & Kurucz, R. L. 2004, ArXiv e-prints, astro-ph/0405087v1

Caulet, A., Gruendl, R. A., & Chu, Y.-H. 2008, ApJ, 678, 200

Cesaroni, R., Galli, D., Lodato, G., Walmsley, C. M., & Zhang, Q. 2007, Protostars and Planets V, 197

Chandler, C. J., & Richer, J. S. 2000, ApJ, 530, 851

Chandler, C. J., Terebey, S., Barsony, M., Moore, T. J. T., & Gautier, T. N. 1996, ApJ, 471, 308

Chandrasekhar, S. 1960, New York: Dover

Chengalur, J. N., Lewis, B. M., Eder, J., & Terzian, Y. 1993, ApJS, 89, 189

Chiang, E. I., & Goldreich, P. 1997, ApJ, 490, 368

Chu, Y.-H. et al. 2005, ApJ, 634, L189

Churchwell, E. 2002, ARA&A, 40, 27

Clarke, C. J., Bonnell, I. A., & Hillenbrand, L. A. 2000, Protostars and Planets IV, 151

Close, L. M., Roddier, F., Northcott, M. J., Roddier, C., & Graves, J. E. 1997, ApJ, 478, 766

Cohen, M. 1973, MNRAS, 161, 97

Cohen, M. et al. 2007, ApJ, 669, 343

Cohen, M., Wheaton, W. A., & Megeath, S. T. 2003, AJ, 126, 1090

Cohen, R. S., Cong, H., Dame, T. M., & Thaddeus, P. 1980, ApJ, 239, L53

Cotera, A. S. et al. 2001, ApJ, 556, 958

Crapsi, A., van Dishoeck, E. F., Hogerheijde, M. R., Pontoppidan, K. M., & Dullemond, C. P. 2008, A&A, 486, 245

Cyganowski, C. et al. 2008, accepted for publication in AJ

D'Alessio, P., Calvet, N., & Hartmann, L. 2001, ApJ, 553, 321

D'Alessio, P., Calvet, N., Hartmann, L., Franco-Hernández, R., & Servín, H. 2006, ApJ, 638, 314

D'Alessio, P., Calvet, N., Hartmann, L., Lizano, S., & Cantó, J. 1999, ApJ, 527, 893

D'Alessio, P., Canto, J., Calvet, N., & Lizano, S. 1998, ApJ, 500, 411

D'Alessio, P., Merín, B., Calvet, N., Hartmann, L., & Montesinos, B. 2005, Revista Mexicana de Astronomia y Astrofisica, 41, 61

Dame, T. M. et al. 1987, ApJ, 322, 706

Darwin, G. 1889, Philosophical Transactions of the Royal Society of London. A, 1

Deharveng, L., Lefloch, B., Kurtz, S., Nadeau, D., Pomarès, M., Caplan, J., & Zavagno, A. 2008, A&A, 482, 585

Demyk, K., Jones, A. P., Dartois, E., Cox, P., & D'Hendecourt, L. 1999, A&A, 349, 267

Desch, S. J., & Mouschovias, T. C. 2001, ApJ, 550, 314

Dowell, C. D. et al. 2003, Millimeter and Submillimeter Detectors for Astronomy. Edited by Phillips, 4855, 73

Draine, B. T. 2003, ARA&A, 41, 241

Draine, B. T., & Lee, H. M. 1984, ApJ, 285, 89

Dullemond, C. P., Dominik, C., & Natta, A. 2001, ApJ, 560, 957

Duschl, W. J., Gail, H.-P., & Tscharnuter, W. M. 1996, A&A, 312, 624

Dutrey, A., Guilloteau, S., Duvert, G., Prato, L., Simon, M., Schuster, K., & Menard, F. 1996, A&A, 309, 493

Dutrey, A., Guilloteau, S., & Simon, M. 1994, A&A, 286, 149

Elmegreen, B. G., & Lada, C. J. 1977, ApJ, 214, 725

Evans, N. J. et al. 2003, PASP, 115, 965

Fazio, G. G. et al. 2004, ApJS, 154, 10

Felli, M., Testi, L., Schuller, F., & Omont, A. 2002a, VizieR On-line Data Catalog, 339, 20971

——. 2002b, A&A, 392, 971

Flaherty, K. M., Pipher, J. L., Megeath, S. T., Winston, E. M., Gutermuth, R. A., Muzerolle, J., Allen, L. E., & Fazio, G. G. 2007, ApJ, 663, 1069

Flynn, C., Holmberg, J., Portinari, L., Fuchs, B., & Jahreiß, H. 2006, MNRAS, 372, 1149

Foster, P. 1994, Clouds; cores and low mass stars, 65, 105

Foster, P. N., & Chevalier, R. A. 1993, ApJ, 416, 303

Fraser, H. J., Collings, M. P., McCoustra, M. R. S., & Williams, D. A. 2001, MNRAS, 327, 1165

Fukagawa, M. et al. 2004, ApJ, 605, L53

Furlan, E. et al. 2005, ApJ, 628, L65

Galli, D. 2005, Ap&SS, 295, 43

Galli, D., & Shu, F. H. 1993, ApJ, 417, 220

Gillett, F. C., & Forrest, W. J. 1973, ApJ, 179, 483

Goicoechea, J. R., Berné, O., Gerin, M., Joblin, C., & Teyssier, D. 2008, ApJ, 680, 466

Goodwin, S. P., Nutter, D., Kroupa, P., Ward-Thompson, D., & Whitworth, A. P. 2008, A&A, 477, 823

Goodwin, S. P., Whitworth, A. P., & Ward-Thompson, D. 2004, A&A, 423, 169

Gould, R. J., & Salpeter, E. E. 1963, ApJ, 138, 393

Grady, C. A., Woodgate, B., Bruhweiler, F. C., Boggess, A., Plait, P., Lindler, D. J., Clampin, M., & Kalas, P. 1999, ApJ, 523, L151

Green, J. D., Hartmann, L., Calvet, N., Watson, D. M., Ibrahimov, M., Furlan, E., Sargent, B., & Forrest, W. J. 2006, ApJ, 648, 1099

Greene, T. P., Wilking, B. A., Andre, P., Young, E. T., & Lada, C. J. 1994, ApJ, 434, 614

Groenewegen, M. A. T., & Blommaert, J. A. D. L. 2005, A&A, 443, 143

Grosso, N., Alves, J., Wood, K., Neuhäuser, R., Montmerle, T., & Bjorkman, J. E. 2003, ApJ, 586, 296

Gutermuth, R. A., Megeath, S. T., Muzerolle, J., Allen, L. E., Pipher, J. L., Myers, P. C., & Fazio, G. G. 2004, ApJS, 154, 374

Habart, E., Natta, A., & Krügel, E. 2004, A&A, 427, 179

Haisch, K. E., Lada, E. A., & Lada, C. J. 2001a, ApJ, 553, L153

Haisch, K. E., Lada, E. A., Piña, R. K., Telesco, C. M., & Lada, C. J. 2001b, AJ, 121, 1512

Haro, G. 1952, ApJ, 115, 572

Hartigan, P., Edwards, S., & Ghandour, L. 1995, ApJ, 452, 736

Hartmann, L. 2001, Accretion Processes in Star Formation

Hartmann, L., Calvet, N., Gullbring, E., & D'Alessio, P. 1998, ApJ, 495, 385

Hartmann, L., Kenyon, S., & Hartigan, P. 1993, Protostars and planets III, 497

Hartmann, L., & Kenyon, S. J. 1985, ApJ, 299, 462

——. 1996, ARA&A, 34, 207

Hartmann, L., Megeath, S. T., Allen, L., Luhman, K., Calvet, N., D'Alessio, P., Franco-Hernandez, R., & Fazio, G. 2005, ApJ, 629, 881

Harvey, P., Merín, B., Huard, T. L., Rebull, L. M., Chapman, N., Evans, N. J., & Myers, P. C. 2007, ApJ, 663, 1149

Harvey, P. M. et al. 2006, ApJ, 644, 307

——. 2008, ApJ, 680, 495

Hatchell, J., & van der Tak, F. F. S. 2003, A&A, 409, 589

Heathcote, S., Morse, J. A., Hartigan, P., Reipurth, B., Schwartz, R. D., Bally, J., & Stone, J. M. 1996, AJ, 112, 1141

Hennemann, M., Birkmann, S. M., Krause, O., & Lemke, D. 2008, A&A, 485, 753

Herbig, G. H. 1951, ApJ, 113, 697

——. 1952, Journal of the Royal Astronomical Society of Canada, 46, 222

——. 1957a, Non-stable stars, 3, 3

——. 1957b, ApJ, 125, 612

——. 1960, ApJS, 4, 337

Herbst, W., Herbst, D. K., Grossman, E. J., & Weinstein, D. 1994, AJ, 108, 1906

Hildebrand, R. H. 1983, ROYAL ASTRON. SOC. QUART. JRN. V.24, 24, 267

Hillenbrand, L. A. 1997, AJ, 113, 1733

Hoare, M. G., Lumsden, S. L., Oudmaijer, R. D., Busfield, A. L., King, T. L., & Moore, T. L. J. 2004, Milky Way Surveys: The Structure and Evolution of our Galaxy, 317, 156

Hogerheijde, M. R., van Dishoeck, E. F., Blake, G. A., & van Langevelde, H. J. 1998, ApJ, 502, 315

Hollenbach, D., Johnstone, D., Lizano, S., & Shu, F. 1994, ApJ, 428, 654

Hora, J. L. et al. 2008, AJ, 135, 726

Hora, J. L., Latter, W. B., Allen, L. E., Marengo, M., Deutsch, L. K., & Pipher, J. L. 2004, ApJS, 154, 296

Houck, J. R. et al. 2004, ApJS, 154, 18

Indebetouw, R. et al. 2005, ApJ, 619, 931

Indebetouw, R., Robitaille, T. P., Whitney, B. A., Churchwell, E., Babler, B., Meade, M., Watson, C., & Wolfire, M. 2007, ApJ, 666, 321

Jeans, J. 1902, Philosophical Transactions of the Royal Society of London. A, 1

Jennings, R. E., Cameron, D. H. M., Cudlip, W., & Hirst, C. J. 1987, Royal Astronomical Society, 226, 461

Jørgensen, J. K. et al. 2006a, ApJ, 645, 1246

Jørgensen, J. K., Johnstone, D., van Dishoeck, E. F., & Doty, S. D. 2006b, A&A, 449, 609

Jørgensen, J. K. et al. 2005, ApJ, 631, L77

Joy, A. H. 1945, ApJ, 102, 168

Jura, M. 1986, ApJ, 303, 327

Kemper, F., Vriend, W. J., & Tielens, A. G. G. M. 2004, ApJ, 609, 826

Kenyon, S. J., Calvet, N., & Hartmann, L. 1993a, ApJ, 414, 676

Kenyon, S. J., & Hartmann, L. 1987, ApJ, 323, 714

——. 1995, ApJS, 101, 117

Kenyon, S. J. et al. 1994, AJ, 107, 2153

Kenyon, S. J., Hartmann, L. W., Strom, K. M., & Strom, S. E. 1990, AJ, 99, 869

Kenyon, S. J., Whitney, B. A., Gomez, M., & Hartmann, L. 1993b, ApJ, 414, 773

Kenyon, S. J., Yi, I., & Hartmann, L. 1996, ApJ, 462, 439

Kessler, M. F. et al. 1996, A&A, 315, L27

Keto, E. 2007, ApJ, 666, 976

Kim, S.-H., Martin, P. G., & Hendry, P. D. 1994, ApJ, 422, 164

Kimeswenger, S. 2001, Revista Mexicana de Astronomia y Astrofisica, 37, 115

Kitamura, Y., Momose, M., Yokogawa, S., Kawabe, R., Tamura, M., & Ida, S. 2002, ApJ, 581, 357

Koerner, D. W., Sargent, A. I., & Beckwith, S. V. W. 1993, Icarus, 106, 2

Konigl, A., & Pudritz, R. E. 2000, Protostars and Planets IV (Book - Tucson: University of Arizona Press; eds Mannings, 759

Kroupa, P. 2001, MNRAS, 322, 231

Krumholz, M. R., McKee, C. F., & Klein, R. I. 2005, ApJ, 618, L33

Kuan, P. 1975, ApJ, 202, 425

Kuhi, L. V. 1974, A&AS, 15, 47

Lada, C. J. 1987, IN: Star forming regions; Proceedings of the Symposium, 115, 1

Lada, C. J., & Adams, F. C. 1992, ApJ, 393, 278

Lada, C. J., & Lada, E. A. 2003, ARA&A, 41, 57

Lada, C. J. et al. 2006, AJ, 131, 1574

Lamers, H. J. G. L. M., & Cassinelli, J. P. 1999, Introduction to Stellar Winds

Laor, A., & Draine, B. T. 1993, ApJ, 402, 441

Larson, R. B. 1981, Royal Astronomical Society, 194, 809

Larson, R. B., & Starrfield, S. 1971, A&A, 13, 190

Lecar, M., Podolak, M., Sasselov, D., & Chiang, E. 2006, ApJ, 640, 1115

Leger, A., & Puget, J. L. 1984, A&A, 137, L5

Lin, D. N. C., & Papaloizou, J. 1979a, MNRAS, 188, 191

——. 1979b, MNRAS, 186, 799

Lindqvist, M., Winnberg, A., Habing, H. J., & Matthews, H. E. 1992, A&AS, 92, 43

Loinard, L., Rodríguez, L. F., D'Alessio, P., Wilner, D. J., & Ho, P. T. P. 2002, ApJ, 581, L109

Lombardi, M., Alves, J., & Lada, C. J. 2006, A&A, 454, 781

Lonsdale, C. J. et al. 2003, PASP, 115, 897

Looney, L. W., Mundy, L. G., & Welch, W. J. 2003, ApJ, 592, 255

Lucas, P. W., & Roche, P. F. 1997, MNRAS, 286, 895

Lucy, L. B. 1999, A&A, 344, 282

Lugo, J., Lizano, S., & Garay, G. 2004, ApJ, 614, 807

Luhman, K. L., Whitney, B. A., Meade, M. R., Babler, B. L., Indebetouw, R., Bracker, S., & Churchwell, E. B. 2006, ApJ, 647, 1180

Lutz, D. 1999, The Universe as Seen by ISO. Eds. P. Cox & M. F. Kessler. ESA-SP 427., 427, 623

Lynden-Bell, D., & Pringle, J. E. 1974, MNRAS, 168, 603

Marengo, M., Reiter, M., & Fazio, G. G. 2008, Ixth torino workshop on evolution and nucleosynthesis in agb stars and the iind perugia workshop on nuclear astrophysics. aip conference proceedings

Marsh, K. A., & Mahoney, M. J. 1992, ApJ, 395, L115

——. 1993, ApJ, 405, L71

Masunaga, H., & Inutsuka, S.-I. 2000, ApJ, 531, 350

Mathieu, R. D. 1994, ARA&A, 32, 465

Mathis, J. S., Rumpl, W., & Nordsieck, K. H. 1977, ApJ, 217, 425

McKee, C. F., & Tan, J. C. 2003, ApJ, 585, 850

Megeath, S. T. et al. 2004, ApJS, 154, 367

——. 2005a, Massive star birth: A crossroads of Astrophysics, 227, 383

Megeath, S. T., Hartmann, L., Luhman, K. L., & Fazio, G. G. 2005b, ApJ, 634, L113

Meixner, M. et al. 2006, AJ, 132, 2268

Mendoza, E. E. 1966, ApJ, 143, 1010

——. 1968, ApJ, 151, 977

Mercer, E. P. et al. 2007, ApJ, 656, 242

Merin, B. et al. 2008, eprint arXiv, 0803, 1504

Miyake, K., & Nakagawa, Y. 1993, Icarus, 106, 20

——. 1995, ApJ, 441, 361

Mohanty, S., Jayawardhana, R., & Basri, G. 2005, ApJ, 626, 498

Moriarty-Schieven, G. H., Butner, H. M., & Wannier, P. G. 1995a, ApJ, 445, L55

Moriarty-Schieven, G. H., Wannier, P. G., Mangum, J. G., Tamura, M., & Olmsted, V. K. 1995b, ApJ, 455, 190

Mueller, K. E., Shirley, Y. L., Evans, N. J., & Jacobson, H. R. 2002, ApJS, 143, 469

Murakami, H. et al. 2007, Publications of the Astronomical Society of Japan, 59, 369

Myers, P. C., Fuller, G. A., Mathieu, R. D., Beichman, C. A., Benson, P. J., Schild, R. E., & Emerson, J. P. 1987, ApJ, 319, 340

Nakamura, F., Matsumoto, T., Hanawa, T., & Tomisaka, K. 1999, ApJ, 510, 274

Neugebauer, G. et al. 1984, ApJ, 278, L1

Nutter, D., & Ward-Thompson, D. 2007, MNRAS, 374, 1413

Omont, A. et al. 2003, A&A, 403, 975

Omukai, K., & Palla, F. 2001, ApJ, 561, L55

Osorio, M., Lizano, S., & D'Alessio, P. 1999, ApJ, 525, 808

Ossenkopf, V. 1993, A&A, 280, 617

Ossenkopf, V., & Henning, T. 1994, A&A, 291, 943

Padgett, D. L., Brandner, W., Stapelfeldt, K. R., Strom, S. E., Terebey, S., & Koerner, D. 1999, AJ, 117, 1490

Persi, P., Gómez, M., Tapia, M., Roth, M., DeBuizer, J. M., & Marenzi, A. R. 2008, AJ, 135, 2279

Pinte, C. et al. 2008, eprint arXiv, 0808, 619

Poulton, C. J., Robitaille, T. P., Greaves, J. S., Bonnell, I. A., Williams, J. P., & Heyer, M. H. 2008, MNRAS, 384, 1249

Povich, M. S. et al. 2008, submitted to ApJ

Preibisch, T., Weigelt, G., & Zinnecker, H. 2001, The Formation of Binary Stars, 200, 69

Price, S. D., Egan, M. P., Carey, S. J., Mizuno, D. R., & Kuchar, T. A. 2001, AJ, 121, 2819

Pringle, J. E. 1981, ARA&A, 19, 137

Pudritz, R. E., Ouyed, R., Fendt, C., & Brandenburg, A. 2007, Protostars and Planets V, 277

Reach, W. T. et al. 2005, PASP, 117, 978

Reipurth, B., & Bally, J. 2001, ARA&A, 39, 403

Ressler, M. E., & Barsony, M. 2003, ApJ, 584, 832

Rice, W. K. M., Wood, K., Armitage, P. J., Whitney, B. A., & Bjorkman, J. E. 2003, MNRAS, 342, 79

Rieke, G. H., & Lebofsky, M. J. 1985, ApJ, 288, 618

Rieke, G. H. et al. 2004, ApJS, 154, 25

Rucinski, S. M. 1985, AJ, 90, 2321

Rydgren, A. E., Strom, S. E., & Strom, K. M. 1976, ApJS, 30, 307

Sahai, R., Claussen, M., Contreras, C. S., Morris, M., & Sarkar, G. 2008, ApJ, 680, 483

Samus, N. N., Durlevich, O. V., & et al. 2004, VizieR On-line Data Catalog, 2250, 0

Sanders, D. B., Scoville, N. Z., & Solomon, P. M. 1985, ApJ, 289, 373

Seale, J. P., & Looney, L. W. 2008, ApJ, 675, 427

Sellgren, K. 1984, ApJ, 277, 623

Shakura, N. I., & Syunyaev, R. A. 1973, A&A, 24, 337

Shang, H., Li, Z.-Y., & Hirano, N. 2007, Protostars and Planets V, 261

Shepherd, D. 2005, Massive star birth: A crossroads of Astrophysics, 227, 237

Shepherd, D. S. et al. 2007, ApJ, 669, 464

Shu, F., Najita, J., Ostriker, E., Wilkin, F., Ruden, S., & Lizano, S. 1994, ApJ, 429, 781

Shu, F. H. 1977, ApJ, 214, 488

Shu, F. H., Adams, F. C., & Lizano, S. 1987, ARA&A, 25, 23

Sicilia-Aguilar, A. et al. 2006, ApJ, 638, 897

Siess, L., Dufour, E., & Forestini, M. 2000, A&A, 358, 593

Simon, J. D. et al. 2007, ApJ, 669, 327

Simon, R., Rathborne, J. M., Shah, R. Y., Jackson, J. M., & Chambers, E. T. 2006, ApJ, 653, 1325

Sjouwerman, L. O., van Langevelde, H. J., Winnberg, A., & Habing, H. J. 1998, A&AS, 128, 35

Skrutskie, M. F. et al. 2006, AJ, 131, 1163

Sollins, P. K., Zhang, Q., Keto, E., & Ho, P. T. P. 2005, ApJ, 624, L49

Stamatellos, D., Whitworth, A. P., Bisbas, T., & Goodwin, S. 2007, A&A, 475, 37

Stapelfeldt, K. R., Krist, J. E., Menard, F., Bouvier, J., Padgett, D. L., & Burrows, C. J. 1998, ApJL, 502, L65

Stapelfeldt, K. R., Ménard, F., Watson, A. M., Krist, J. E., Dougados, C., Padgett, D. L., & Brandner, W. 2003, ApJ, 589, 410

Stark, A. A., & Blitz, L. 1978, ApJ, 225, L15

Stark, D. P., Whitney, B. A., Stassun, K., & Wood, K. 2006, ApJ, 649, 900

Stutzki, J., Bensch, F., Heithausen, A., Ossenkopf, V., & Zielinsky, M. 1998, A&A, 336, 697

Tamura, M., Gatley, I., Waller, W., & Werner, M. W. 1991, ApJ, 374, L25

Tamura, M., Ohashi, N., Hirano, N., Itoh, Y., & Moriarty-Schieven, G. H. 1996, AJ, 112, 2076

Terebey, S., Beichman, C. A., Gautier, T. N., & Hester, J. J. 1990, ApJ, 362, L63

Terebey, S., Chandler, C. J., & Andre, P. 1993, ApJ, 414, 759

Terebey, S., Shu, F. H., & Cassen, P. 1984, ApJ, 286, 529

Tobin, J. J., Hartmann, L., Calvet, N., & D'Alessio, P. 2008, ApJ, 679, 1364

Tout, C. A., & Pringle, J. E. 1992, Royal Astronomical Society, 259, 604

Ulrich, R. K. 1976, ApJ, 210, 377

Valenti, J. A., Basri, G., & Johns, C. M. 1993, AJ, 106, 2024

van der Marel, R. P., Alves, D. R., Hardy, E., & Suntzeff, N. B. 2002, AJ, 124, 2639

van der Tak, F. F. S., van Dishoeck, E. F., Evans, N. J., & Blake, G. A. 2000, ApJ, 537, 283

van Dishoeck, E. F. 2004, ARA&A, 42, 119

Velusamy, T., & Langer, W. D. 1998, Nature, 392, 685

Vicente, S. M., & Alves, J. 2005, A&A, 441, 195

Vig, S., Testi, L., Walmsley, M., Molinari, S., Carey, S., & Noriega-Crespo, A. 2007, A&A, 470, 977

Vorobyov, E. I., & Basu, S. 2005, ApJ, 633, L137

Watson, C. et al. 2008, ApJ, 681, 1341

Weaver, W. B., & Jones, G. 1992, ApJS, 78, 239

Weintraub, D. A., Zuckerman, B., & Masson, C. R. 1989, ApJ, 344, 915

Werner, M. W. et al. 2004, ApJS, 154, 1

White, R. J., & Hillenbrand, L. A. 2004, ApJ, 616, 998

Whitney, B. A., & Hartmann, L. 1993, ApJ, 402, 605

Whitney, B. A. et al. 2004a, ApJS, 154, 315

Whitney, B. A., Indebetouw, R., Bjorkman, J. E., & Wood, K. 2004b, ApJ, 617, 1177

Whitney, B. A., Kenyon, S. J., & Gomez, M. 1997, ApJ, 485, 703

Whitney, B. A. et al. 2008, AJ, 136, 18

Whitney, B. A., Wood, K., Bjorkman, J. E., & Cohen, M. 2003a, ApJ, 598, 1079

Whitney, B. A., Wood, K., Bjorkman, J. E., & Wolff, M. J. 2003b, ApJ, 591, 1049

Whittet, D. C. B., Gerakines, P. A., Hough, J. H., & Shenoy, S. S. 2001, ApJ, 547, 872

Whitworth, A. P., & Ward-Thompson, D. 2001, ApJ, 547, 317

Wolf, S. 2003, ApJ, 582, 859

Wolf, S., & Voshchinnikov, N. V. 2004, Computer Physics Communications, 162, 113

Wolfire, M. G., & Cassinelli, J. P. 1987, ApJ, 319, 850

Wood, D. O. S., & Churchwell, E. 1989, ApJ, 340, 265

Wood, K., Lada, C. J., Bjorkman, J. E., Kenyon, S. J., Whitney, B., & Wolff, M. J. 2002a, ApJ, 567, 1183

Wood, K., Smith, D., Whitney, B., Stassun, K., Kenyon, S. J., Wolff, M. J., & Bjorkman, K. S. 2001, ApJ, 561, 299

Wood, K., & Whitney, B. 1998, ApJ, 506, L43

Wood, K., Wolff, M. J., Bjorkman, J. E., & Whitney, B. 2002b, ApJ, 564, 887

Wood, K., Wolk, S. J., Stanek, K. Z., Leussis, G., Stassun, K., Wolff, M., & Whitney, B. 2000, ApJ, 542, L21

Wooden, D. H., Rank, D. M., Bregman, J. D., Witteborn, F. C., Tielens, A. G. G. M., Cohen, M., Pinto, P. A., & Axelrod, T. S. 1993, ApJS, 88, 477

Yorke, H. W., & Sonnhalter, C. 2002, ApJ, 569, 846

Young, C. H., & Evans, N. J. 2005, ApJ, 627, 293

Young, C. H. et al. 2004, ApJS, 154, 396

Young, C. H., Shirley, Y. L., Evans, N. J., & Rawlings, J. M. C. 2003, ApJS, 145, 111

Young, E. T., Lada, C. J., & Wilking, B. A. 1986, ApJ, 304, L45

Yun, J. L., Djupvik, A. A., Delgado, A. J., & Alfaro, E. J. 2008, A&A, 483, 209

Zealey, W. J., Suters, M. G., & Randall, P. R. 1993, ASTRON. SOC. OF AUSTRALIA. PROCEEDINGS V.10:3, 10, 203

Zinnecker, H., McCaughrean, M. J., & Wilking, B. A. 1993, Protostars and planets III, 429

Acronyms

2MASS	Two-Micron All-Sky Survey
AGB	asymptotic giant branch
AGN	active galactic nuclei
ALMA	*Atacama Large Millimetre/sub-millimetre Array*
BCD	basic calibrated data
CDF	cumulative distribution function
CTTS	Classical T Tauri Star
EPS	Encapsulated Postscript
ERT	*equation of radiation transfer*
FITS	Flexible Image Transport System
FWHM	full-width at half maximum
GLIMPSE	Galactic Legacy Infrared Mid-Plane Survey Extraordinaire
GMC	giant molecular cloud
HST	*Hubble Space Telescope*
IMF	initial mass function
IRAC	InfraRed Array Camera
IRAS	InfraRed Astronomical Satellite
IRS	InfraRed Spectrograph
ISO	Infrared Space Observatory
ISM	interstellar medium
JWST	*James Webb Space Telescope*
LMC	Large Magellanic Cloud
LPV	long period variable

LTE	local thermodynamic equilibrium
MHD	magneto-hydrodynamic
MIPS	Multiband Imaging Photometer for Spitzer
MSX	Midcourse Space eXperiment
OMC	Orion Molecular Cloud
PAH	polycyclic aromatic hydrocarbon
PBCD	post-basic calibrated data
PDF	probability distribution function
PMS	pre-main-sequence
PNe	planetary nebulae
PRF	point response function
PSF	point spread function
SED	spectral energy distribution
SMC	Small Magellanic Cloud
SSC	*Spitzer* Science Center
TMC	Taurus Molecular Cloud
UIR	unidentified infrared emission
WTTS	weak-lined T Tauri star
YSO	young stellar object
ZAMS	zero-age main-sequence